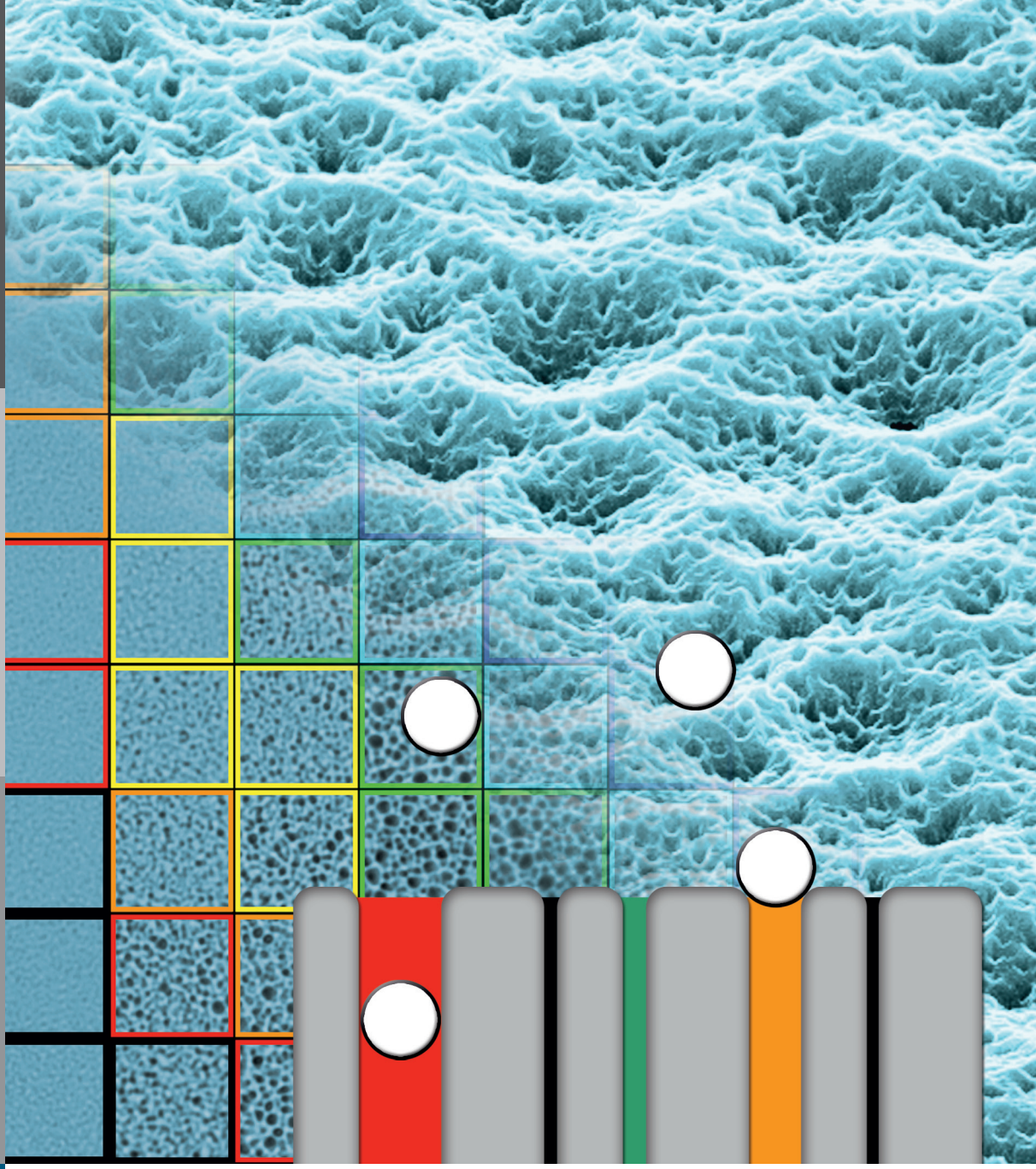

Growth, Etching, and Stability of Sputtered ZnO:Al for Thin-Film Silicon Solar Cells

Jorj Ian Owen

JÜLICH
FORSCHUNGSZENTRUM

Mitglied der Helmholtz-Gemeinschaft

Schriften des Forschungszentrums Jülich
Reihe Energie & Umwelt / Energy & Environment Band / Volume 125

Forschungszentrum Jülich GmbH
Institute of Energy and Climate Research (IEK)
Photovoltaics (IEK-5)

Growth, Etching, and Stability of Sputtered ZnO:Al for Thin-Film Silicon Solar Cells

Jorj Ian Owen

Schriften des Forschungszentrums Jülich
Reihe Energie & Umwelt / Energy & Environment Band / Volume 125

ISSN 1866-1793 ISBN 978-3-89336-749-8

Bibliographic information published by the Deutsche Nationalbibliothek.
The Deutsche Nationalbibliothek lists this publication in the Deutsche
Nationalbibliografie; detailed bibliographic data are available in the
Internet at http://dnb.d-nb.de.

Publisher and Distributor:	Forschungszentrum Jülich GmbH Zentralbibliothek 52425 Jülich Phone +49 (0) 24 61 61-53 68 · Fax +49 (0) 24 61 61-61 03 e-mail: zb-publikation@fz-juelich.de Internet: http://www.fz-juelich.de/zb
Cover Design:	Grafische Medien, Forschungszentrum Jülich GmbH
Printer:	Grafische Medien, Forschungszentrum Jülich GmbH
Copyright:	Forschungszentrum Jülich 2011

Schriften des Forschungszentrums Jülich
Reihe Energie & Umwelt / Energy & Environment Band / Volume 125

D 82 (Diss.,RWTH Aachen University, 2011)

ISSN 1866-1793
ISBN 978-3-89336-749-8

The complete volume is freely available on the Internet on the Jülicher Open Access Server (JUWEL)
at http://www.fz-juelich.de/zb/juwel

Table of Contents

List of Figures

List of Tables

Lists of Abbreviations

acronym	meaning
AFM	atomic force microscope
AM 1.5	solar spectrum at an air mass of 1.5
CG	Corning glass
CVD	chemical vapor deposition
DC	direct current (constant electric potential)
DI	deionized
FIB	focused ion beam
FWHM	full width at half maximum
i-type	intrinsic (not doped)
MF	mid-frequency (40 kHz)
mpp	maximum power point
n-type	negatively doped
PECVD	plasma-enhanced chemical vapor deposition
PEN	polyethylene naphthalate
pH	potential of hydrogen
p-type	positively doped
RF	radio frequency (13.56 MHz)
RMS	root mean square
RT	room temperature (approximately 25 °C)
SEM	scanning electron microscope
SIMS	secondary ion mass spectrometer
STDV	standard deviation
STM	scanning tunneling microscope
TCO	transparent conductive oxide
TEM	transmission electron microscope
XRD	x-ray diffraction

chemical symbols	meaning
Ag	silver
Al, Al^{3+}	aluminum, aluminum ion
Al_2O_3	aluminum oxide
Ar, Ar^+	argon, argon ion
B, B^{3+}	boron, boron ion
$B(CH_3)_3$	trimethylborane
CdO:In	indium-doped cadmium oxide
CH_2I_2	diiodomethane
CH_3CO_2H	acetic acid
Cl, Cl^-	chlorine, chloride ion
CO_2	carbon dioxide
Cs, Cs^+	cesium, cesium ion
D, D^-	deuterium, deuterium ion
D_2O	deuterium oxide (heavy or deuterated water)
F, F^-	fluorine, fluoride ion
Ga, Ga^{3+}	gallium, gallium ion
GaAr	gallium arsenide
H, H_2	hydrogen, hydrogen molecule
HCl	hydrochloric acid
HF	hydrofluoric acid
HNO_3	nitric acid
H_2O	water
H_2O_2	hydrogen peroxide
H_3O^+	hydronium ion
H_3PO_4	phosphoric acid
H_2SO_4	sulfuric acid
In, In^{3+}	indium, indium ion
In_2O_3:Sn	tin-doped indium oxide
KOH	potassium hydroxide
MgO	magnesium oxide
N, N_2	nitrogen, nitrogen molecule
NaOH	sodium hydroxide
NF_3	nitrogen trifluoride
O, O_2	oxygen, oxygen molecule
OH^-	hydroxide ion
PH_3	phosphine
Pt	platinum
Si	silicon
SiH_4	silane
SiO_x	silicon oxide
SnO_2:F	fluorine-doped tin oxide
Zn, Zn^{2+}	zinc, zinc ion
ZnO, ZnO^-	zinc oxide, zinc oxide ion
ZnO:Al, ZnO:B	aluminum-doped zinc oxide, boron-doped zinc oxide
$Zn(OH)_2$	zinc hydroxide

units	meaning
A	ampere (electric current)
C	coulomb (electric charge)
c	centi (10^{-2})
eV	electron volt (work)
F	farad (capacitance)
g	gram (weight)
hr.	hour (time)
Hz	hertz (frequency)
J	joule (work)
K	Kelvin (temperature)
k	kilo (10^{3})
M	mega (10^{6})
mol	mole (6.022×10^{23})
m, m	milli (10^{-3}), meter (distance)
min.	minute (time)
n	nano (10^{-9})
Pa	Pascal (pressure)
RPM	rotations per minute (rotational frequency)
s	second (time)
sccm	standard cubic centimeter per minute (flow rate)
sq.	square (geometric)
V	volt (electric potential)
W	watt (rate of energy conversion)
w/w%	relative percent weight
°	degree (angle)
°C	degree Celsius (temperature)
µ	micro (10^{-6})
Ω	ohm (electrical resistance)

equation symbols	meaning
A	absorption
A_{col}	collision frequency factor
AFM_{mean}, $AFM_{95\%}$	mean AFM height, height at 95 % maximum AFM scan
a_{latt}, c_{latt}	lattice constants for a hexagonal crystal
a_0^*	effective Bohr radius
B	magnetic field
c	speed of light in vacuum (2.998×10^8 m/s)
c_n, c_μ, c_L	constants between 0 and 1 governing rate of asymptotic approach
d, d_{bulk}, d_{etch}, d_{surf}	thickness, thickness of bulk, thickness after etching, thickness of surface
E	electric field
E_a, E_b, E_F, E_γ	activation energy, barrier energy, Fermi energy, photon energy
e	electron charge (1.602×10^{-19} C)
FF	fill factor
F_L	Lorentz force
h, $\hbar$	Planck's constant (6.626×10^{-34} J s), reduced Planck's constant (1.054×10^{-34} J s)
I	current
j, j_x, j_{sc}, j_γ	current density, current density along particular direction, short circuit current density, photo current density
k	reaction rate
k_B	Boltzmann's constant (k_B=1.38110^{-23} J K^{-1})
L_{vert}, L_{lat}, L_∞	vertical grain size, lateral grain size (diameter), lateral grain size at infinite film thickness
m_e, m_e^*, m_h^*	mass of an electron (9.109×10^{-31} kg), effective mass of an electron, effective mass of a hole
N_e, N_γ	number of electron hole pairs, number of incident photons
n, n_{bulk}, n_{crit}, n_{meas}, n_{surf}, n_∞	carrier concentration, bulk carrier concentration, critical carrier concentration, measured carrier concentration, surface carrier concentration, carrier concentration at infinite film thickness
P_{ideal}, P_{mpp}, P_0	power of ideal diode, power at maximum power point, illuminated power
QE	quantum efficiency
Q_t	trap density
R	reflection
R_{el}	electronic resistance
R_{gas}	gas constant (8.314 J K^{-1} mol^{-1})
R_H, R_{bulk}, R_{meas}, R_{surf}	Hall coefficient, bulk Hall coefficient, measured Hall coefficient, surface Hall coefficient
R_{sh}	sheet resistance
SR	spectral response
T, T_m, T_s	absolute temperature, melting temperature, substrate temperature
T_t, T_d	total transmission, diffuse transmission
V, V_H, V_{oc}	voltage (electric potential), Hall voltage, open circuit voltage
v, v_{ave}	velocity, average velocity
z	height

equation symbols	meaning
β_{Br}	the full width at half max of a peak satisfying Bragg's equation
Δd	removed thickness
ΔE_{BM}	increase in optical band gap due to Burstein-Moss effect
ΔQE	change in quantum efficiency
δ_{RMS}	root mean square roughness
ε, ε_∞	static dielectric constant, high-frequency dielectric constant
ε_0	permittivity of free space (8.854×10^{-12} F/m)
θ, θ_{Br}	angle of inclination, angle satisfying Bragg's equation
λ	wavelength
μ, μ_{bulk}, μ_{gb}, μ_{meas}, μ_{surf}, μ_0, μ_∞	mobility, bulk mobility, grain boundary limited mobility, measured mobility, surface mobility, mobility within a grain, mobility at infinite film thickness
η	efficiency of energy conversion
π	ratio of circle circumference to diameter (3.142)
ρ	resistivity
σ, σ_{bulk}, σ_{meas}, σ_{surf},	conductivity, bulk conductivity, measured conductivity, surface conductivity
τ	average time between collisions
Φ_γ	photon flux
ω	angular frequency
ω_p	plasma frequency

Abstract

Aluminum-doped zinc oxide (ZnO:Al) can fulfill many requirements in thin-film solar cells, acting as (1) a transparent contact through which the incident light is transmitted, (2) part of the back reflector, and (3) a source of light scattering. Magnetron sputtered ZnO:Al thin-films are highly transparent, conductive, and are typically texturized by post-deposition etching in a dilute hydrochloric acid (HCl) solution to achieve light scattering. The ZnO:Al thin-film electronic and optical properties, as well as the surface texture after etching, depend on the deposition conditions and the post-deposition treatments. Despite having been used in thin-film solar cells for more than a decade, many aspects regarding the growth, effects of heat treatments, environmental stability, and etching of sputtered ZnO:Al are not fully understood. This work endeavors to further the understanding of ZnO:Al for the purpose improving silicon thin-film solar cell efficiency and reducing ZnO:Al production costs.

With regard to the growth of ZnO:Al, the influence of various deposition conditions on the resultant electrical and structural properties and their evolution with film thickness were studied. The surface electrical properties extracted from a multilayer model show that while carrier concentration of the surface layer saturates already at film thickness of 100 nm, the surface mobility continues to increases with film thickness, and it is concluded that electronic transport across grain boundaries limits mobility in ZnO:Al thin films. ZnO:Al deposited onto a previously etched ZnO:Al surface grows epitaxially, preserving both the original orientation and grain structure. Further, it is determined that a typical ZnO:Al used in thin-film silicon solar cells grows Zn-terminated on glass substrates.

Concerning the affects of heat treatments and stability, it is demonstrated that a layer of amorphous silicon can protect ZnO:Al from degradation during annealing, and the mobility of ZnO:Al films can be increased up to 76 cm^2/Vs by annealing at high temperatures. Further, it is observed that this annealing process does not affect the morphology of the film and increases the total transmission in the solar cell relevant portion of the spectrum. Accelerated aging in a damp-heat is shown to affect the mobility primarily, and is thus likely related to poor transport across grain boundaries. Using deuterium as an isotopic marker, it is observed that the deuterium uptake was fairly linear with time and penetrated the whole film within 24 hours. Additionally, the deuterium is quickly replaced by hydrogen upon damp-heat treatment in water. It is concluded that the electrical degradation is related to the penetration of water via grain boundaries, and that the bulk of the reactions causing this degradation are fairly weak, such as the formation of zinc hydroxide. Additionally, the annealed high-mobility ZnO:Al films prove to be very stable in the damp-heat environment, exhibiting electron mobilites above 70 cm^2/Vs after 1000 hours of exposure.

The initial points of attack during HCl etching of ZnO:Al, and the long-term etch evolution are shown to be related to certain grain boundaries built into the film during growth. The density of craters from an HCl etch is controllable by altering the temperature and concentration of the etching solution. It is further demonstrated that most acids exhibit etching behavior similar to that of HCl. Hydrofluoric acid (HF), however, exhibits unique etching characteristics with higher crater densities and sharper features. The crater density and shape are also shown to be controllable by etching in various concentrations of HF and in various mixtures of HF

and HCl. Additional etching experiments are made to develop a polycrystalline ZnO:Al etching model. It is shown that basic and acidic solutions attack the same points on a polycrystalline ZnO:Al sample. The dependence of crater density on the acid concentration, temperature, and type holds true for single crystal ZnO. Planar and cross-sectional transmission electron microscopy (TEM) measurements confirmed grain boundaries as the most prevalent catalysts for etching. A three-postulate etching model is proposed, the basics of which are: (1) every grain boundary has certain potential to etch, and this potential depends on the compactness of the grain boundary;(2) the etchant solution and conditions define an etching threshold, and grain boundaries with etching potentials above the threshold are actively etched; and (3) the vertical and horizontal etch rates are defined by the solution, and vertically limited etching leads to the characteristic crater opening angles while a horizontal limited etch yields sharper structures.

Examples on how the better understanding of ZnO:Al can lead to more efficient solar cells and more reliable ZnO:Al film preparation are also given. It is shown that the efficiency of amorphous silicon solar cells can be increased by optimizing the ZnO:Al crater size, and that the light trapping and efficiency in tandem silicon solar cells can be improved by fabricating modulated ZnO:Al surfaces. Finally, it is shown that by developing a better method for separating electro-optical optimization from texturization, industrially relevant low cost ZnO:Al films can be textured effectively, such that the efficiency of microcrystalline silicon solar cell on these substrates rival those of the relatively expensive laboratory ZnO:Al films.

Zusammenfassung

Aluminiumdotiertes Zinkoxid (ZnO:Al) erfüllt mehrere Funktionen in Dünnschicht-Solarzellen: es dient (1) als transparente Kontaktschicht, durch die das einfallende Licht in die Solarzelle einfällt, (2) als Teil des Rückreflektors und (3) erzeugt effektive Lichtstreuung durch seine raue Oberfläche. Magnetron-gesputterte ZnO:Al-Schichten sind hochtransparent und leitfähig und werden in der Regel nach der Abscheidung durch einen Ätzprozess in verdünnter Salzsäure (HCl) aufgeraut. Die elektronischen und optischen Eigenschaften der ZnO:Al-Schichten sowie die Oberflächenstruktur nach dem Ätzen hängen empfindlich von den Depositionsbedingungen und möglichen anschließenden Nachbehandlungsprozessen ab. Obwohl gesputtertes ZnO:Al in Dünnschichtsolarzellen seit mehr als zehn Jahren als Frontkontakt verwendet wird, sind viele Aspekte bezüglich des Wachstums, des Einflusses thermischer Behandlung und des Ätzens nicht vollständig geklärt. Ziel dieser Arbeit ist es, das Verständnis von ZnO:Al zu erweitern, um mit diesen Erkenntnissen den Wirkungsgrad von Silizium-Dünnschichtsolarzellen zu verbessern und die Produktionskosten für ZnO:Al zu senken.

Im Hinblick auf das Wachstum von ZnO:Al wird der Einfluss der Depositionsbedingungen auf die daraus resultierenden elektrischen und strukturellen Eigenschaften untersucht. Die elektrischen Eigenschaften des ZnO:Al-Materials nahe der Schichtoberfläche werden aus einem Mehrschicht-Modell extrahiert. Während die Ladungsträgerkonzentration nahe der Oberfläche bereits nach nur 100 nm eine Sättigung erreicht, nimmt die Beweglichkeit auch noch oberhalb von 500 nm weiter zu. Daraus lässt sich folgern, dass Korngrenzen den elektronischen Transport in ZnO:Al-Schichten limitieren. ZnO:Al, welches auf eine zuvor geätzte ZnO:Al-Oberfläche abgeschieden wurde, wächst epitaktisch, wobei sowohl die ursprüngliche Orientierung als auch die Kornstruktur erhalten bleibt. Ferner wird indirekt nachgewiesen, dass typisches ZnO:Al, welches in Silizium-Dünnschichtsolarzellen verwendet wird, Zn-terminiert auf Glassubstraten wächst.

Im weiteren Verlauf dieser Arbeit wird der Einfluss der thermischen Behandlung der Schichten untersucht und es wird gezeigt, dass eine amorphe Siliziumschicht das ZnO:Al vor Degradation während der thermischen Behandlung schützen kann und die Beweglichkeit der ZnO:Al-Schichten durch Tempern bei hohen Temperaturen auf Werte bis zu 76 cm^2/Vs erhöht werden kann. Diese thermische Behandlung hat keinen Einfluss auf die Morphologie des ZnO:Al-Films und die Transmission des ZnO:Al im für die Solarzellen relevanten Spektralbereich wird dadurch erhöht. Es stellt sich heraus, dass beschleunigte Alterung in feuchter Wärme den Transport über Korngrenzen behindert und somit in erster Linie die Beweglichkeit beeinträchtigt. Mit Deuterium als Isotopen-Markierung wird beobachtet, dass die Deuterium-Aufnahme nahezu linear mit der Zeit zunimmt, und dass das Deuterium innerhalb von 24 Stunden die gesamte Schicht durchdringt. Zusätzlich kann Deuterium zu einem großen Teil bei feuchter Wärme-Behandlung schnell durch Wasserstoff ausgetauscht werden. Daraus lässt sich folgern, dass die elektrische Degradation dem Eindringen von Wasser über Korngrenzen zugeordnet werden kann und die Mehrheit der beteiligten Prozesse auf relativ schwache Reaktionen zurückzuführen sind, wie die Bildung von Zinkhydroxid. Zusätzlich erweisen sich die getemperten ZnO:Al-Dünnschichten als sehr stabil in einer feuchten und warmen Umgebung und besitzen selbst nach 1000 Stunden Exposition noch eine Elektronenbeweglichkeit von über 70 cm^2/Vs.

Zusammenfassung

Die anfänglichen Angriffspunkte beim Ätzen von ZnO:Al in Säuren und die langfristige HCl-Ätzentwicklung werden auf bestimmte Korngrenzen zurückgeführt, die sich während des Wachstums in der Schicht gebildet haben. Die sich entwickelnde Kraterdichte beim Ätzen in HCl ist durch Veränderung der Temperatur und der Konzentration der Ätzlösung steuerbar. Weiterhin wird gezeigt, dass die meisten Säuren ein ähnliches Ätzverhalten wie HCl aufweisen. Flusssäure (HF) hingegen besitzt einzigartige Ätzeigenschaften und führt zu höheren Kraterdichten und steileren Strukturen auf ZnO:Al-Oberflächen. Die Kraterdichte und -form erweisen sich dabei als kontrollierbar durch die Konzentration von HF oder eine Mischung von HF und HCl. Zur Entwicklung eines Ätzmodells für polykristalline ZnO:Al-Schichten wurden zusätzliche Ätzexperimente durchgeführt. Dabei hat sich ergeben, dass basische und saure Lösungen die gleichen Strukturen auf einer polykristallinen ZnO:Al–Probe angreifen. Die Abhängigkeit der Kraterdichte von der Säurekonzentration, von der Temperatur und vom Typ der Säure gilt ebenso für einkristallines ZnO. Transmissionselektronenmikroskopie (TEM) in planarer Konfiguration und an ZnO:Al-Querschnitten bestätigen Korngrenzen als wichtigstes Kriterium für den Ätzangriff. Basierend auf den gewonnenen Erkenntnissen wird ein Ätzmodell mit drei wichtigen Postulaten vorgeschlagen: (1) jede Korngrenze besitzt ein gewisses Potential für einen Ätzangriff, welches von der Kompaktheit der Korngrenze abhängt; (2) die Ätzlösung und die Bedingungen des Ätzprozesses definieren eine Schwelle, Korngrenzen mit Ätzpotentialen oberhalb dieser Schwelle werden aktiv geätzt; (3) die vertikalen und horizontalen Ätzraten werden durch die Lösung definiert. Vertikal begrenztes Ätzen führt zu charakteristischen Krateröffnungswinkeln während horizontal begrenztes Ätzen steilere Strukturen liefert.

Abschießend werden Beispiele gegeben, wie das bessere Verständnis von ZnO:Al zu effizienteren Solarzellen und zu zuverlässigeren Herstellungsprozessen für ZnO:Al führt. Der Wirkungsgrad von amorphen Silizium-Solarzellen kann durch Optimierung der ZnO:Al-Kratergröße erhöht werden und der Lichteinfang sowie der Wirkungsgrad in Tandem-Silizium-Solarzellen kann durch die Herstellung modulierter ZnO:Al-Oberflächen verbessert werden. Die im Rahmen der Arbeit entwickelte Methode zur Trennung der elektro-optischen Optimierung von der Texturierung ermöglicht es industrierelevante, kostengünstige ZnO:Al-Schichten so effektiv zu texturieren, dass der Wirkungsgrad mikrokristalliner Silizium-Solarzellen auf solch günstigen TCO-Substraten mit denen auf relativ teuren Labor-ZnO:Al-Schichten konkurrieren kann.

1. Introduction

There are many reasons to switch to renewable energy sources: concerns about the limited supply of fossil fuels and uncertainties about how long reserves will hold out [1]; love of the environment or fears of the potential impact burning fossil fuels may have on it [2,3]; or concerns over energy security and dependency [4]. While sentiments such as these may motivate a minority of people to make a conscious change to renewable energy sources, the majority of people will not switch until it is in their best economic interest to do so [5].

The sun is the most prevalent source of energy on earth, with more energy incident in one hour than consumed by people in one year [6]. The first solar cell was made in 1954 using a junction between positively (p-type) and negatively (n-type) doped silicon [7]. For such p-n junction devices, the weakly bound electrons and holes diffuse into the neighboring p- and n-type regions, respectively, to settle in lower energy states and create a built-in electric potential. When light is absorbed electron-hole pairs (excitons) are generated; they diffuse in the material until recombination. When they reach the region of the electric field (space charge region), the excitons can be split as the electrons and holes are drawn towards the n- and p-type regions, respectively. Energy conversion efficiencies as high as 25 % have been achieved on monocrystalline silicon [8]. High-efficiency solar cells such as this, or the even more efficient multijunction solar cells with efficiencies over 40 % under concentrated illumination [9], are ideal for celestial or remote terrestrial applications, where transportation and installation are the greatest cost. These types of solar cells are far too expensive for day-to-day use, however, and low cost solar cells are necessary to reach grid parity, the point where the cost of solar power is equal to that of the predominantly fossil-based power grid [5].

Silicon thin-film solar cells are one such low-cost alternative, having active layers with only one percent the thickness (less than two micrometers) of that used in crystalline silicon solar cells [10]. Additionally, unlike crystalline solar cells, which are limited in size and shape to that of the ingot or otherwise created wafer, thin-film technology can be scaled to a given substrate, including low-cost large-area glass and flexible plastic or metal [11]. A typical structure for a silicon thin-film solar cell in superstrate configuration consists of a glass substrate, then a transparent conductive oxide (TCO) front contact, followed by the active silicon layers, and finally the metal back contact and reflector. The TCO is used to provide good electrical contact while absorbing or reflecting a minimum of the incoming light.

The thin active layers of a thin-film solar cell do not absorb as much light as the comparatively thick crystalline devices. To increase the effective path length the light takes through the solar cell, light scattering structures in combination with a back reflector are introduced [12]. For silicon thin-film solar cells, these light scattering structures are often introduced by the TCO layer [13,14]. A good TCO layer must therefore fulfill many requirements: it must be transparent over as much of the solar spectrum as possible, conductive enough to transport electrons without limiting the solar cell by a high sheet resistance, and must exhibit a rough

surface to introduce light trapping effects. Additionally, from a cost perspective, the material must be abundant and easy to deposit over large areas.

ZnO is one such material. It has a wide and direct band gap of 3.4 eV, making it transparent in the visible region, and can be easily made an n-tpye conductor by degenerately doping it (typically with a group 13 element). Both constituent elements are abundant, and can be deposited by large area processes such as sputtering, chemical vapor deposition (CVD), spray pyrolysis, and chemical solution deposition [13,15-17]. Of these ZnO deposition methods, sputtering and CVD have yielded substrates with good light trapping texture. The texture can be introduced to the ZnO surface during growth using CVD or sputtering under water vapor rich conditions [15,18]. For sputtered ZnO films, the light scattering textures are typically introduced after deposition by chemical etching in a hydrochloric acid (HCl) solution [19].

Despite having been used in thin-film solar cells for more than a decade, many aspects regarding the growth, electrical properties, and etching of sputtered aluminum-doped ZnO (ZnO:Al) are not fully understood. This work endeavors to further the understanding of ZnO:Al for the purpose of improving silicon thin-film solar cell efficiency and reducing ZnO:Al production costs.

ZnO grows in a wurtzite crystal structure, and it has been observed that sputtered ZnO films generally grow with the c-axis perpendicular to the underlying substrate [20,21]. The c-axis of a ZnO crystal is polar, and can thus be either Zn- or O-terminated. It has been observed that the electrical properties of sputtered doped ZnO depend strongly on the sputtering conditions, such as substrate temperature, pressure, and doping concentration, as well as the thickness of the film [22-26].

One of the challenges with sputtered doped ZnO:Al is finding the balance between electrical and optical properties. Conductivity can be increased by increasing the electron mobility, electron concentration, or film thickness. Increasing conductivity by increasing the electron concentration (doping), however, leads to an increase in free carrier absorption in the useful wavelength region of solar cells [27]. Simply increasing ZnO:Al thickness increases absorption, but also increases the cost of the resultant solar cell both in material and deposition time. The optimal way to increase conductivity is thus by increasing the mobility of the electrons. Ruske *et al.* introduced a method for improving mobility by capping ZnO:Al films with silicon then annealing them at high temperatures (650 °C) [28]; but heat treatments can also have detrimental effects on the electrical properties of ZnO:Al. For example, the accelerated aging of ZnO:Al in a damp-heat atmosphere has shown that the electrical conductivity decreases with exposure time [29,30].

Since sputtered ZnO:Al films are generally flat, they are often texturized by etching in an acidic solution to introduce light scattering surface features [19]. Texturizing after deposition allows for the separate optimization of electro-optical properties and surface texture. However, it has often been observed that the density and shape of the resultant craters depend strongly on deposition conditions [24,25,31], and the two processes (sputtering and etching) are not independent. Thus, the current state-of-the-art is to tailor the deposition conditions of ZnO:Al to optimize electrical, optical, and the resultant etch features simultaneously. This situation is complicated further when moving to industrial ZnO:Al thin-film production, as the throughput also needs to be taken into account.

Trends between the deposition and resultant surface structures after etching have been observed. Kluth *et al.* [25] modified the Thornton model of sputtered metal growth [32] to show

the relationship between the deposition parameters of temperature and pressure and etching properties. Specifically, parameters leading to compact film growth, such as a high substrate temperature or low deposition pressure, yield films where fewer craters form after etching. Berginski *et al.* furthered this empirical model by showing that increasing the dopant (aluminum) content increased the compactness of the ZnO:Al film, leading to a decrease in crater density.

The acidic etching process is well understood for ZnO:Al single crystal. Craters form only at defects on the Zn-terminated side, exhibiting crater walls that follow the (101) plane, and pyramid formation combined with fast overall etching on the O-terminated side [33,34]. However, very little has been published with regard to a polycrystalline ZnO:Al etch model [31,35].

This work will proceed as follows: First, in Chapter 2, a review of the relevant previous research is presented; showing the status of the prior knowledge provides a basis for the further experiments performed within this work. Next, the experimental techniques are presented in Chapter 3. This chapter describes not only the physical actions performed to make the samples, such as deposition and etching conditions, but also the experimental methods used to characterize the samples.

Results from new experiments on ZnO:Al begin in Chapter 4, which focuses on the growth of sputtered ZnO:Al on different substrates under various conditions. The evolution of ZnO film properties during deposition, stopping and restarting deposition, and breaking vacuum are investigated. The orientation of new ZnO:Al grown on a previously texturized ZnO:Al film, and the termination of the c-axis growth are determined.

Chapter 5 examines the effects heat treatments, such as annealing and damp-heat, have on sputtered ZnO:Al films further. The effects of annealing on the electrical and morphological properties of sputtered ZnO:Al thin-films are examined. To better understand the damp-heat degradation process, the accelerated aging process is performed in a deuterated water (D_2O) atmosphere.

The rest of the results chapters, Chapters 6-8, address the etching of ZnO:Al. Chapter 6 examines the etching of ZnO:Al thoroughly with focus on etching conditions like temperature, concentration, and type of etchant. Chapter 7 summarizes the etching trends observed in Chapter 6 and by others, gives additional clarifying experiments, and culminates with the presentation of an etching model for polycrystalline ZnO:Al.

While Chapters 4-7 are largely fundamental in nature, Chapter 8 is application oriented. It gives a few examples on how the goal of this work, developing a better understanding of sputtered ZnO:Al, can be used to create more efficient silicon thin-film solar cells and reduce the cost of ZnO:Al production. Various ZnO:Al films with specific etch morphologies are applied in amorphous and microcrystalline silicon single and tandem junction solar cells. A short summary and outlook on further work is provided in Chapter 9.

2. Fundamentals

This chapter presents the results upon which this work is based and to which this work relies for explanation. To begin, the various types of transparent conducting films are introduced and motivations for using ZnO as the TCO in thin-film solar cells are given. The structure, electrical properties, optical properties, and etching characteristics of ZnO are then discussed. Since these properties depend on one another, the discussion in the section is presented in as general a manner as possible, referring to the ZnO single crystal case when applicable. Sputter deposition, the process used to fabricate all ZnO:Al thin-films within this work, is then presented. All of the previously presented sections are brought together, discussing the growth models and trends observed previously between electrical, optical, and etching characteristics of sputtered ZnO films. The previously observed effects of post-deposition annealing and damp-heat treatments are discussed. Finally, the basics of a thin-film silicon solar cell fabrication and characterization are presented.

2.1. Transparent Conducting Films

To fabricate devices such as flat panel displays or thin-film solar cells, it is necessary to make electrical contact on a layer that must also be transparent to the emitted or incident photons. There are both organic and inorganic materials that fulfill the requirements to be both conductive and transparent in the visible range. On the organic side, conductive polymers such as poly(3,4-ethylenedioxythiophene), networks of carbon nanotubes, and graphene are possible materials [36-38]. On the inorganic side, degenerately doped metal oxides, often referred to as transparent conducting oxides (TCO), such as indium-doped cadmium oxide (CdO:In), tin-doped indium oxide (In_2O_3:Sn), fluorine-doped tin dioxide (SnO_2:F), and aluminum-doped zinc oxide (ZnO:Al) are potential candidates. Freeman *et al.* stated that a good TCO must fulfill three requirements: (1) the conduction band must have strong curvature to give high carrier mobilities; (2) the valence and conduction band must be separated by a band gap wide enough to transmit the visible spectrum; and (3) it must retain good optical properties with high doping levels [39]. In 2005, Minami published a review of the various TCOs [40].

For large scale production of high efficiency thin-film solar cells, considerations besides transparency and conductivity of a material must be taken into account. For sustainable large scale production, the scarcity of the composing elements [41] and costs of material production, as well as the ability to deposit on a large scale, cannot be ignored. For health and environmental consideration, the toxicology of the material must be taken into account. Additionally, for silicon thin-film solar cells, the ability to introduce light scattering textures within the transparent conductive layer should also be considered. With these additional constraints in

mind, the two best candidates for transparent contacts in thin-film silicon solar cells are SnO_2:F and ZnO:Al.

This work focuses solely on improving ZnO:Al for solar cell applications. It should, however, be noted that SnO_2:F has also proven to be a successful front contact in amorphous silicon thin film solar cells [14,42,43]. SnO_2:F and ZnO:Al have similar optical and electrical properties, but the chemical properties lend different advantages and disadvantages to each. SnO_2:F has a formation energy of 6.0 eV, as compared to ZnO at 3.6 eV, making it less susceptible to environmental or acidic degradation [43,44]. On the other hand, ZnO has proven much more stable than SnO_2 in a hydrogen plasma, such as those used in the plasma enhanced chemical vapor deposition (PECVD) of silicon [45,46].

It is worth noting additionally that ZnO can be doped by other column 13 elements, such as boron, gallium, and indium [15,47-49]. The bond lengths between gallium and oxygen are closest to those of zinc and oxygen [47].

2.2. ZnO Structure

Both undoped and doped ZnO generally crystallize in a wurtzite crystal structure, although they can be grown with zincblende structure when produced on another cubic lattice such as gallium arsenide (GaAr) [50], or with rocksalt structure when grown at high pressures or when strongly alloyed with another material such as magnesium oxide (MgO) [51,52]. The wurtzite crystal structure, as shown for ZnO in Figure 2.1, is part of the hexagonal crystal system and generally characterized by two lattice constants a=0.325 nm and c=0.521 nm as measured by x-ray diffraction (XRD) measurements at room temperature [53]. The ratio of c/a=1.60 is close to the ideal ratio for a hexagonal cell $c/a=(8/3)^{1/2}\approx1.63$. It can be thought of as two (one for each type of atom) interpenetrating hexagonal close-packed sublattices offset along the c-axis, so a unit cell has two of each type of atom (solid lines Figure 2.1). In this structure, atoms of one kind are tetrahedrally bonded to the four nearest neighbors of the other kind.

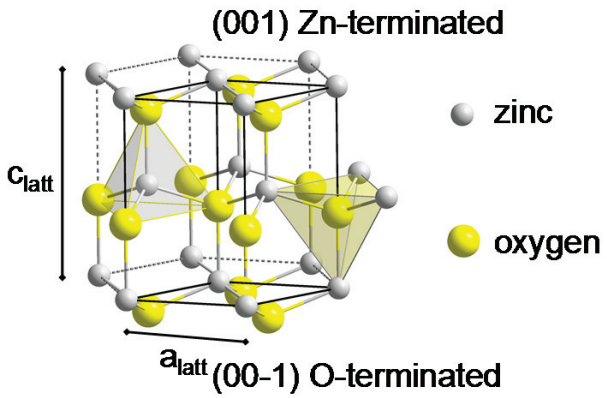

Figure 2.1: Wurtzite crystal structure of ZnO. The polar Zn- and O-terminated faces of the c-axis are indicated. The unit cell containing two of each atom is indicated by solid black lines. Zinc and oxygen atoms are tetrahedrally bonded to the four nearest oxygen and zinc atoms, respectively.

The wurtzite crystal structure does not have inversion symmetry along the c-axis, so the (001) and (00-1) planes are Zn- and O-terminated, respectively; see Figure 2.1. The Zn-O bond is primarily ionic, these polar bonds lead to planes of positively charged zinc and negatively charged oxygen atoms perpendicular to the c-axis. The combination of a lack of inversion symmetry and the polarization of the atomic planes gives ZnO the properties of being both piezoelectric (internal generation of an electric field resulting from an applied mechanical force, and *vice versa*) and pyroelectric (internal generation of an electric field resulting from a change in the crystal temperature, and *vice versa*).
ZnO has a density of 5.6 g/cm^3 at room temperature. The thermal expansion coefficients depend on temperature; at room temperature. they have a value of $\Delta a/a=4.8\text{x}10^{-6}$ K^{-1} (perpendicular to the c-axis) and $\Delta c/c=2.9\text{x}10^{-6}$ K^{-1} (parallel to the c-axis) [54]. At 327 °C (600 K), the thermal expansion coefficients are larger with values of $\Delta a/a=7.9\text{x}10^{-6}$ K^{-1} and $\Delta c/c=4.7\text{x}10^{-6}$ K^{-1} [55]. The melting point of ZnO is 1975 °C.

2.3. Electrical properties of ZnO

ZnO used as TCO in thin-film solar cells must be highly conductive. To understand the electrical properties of such a material, the Drude model for conduction in metals is first presented. The various types of doping and level to which a material can be doped are then discussed. The electrical transport in a material is limited by various scattering mechanisms; the scattering mechanisms present in ZnO:Al are discussed. Finally, the Hall effect, a method used to characterize the electrical properties of materials, is presented.

2.3.1. Conduction in Metals

It has long been known that the relationship between the current (I) flowing through a material depends proportionally on the voltage (V) applied across the material and inversely proportional to the resistance (R_{el}) of the material; as given by Ohm's law,

$$I = \frac{V}{R_{el}}. \tag{2.1}$$

A more generalized form of this law, which does not depend on the dimensions of the sample, states that the current density (j) at a given location in a material depends on the product of the electric field at the location (E) and the conductivity (σ) of the material,

$$\vec{j} = \sigma \vec{E}. \tag{2.2}$$

Where the conductivity and its inverse, resistivity (ρ),

$$\sigma = \frac{1}{\rho}, \tag{2.3}$$

depend on the material through which the current is flowing.

Although the conduction of electrons through a metal is essentially quantum mechanical in nature, in 1900 Drude proposed a very successful model for electron transport in metals [56]. In the Drude model, metals are assumed to consist of fixed positively charged ions and free negatively charged electrons. The only interaction considered is the collision between the mobile

electrons and the fixed ions. These assumptions allow the electrons to be treated as a gas and analyzed by kinetic theory. In this case, the current density is equal to the product of the electron density (n), the electron charge (e=1.602x10^{-19} C), and the average velocity of the electrons (v_{ave}),

$$\vec{j} = -ne\vec{v}_{ave} \quad \textbf{(2.4)}$$

In the absence of an electric field, an electron is just as likely to move in one direction as another, and the average velocity of the electrons is zero. When an electric field is applied, the electrons are accelerated opposite the electric field between collisions with fixed positive ions. The average electron velocity under these conditions is given by,

$$\vec{v}_{ave} = -\frac{e\tau}{m_e^*}\vec{E} \quad \textbf{(2.5)}$$

where τ is the average time between collisions, and m_e^* is the effective mass of the electrons. The effective mass is a way of taking into account the interactions not considered in the classical theory by assigning a mass other than that of an electron (m_e=9.109x10^{-31} kg). Thus, Equation (2.4) can be rewritten as

$$\vec{j} = \frac{ne^2\tau}{m_e^*}\vec{E} \quad \textbf{(2.6)}$$

In view of the general form of Ohm's law, Equation (2.2), the conductivity as given by the Drude model is

$$\sigma = \frac{ne^2\tau}{m_e^*} = en\mu \quad \textbf{(2.7)}$$

where carrier mobility (μ) is defined as the ratio of the average velocity achieved in an electric field to the strength of the electric field ($\mu = v_{ave}/E = e\tau/m_e^*$). For ZnO, the effective mass of an electron is m_e^*=0.24 m_e [57].

2.3.2. Doping ZnO

ZnO is a direct bandgap semiconductor with a gap of 3.4 eV. As a semiconductor, the intrinsic Fermi level (energy with a probability of occupation of half) lies within the bandgap. Thus, in stoichiometric ZnO, very few electrons are excited (thermally or optically) from the valence to the conduction band, exhibiting carrier densities as low as n=10^{14} cm^{-3} [58,59]. To use ZnO as a TCO, the carrier concentration must be increased by various means, including intrinsic, extrinsic, and hydrogen doping. When the carrier concentration is increased far enough, the ZnO becomes degenerately doped and it behaves as if it were a metal.

Intrinsic doping: Doping that results from defects within the crystal structure. In ZnO, the small deviations from the stoichiometric composition result in vacancies of oxygen atoms or zinc atoms on interstitial lattice sites. In such cases, the zinc valence electrons are not tetrahedrally bonded to oxygen atoms (see Figure 2.1). The Zn-Zn bond is much weaker, thus energies much smaller than that of the bandgap can excite the electrons from the valence to the conduction band. Unintentionally doped ZnO is n-type, and carrier concentrations larger than n>10^{20} cm^{-3} have been reported [60]. However, it has also been reported that tempering under atmospheric conditions reduces the carrier concentration of the intrinsically doped ZnO films

permanently, attributed to the chemisorption of oxygen [49]. ZnO:Al doped solely intrinsically is thus generally not used for TCO applications.

Extrinsic doping: Doping that results from introducing a foreign atomic species to the crystal structure. For ZnO, n-type doping is relatively easy to accomplish while p-type remains elusive. It is typical for wide bandgap semiconductors to be easily doped n- or p-type, but not both. This asymmetry has been attributed to the fact that a wide bandgap semiconductor has a low valence band maximum or high conduction band minimum with respect to the vacuum level, leading to the so-called 'doping pinning rule' [61]; materials with a low valence band tend to be p-type and a high conduction band tend to be n-type. As mentioned previously, the intrinsic defects are n-type, so p-type dopants must first compensate for these carriers.

N-type doping in ZnO is generally done using a column 13 element, specifically boron, aluminum, gallium, and indium. These elements have one additional valence electron compared to the column 12 element zinc. During deposition, B^{3+}, Al^{3+}, Ga^{3+}, and In^{3+} ions are substituted for the Zn^{2+}, leaving one additional weakly bound electron [15,49]. The donor binding energies (the energy required to free the extra valence electron) are 53.0, 54.5, and 63.2 meV for aluminum, gallium, and indium, respectively [62]. These are much smaller than the 3.4 eV required to excite and electron from the valence to the conduction band.

Hydrogen doping: Doping that results from the incorporation of hydrogen into the crystal lattice. The doping effect of hydrogen is listed separately from intrinsic and extrinsic doping, since it can play a role in both types of doping. While hydrogen is not truly an intrinsic defect in ZnO, the incorporation of hydrogen into the film during growth is unavoidable. In this respect, hydrogen doping is an intrinsic property of the film, as the doping effect is not intentional. The hydrogen incorporation depends strongly on ZnO preparation with concentrations as low as $5\text{x}10^{16}$ cm^{-3} in single crystals and as high as 10^{20} cm^{-3} in magnetron sputtered polycrystalline ZnO:Al films [44]. In many semiconductors hydrogen doping compensates extrinsic dopants, however, in ZnO:Al hydrogen doping tends to exhibit n-type behavior [63]. Hofmann *et al.* showed that in ZnO, incorporated hydrogen is always a shallow donor [64].Thus, ZnO films can be extrinsically doped by introducing hydrogen to the ZnO during growth [65]. The donor binding energy for the electron to the hydrogen atom is about 60 meV [66], which is on par with the column 13 dopants.

Degenerately doped: In a semiconductor, increasing the carrier concentration shifts the Fermi level from the middle of the band gap toward the valence or conduction bands, for p- and n-typed doping, respectively. When doping reaches a sufficiently high level, the Fermi level crosses into the valence or conduction band and the material is said to be degenerate. Once this level of doping has been reached, the material behaves like a metal, having no bandgap to overcome and requiring very little energy to free the carriers from the weak bonds. The optical bandgap still exists, however, and the semiconductor remains transparent to light with energy smaller than the bandgap. The critical carrier concentration (n_{crit}) required for a semiconductor to become degenerate is given by the Mott criterion [67],

$$n_{crit}^{1/3} a_0^* \approx 0.26 \qquad \textbf{(2.8)}$$

The effective Bohr radius (a_0^*) is given by

$$a_0^* = \frac{h^2 \varepsilon \varepsilon_0}{\pi e^2 m_e^*}, \tag{2.9}$$

where h, ε_0, and ε are the Planck's constant (h=6.626x10^{-34} J s), the permittivity of free space (ε_0=8.854x10^{-12} F/m), and the static dielectric constant, respectively. The static dielectric constant for ZnO is ε=8.656 [57]. Thus, for ZnO, the effective Bohr radius is a_0^*≈1.7 nm and the critical carrier concentration is n_{crit}≈5x10^{18} cm^{-3}. This carrier concentration is far below those typically used throughout this work, which can be assumed electrically to behave metallically.

2.3.3. Electrical Transport

In degenerately doped polycrystalline materials such as the ZnO:Al used within this work, the two main mechanisms limiting electron transport are: (1) the high rate of collisions between the charge carrier and the oppositely charged dopant nuclei, known as ionized impurity scattering; and (2) the limited transport across grain boundaries as potential energy barriers form due to the high density of defects, know as grain barrier limited transport. This section addresses these and other scattering mechanisms that lead ultimately to the mobility that carriers have within the ZnO:Al film.

The mobility measured in Hall measurements (Section 2.3.4 (page 16)) results from the combination of many simultaneously acting electrical transport limiting processes. Thus, the measured mobility must be less than any single scattering process and the various single mobilities are summed using a reciprocal relationship,

$$\frac{1}{\mu_{meas}} = \sum_i \frac{1}{\mu_i}. \tag{2.10}$$

Ionized impurity scattering: Scattering of the charge carriers by the ionized dopant atoms. For nondegenerate semiconductors, the scattering can be represented as the deflection in the path of the charge carrier due to the Coulomb attraction between the carrier and the shielded ion nucleus. For semiconductors with doping levels above the Mott criterion (Equation (2.8)), it can no longer be assumed that the impurity states are individual. Masetti *et al.* gave an empirical model for the mobility as a function of carrier concentration [68]. Ellmer and Mientus extended this empirical fit to ZnO [69]. This type of scattering becomes a dominant process at carrier concentrations above 10^{19} cm^{-3}. Additional details on ionized impurity scattering can be found elsewhere [70-72].

Grain barrier limited transport: Depending on the size of the grains in polycrystalline materials, the grain boundaries can constitute the majority of defects in such materials. Seto [73] proposed and Baccarani *et al.* [74] improved a model for electrical transport through polycrystalline silicon. Ellmer *et al.* have shown that this model is also applicable to polycrystalline ZnO:Al [44,69,75]. The basics of the model are as follows: in polycrystalline ZnO films, the majority of crystal defects are localized at the boundaries between individual grains. These crystallographically disturbed regions lead to defects with energies in the band gap. The defects can trap the free carriers within the grains, which in turn causes the formation of a charge depletion or accumulation region in n- and p-type materials, respectively. Thus, for a carrier to participate in conduction, it must overcome the potential energy of the grain barrier (E_b).

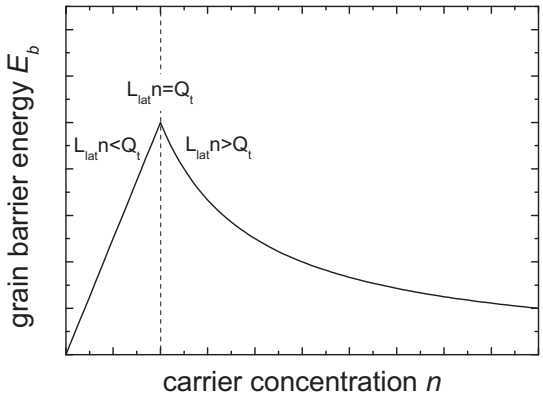

Figure 2.2: Grain barrier energy as a function of carrier concentration. All units are arbitrary.

Transport is then limited by thermionic emission (the heat-induced flow of charge carriers over a potential energy barrier), and the grain boundary limited mobility (μ_{gb}) can be represented as,

$$\mu_{gb} = \mu_0 \exp\left(\frac{-E_b}{k_b T}\right); \tag{2.11}$$

where k_B, and T are Boltzmann's constant (k_B=1.38110^{-23} J K^{-1}) and the absolute temperature (in Kelvin), respectively. The prefactor, μ_0, can be thought of as the mobility within a grain [73], and is given by,

$$\mu_0 = \frac{e L_{lat}}{\sqrt{2\pi m_e^* k_B T}}. \tag{2.12}$$

In this equation, L_{lat} represents the lateral grain size. In a sample with a carrier density of n within the grain and a sheet trap density of Q_t at the grain boundary, the potential energy barrier is given by,

$$E_b = \frac{e^2 L_{lat}^2 n}{8\varepsilon\varepsilon_0} \quad for \quad L_{lat} n < Q_t \tag{2.13a}$$

and

$$E_b = \frac{e^2 Q_t^2}{8\varepsilon\varepsilon_0 n} \quad for \quad L_{lat} n > Q_t \tag{2.13b}$$

.

Three different relationships between the number of carriers within a grain (the product of the grain diameter (L_{lat}) and carrier density (n)) and the trap density (Q_t) are worth exploring. (1) The number of carriers within a grain is less than the number of traps at the grain boundary ($L_{lat}n<Q_t$), Equation (2.13a). In this case, the carriers in the grains are completely depleted and the potential energy barrier will increase linearly with increasing carrier density or quadratically with increasing grain size, see Figure 2.2. (2) The number of carriers within a grain is equal to the number of traps at the grain boundary ($L_{lat}n=Q_t$), Equation (2.13a or b). In this case, the carriers in the grains are completely depleted and the traps are completely full giving the potential energy barrier a maximum value, see Figure 2.2. (3) The number of carriers within a grain is greater than the number of traps at the grain boundary ($L_{lat}n>Q_t$), Equation (2.13b). In this case, the traps at the grain boundary are completely full and the potential energy barrier will decrease as the inverse of the increasing carrier concentration, see Figure 2.2.

The trap densities in polycrystalline ZnO films have been estimated to range between Q_t=5x10^{12} and 3x10^{13} cm^{-3}, with the trap density strongly depending on deposition conditions [69]. Within this work, the ZnO:Al thin-films typically have a carrier concentration of n=5x10^{20} cm^{-3}, and grain diameters around L_{lat}=75 nm (see Section 4.1.2 (page 63)). Thus, in general, the number of carriers within a grain is $L_{lat}n$≈4x10^{15}, which is much larger than the number of traps at the grain boundary: the potential energy barrier is given by Equation (2.13b).

Phonon scattering: The scattering of charge carriers by vibrations in the crystal lattice (phonons). Since ZnO has more than one atom in the unit cell, both high (optical) and low (acoustic) frequency phonons occur. High frequency optical phonons arise from the oscillation of neighboring ions against each other. These vibrations induce an electric field that can scatter the charge carrier [76]. Lower frequency acoustic phonons distort the crystal lattice, causing energetic shifts of the band edges, which can scatter the charge carriers [44,77]. In ZnO, acoustic phonon scattering is generally much smaller than optical phonon scattering [78].

Piezoelectric mode scattering: Phonon scattering of charge carriers unique to piezoelectric crystals. Piezoelectric materials, such as ZnO (Section 2.2 (page 10)), do not exhibit inversion symmetry. Acoustic phonons along the c-axis induce an electric field that scatters charge carriers. Zook calculated that the directionally dependent scattering of charge carriers leads to anisotropic mobilities [79]. The ratio of mobility perpendicular to the c-axis to the mobility parallel to the c-axis was calculated to be 2.8 at 77 K [79]. However, at room temperature, optical phonon scattering is the dominant phonon related scattering mechanism and mobility is isotropic [80].

Neutral impurity scattering: The scattering of charge carriers by uncharged impurity atoms. Erginsoy derived an expression for the mobility as a function of the density of neutral impurities [81]. The scattering caused by neutral impurities in ZnO:Al is small, since most of the impurity atoms (hydrogen) are ionized at room temperature (RT) since their activation energy is only 60 meV [66].

Dislocation scattering: The scattering of charge carriers by crystallographic dislocations. Like grain boundaries, the crystallographically disturbed regions resulting from screw or edge dislocations lead to defects with energies in the bandgap. These defects can trap and scatter the charge carriers. Since dislocations are one-dimensional, the density of traps resulting from two-dimensional defects (surfaces and grain boundaries) is generally much higher in polycrystalline ZnO films. Additional details on dislocation scattering can be found elsewhere [82].

2.3.4. Hall Effect

The Hall effect, named after its discoverer Edwin Hall, is the voltage (V_H) that is established along the y-axis when an electrical current (I) flows through a material in the x-axis direction, while a magnetic field (B) is applied perpendicularly along the z-axis. The flowing electrons experience a Lorentz force (F_L) from the magnetic field that is perpendicular to the direction of flow and the magnetic field, as given by

$$\vec{F}_L = e\left[\vec{E} + (\vec{v} \times \vec{B})\right], \tag{2.14}$$

where v is the velocity of the electron. The deflected electrons accumulate on one side of the sample until this transverse electric field balances the Lorentz force. For metals (or materials with primarily one type of carrier), the electric field established across the sample (Hall voltage) is given by,

$$V_H = \frac{-IB}{edn}, \tag{2.15}$$

where d is the thickness of the sample. The carrier type (electrons or holes) is determined by the sign of the Hall voltage. The Hall coefficient (R_H) is defined as the ratio between the transverse electric field (V_H) and the product of the current along the x-axis (j_x) and the magnetic field (B),

$$R_H = \frac{V_H}{j_x B}. \tag{2.16}$$

Since the current density is the current divided by the thickness ($j_x=I/d$), the Hall coefficient is inversely proportional to the carrier concentration (n),

$$R_H = \frac{-1}{en}. \tag{2.17}$$

Hall effect measurements are generally made using four point contacts in van der Pauw (coplanar) geometry [83]. For such measurements, the electrical properties of the material such as resistivity (conductivity), mobility, and carrier concentration can be calculated. During measurement, the current (I) and magnetic field (B) are known, and the sheet resistance (R_{sh}) and Hall voltage (V_H) are directly measured. If the thickness of the film (d) is known, the carrier concentration (n) and resistivity (ρ) can be calculated using Equation (2.15) and

$$\rho = R_{sh} d, \tag{2.18}$$

respectively. With these values, the carrier mobility (μ) can be calculated using Equation (2.7).

It has been shown that electron mobility and carrier concentration increase with thickness in sputter deposited ZnO thin-films on both glass and polyethylene naphthalate (PEN) substrates [22,23]. In both cases, the carrier concentration depended much less strongly than mobility on thickness [22,23]. Surface morphology of the as-deposited ZnO films has been reported on PEN and Si substrates [23,84]. It has been observed that as thickness increased, the grain size also increased in a "survival of the fastest" growth mechanism as developed by van der Drift [85]. Better grain quality has also been observed with increasing film thickness by x-ray diffraction (XRD) techniques [22,84].

Since the electrical properties as measured by Hall effect measurements pertain to the film as a whole, changes at the surface due to an increase in thickness are muted due to the averaging effect of measuring the whole film. Within this work, the electrical properties at the surface were calculated using the two layer and continuous variation models.

Two layer model: Petritz [86] showed that the Hall coefficient (R) and conductivity (σ) determined by Hall effect measurements on a sample with two layers and a magnetic field oriented perpendicularly to the broad area of the sample could be represented by

$$R_{meas} = \frac{d\,(R_{bulk}\,\sigma_{bulk}^2\,d_{bulk} + R_{surf}\,\sigma_{surf}^2\,d_{surf})}{(\sigma_{bulk}\,d_{bulk} + \sigma_{surf}\,d_{surf})^2} \tag{2.19}$$

and

$$\sigma_{meas} = \frac{\sigma_{bulk}\,d_{bulk} + \sigma_{surf}\,d_{surf}}{d}\,, \tag{2.20}$$

respectively. The subscripts *meas*, *bulk*, and *surf* indicate that the Hall coefficient or conductivity pertain to that measured, of the bulk, or at the surface, respectively. The thickness of the whole film (d) is also separated into that of the bulk (d_{bulk}) and the surface (d_{surf}), where $d = d_{bulk} + d_{surf}$.

Substituting Equation (2.17) for the three Hall coefficient values and Equation (2.7) for the three conductivity values, equations in terms of the measured carrier mobility and concentration can be obtained. Solving these equations for the surface properties yields,

$$\mu_{surf} = \frac{\mu_{meas}^2\,n_{meas}\,d - \mu_{bulk}^2\,n_{bulk}\,d_{bulk}}{\mu_{meas}\,n_{meas}\,d - \mu_{bulk}\,n_{bulk}\,d_{bulk}} \tag{2.21}$$

and

$$n_{surf} = \frac{(\mu_{meas}\,n_{meas}\,d - \mu_{bulk}\,n_{bulk}\,d_{bulk})^2}{(\mu_{meas}^2\,n_{meas}\,d - \mu_{bulk}^2\,n_{bulk}\,d_{bulk})\,d_{surf}}\,, \tag{2.22}$$

respectively, where once again the subscripts *meas*, *bulk*, and *surf* indicate that the carrier mobility or concentration pertain to that measured, of the bulk, or at the surface. With these equations, the electrical properties of the surface are calculated by attributing the change in electrical properties between two film thicknesses to the difference in thickness between them.

Continuous variation model: Petritz [86] showed additionally that the two layer model could be extended to include any number of layers. The measured Hall coefficient and conductivity for a continuously varying system are given, respectively, by

$$R_{meas} = \frac{d\int_0^d R(z)\,\sigma^2(z)\,dz}{\left[\int_0^d \sigma(z)\,dz\right]^2} \tag{2.23}$$

and

$$\sigma_{meas} = \frac{1}{d}\int_0^d \sigma(z)\,dz\,. \tag{2.24}$$

Where $R(z)$ and $\sigma(z)$ are the Hall coefficient and conductivity as a function of thickness, respectively. The thickness dependent functions for the Hall coefficient and conductivity can be expressed as functions of the mobility and carrier concentration using, respectively,

$$R(z) = \frac{-1}{e\,n(z)}\,, \tag{2.25}$$

and

$$\sigma(z) = e\,\mu(z)\,n(z)\,. \tag{2.26}$$

Where $\mu(z)$ and $n(z)$ are the carrier mobility and concentration as a function of thickness, respectively. Substituting the definitions of the Hall coefficient (Equations (2.17) and (2.25)) and conductivity (Equations (2.7) and (2.26)) into the continuously varying model (Equations (2.23) and (2.24)), the measured mobility and carrier concentration can be expressed as, respectively,

$$\mu_{meas} = \frac{\int_0^d \mu^2(z)\, n(z)\, dz}{\int_0^d \mu(z)\, n(z)\, dz} \qquad \textbf{(2.27)}$$

and

$$n_{meas} = \frac{\left[\int_0^d \mu(z)\, n(z)\, dz\right]^2}{d\int_0^d \mu^2(z)\, n(z)\, dz} \qquad \textbf{(2.28)}$$

.

2.4. Optical Properties of ZnO:Al

When light is incident on ZnO:Al, it can be transmitted, absorbed, or reflected. Which of these processes is most likely to occur depends primarily on the material and wavelength (λ) of the incoming light. Experimentally, the total transmission (T_t) and the reflection (R) can be measured, and the absorption (A) is assumed to constitute the rest of the incident radiation,

$$A(\lambda) = 1 - T_t(\lambda) - R(\lambda)\,. \qquad \textbf{(2.29)}$$

The likelihood of transmission can be derived from the Drude (free electron) model (section 2.3 (page 11)). The permittivity (resistance to the formation of an electric field within a medium) is given by the dielectric function (ε) as a function of angular frequency (ω) as

$$\varepsilon(\omega) = 1 - \frac{ne^2}{\varepsilon_\infty \varepsilon_0 m_e^* \omega^2} = 1 - \frac{\omega_p^2}{\omega^2} \qquad \textbf{(2.30)}$$

,

where ε_∞ is the high-frequency dielectric constant (for a ZnO thin-film ε_∞=3.61 [87]).The plasma frequency (ω_p) is defined as

$$\omega_p = \sqrt{\frac{ne^2}{\varepsilon_\infty \varepsilon_0 m_e^*}} \qquad \textbf{(2.31)}$$

.

The derivation of Equation (2.30) from the equations of motion for a free electron gas can be found elsewhere [88]. Wavelength and angular frequency are related by

$$\lambda = \frac{2\pi c}{\omega} \qquad \textbf{(2.32)}$$

,

where c is the speed of light in vacuum (c=2.998x10^8 m/s).

Ideally, when the angular frequency of the incoming light is greater than the plasma frequency ($\omega > \omega_p$), the dielectric function is positive and light can propagate (transmit) through the material. When the angular frequency of the incoming light is less than the plasma frequency ($\omega < \omega_p$), the dielectric function is negative and light cannot propagate through the

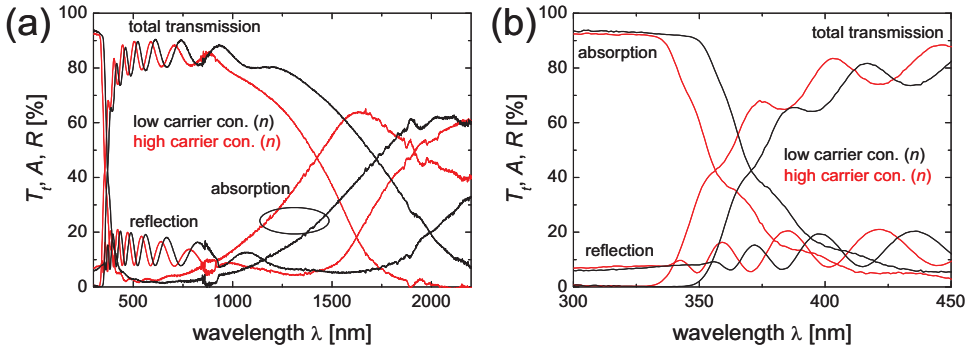

Figure 2.3: Total transmission (T_t), absorption (A), and reflection (R) of ZnO:Al with low (black) and high (red) aluminum concentration between wavelengths (λ) (a) 300 and 2200 nm and (b) 300 and 450 nm.

material and the light is reflected. When the angular frequency of the incoming light is equal to the plasma frequency ($\omega = \omega_p$), the dielectric function is zero and equal portions are transmitted and reflected. The plasma frequency is the resonance frequency of the charge carriers, and the incoming light is absorbed strongly. The polycrystalline ZnO:Al films are far from perfect crystals, and the effects of the plasma frequency are not confined to one particular wavelength. The width of the absorption peak about the plasma frequency depends on the mobility of the charge carriers [28]; samples with higher mobilities exhibit more sharply-defined resonance peaks. The absorption at the plasma frequency will be referred to as free carrier absorption throughout this work.

The optical properties of ZnO:Al depend on the electrical properties strongly. Figure 2.3 gives the transmission, absorption, and reflection as of unetched ZnO:Al films with low and high carrier concentrations (n) as a function of the wavelength of the incident light. The optical properties will be discussed in three regions, the ultraviolet region between 300 and 400 nm, the visible and near infrared region between 400 and 1000 nm, and the infrared region between 1000 and 2200 nm.

Ultraviolet region (300-400 nm): Figure 2.3 (b) magnifies the higher energy region of the optical spectrum in Figure 2.3 (a). The ZnO film with a low carrier concentration (black) exhibits high absorption between 300 and 350 nm. The absorption then drops off and becomes quite small by 400 nm, the transmission shows the opposite effect. This sharp transition is related to the band gap of ZnO, around 3.4 eV. The energy of the incoming light (E_γ) as a function of wavelength (λ) is given by Planck's relation,

$$E_\gamma(\lambda) = \frac{h\,c}{\lambda}\,. \qquad \textbf{(2.33)}$$

If the energy of the incoming light is greater than the band gap of ZnO (about 350 nm), it is readily absorbed; otherwise it is transmitted primarily through the ZnO:Al.

Increasing the carrier concentration in ZnO:Al shifts the absorption edge towards a higher wavelength [24,89]; see Figure 2.3 (b, red). This effect of a wider optical band gap with increased carrier concentration is also observed for other semiconductors [90-92]. Burstein [90] and Moss [91] explained that this increase in the optical band gap is due to full energy states in the conduction band. If the lowest energy states in the conduction band are occupied, accord-

ing to the Pauli exclusion principle, new states must be at higher unoccupied energies. This so-called Burstein-Moss shift causes the absorption edge to shift to higher energies allowing more transmission of ultraviolet light in ZnO:Al [89]. The increase in the energy of the band gap (ΔE_{BM}) is given by

$$\Delta E_{BM} = \frac{\hbar^2}{2}(3n\pi^2)^{2/3}\left(\frac{1}{m_e^*}+\frac{1}{m_h^*}\right), \qquad \textbf{(2.34)}$$

where $\hbar$ is the reduced Planck's constant ($\hbar=h/2\,\pi$=1.054x10^{-34} J s) and m^*_h is the effective mass of holes.

Visible and near infrared regions (400-1000 nm): Depending on the band gap of the active material, the visible and near infrared regions, as well as the transmitted portion of the ultraviolet spectrum, make up the usable solar spectrum for solar cells. Thus, for efficient solar cells, the transmission through ZnO:Al in this region is of particular interest. The example ZnO films have transmissions that oscillate between 80 and 90 % in this region, see Figure 2.3 (a). The oscillations are caused by constructive and destructive interference from the thin ZnO:Al films, which have a thickness (around 800 nm) on the order of the wavelength of the incoming light. The offset of the interference fringes between the two samples shown in Figure 2.3 (a) are due to slightly different film thicknesses. These interference fringes disappear and the transmission moves to an average value when the surface is randomly texturized.

The transmission begins to decrease and absorption increases towards the lower energy end of the usable solar spectrum. This absorption is the tail of the free carrier absorption peak, which will be discussed with the optical properties of the infrared region.

Infrared region (1000-2200 nm): In the infrared region, the transmission decreases while first the absorption and then the reflection increase, see Figure 2.3 (a). In this region the dielectric function goes from positive to negative (Equation (2.30)). The exact position of this transition and the plasma frequency (Equation (2.31)) depends on the carrier concentration. Notice in Figure 2.3 (a) that increasing the carrier concentration shifts the free carrier absorption peak towards the shorter wavelength region.

To summarize, there are both positive and negative effects of doping on the optical properties over the solar cell-relevant portion of the solar spectrum. Increasing doping increases the optical band gap, which allows more ultraviolet light to be transmitted. On the other hand, increasing doping shifts the plasma frequency to higher energy levels, which increases the free carrier absorption of longer wavelength visible and near infrared light.

2.5. Etching ZnO

It is advantageous to introduce light trapping features to improve the efficiency of silicon thin-film solar cells. Such features can be introduced to the ZnO:Al layer by chemical etching [19]. This section discusses how ZnO single crystals etch, what chemical reactions occur, and the rate at which reactions occur. The etching of sputtered polycrystalline ZnO:Al depends

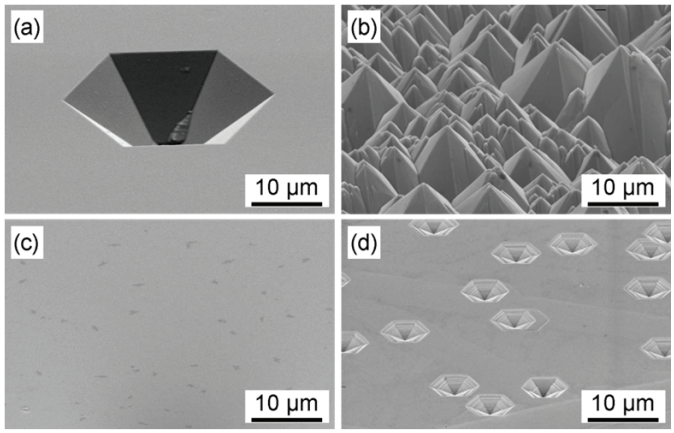

Figure 2.4: SEM images of (a) Zn- and (b) O-terminated ZnO single crystals etched in HCl, and (c) Zn- and (d) O-terminated ZnO single crystals etched in NaOH. From Hüpkes *et al.* [31].

strongly on the deposition conditions, therefore, the etching of such material is discussed together with the growth models in Section 2.7 (page 25).

As discussed in Section 2.2 (page 10), wurtzite crystal structure does not have inversion symmetry along the c-axis, as such the (001) and (00-1) planes are Zn- and O-terminated, respectively (Figure 2.1). Since the Zn-O bond is primarily ionic, the Zn-terminated surface is positively charged and the O-terminated surface is negatively charged. Gatos and Lavine developed an etch model for the polar (111) surfaces of III-V semiconductors [93]. Mariano and Hanneman used the polar surface model to explain the different etching behaviors of ZnO surfaces [33].

Figure 2.4 contains scanning electron microscopy (SEM) images of Zn- and O-terminated single ZnO crystals etched in acidic (HCl) and basic (NaOH) solutions, from *Hüpkes et al.* [31]. As explained by Mariano and Hanneman, the positively charged Zn-terminated side repels the positively charged hydronium ions (H_3O^+) within the acid, so etching only occurs at crystal defects forming hexagonal craters (Figure 2.4 (a)) [33]. The walls of these craters are the (101) crystal planes, and have an opening angle of 123° between parallel faces and 130° between opposing vertices. Alternatively, the hydronium ions are attracted to the negatively charged O-terminated side, and this side is rapidly etched, forming hexagonal pyramids over the whole surface. In a basic solution, the negatively charged hydroxide ions (OH^-) are repelled by the negatively charged O-terminated side, and like acids on the Zn-terminated side, etching only occurs at certain points forming hexagonal craters (Figure 2.4 (d)). On the Zn-terminated side no characteristic structures developed with NaOH etching (Figure 2.4 (c)) [31]; however, the model of Mariano and Hanneman predicts that material may still be removed [33].

As just discussed, ZnO is an amphoteric oxide, reacting in both acidic and basic solutions. In an acidic solution, such as HCl, the acid dissociates almost completely to hydronium (H_3O^+) and chloride (Cl^-) ions in the water. The hydronium ions (H_3O^+) oxidize the zinc atoms in ZnO to form zinc ions (Zn^{2+}) and water (H_2O). The zinc ion (Zn^{2+}) can then form various complexes with up to six ligands (chloride ions (Cl^-) and water molecules), where the metallic zinc ion is at the center of the complex. The complexes tend to be tetraedric or octaedric with a total of

four or six chloride ions and water ligands, respectively. The oxidation reaction and complex formation just described are as follows:

$$ZnO_{(s)} + 2\,H_3O^+_{(aq)} \rightarrow Zn^{2+}_{(aq)} + 3\,H_2O_{(l)} \qquad \textbf{(2.35a)}$$

and

$$Zn^{2+}_{(aq)} + (x)\,Cl^-_{(aq)} + (n-x)\,H_2O \;\overset{\rightarrow}{\leftarrow}\; \left[ZnCl_x(H_2O)_{(n-x)}\right]^{(2-x)}_{(aq)} \qquad \textbf{(2.35b)}$$
$$n = 4\ or\ 6,\ 0 \le x \le n$$

In a basic solution, such as potassium hydroxide (KOH), the dissolved salt forms hydroxide (OH^-) and potassium (K^+) ions in the water. The water (H_2O) converts the zinc atoms in ZnO into zinc ions (Zn^{2+}) and hydroxide (OH^-). The zinc ion (Zn^{2+}) can then form complexes with four hydroxide ions (OH^-), where the metallic zinc ion is at the center of the complex and the hydroxide ions attach as ligands. The reaction and complex formation just described are as follows:

$$ZnO_{(s)} + H_2O_{(l)} \rightarrow Zn^{2+}_{(aq)} + 2\,OH^-_{(aq)} \qquad \textbf{(2.36a)}$$

and

$$Zn^{2+}_{(aq)} + 4\,OH^-_{(aq)} \;\overset{\rightarrow}{\leftarrow}\; \left[Zn(OH)_4\right]^{2-}_{(aq)} \qquad \textbf{(2.36b)}$$

Additional details on the reactions that occur in acidic and basic solutions can be found elsewhere [94].

The rate at which these processes occur and the chemical character of the complexes formed depend on the solution. In general, the dependency of the reaction rate (k) on the temperature is given by the Arrhenius equation,

$$k = A_{col}\exp\left(\frac{-E_a}{R_{gas}\,T}\right), \qquad \textbf{(2.37)}$$

where A_{col}, E_a, R, and T, are the collision frequency factor, activation energy, gas constant (R_{gas}=8.314 J K^{-1} mol^{-1}), and absolute temperature, respectively. Thus, for a given reaction (E_a=constant), the rate of reaction can be increased by increasing the temperature or the collision frequency. For low acid concentrations, the collision frequency increases with concentration [95]. The collision frequency also depends on the solute used and the degree to which it dissociates in water. Strong acids, such as HCl, dissociate fully increasing the collision frequency, while weak acids, such as HF, only partly dissociate leading to reaction rates lower than those observed in strong acid (for the same concentration).

2.6. Deposition of ZnO:Al

Doped ZnO thin-films can be prepared through a wide variety of methods, including magnetron sputtering [13,19], chemical vapor deposition (CVD) [15,96], spray pyrolysis [16,48], pulsed laser deposition [97,98], evaporation [99,100], chemical solution deposition [17,101], and electro-chemical deposition [102]. Of these doped ZnO thin-film preparation techniques, magnetron sputtering and CVD have shown the most promise for large scale thin-film silicon solar cell production, as these techniques can yield large-area thin-films that can be texturized effectively to introduce light trapping features [13,15]. Within this work, only ZnO:Al films prepared by magnetron sputtering are used.

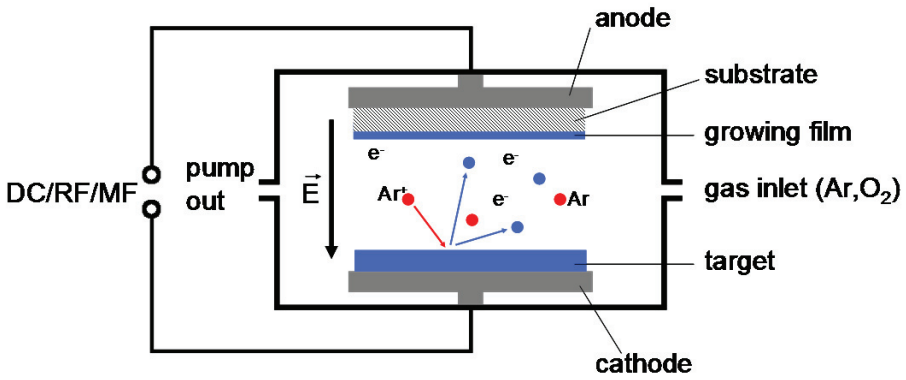

Figure 2.5: Schematic diagram of the sputtering process. Argon ions (red) impinge upon a target ejecting target material (blue) that can deposit on the substrate.

Sputtering is a process where energetic particles impinge upon a target substrate, ejecting atoms of the target material; a schematic diagram is given in Figure 2.5. Sputter deposition is performed within a vacuum chamber where a target (material to be sputtered) and a substrate (surface on which material is to be deposited) are mounted on a cathode and an anode, respectively. A noble gas (argon within this work) is introduced as sputtering gas, and a small fraction of these gas atoms is ionized initially. Applying an electric potential between the cathode and anode accelerates the positively charged gas ions towards the cathode and the negatively charged electrons towards the anode. The accelerated ions collide with other neutral gas ions on the way. If the kinetic energy of the ion is greater than the ionization energy of the gas, the collision can cause an additional ion to form. When performed with the right combination of electric potential and gas pressure, the atmosphere will consist of gas ions, electrons, and neutral gas atoms, and a self-sustaining plasma glow discharge is formed. If the ions have enough momentum, target atoms or clusters are ejected in vapor phase when they impinge upon the surface. The target vapor spreads throughout the chamber, condensing on the substrate in front of the anode as well as the chamber walls.

Historically, one of the challenges with sputter deposition was a very low deposition rate. The pressures required to achieve glow discharge were high, yielding a relatively small mean free path for the ejected target material, and thus a low deposition rate. Decreasing the pressure increased the mean free path of particles; however, the plasma became unstable as fewer gas ionizing collisions occurred. To increase the mean free path of the sputtered material (or neutrally charged atoms) without making the plasma unstable, the plasma is magnetically confined to the target side of the chamber by applying a magnetic field parallel to the target (perpendicular to the electric field) in so-called magnetron sputtering [103]. In the presence of a magnetic field, the electrons experience a Lorentz force (Equation (2.14)) making them move in a drifting closed loop. Since the mass of an ion is much larger than that of an electron the Lorentz force on the ion is negligible. This magnetic trapping of the electrons combined with the ambipolar diffusion of ions and electrons in plasma increases the plasma density in front of the target. With a higher localized plasma density, the chamber pressure can be reduced, increasing the mean free path of the neutral particles and the deposition rate.

Confining the plasma, however, leads to uneven erosion of the target. Various schemes have been introduced to address the inefficient use of the target material, including moving magnets [104], alternative magnetic field configurations [105], and rotatable cylindrical targets [26,106].

During sputtering, the positive gas ions are deposited on the target surface. If the target is very conductive, the ions will be neutralized by electrons in the cathode. If the target is insufficiently conductive, however, a charge that counteracts the electric field will build. The change in electric field can cause arcing, which may lead to target damage, or extinguish the plasma, as the charged particles are no longer accelerated by an electric field. Alternating the electric field prevents the buildup of charge because electrons are drawn to the cathode, neutralizing the charged ions. The alternating electric field is typically driven in the mid-frequency (MF, 40 kHz) or radio frequency (RF, 13.56 MHz) range. High frequencies such as these are chosen so the relatively light electrons follow the signal, while the relatively heavy ions do not. In general, a constant electric potential (DC) can be used for metallic targets, while and alternating electric potential (MF or RF) must be used for semiconducting or insulating targets.

For metal oxides (such as ZnO), the thin-films can be prepared alternatively by sputtering from a metallic target in an oxygen rich environment. This process is known as reactive sputtering, where the flow of both the sputtering gas (argon) and the reactive gas (oxygen) are controlled. Reactive sputtering can reduce costs as less expensive metallic targets can be used. Further, the additional parameter (reactive gas flow) can be used to alter the thin-film growth.

2.7. Polycrystalline Growth Models and Etching Trends

The electrical, optical, and etching properties of sputtered ZnO films depend on growth conditions. This section lists some of the processes that occur during growth, outlines the important sputtering parameters, and presents the growth models and etching trends observed previously.

Figure 2.6 gives a schematic diagram of some of the processes that occur during the growth of sputtered thin-films. Atoms and clusters sputtered from the target travel through the plasma and across the vacuum to the substrate, deflecting by collision along the way. These defections cause a broadening of the angular distribution of the arriving particles. If the particles have a low kinetic energy upon arrival they can be absorbed (adatoms) and diffuse along the surface to find the lowest energy site to which to bond. This depends on the bond energy between the

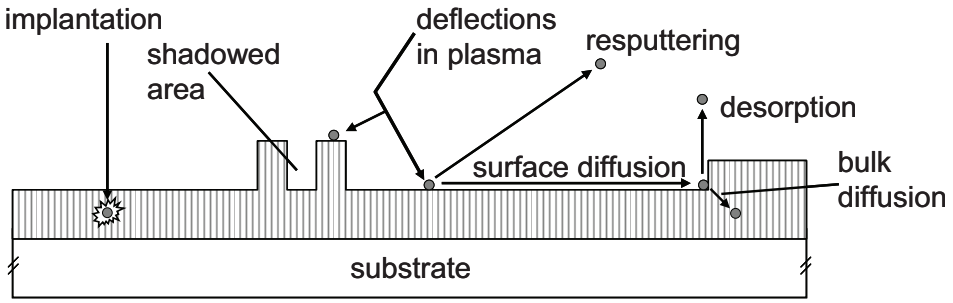

Figure 2.6: Schematic diagram of some of the processes that occur during growth by magnetron sputtering.

absorbed particle and the surface and number of bonding partners available. On the other hand, if the particles have a high kinetic energy upon arrival, they can be implanted within the growing film. In such implantation the particles cannot seek out a lowest energy bonding site. Additionally, the energy imparted to the surface by the collision of high energy particles may knock other particles from the growing surface back into the vacuum as a vapor, in so-called resputtering.

The distance a particle can diffuse on the surface depends strongly on the mass. Small particles may diffuse over relatively large distances on the surface before depositing, while the diffusion of large clusters is much more limited. Large clusters or groups of clusters may create shadowed areas where the growth rate is lower, as fewer incoming particles will be incident in these areas because of the broadened angular distribution of incoming particles.

An absorbed particle can also diffuse into the film bulk, but the amount of energy required to do this is much more than that required to diffuse along the surface. Additionally, an atom or particle with enough energy may desorb from the growing surface.

The rate at which these and other growth processes occur depend on the deposition conditions. The substrate temperature influences strongly the ability of incoming particles to diffuse along the surface, into the bulk, or desorb. The pressure influences the rate and mean free path of the incoming particles strongly, with lower pressure processes having lower growth rates and longer mean free paths (more implantation). Other important deposition parameters include power, dopant concentration, deposition time (film thickness), and for reactive sputtering, the relative oxygen pressure.

The electrical, optical, and etching characteristics of ZnO:Al films depend on these parameters. Changing a parameter may improve one of these characteristic, but simultaneously degrade another characteristic. For example, increasing the dopant concentration leads to better electrical properties (Section 2.3.2 (page 12)), but also increases the free carrier absorption of light (Section 2.4 (page 19)), which reduces the optical properties. Further, as discussed later in this section, changing the dopant concentration also alters the texture of the film after etching.

The rest of this section presents the reported growth models and etching trends. These provide some understanding of the relationship between deposition parameters and the resultant film properties.

Survival-of-the-fastest: As mentioned briefly with the Hall effect, the grain size of sputtered ZnO:Al increased with increasing thickness [22,23]. Van der Drift attributed the domination of certain crystal orientations over others to a survival-of-the-fastest mechanism, where the fastest growing orientations overgrow slower [85]. For ZnO, the c-axis orientation has a minimum of surface free energy [107,108]. Thus, in equilibrium, the c-axis growth dominates and orients perpendicularly to the underlying substrate [20]. Additionally, it has been observed that for sputtered ZnO films, growth along the c-axis is faster when Zn-terminated than when O-terminated [109,110].

Thornton model: Movchan and Demichishin found three types of growth modes for evaporated metals [111]. The growth mode observed for a given deposition depended on the ratio between the substrate temperature (T_s) and the melting temperature (T_m) of evaporated metal [111]. Thornton extended this three growth mode model to sputtered metal films, including sputtering pressure as a parameter in addition to the substrate temperature [32], see Figure 2.7.

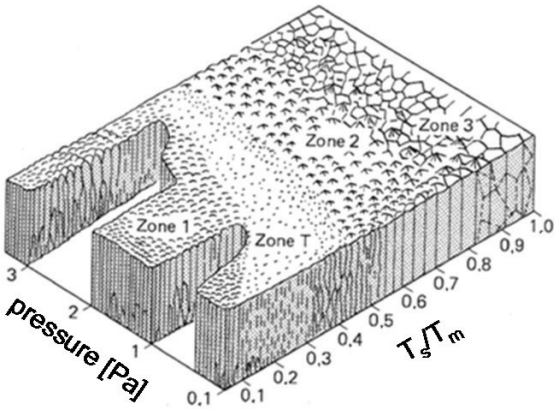

Figure 2.7: Thornton model for sputtered metal growth [32].

Zone 1 of the Thornton model consists of a relatively loosely packed material. In Figure 2.7, at 0.1 Pa this zone can be seen for relative temperatures (T_s/T_m) less than 10 % of the melting temperature. Low substrate surface temperatures lead to small adatom mobility, and the incoming material deposit close to the absorption site. As such, the crystallites grow according to the incident sputter flux and voids rather than grain boundaries may form between tapered neighbors. As the pressure is increased, the loosely packed zone 1 material is seen at higher temperatures up to 40 % of the melting temperature for a pressure of 3 Pa. The increase in pressure decreases the mobility of adatoms further, as more argon atoms are also absorbed and the kinetic energy of the incoming particles is reduced.

Zone 2 consists of large columnar grains separated by grain boundaries. In Figure 2.7, at 0.1 Pa this zone can be seen for relative temperatures (T_s/T_m) between 40 and 75 % of the melting temperature. The surface mobility in this region is quite high, and adatoms can diffuse to preferred bonding sites. Effects from shadowing are negligible, and grain boundary migration and recrystallization may occur, increasing the average grain size.

A transition region with dense fibrous grains, zone T, exists between zones 1 and 2. In Figure 2.7, at 0.1 Pa this zone can be seen for relative temperatures (T_s/T_m) between 10 and 40 % of the melting temperature. This region exhibits characteristics between those of zones 1 and 2. The increase in adatom mobility yields more dense films, but temperatures are not high enough for grain boundaries to recrystallize, yielding smaller grain sizes than those in zone 2.

Increasing the substrate temperature even further leads to zone 3 growth, as characterized by dense packing and flat surface morphology. In Figure 2.7, at 0.1 Pa this zone can be seen for relative temperatures (T_s/T_m) above 75 % of the melting temperature. In this region, the temperature is high enough that adatoms can diffuse into the bulk and the bulk itself can recrystallize.

Modified Thornton model: Kluth *et al.* modified the Thornton model to describe the post-deposition etching trends of ZnO:Al by the compactness of a film [25]. Like Thornton, the compactness of a film depends on the substrate temperature and pressure during deposition [32]. The modifications made to the Thornton model include: (1) The normalized temperature axis (T_s/T_m) is replaced with a substrate temperature (T_s) axis. Since, the melting temperature of ZnO (1975 °C) is much higher than most metals, the typical substrate temperatures

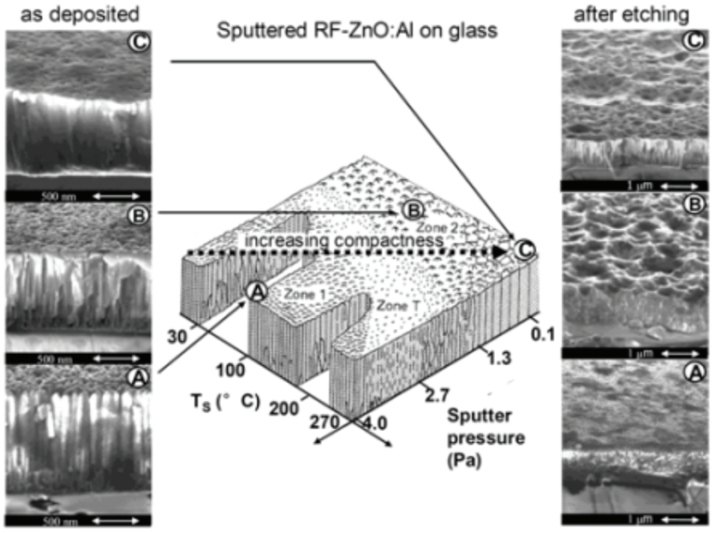

Figure 2.8: The modified Thornton model as given by Kluth *et al.* [25].

used for sputtering (between 80 and 400 °C) are quite small on the normalized scale. (2) The pressure and temperature axis are exchanged. Kluth *et al.* noticed that pressure played a more important role than substrate temperature in the type of crater formation occurring after deposition [25]. (3) Zone 3 from the Thornton model is not included. Recrystallization of the bulk only occurs at temperatures close to the melting temperature, and once again such high substrate temperatures are not typically applied during ZnO sputtering.

The modified Thornton model is shown in Figure 2.8. [25]. Kluth *et al.* denoted three types of surfaces that can occur after HCl etching, (A), (B), and (C). SEM images of the three types of films are also shown in Figure 2.8, both as-deposited and after etching. All films were predominantly c-axis oriented. Cross-sectional SEM images showed the same trends as the Thornton model, with the grain boundaries becoming more compact with increasing substrate temperature and decreasing deposition pressure. The type A etch is relatively isotropic and progresses at a high rate. This leads to etched surfaces which appear very similar to unetched surfaces. Type B and C etch anisotropically, with craters with opening angles between 120 and 140° forming at particular locations on the surface. Type B and C etches are distinguished by comparing the crater surface coverage. For type B films, the sites of crater formation are dense enough to yield surfaces that are homogenously covered with craters, while for the more compact type C film, the sites of crater formation are fewer and surfaces are only partly covered with large craters [25].

Hüpkes *et al.* showed that for reactively sputtered ZnO:Al thin-films the surface morphology after etching depended on the deposition pressure and substrate temperature [112]. The same trends were observed as those for sputtering from ceramic targets; specifically, higher pressures leading to less compact homogeneously etching films, lower pressures leading to crater formation, and even lower pressures leading to isolated crater formation [112].

Dopant concentration dependence: Berginski *et al.* showed that the modified Thornton model could be extended to ZnO:Al films deposited from targets with different aluminum con-

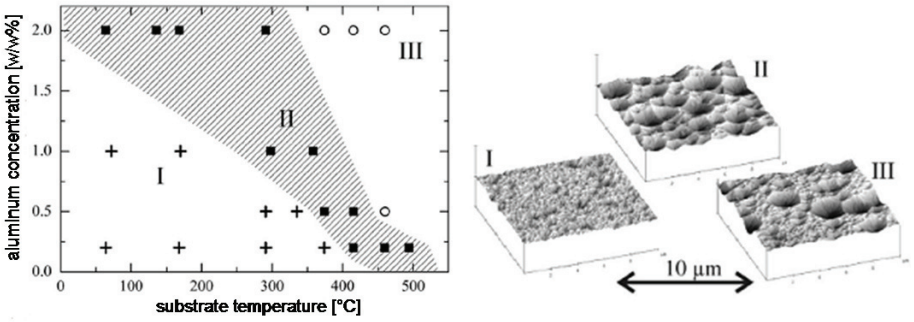

Figure 2.9: Etching characteristics as a function of the target aluminum concentration and substrate temperature, from Berginski *et al.* [24].

centrations [24]. In the experiment, Berginski *et al.* sputtered ZnO:Al from ceramic targets with Al_2O_3 concentrations between 0.2 and 2 w/w% with various substrate temperatures. The surfaces were characterized by AFM after etching and determined to exhibit one of three surface structures (I), (II), or (III), see Figure 2.9 [24]. Results showed that decreasing the aluminum content in sputtered films (below 2 w/w%) yielded with poorer quality. However, the quality could be recovered by increasing the substrate temperature.

The etched surface types I, II, and III given by Berginski *et al.* correspond to the etched surface types A, B, and C given by Kluth *et al.*, respectively. Within this work, the characterization of surface etching behavior follows the notation of Berginski *et al.*

Reactive sputtering and different etchants: Up to this point, the texturization of polycrystalline ZnO:Al thin-films has been limited to those texturized by an acidic (HCl) etch. Hüpkes *et al.* reactively deposited ZnO:Al films with different oxygen partial pressures [31]. The films were then etched chemically in both an acidic (HCl) and a basic (KOH) solutions, as well as physically etched with a mixture of oxygen and argon ions [31]. Figure 2.10 gives a matrix of SEM images of the various reactively deposited ZnO:Al films after the etches.

There are two major results from this experiment. First, like substrate temperature, sputter

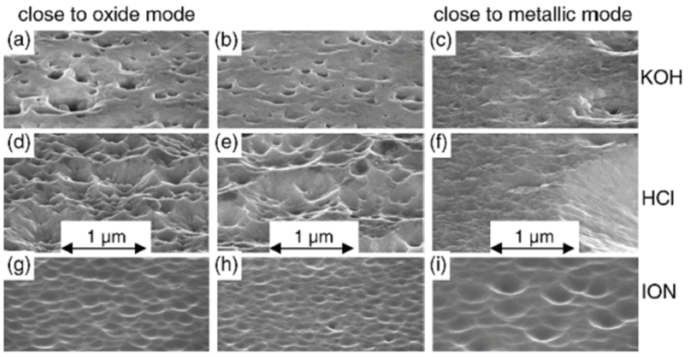

Figure 2.10: Matrix of SEM images of reactively sputtered and variously etched ZnO:Al films, from Hüpkes *et al.* The films were sputtered close to oxide mode (left column), between oxide and metallic mode (middle column), and close to metallic mode (right column), then etched by KOH (a-c, top row), HCl (d-f, middle row), and ion bombardment (g-i, bottom row) [31].

pressure, and dopant concentration, different oxygen partial pressures lead to different etching behaviors. The HCl-etched ZnO:Al films deposited close to oxide mode and between oxide and metallic mode exhibit type II structure (complete surface coverage by craters), while the film deposited close to metallic mode exhibited type III structure (few large craters). Thus, for reactively sputtered ZnO:Al films the compactness increases going from oxide to metallic mode. Kluth *et al.* observed similar effects on etching behavior when adding small amounts of oxygen to a ceramic sputtering process [113]. This idea is supported by other experiments that link the surface structure of the as-deposited films to the etching behavior [114,115].

Second, the density of crater formation for the various etching methods increase or decrease together. While the shape and density of the resultant craters are quite different between the KOH, HCl, and ion beam etching methods, all etchant types showed higher crater densities close to oxide mode and lower crater densities closer to metallic mode. From these results, Hüpkes *et al.* concluded that the sites of crater formation were built into the film during deposition [31].

2.8. Post-Deposition Heat Treatments

A reoccurring theme throughout this work is the strong dependence of electrical, optical, and etching properties on the deposition conditions. This section presents some heat treatments performed on the ZnO:Al after deposition that alter the properties of ZnO:Al films. Specifically, these are annealing, which can improve or degrade electrical and optical properties of ZnO:Al films; and damp-heat, which tests the long-term environmental stability of ZnO:Al films.

2.8.1. Annealing of ZnO:Al

At room temperature in air, the electrical properties of intrinsic and doped ZnO are quite stable, showing no significant degradation within a year [60,116]. Annealing ZnO at higher temperatures can affect the electrical and optical properties of the thin-film strongly.

Minami *et al.* annealed sputtered intrinsic ZnO films in various inert environments (vacuum, nitrogen, and argon), as well as in a reducing atmosphere (air) at temperatures up to 400 °C [116]. They observed that the resistivity of the films increased under all annealing conditions. In similar experiments, Minami *et al.* [60] and Takata *et al.* [117] annealed ZnO:Al in the same inert and reducing atmospheres at temperatures up to 400 °C. It was found that films with an aluminum content of at least one percent did not degrade significantly upon annealing, regardless of atmosphere. Minami *et al.*, however, showed that the electrical properties of ZnO:Al thin-films were no longer stable when annealed at temperatures above 400 °C in air and 600 °C in argon [118]. It has been proposed that the degradation in electrical properties are due to the chemisorption of oxygen at grain boundaries, which in turn increases potential barriers at the grain boundaries (Section 2.3.3 (page 14)) [117].

Berginski *et al.* showed that the carrier concentration could be controllably decreased by annealing in vacuum, while the mobility remained fairly constant [119]. This provided a way to control the electro-optical properties after deposition, as decreasing the carrier concentration decreases both the Burstein-Moss shift and free carrier absorption (see Section 2.4 (page 19)). Annealing ZnO:Al films alters not only the electronic and optical properties, but also the etch-

ing characteristics, with annealed samples exhibiting a decrease in crater density [120]. To alter the electro-optical properties without altering the resultant surface structures, Berginski *et al.* etched the ZnO:Al films prior to annealing [119].

Recently Ruske *et al.* investigated thermal treatment conditions for increasing the mobility without altering the carrier concentration strongly [28]. To do so, ZnO:Al films were capped with an amorphous silicon prior to annealing. This silicon cap greatly reduces the amount of oxygen chemisorbed during annealing which leads to film degradation. Additionally, the high temperatures heal dislocations and defects at the grain boundaries, leading to better electron transport [28]. Despite similar carrier concentrations, the optical properties are slightly altered, as the higher electron mobility leads to a better defined plasma frequency, with stronger absorption at the plasma frequency but less strong absorption in the tails of the plasma frequency (a portion of which is in the visible and near infrared region) [121].

2.8.2. Damp-heat degradation of ZnO:Al

Damp-heat is one of the performance tests thin-film solar cells must pass to receive International Electrotechnical Committee 61646 certification. To pass this test, solar cells must show less than five percent degradation in efficiency after 1000 hours of exposure to a damp-heat at 85 °C ± 2 °C with a relative humidity of 85 % ± 5 % [122]. It is assumed that the physical and chemical degradation processes observed under these harsh conditions are the same as those which occur under standard conditions over much longer periods of time. Thus, such tests attempt to accelerate the aging process.

The electrical degradation occurring during a damp-heat test can come from degradation within any of the solar cell layers, or at any of the interfaces. In several studies the effects of damp-heat degradation are limited to those of the layer ZnO:Al by exposing bare ZnO:Al films (on a glass substrate) to the damp-heat. This further accelerates the ZnO:Al degradation process because ZnO:Al capped with the layers to complete the solar cell (silicon and silver) have proven quite stable even without additional encapsulation [123].

The degree to which a film degrades in damp-heat depends on the deposition conditions strongly. Klenk *et al.* [20] and Greiner *et al.* [30] observed that ZnO deposited onto rough substrates degraded more quickly than ZnO deposited onto smooth substrates. Tohsophon *et al.* saw that thinner ZnO:Al films were more quickly penetrated [124]. Kluth *et al.* [113] and Tohsophon *et al.* [124] studied the effect of process pressure during sputtering on damp-heat degradation and found that film deposited at low pressures degraded less than those deposited at higher pressures. In general, growth conditions that yield compact films show better stability in a damp-heat [125].

Many authors have concluded that the degradation is related to grain boundaries [30,124,126,127]; even if it is not the site where degradation occurs, the grain boundaries provide the fastest ways for humidity penetrate the film [43]. Greiner *et al.* showed that the optical properties of ZnO:Al films were only slightly altered by damp-heat exposure, while the electrical properties were much more strongly affected [30]. From this it can be concluded that the degradation is related to distortion in electrical transport [125], such as barriers at grain boundaries [73] (see Section 2.3.3 (page 14)). Lin *et al.* [126] and Minami *et al.* [127] attributed the degradation in electrical properties of polycrystalline ZnO thin-films to oxygen adsorption at the grain boundaries. Tohsophon *et al.* showed that the electrical properties of degraded

ZnO:Al films could be restored to almost as-deposited levels by annealing at 150 °C [124]. Thus, whichever chemical process accounts for the degradation, it must be reversible at fairly low temperatures.

When discussing film degradation, it is worth noting Kirchhoff's current law, which states for any junction in an electrical circuit the sum of the currents (I) flowing in and out of a junction are equal

$$\sum_{k=1}^{n} I_k = 0 \,. \tag{2.38}$$

This law comes from the conservation of electric charge. Thus, for the measured electrical properties of the film to be altered, electrical properties of the whole film must be altered, otherwise another current path would be taken.

2.9. Silicon Thin-Film Solar Cells

One of the goals of developing a better understanding of sputtered ZnO:Al is to use this knowledge to create more efficient silicon thin-film solar cells. This section first introduces the basic physical concepts of a solar cell and the materials used for their construction, then gives the basic methods used to characterize the solar cells.

2.9.1. Principles and Construction of Silicon Thin-Film Solar Cells

Solar cells are opto-electronic devices that use the photovoltaic effect to convert sunlight into electric power. As mentioned in the introduction, thin-film silicon solar cells are a low-cost alternative to crystalline silicon solar cells, with active layers having only one percent the thickness (less than two micrometers) [10]. For a solar cell to work two requirements must be satisfied: (1) incoming sunlight must be incident upon a material which can absorb it, exciting a electron from the valence to the conduction band leaving a hole in the valance band in the process; and (2) the electron-hole pair must be separated before they recombine, reemitting the light.

With regard to the first requirement for solar cells, that incoming light be incident upon a material that can absorb it, it is necessary to introduce a conductive yet transparent window layer (such as a TCO). This layer provides good electrical contact, while transmitting as much of the solar spectrum as possible. Within this work, ZnO:Al fulfills this window layer role, conductive (Section 2.3 (page 11)) yet still transmitting most of the solar spectrum (Section 2.4 (page 19). Within this work, various forms and combinations of silicon are used as the active (light absorbing) layer, including amorphous silicon, microcrystalline silicon, and tandem amorphous/microcrystalline silicon layers. The following gives additional information about each of these absorbers.

Amorphous silicon: Silicon that lacks long range order. In amorphous silicon, the fourfold tetrahedral bonding to neighboring silicon atoms is often lost, leading to strained and dangling bonds. Amorphous silicon has a quasi-direct band gap between 1.7 and 1.8 eV. Amorphous silicon can thus absorb light with a wavelength less than 800 nm. The absorption coefficient in the short wavelength range is generally high, allowing for the use of very thin layers (around

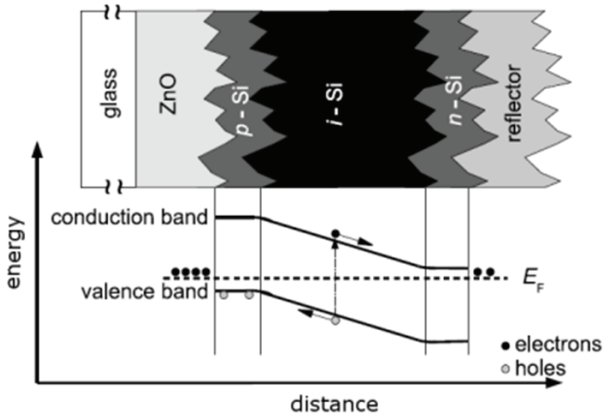

Figure 2.11: Schematic diagram for a texturized single junction silicon thin-film solar cell (above). Simplified band diagram resulting from the p- and n-doped layers (bottom).

400 nm). The high density of dangling bonds leads to poor conduction in amorphous silicon; however, the conductivity can be improved through hydrogen passivation. Some of the passivated bonds degrade under illumination, and the efficiency of amorphous silicon solar cells decrease with time. This degradation is known as light-induced degradation or the Staebler-Wronski effect [128].

Microcrystalline silicon: Crystalline silicon grains within an amorphous matrix. In microcrystalline silicon most of the silicon atoms are tetrahedrally bonded to the four neighboring silicon atoms, leading to a band structure similar to that of crystalline silicon. Microcrystalline silicon has a band gap of 1.1 eV. The smaller band gap as compared to amorphous silicon allows for the absorption of a larger portion of the solar spectrum, down to about 1100 nm. Since only a small fraction of the microcrystalline silicon is in the amorphous state, solar cells on this material do not suffer from the Staebler-Wronski effect to the same extent as amorphous silicon.

Because of microcrystalline silicon's indirect band gap, the absorption of light generally requires a change in momentum by the absorption or emission of a phonon. Light with high enough energy can be directly excited across the gap, however in silicon this requires an energy of 3.4 eV, exceeding most of the visible spectrum. Since the absorption of light in microcrystalline silicon generally requires an interaction with an additional particle (phonon), the absorption coefficient can be low, especially in the long wavelength region. To increase the probability of absorption, microcrystalline silicon solar cells are generally thicker than amorphous solar cells (around 1.5 µm).

Tandem amorphous/microcrystalline silicon: A stack with an amorphous then a microcrystalline solar cell. This structure allows more efficient partitioning of the solar spectrum, with shorter wavelength light being absorbed in the amorphous silicon 'top' cell and longer wavelength light being absorbed in the microcrystalline silicon 'bottom' cell. The energy conversion efficiencies achievable in tandem cells are higher than those of single junctions [129].

Since the cells are connected in series, the current through the stack is limited to the lowest current of the two subcells. Care must thus be taken to find the optimal thicknesses for the two subcells. Additionally, the top amorphous subcell will exhibit a larger amount of light induced degradation than the bottom cell.

With regard to the second requirement for solar cells, that the electrons and holes are separated before they recombine, regions of the silicon are doped during growth to form a built-in potential, and front and back contacts to the silicon are made, see Figure 2.11. The deposition order and function of the layers are as follows: ZnO:Al is deposited onto a glass substrate and texture etched to act as a window layer, hole conductor, and source of light trapping. Three silicon layers are then deposited; first a thin (15-20 nm) positively doped (p-type) region, then a thicker (400-1500 nm) intrinsic region, and finally a thin (15-20 nm) negatively doped (n-type) region. The weakly bound electrons and holes in the n- and p-type regions, respectively, are thermally excited and diffuse to the opposite sides creating a built-in potential across the intrinsic region. Electrons excited into the conduction band by the absorption of light in the intrinsic region are accelerated towards the n-type region, while the holes are accelerated towards the p-type region. Lastly, a back contact is deposited, which also serves the function of a reflector, further enhancing light trapping effects. The front (ZnO:Al) and back contact thus collect the holes and electrons, respectively.

2.9.2. Characterization of Solar Cells

To characterize completed solar cells, the current (I) is measured as a function of voltage (V) while illuminated by light with a known power (P_0). Given a well defined cell area, the current density (j) as a function of voltage can be calculated, which allows easier comparison between cells with different areas. Figure 2.12 gives a typical curve for current density as a function of the applied voltage under illumination. Exact values are omitted, as they depend strongly on the type of active layer used, as well as the deposition conditions.

Figure 2.12 also shows values often used to characterize the current density-voltage curve. The short circuit current density (j_{sc}) is the current density across the device when the voltage is zero (V=0). The open circuit voltage (V_{oc}) is the difference in electric potential when there is no external load (j=0). The maximum power point (mpp) is defined as the point where the converted power (P_{mpp}) is largest, that is, when the product of the measured current and voltage is at a minimum (maximum output). The maximum power point can be characterized by its current density (j_{mpp}) and voltage (V_{mpp}). The fill factor (FF) is defined as the ratio of the maximum convertible power to the maximum power of an ideal diode (P_{ideal}),

$$FF = \frac{P_{mpp}}{P_{ideal}} = \frac{V_{mpp}\ j_{mpp}}{V_{oc}\ j_{sc}} \quad . \tag{2.39}$$

The conversion efficiency (η) of the solar cell can be calculated by taking the ratio between the maximum converted power and the power of the incident light,

$$\eta = \frac{P_{mpp}}{P_0} = \frac{V_{oc}\ j_{sc}\ FF}{P_0} \quad . \tag{2.40}$$

Another useful method of characterizing a solar cell is by looking at its electrical sensitivity to the wavelength of the incoming light; the quantum efficiency (QE) is one such measurement.

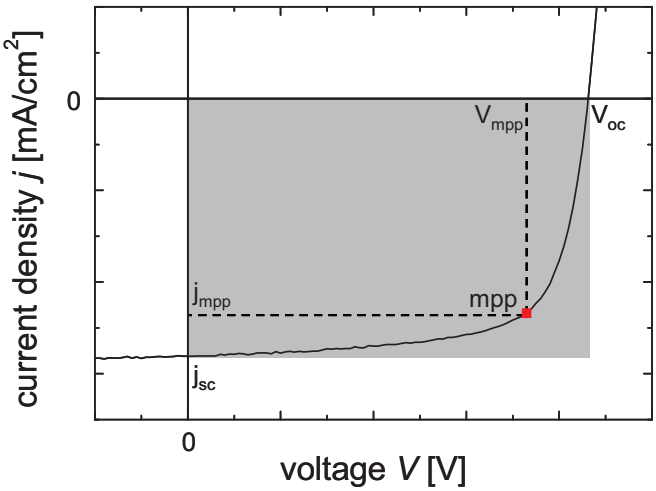

Figure 2.12: Typical curve for current density as a function of voltage under illumination.

The quantum efficiency is defined as the ratio between the number of collected photo-generated electron-hole pairs (N_e) and the number of incident photons (N_γ) for a given wavelength (λ),

$$QE(\lambda) = \frac{N_e(\lambda)}{N_\gamma(\lambda)} \quad \textbf{(2.41)}$$

The short circuit current density (j_{sc}) of a solar cell can be calculated from the quantum efficiency by integrating the product of the electron charge, the quantum efficiency (QE), and the photon flux (Φ_γ) of the spectrum over the wavelengths in the spectrum,

$$j_{sc} = e \int QE(\lambda)\, \Phi_\gamma(\lambda)\, d\lambda \,. \quad \textbf{(2.42)}$$

In this way the short circuit current density can be calculated for any arbitrary spectrum.

3. Experimental

This chapter gives the experimental details on how samples were prepared and characterized. The sections covering sample preparation follow the order typically used for silicon thin-film solar cells preparation on sputtered ZnO:Al; first ZnO:Al deposition, then ZnO:Al treatments such as texturization and annealing, and finally solar cell fabrication. The various methods used to characterize the ZnO:Al and solar cells are then introduced. Some of the characterization methods used were developed within this work, and for these new methods, additional experimental details are given, since they may be applicable to other areas of research.

3.1. ZnO:Al Deposition

ZnO:Al deposition was performed in two systems, the 'small area sputtering system' (Kurt J. Lesker Company) and the 'large area sputtering system' (VISS 300, Von Ardenne Anlagentechnik) which handle samples sizes up to 10x10 and 30x30 cm^2 samples, respectively. Unless otherwise specified, depositions were made onto 10x10 cm^2 glass (Eagle XG, Corning) substrates. Prior to deposition, substrates were cleaned by sonication in a warm (65 °C) basic solution. The following sections give the specific deposition details for the small and large area sputtering systems.

3.1.1. Small Area Sputtering System

The small area sputtering system is a static deposition system, where a circular target with a diameter of 15.24 cm (6 inches) is mounted onto a cathode 10 cm away from the substrate holder. During presputtering a movable shutter separates the direct path between the target and the substrate. Samples are heated from the backside by radiative heating from an isothermal metal plate located two centimeters above the substrate holder, the metal plate is heated by two halogen lamps. Two turbo pumps, one for the loading chamber and one for the sputtering chamber, evacuate the system. During sputtering, the pressure is controlled by an adjustable valve in front of the turbo pump, and the sputtering gas stream is controlled by mass flow controllers.

The thickness of the ZnO:Al films prepared in the small area sputtering system is rather inhomogeneous. A circle with a diameter of five centimeters in the center of the substrate is relatively homogeneous having thickness deviations of a few percent, but outside this center, the thickness decreases radially, exhibiting decreases of about 10 and 20 % on the edge and in a corner (on a 10x10 cm^2 sample), respectively. All measurements of films prepared in the small area sputtering system were made within the relatively homogeneous center. More details on the homogeneity of the ZnO:Al films prepared in the small area sputtering system can be found elsewhere [130].

While different types of samples were prepared in the small area sputtering system, most of the sputtering parameters were held constant at optimized values [131]. A base pressure of

$3x10^{-5}$ Pa was reached before proceeding for all depositions. Sputtering was performed with RF excitation at 13.56 MHz from a ceramic $ZnO:Al_2O_3$ target with 0.5 w/w% Al_2O_3. Argon was used as the sputtering gas and the flow rate was held constant at flow eight standard cubic centimeters per minute (sccm). The sputter power and pressure were 225 W and 0.3 Pa, respectively. Prior to opening the shutter between the target and the substrate, the target was presputtered for five minutes at identical conditions.

Four different sputtering conditions will be referred to throughout the text. They will be referred to as follows, 'heated single deposition', 'RT single deposition', 'RT hourly pulsed', and 'RT daily pulsed'. Heated single deposition samples were deposited with an approximate substrate temperature of 400 °C. To get this substrate temperature, the isothermal metal plate was heated to a temperature of 525 °C [120]. All material was deposited in a single deposition. RT single deposition samples were not intentionally heated, and all material was deposited in one continuous deposition. However, inadvertent heating from hot incoming atoms occurred. RT hourly pulsed samples were not intentionally heated, to limit heating from the incoming atoms the deposition was carried out in five minute pulses, which corresponds to a deposition of approximately 100 nm. Between pulses the sample cooled in vacuum for one hour. RT daily pulsed samples were deposited in the same manner as the RT hourly pulses; only instead of cooling for one hour in vacuum, samples were removed from the sputtering system and exposed to atmosphere for at least 24 hours between five minute pulses.

3.1.2. Large Area Sputtering System

The large area sputtering system is a very flexible deposition system with two loading chambers and three process chambers for different sputtering methods. In this system, a substrate holder with a maximum size of 30x30 cm^2 passes in front of various targets at a distance of 8 cm. The system is operated generally in a dynamic mode (with the substrate holder moving during deposition). Samples are heated from the back side by radiative heaters located in both the loading and process chambers. Samples were heated for at least one hour prior to deposition. Turbo pumps evacuate the system to a base pressure of $8x10^{-5}$ Pa before deposition. During sputtering, the pressure is controlled by butterfly valves in front of the turbo pumps, and the flow of the argon sputtering gas and reactive oxygen gas streams are controlled by mass flow controllers. The target was presputtered for at least 10 minutes before the substrates made a first pass in front of the target. For all samples within this work the single substrate 30x30 cm^2 holder was replaced with a 3x3 matrix of 10x10 cm^2 samples.

Films prepared in the large area sputtering system have relatively homogeneous thicknesses with a maximum variation around six percent over the 30x30 cm^2 area. The thickness variation over a single 10x10 cm^2 sample was even less at around two percent. Thus, for a standard thickness deposition with a goal of 800 nm, the thickness could vary up to 50 nm from one 10x10 cm^2 substrate to another, and less than 20 nm over a single substrate.

3.1.2.1. Standard ZnO:Al

The bulk of the experiments performed in this work were performed on the so-called 'standard' ZnO:Al substrate, for which the ZnO:Al films were deposited onto CG by dual magnetron sputtering from planar ceramic targets. The plasma excitation frequency was in the RF range

at 13.56 MHz. The dimensions of the planar targets were 75x10 cm^2. The ceramic target consisted of ZnO:Al_2O_3 with 1 w/w% Al_2O_3. Depositions were performed at a temperature, pressure, discharge power, and argon flow of 300 °C, 0.1 Pa, 1.5 kW, and 100 sccm, respectively. Depositions were made in dynamic mode with the substrate passing in front of the target 32 times. Under such sputtering conditions the deposition rate was 6 nm · m/min; additional details on the ZnO:Al film properties are given elsewhere [24].

3.1.2.2. High-Rate Ceramic ZnO:Al

High-rate ZnO:Al films were deposited onto CG by dual magnetron sputtering from cylindrical ceramic targets. The plasma excitation was in the mid-frequency (MF) range at 40 kHz. The length and diameter of the cylindrical targets were 75 and 16 cm, respectively. The ceramic target consisted of ZnO:Al_2O_3 with 0.5 w/w% Al_2O_3. Deposition was performed at a temperature, pressure, discharge power, and argon flow of 350 °C, 1.5 Pa, 14 kW, and 200 sccm, respectively. Depositions were made in dynamic mode with the substrate passing in front of the target four times. Under such sputtering condition the deposition rate was 100 nm · m/min; additional details on the ZnO:Al film properties are given elsewhere [132].

3.1.2.3. High-Rate Reactive ZnO:Al

High-rate reactively sputtered films were deposited onto CG by dual magnetron sputtering from cylindrical metallic targets. The plasma excitation was in the mid-frequency (MF) range at 40 kHz. The length and diameter of the cylindrical targets were 75 and 16 cm, respectively. The metallic target consisted of Zn:Al with 0.5 w/w% Al. Deposition was performed at a temperature, pressure, oxygen partial pressure, discharge power, and argon flow of 350 °C, 1 Pa, 0.1 Pa, 10 kW, and 200 sccm, respectively. The oxygen flow was controlled by plasma emission monitoring (PEM). Depositions were made in dynamic mode with the substrate passing in front of the target five times. Under such sputtering condition the deposition rate was 120 nm · m/min. Additional details on the resulting ZnO:Al properties can be found elsewhere [133].

3.2. Post-Deposition Processes

This section introduces processes done to the ZnO:Al films following deposition. Processes include chemical etching, annealing, and damp-heat degradation.

3.2.1. Etching

Sputtered ZnO:Al films are relatively flat in the as-deposited state. Films can be etched in acidic or basic solutions to introduce light trapping features. The etch rate of a solution depends on the etchant, concentration, and temperature. To compare the etching effects of different solutions, etching times were adjusted such that approximately 150 nm of the ZnO:Al was removed, unless otherwise specified. It is important to note that the removed thickness is determined by surface profiler. The relatively large stylus cannot penetrate deeply into the etched

features, making the removed thickness measured a lower limit for the actual removed film thickness; additional details will be given in Section 3.4.1 (page 42). Unless otherwise specified, etches were performed at RT, which, though it can fluctuate by a few degrees depending on the season, is generally assumed to be 25 °C.

3.2.1.1. Standard Etch

The current state-of-the-art for texturizing sputtered ZnO:Al for thin-film silicon solar cells is to etch in dilute hydrochloric acid (HCl) solution [13]. The standard etch referred to in this work implies that etching was performed at RT in an HCl solution with a concentration of 0.5 w/w%. The etch time in the standard solution was generally between 40 and 50 seconds for a standardly deposited ZnO:Al substrate (see Section 3.1.2.1 (page 38)).

3.2.1.2. Other Etchants

Besides the standard HCl acidic etch, other acidic etchants were examined within this work, including sulfuric (H_2SO_4), nitric (HNO_3), phosphoric (H_3PO_4), acetic (CH_3CO_2H), and hydrofluoric (HF) acid. Etching in a basic solution of potassium hydroxide (KOH) was also examined. Further, etches were performed in mixed acid solutions including; *aqua regia*, one part HNO_3 and three parts HCl; 'piranha', a mixture of three parts H_2SO_4 and seven parts hydrogen peroxide (H_2O_2); and various mixtures of HF and HCl.

The solution concentrations are given as the relative percentage of the acid weight to the total weight of the solution (w/w%). The acid concentrations were generally around 0.5 to 1 w/w%, although acid concentrations as high as 25 w/w% for CH_3CO_2H, and as low as 0.03125 w/w% for HCl were used.

When etching at temperatures above RT, a hot plate was used to heat the solution and a digital thermometer, with an accuracy of 0.1 °C, was used to control the temperature. Solutions were periodically stirred and the accuracy of the etching temperature was determined by measuring the temperature before and after sample etching. To limit temperature-related effects from etching a relatively cold sample in a hot etchant, samples were first brought to roughly the same temperature as the etching solution by submerging them in a beaker of water on the same hotplate for a few seconds before moving the samples to the etchant. No ZnO:Al etch rate was observed from this short bath in hot water. It should also be noted that HCl etch rates were very similar during the heating and cooling of the solution, indicating the evaporation of HCl or H_2O was not strongly favored over the other, as a change in concentration would alter the etch rate.

3.2.2. Annealing

To improve the mobility of the electrons in ZnO:Al films samples were annealed (Section 2.8.1 (page 30)). Prior to annealing, ZnO:Al samples were capped with an n-type amorphous silicon layer. This layer was deposited by PECVD (see Section 3.3 (page 41)), and had a thickness of approximately 50 nm. During annealing, the capped ZnO:Al was placed in a quartz oven at 250 °C. The temperature was then slowly increased at a rate of 1.5 °C/min to 650 °C where it was annealed for 24 hours. Following annealing, the temperature was slowly decreased at a rate

of 1.5 °C/min until 250 °C, when the samples were removed from the oven. Annealing was performed at atmospheric pressure in a nitrogen atmosphere.

To characterize the ZnO:Al post annealing, it was necessary to remove the amorphous silicon cap. This was done by dry etching using nitrogen trifluoride (NF_3) in a PECVD reactor. Etching was performed at a temperature, pressure, power, and NF_3 flow of 40 °C, 67 Pa, 110 W, and 40 sccm, respectively. Etches were performed for 45 seconds, which is long enough to ensure complete silicon removal. Due to the selective nature of the NF_3 etch, no ZnO:Al etching was detected even with longer etching times of 20 minutes. More details on the annealing process can be found elsewhere [28].

3.2.3. Damp-Heat Degradation

Exposing materials to a damp-heat environment is a method of accelerating the aging process (see Section 2.8.2 (page 31)) [134]. Damp-heat experiments are generally performed at 85 °C and 85 percent humidity [122]. Within this work, damp-heat experiments were done in water (H_2O) and deuterated water (D_2O) rich environments. ZnO:Al samples were placed in a glass exsiccator with a few milliliters of either H_2O or D_2O. This exsiccator was placed in an oven set to 95 °C; a built-in thermometer measuring near the exsiccator registered approximately 88 °C, the temperature inside the exsiccator is likely slightly cooler. Thus, the damp-heat experiments were performed under conditions close to the standard. Samples were exposed to a damp heat for periods between 24 and 1000 hours. The water was consumed at a rate around one milliliter per day, and was periodically checked and refilled when needed. All damp-heat treatments were performed in the presence of the standard atmospheric gasses, including primarily nitrogen (N_2, 78.09 %), oxygen (O_2, 20.95 %), argon (Ar, 0.93 %), and carbon dioxide (CO_2, 0.039 %).

3.3. Solar Cell Deposition

All silicon depositions were made using an in-house modified PECVD system (Materials Research Group). This system has two loading and two process chambers; each chamber is equipped with coil heaters and can handle samples with sizes up to 30x30 cm^2. To limit dopant contamination, one chamber was used for depositing the doped p- and n-type silicon, while the other was only used for depositing the intrinsic silicon. A plasma excitation frequency in the RF range at 13.56 MHz was used to enhance gas decomposition, allowing substrate temperatures to be kept under 250 °C. Hydrogen (H_2) and silane (SiH_4) were used as the precursor gasses throughout for silicon deposition. Trimethylborane ($B(CH_3)_3$) and phosphine (PH_3) gasses were introduced during p- and n-type silicon growth, respectively. All doped layers had an approximate thickness of 20 nm. To ensure homogeneous gas distribution, all gasses were introduced to the plasma through a showerhead. Additional details on the PECVD system can be found elsewhere [135].

Three types of active layers were used within this work, amorphous silicon, microcrystalline silicon, and tandem amorphous/microcrystalline silicon. For all silicon depositions the doped p- and n-type regions had an approximate thickness of 10 nm. To complete the solar cells, layers of ZnO:Al and silver were deposited. These layers serve the dual purpose of reflecting light and

collecting current. The deposition parameter and post-deposition treatments of the active silicon layers and the back reflector are as follows.

Amorphous silicon: Amorphous silicon cells were deposited with p-i-n configuration. Deposition was performed at a temperature, pressure, power, silane flow, and hydrogen flow of 200 °C, 400 Pa, 30 W, 36 sccm, and 300 sccm, respectively. These deposition conditions yielded a silicon growth rate of 0.15 nm/s.

Microcrystalline silicon: Microcrystalline silicon cells were deposited with p-i-n configuration. Deposition was performed at a temperature, pressure, power, silane flow, and hydrogen flow of 160 °C, 1067 Pa, 400 W, 19 sccm, and 2000 sccm, respectively. These deposition conditions yielded a silicon growth rate between 0.35-0.5 nm/s.

Tandem Amorphous/Microcrystalline Silicon: Tandem amorphous then microcrystalline solar cells were deposited with p-i-n-p-i-n configuration. The deposition conditions for the individual amorphous and microcrystalline subcells are the same as those listed for the single junction cells.

Back Reflectors and Contacts: ZnO:Al was deposited by RF sputtering from a ceramic target consisting of ZnO:Al_2O_3 with 1 w/w% Al_2O_3. Depositions were performed in the large area sputtering system (Section 3.1.2 (page 38)) at RT. The pressure, discharge power, argon flow, and oxygen flow were 0.5 Pa, 1.5 kW, 99.5 sccm, and 0.5 sccm, respectively. Silver was thermally evaporated through a mask to define 18 individual 1x1 cm^2 test cells. The back contact ZnO:Al and silver layers had a thickness of about 80 and 700 nm, respectively.

To avoid current collection from areas outside the defined silver pad, the ZnO:Al not covered by silver was removed by etching in a 0.5 w/w% HCl solution. The cells were then annealed in an oven at 160 °C for 45 minutes under standard atmospheric conditions improve the electrical contacts.

3.4. Characterization Methods

To determine the affects of modifications made in the deposition or post-deposition treatments, the ZnO:Al and the solar cells must be reproducibly characterized. This section presents the various methods used to image surfaces and characterize the structural, electrical, and optical properties of ZnO:Al and the solar cells. New methods for analyzing particular locations and representing changes to surfaces were developed and are presented within this section.

3.4.1. Thickness and Etch Rate

A surface profiler (Dektak 3030, Veeco) equipped with a 12 µm diameter stylus was used to determine film thickness. To measure the thickness of the thin-films a step between the underlying substrate and the top of the film must be made. For ZnO:Al such steps were made by masking off a small circle with an approximate diameter of 1 mm with hydrophobic ink. The area around the ink point is then etched, usually with 2 w/w% HCl, until the underlying CG

substrate is reached. The hydrophobic ink points were then removed using isopropyl alcohol, and the thickness measured as a bump on the CG. For silicon, the steps were made using laser ablation of the silicon layer [136]. The laser emits 532 nm light; this wavelength is strongly absorbed in the silicon, while the ZnO:Al remains relatively unaffected. The thickness is then measured as a step down to the underlying ZnO:Al layer between silicon regions.

Surface profiler measurements at the same location showed less than one percent deviation with repeated measurements on a standard ZnO:Al film (800 nm). Fluctuations due to slight inhomogeneities in ZnO:Al film thickness(see Section 3.1.2 (page 38)) are a more significant source of thickness measurement error. The error in thickness on rough films is slightly higher, due to the scattering of data.

Since the craters on the ZnO:Al surface resulting from etching generally have diameters smaller than 2 µm, the comparably large stylus will penetrate only a few nanometers into the crater. The surface profiler measurements thus give a lower limit in determining etch rates, as the thickness of the most slowly etched points (those on the crater rims) are effectively measured. Etch rates determined by surface profiler alone, are thus, underestimated as the thickness is overestimated.

Volume based etch rates must take the ZnO:Al surface topography as measured by atomic force microscopy (AFM, see next section) into account. To this end, a more general removed amount of ZnO:Al can be calculated as not only the difference between the etched (d_{etch}) and as-deposited (d) thicknesses (from surface profiler measurements), but also the difference between the mean (AFM_{mean}) and 95% of the maximum ($AFM_{95\%}$) AFM values. Specifically, the average removed thickness (Δd) which takes crater depth into account is given by

$$\Delta d = (d_{etch} - d) + (AFM_{mean} - AFM_{95\%}) . \qquad \textbf{(3.1)}$$

Using 95% of the maximum thickness assumes the stylus of the surface profiler hardly penetrates the craters.

3.4.2. Atomic Force Microscopy (AFM)

"AFM can be viewed as an extension of a toddler's way of 'grasping' the world by touching and feeling" [137]; as a nanometer-scale mechanical 'tip' is scanned across a surface using piezoelectric elements to 'feel' the surface. As a tip is scanned across a surface, laser light incident on the back of the cantilever is deflected differently as the surface features change; this deflection is measured using a photodiode. Much of the technology for the AFM came from that developed for the scanning tunneling microscope (STM) [138,139]. Unlike the STM, however, the AFM can be used to measure both conducting and insulating surfaces and does not require the sample to be in ultra-high vacuum [138,139]. In fact, AFM measurements can even be done within liquids [140]. There are two major operation modes for AFM, contact and non-contact. In contact mode, an AFM tip is brought in contact with the surface and is then scanned. The potential across the piezoelectric electric z-axis (height) control is adjusted during the scan to maintain constant deflection. The surface topography is determined from the change in the applied potential. In non-contact mode, an AFM tip is driven near its resonance frequency. When the tip is close to the sample surface (1 to 10 nm) the van der Waals forces attract the tip increasing the amplitude and decreasing the oscillation frequency of the tip. The piezoelectric elements are adjusted such that the amplitude of the oscillation remains constant; the surface topography is calculated from this modulation. Since the AFM tips should not contact the

sample in non-contact measurements the tips tend to wear more slowly, allowing on average more scans before tip replacement.

There are challenges with the AFM, such as the maximal scan sizes and the relatively long times required to image surfaces. The AFM scan sizes are limited by the range of piezoelectric elements, and a typical image takes between 30 and 120 minutes to acquire. Other surface imaging techniques such as the scanning electron microscopy (SEM, Section 3.4.5 (page 52)) can image much larger areas in a matter of seconds. The AFM (Nanostation 300, SIS) used in this work was limited to an 82.5x82.5 µm^2 scan area. Additionally, measurement artifacts and limitations such as thermodrift, piezo-creep, and variations in the shape of the AFM tip distort the acquired image [141-143].

On the other hand, the AFM possesses some important advantages that make it the most often used surface imaging tool within this work. AFM images are stereoscopic, and AFM imaging (in non-contact mode) is non-destructive. The following sections discuss how such advantages can be used to analyze surfaces statistically, calculate densities of grains or craters, as well as image the same location between etching steps without modifying the etching properties.

3.4.2.1. Statistical Evaluations of AFM Data

Since AFM measurements yield stereoscopic images, statistical analysis of the surface can be performed. This work includes the following three statistical analysis methods; root mean square (RMS) roughness, distribution of heights, and angular distribution. The RMS roughness (δ_{RMS}), as given by

$$\delta_{RMS} = \sqrt{\frac{1}{M\,N}\sum_{k=0}^{M-1}\sum_{l=0}^{N-1}\left[z\left(x_k, y_l\right)\right]^2} \quad , \tag{3.2}$$

is a statistical measure of variations in the height magnitude, where M and N are the number of points scanned in the x and y directions, and z is the height at a given x and y coordinate; k and l are solely for indexing purposes. Since two completely different surfaces can give the same RMS roughness values [141,144], one must be careful when interpreting. The standardly etched ZnO:Al surfaces (Section 3.2.1.1 (page 40)), however, have preferential opening angles [42], so major ambiguities due to different surface structures should not arise under these etching conditions.

The distribution of heights is calculated by counting the AFM feature heights that fall within a given step size. Results are presented as histograms, where the fraction of the surface within each 10 nm increment is given as a function of feature height. The surface angular distribution is calculated by counting the number of local surface angles that fall within a given step size. The local surface angles are calculated by comparing the normal vector of three neighboring AFM measured points to that of the whole AFM scan [145,146]. Results are presented as histograms, where the fraction of the surface exhibiting angles within a given one degree increment is given as a function of the surface angle.

These statistical analysis values depend on the data leveling method used. In general, the AFM data of etched surfaces were leveled using a simple plane level. For as-deposited or other very flat surfaces which have feature sizes close to the limit of what the AFM could measure, effects such as thermodrift, piezo-creep are observable [141-143]. To correct for such distortions

the AFM data of relatively flat samples were generally leveled using a median or second order polynomial level. For most samples, the average height value was generally set to zero, making the comparison between two measurements easier.

Figure 3.1 gives the RMS, height distribution, and angular distribution for three surfaces at different points in the texturization process, specifically, as-deposited, optimally etched, and over-etched (CG exposed). The percentage of these surfaces within a given 10 nm increment and a given angle within one degree increments are shown in Figure 3.1 (a) and (b), respectively.

Since as-deposited surfaces (solid black line) are relatively flat, the height distribution is very sharp (Figure 3.1 (a)) and the peak in the surface angular distribution is at a relatively shallow angle of 10° (Figure 3.1 (b)). On the other hand, both standardly (dashed red line) and over- (dotted blue line) etched surfaces exhibit fairly broad distributions in feature height, and steeper surface angles are observed, Figure 3.1 (a) and (b) respectively. Over-etched samples exhibit two peaks in the height and surface angular distributions. The first peak located at the deepest feature height and shallowest angles corresponds to the glass, while the second broader peak at higher height and steeper angles corresponds to the standard ZnO:Al texture (similar to the peaks of the standardly etched sample).

Ideally the peak related to the glass should be sharper; RMS roughnesses of about 1 nm were measured on the glass layer alone. Thus, distortions and artifacts also appear in the scans

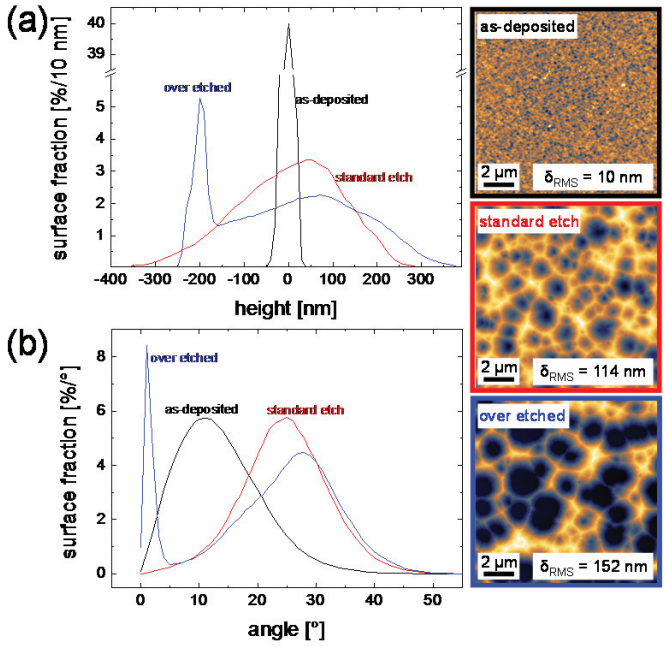

Figure 3.1: Statistical evaluations of ZnO:Al at three different stages in the etching process: as-deposited (black solid line), standardly etched (red dashed line), and over-etched (blue dotted line). (a) Fraction of the surface exhibiting a given height quantized into 10 nm increments, and (b) fraction of the surface exhibiting a given angle quantized into one degree increments. For reference, the AFM images from which these statistics were calculated are shown on the right side.

of larger structures. The reproducibility of a scan is very good at the same location, showing less than a percent variation in RMS roughness. The statisctics resulting from different (10x10 µm²) scans at very close locations on a same sample were generally within 5 % of eachother.

3.4.2.2. Grain and Crater Densities from AFM Data

AFM data can also be analyzed to estimate the ZnO:Al grain and crater size for unetched and etched surfaces, respectively. Since grain boundaries and crater boundaries do not all start at the same height for a given sample, using a simple height threshold for marking the boundaries tends to drastically underestimate the number of grains or craters. Instead grain and crater densities were estimated from AFM data using a watershed algorithm. The watershed algorithm was introduced by Beucher and Lantuéjoul in 1979 [147]. It basically works by first finding the minima on the surface. A source of 'water' is then placed at these local minima and the pores are filled. When the different pools of water meet a watershed boundary is drawn, thus effectively dividing an AFM image into a set of basins. This method works for calculating the size and density of craters. Similarly, images can be inverted and the same process can be used to calculate grain size.

Figure 3.2 shows grains and craters on an AFM image of a standard ZnO:Al surface in the as-deposited and standardly etched states as marked by a watershed algorithm. The images in Figure 3.2 show the inclusion of elements on the border, since only a fraction of these grains or craters are in the images, densities calculated are slightly over estimated. Alternatively, grain or crater densities can be calculated by extrapolating the density of the whole from the grains or craters not on the border. This method also overestimates the crater density as larger fea-

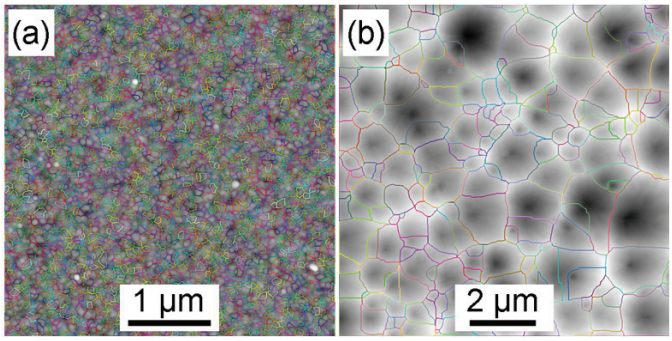

Figure 3.2: (a) Grains and (b) craters as marked by watershed algorithm on AFM images of unetched and standardly etched ZnO:Al.

Table 3.1: Density and area of grains and craters for as-deposited and standardly etched ZnO:Al samples, respectively. Values are given for both including and excluding the border elements.

	including border elements		excluding border elements	
	density [µm^{-2}]	area [nm^2]	density [µm^{-2}]	area [nm^2]
as-deposited	185	5405	191	5240
standardly etched	2.1	4.8x10^5	2.2	4.5x10^5

tures are more likely to be incident on the border, thus counting a larger percentage of small features. Table 3.1 lists grain and crater densities when including or excluding the border elements. Notice that a difference of only three and five percent were observed between including and excluding the border elements for grain and crater density calculations, respectively. The difference is only slight since scanned areas were large with respect to the feature size. In general, grain and crater densities from AFM images throughout this work were calculated by extrapolating the densities from counts that excluded the border elements.

3.4.2.3. Repositioning on the Nanometer Scale

Experiments such as finding the initial points of etching in relation to the as-deposited ZnO:Al films (Section 6.1.1.2, page 92), or following the evolution of an etch as a function of etch time (Section 6.1.1.3, page 96), require multiple non-destructive surface topographical measurements at the same location. Two commercially available and commonly used imaging tools are the AFM and the SEM (see Section 3.4.5 (page 52)). The AFM was chosen as the preferred imaging tool for such experiments since SEM imaging presents some challenges. Firstly, during SEM imaging a thin layer of carbon is deposited on the surface. This carbon layer comes from electron beam induced chemical vapor deposition of back streamed pump oil or contaminations resulting from exposure to air [148]. The presence of a carbon layer alters how the etching proceeds in subsequent etching steps. Secondly, SEM images are not truly stereoscopic. Good insight into the morphology can be obtained using different detectors and angles of incidence [149]; however, statistical evaluations such as those discussed in the previous section are not as reliable on SEM images. An AFM operated in non-contact mode, on the other hand, limits the destruction caused by imaging as the tip should not come into contact with the surface. Further, resultant data is stereoscopic, which allows for easier comparison between etching steps and statistical analysis of the surface (Section 3.4.2.1, page 44).

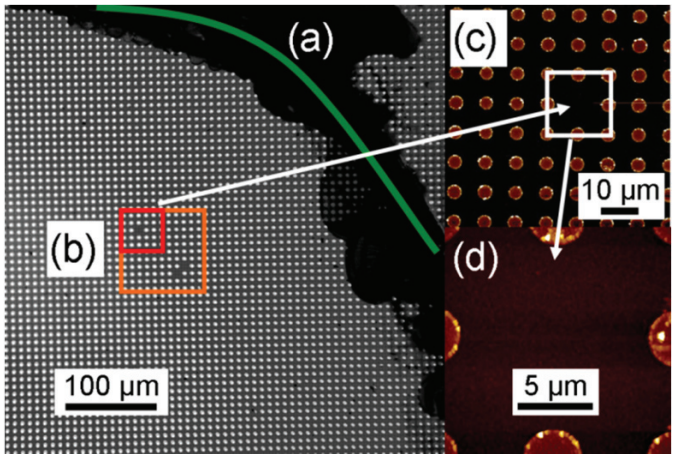

Figure 3.3: Alignment process: (a) Optical image of a manual mark made using a diamond tip (green line). (b) Optical image of defects in the Ag grid (larger orange square), and the area analyzed (small red square). (c) Large AFM scan of the area looking for the defect in the grid of interest. (d) Smaller scan of only the grid defect and the area that can be repositioned.

A photolithographically deposited grid was used to aid with repositioning samples on the nanometer scale. This multistep clean room process proceeds as follows: substrates (usually ZnO:Al sputtered onto a CG) were degreased by bathing in acetone followed by isopropyl alcohol for approximately one minute each. Samples were blown dry with nitrogen, and put on a hot plate set to 180 °C for at least 15 minutes to eliminate any residual water on the surface. Next, the surfaces were coated with a photoresist (AZ 5214E, Clariant) and spun at 4000 RPM for one minute. The samples were then soft-baked on a hot plate at 85 °C for five minutes. The sample and a mask containing the desired pattern were aligned and exposed to ultraviolet light from a 350 W mercury vapor bulb (with the spectral peak at 365 nm) using a mask aligner (MA-6, Karl Süss). Exposure times ranged between ten and 30 seconds. Samples were then etched in a developer (AZ 326 MIF, Clariant) for times between 60 and 240 seconds then rinsed with DI water and dried with nitrogen. Next, 50 nm of silver were thermally deposited onto the surface using a quartz crystal thickness monitor (XTC/2, INFICON) to control the deposition process. Finally, the remaining photoresist and the silver deposited on top of the photoresist were removed by soaking in acetone for multiple hours and subjection to sonication (Sonorex Super RK 103 H, Bandelin). Note that some commonly used processes which create better defined surfaces such as spin coating an adhesion layer prior to the photoresist or reactive ion etching the sample after development were not used. The exclusion of processes such as these created a small percentage of defects in the grid, these defects were used advantageously: they form unique patterns that aid with repositioning.

To position the sample on the nanometer-scale between the multiple etching steps reproducibly, four progressively smaller alignment methods were used as indicated in Figure 3.3. First large scale manual marks were made using a diamond tip for the millimeter-scale alignment of the sample, see Figure 3.3 (a). Second, the photolithographically deposited grid was used to align the sample within 30 µm. The grid consisted of thermally evaporated silver dots with sizes typically between three and four micrometers in diameter (depending on exposure and development times), a spacing of eight micrometers, and a thickness of 50 nm, as shown in Figure 3.3 (b), although other masks with different grid size spacing were also used within this work. Defects in the grid were used as markers and areas to scan since they were spread uniquely across the ZnO:Al surface and provided larger areas to scan. The density of defects in the grid was controlled by changing the exposure and development times during the photolithographic process (longer exposure and development times tending to have fewer defects and larger dots). Third, a large AFM scan was used to further localize (within 1 µm) the defect of interest in the silver grid, see Figure 3.3 (c). Last, the area of interest was aligned using the silver dots and scanned, see Figure 3.3 (d). Using this method and comparing new scans to previous scans provided a method of realignment on the nanometer-scale.

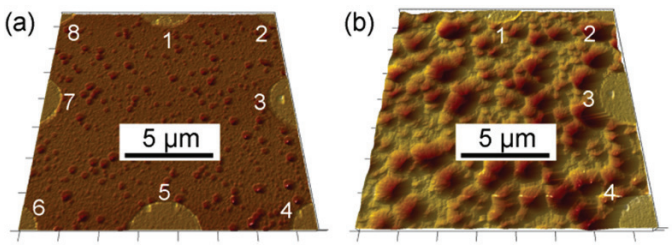

Figure 3.4: AFM scans after a cumulative etching time of (a) 2 and (b) 10 seconds.

A particular challenge with this alignment method is that the markers used for alignment are deposited onto the ZnO:Al which is then etched; thus after longer etching times the markers used for realignment can be lost as the ZnO:Al to which the silver is bonded is etched away. Figure 3.4 (a) and (b) show AFM images in the same location after two and ten cumulative seconds of etching in two second intervals followed by imaging steps, respectively. Notice that all eight silver grid points are still present after the single etching step, while only half remain after five etching steps. Despite the loss of some of the silver markers, repositioning the sample in the AFM was still possible using the remaining markers and larger manual marks. During these ten cumulative seconds of etching, the surface developed unique features that could be identified and remained fairly consistent between etching steps, Figure 3.4 (b). Once the surface has evolved to this point, the silver grid is helpful but no longer necessary for realignment. In this case, realignment could alternatively be done using a modified keystone technique [150]. The intact grid is, however, necessary for nanometer-scale realignment during the initial etching steps as the unique patterns from the as-deposited grains are only identifiable on small area AFM scans (less than 10x10 μm^2).

3.4.2.4. Comparing Etching Steps

Using the repositioning method described in the previous section, it is possible to observe the same location before and after a small etching step. To show slight changes such as observing the initial etching sites (Section 6.1.1.2, page 92), a method for displaying data that show not only morphology, but also a local etch rate is required.

One such method is first exemplarily introduced in two dimensions in Figure 3.5, which gives a schematic of how a local etch rate can be indicated with morphology for a single line

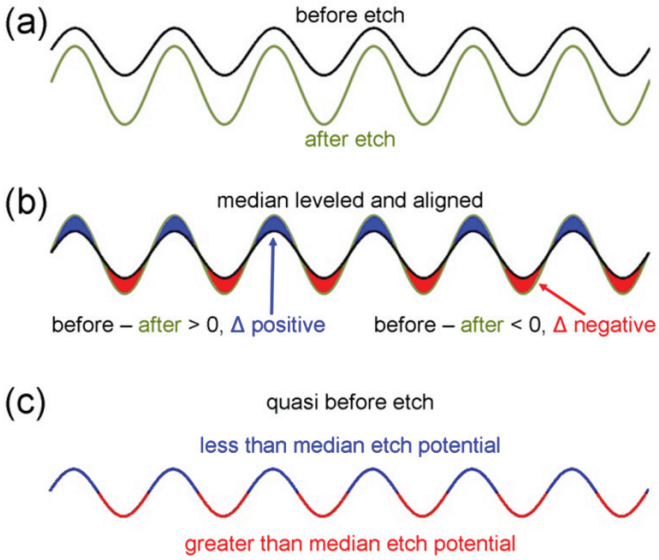

Figure 3.5: Schematic diagram of and AFM scan profile (a) before and after etching, and (b) after median leveling and alignment. Changes are considered positive or negative, depending on the difference between the median level before and after etching.

scan. First, line scans are taken at the same location before and after an etching step, Figure 3.5 (a). The whole surface is etched during the etch process: however, by median leveling and aligning the line scans it is possible to look at the differences and see which areas were most and least strongly etched, see Figure 3.5 (b). Areas that exhibit a lower value after etching are more strongly etched, while areas exhibiting a higher value after etching are less strongly etched. A local etch rate can be shown on the original line scan by taking the etched line scan and adding the strongly etched areas with a red color marker and subtracting the weakly etched areas with a blue marker, see Figure 3.5 (c). Thus, the resultant image is one of the original line scan, but the red and blue colors represent areas which will be more and less strongly etched, respectively.

The process is similar for three dimensional images. First, AFM images are taken at the same location before and after a slight etching step. The AFM measurements are median leveled and a gray scale representing height is set to the same range for both images. To determine which grains are strongly and weakly etched, the AFM images require further post-scan alignment to correct for effects such as thermodrift and piezo-creep [142]. Effects such as these are generally small and can be ignored when looking at large areas or large structures; however when examining small areas with small features and aligning individual ZnO grains, these slight differences were observed. To fine tune the alignment and correct for drift, images were further aligned using the rotation and shear tools of an image manipulation program. The etched image was subtracted from the unetched image, and vice versa, to yield images showing the most and least actively etched locations on the surface, respectively. To reconstruct the unetched sample with colors indicating strong or weak etch potential, the colorized images of the most and least actively etched locations were added and subtracted from the etched image, respectively.

Figure 3.6 (a) gives an example of one such reconstructed image. Notice that when well aligned, both the topography (gray scale) and local etch rate (red-blue) are visible. The same area without a correction for drift is shown in Figure 3.6 (b), and the same image with corrected drift but a misalignment of approximately 40 nm (or one grain size) along the y-axis is shown in Figure 3.6 (c). When the drift is not corrected, only the area close to the well aligned point is clear (Figure 3.6 (b), upper right-hand corner) while areas further away become more unclear until the original topography is lost. Likewise, a slight misalignment of approximately

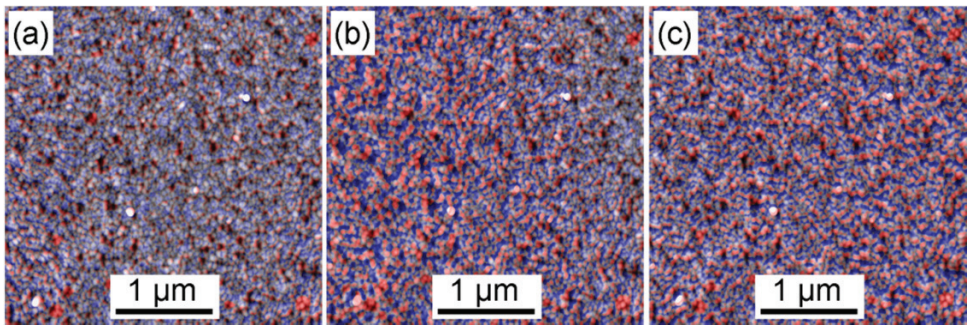

Figure 3.6: Reconstructed as-deposited states with different degrees of alignment. (a) Alignment and drift corrected, (b) upper right-hand corner aligned but the drift is uncorrected, and (c) corrected drift but y-axis misalignment of ten pixels (40 nm or approximately one grain).

one grain yields images where the relationship between grains and etching potential is unclear (Figure 3.6 (c)).

3.4.3. Optical microscope

Because of length of time required to take AFM measurements, it was often useful to first quickly characterize surfaces with an optical microscope (Eclipse L200, Nikon). The resolution of an optical microscope is limited to slightly more than half the wavelength of incoming light, as smaller objective lenses would lead to light diffraction [151]. Thus, light in the middle of the visible spectrum (about 500 nm) can resolve features down to approximately 300 nm. Craters on etched ZnO:Al can range in size from a few hundred nanometers to a couple micrometers in width [42]. These size features are at the limit of what an optical microscope can resolve. Thus, clearer images are obtained on ZnO:Al with larger craters. Optical images were generally taken in transmittance mode (diascopic) rather than reflected mode (episcopic) as the crater boundaries were more clearly resolved.

Despite not being stereoscopic the optical images could also be analyzed using a watershed algorithm when the intensity of light from the optical images is assumed to correspond to different film thicknesses. Figure 3.7 shows an optical image of a standardly deposited and etched ZnO:Al substrate with craters marked by a watershed algorithm. The density and average crater size are 0.66 μm^{-2} and $1.5x10^6$ nm^2, respectively. Notice the crater density is underestimated as compared to AFM measurements (Figure 3.2 and Table 3.1). Approximately three times more craters were observed in the AFM image than optical image. This stems from small craters and single craters resulting from multiple etch sites not being clearly resolved. The discrepancy between optically- and AFM-measured crater density increases with decreasing feature sizes, and factors as large as 16 were observed on samples with crater densities of 28 μm^{-2} (as measured by AFM). Optical images can thus give a fast overview and show general etching trends of surface features, but, due to the limited resolution of the optical microscope, conclusions will be drawn from higher magnification measurements such as AFM or SEM.

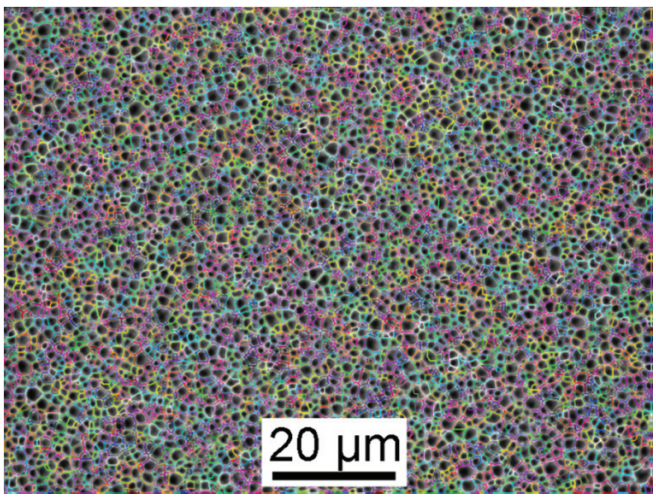

Figure 3.7: Optical image of a standardly deposited and etched ZnO:Al surface with the craters marked by watershed algorithm.

3.4.4. Confocal Microscope

For samples with features too large to be measured by AFM (greater than two micrometers in height or 82.5x82.5 µm^2 in area), but where a stereoscopic view is still required, a confocal microscope (µsurf, Nanofocus AG) was employed. The confocal microscope was invented by Marvin Minsky [152] and uses point illumination and a pinhole aperture before the detector to eliminate unfocused light. Using piezoelectrics to change the focal plane on the nanometer-scale stereoscopic images of the surface are made by assembling the in-focus sections of the images. In this work the confocal microscope was used to analyze crater sizes and densities on etched single crystal ZnO substrates. These craters are much less dense than those on polycrystalline ZnO:Al surfaces, requiring larger areas to be examined for good statistics.

3.4.5. Scanning Electron Microscopy (SEM)

An SEM basically functions by scanning a beam of high-energy focused electrons across a sample surface, while various detectors measure the signals of electrons emitted from the surface. Images of the surface are produced by assigning a contrast to the incoming signal. The beam of electrons are generally created by field emission from a tungsten tip, accelerated and focused into a nanometer-scale beam by condenser coils, and deflected to different areas on the surface by scanning coils. The resultant interactions measured can include inelastic (back scattered) electrons, elastic (secondary) electrons, and electromagnetic radiation (characteristic x-rays). Within this work, only the signal produced by the elastically scattered secondary electrons is examined.

The SEM is relatively surface sensitive with the secondary electrons originating from the first few to tens of nanometers for conductors [153] and insulators [154], respectively. The contrast in SEM images is generally related to the morphology of the surface, but is also affected by the density, conductivity, and shape of the material [149].

There are pros and cons to using the SEM for surface imaging. The SEM is relatively fast, and can image both at low (millimeter-scale) and high (nanometer-scale) magnifications. Additionally, sample cross-sections can be imaged easily by cleaving the sample and imaging it from the side. On the other hand, samples must be conductive. Insulators can be imaged after the deposition of a thin conductive layer: this conductive layer adds features of its own. Most SEMs require the sample chamber to be at relatively high vacuum to keep the mean free electron path large enough to reach the detectors. During sample imaging, a thin layer of carbon is deposited by electron beam induced deposition of back streamed pump oil or contaminations resulting from exposure to air [148]. Lastly, the images produced by most SEMs are not stereoscopic; although good insight into the morphology can be obtained using different detectors and angles of incidence [149].

SEM (Supra 55VP SmartSEM™, Carl Zeiss) images presented in this work were taken with an electron energy of 20 keV. The working distance (the distance between the end of the electron column and the sample) was four millimeters or less.

3.4.6. Transmission Electron Microscopy (TEM)

A TEM is a microscopic technique that images the electrons transmitted through very thin samples (generally less than 100 nm). Due to the small de Broglie wavelength of fast moving electrons, interactions occur between the incident electrons and the sample. Under the ideal circumstances, TEMs can resolve down to the atomic scale. The images produced by the transmission of electrons directly through the sample are called 'bright field' images, since holes in the sample appear bright. The contrast in bright field images can be described as mass-thickness contrast, as thin and amorphous regions scatter a smaller fraction of the incoming electrons and thus appear brightest [151]. For polycrystalline materials, such as sputtered ZnO:Al, the intensity of individual grains can also vary as the orientation varies [151].

While the particle-like nature of electrons is used to obtain a mass-thickness contrast in bright field images, the wave-like nature of electrons can be used to obtain diffraction contrast in the so-called 'dark field' images. Incoming electron waves are Bragg diffracted to various solid angles by the periodic lattices in a sample (also see Section 3.4.8 (page 55)). The aperture of a TEM can be adjusted to admit only electrons diffracted to a particular orientation. Images obtained in such a mode are only bright in areas that diffract electrons to a specified angle while transmitted or other angles of diffraction appear dark. In polycrystalline materials, dark field images can be used to distinguish neighboring grains, as the different orientations will show up in different dark field images [151]. It should also be noted that amorphous regions that by definition have no periodicity or voids also appear dark in dark field images.

To determine possible sources of crater formation, slightly etched standardly deposited polycrystalline ZnO:Al thin-films –both planar and cross-sectional- were examined by TEM (CM20, Philips). Figure 3.8 (a) and (b) contain schematic diagrams showing the relationship between the original sample and the TEM sample for planar and cross-sectional views, respectively. Planar TEM samples were made by the standard techniques of grinding, dimple grinding, and argon ion milling from the glass side. Since points of accelerated etching are randomly distributed over the whole surface, any planar ZnO:Al TEM sample with a large enough imageable area (approximately 1 µm^2) is bound to have multiple etching sites, see Figure 3.8 (a). The same, however, is not true for any randomly made cross-sectional lamella. Even if a crater is observed within a randomly cut lamella it would remain unclear if the deepest point in the lamella came from the deepest point of a crater (although the opening angle could give a rough estimate). The following describes a method to ensure the crater center is located within the lamella.

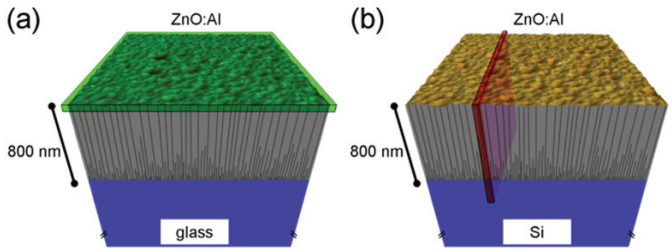

Figure 3.8: Schematic diagrams of the areas imaged with respect to a slightly etched sample by (a) planer and (b) cross-sectional TEM samples.

AFM assisted lamella preparation: To ensure that the middle of a crater is within an approximately 50 nm thick cross-sectional lamella, a sample is cut from a location previously imaged by AFM. SEM images of the cross-sectional view made during the thinning process are compared to the line scans of an AFM scan to determine the location.

Since SEM imaging was used to determine the lamella profile during the thinning process, it was preferable to use a silicon wafer as substrate since it is not an insulator. To find the same location in AFM and SEM, a silver grid was deposited by photolithographic processes, see Section 3.4.2.3 (page 47). An AFM scan was made of the area from which the lamella would originate. Samples were then moved to an SEM equipped with a focused ion beam (FIB, Helios Nanolab 400s, FEI). Using the silver grid, the same location was found in the SEM, and platinum markers with a thickness of around 200 nm were deposited close to the crater of interest using electron beam assisted deposition. Next, an approximately 200 nm thick protective platinum layer was deposited using electron beam assisted deposition over the region containing the crater of interest and previously deposited platinum markers [155]. Then an additional thicker and more rapidly grown platinum layer was deposited at the same location by gallium ion assisted deposition [156].

Using the FIB, a hole was made on one side of the region of interest. The sample was slowly thinned towards the region of interest using a lower energy gallium beam until the platinum markers were observed in the SEM image of the cross-section. The sample was then rotated 180° and FIB was used to cut out the lamella. Figure 3.9 (a) shows a SEM image of the FIB lamella just prior to removal, one side has been thinned to the platinum. The lamella was removed and attached to a TEM sample holder. There it was thinned from the working side until the platinum markers were observed. The last few hundred nanometers were then slowly thinned using the following steps: first, imaging the cross-section by SEM; second, finding the equivalent line scan in the AFM data; third, determining the distance from the side of the cross-section to the middle of the crater; and fourth, using the FIB to thin the appropriate side or sides. These steps were repeated until the sample was thin enough for TEM measurement. Figure 3.9 (b) contains a cross-sectional SEM image of the lamella in the middle of the final AFM assisted thinning process. The platinum markers are indicated, and an AFM line trace from approximately the same location is superimposed over the SEM image.

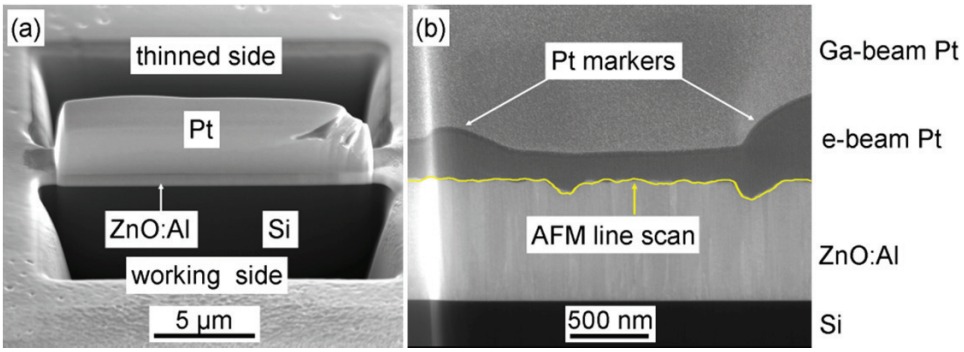

Figure 3.9: SEM images taken during FIB lamella preparation (a) prior to the lamella removal and (b) during the final AFM assisted thinning steps. The methods used to check lamella location are indicated, including thicker electron beam assisted platinum markers, and an AFM line scan (yellow) at approximately the same location.

3.4.7. Secondary Ion Mass Spectrometry (SIMS)

SIMS is a very sensitive method of determining the composition of a specimen, it basically functions by blasting a surface with an ion beam and analyzing what comes out. In SIMS a primary beam of heavy ions are accelerated and impinge upon the sample in question. The impact ejects molecules, neutral atoms, and ions; it is these secondary ions that are analyzed to determine composition. The secondary ion beam is accelerated to a quadrupole mass spectrometer, where the atomic masses of the ions are determined. The spectral output from a SIMS measurement is thus the number of counts per atomic weight.

Within this work, SIMS (Atomica) measurements were made to determine the concentration of deuterium after damp-heat degradation using a cesium ion (Cs^+) source. For such measurements the deuterium ions (D^-) were compared to that of the ZnO matrix ions (ZnO^-). All measurements were made in dynamic mode, analyzing the same position until the glass was reached. In such measurements a profile for the measured element is determined as a function of time. The concentration profile as a function of depth was determined directly from these measurements using the ZnO:Al film thickness as determined by surface profiler (Section 3.4.1 (page 42).

3.4.8. X-Ray Diffraction (XRD)

XRD is a nondestructive method for determining the crystallographic orientation of materials. A common XRD measurement is the so-called θ-2θ scan. In θ-2θ scans, a sample is illuminated by x-rays with a known wavelength (λ) at a defined angle of inclination (θ) and an x-ray detector is placed at the mirror angle (180- θ) to that of the x-ray illumination. This angular relation is known as Bragg-Brentano geometry. The name θ-2θ indicates that if the x-ray source is considered fixed, and if the sample is rotated by an angle of θ the detector must be rotated by an angle of 2θ to keep the mirrored geometry. In θ-2θ measurements, if the sample has crystalline portions parallel to the surface with a periodic lattice plane spacing (d) larger than that of the incoming x-rays, the x-rays will constructively interfere when the Bragg condition,

$$2\,d\sin(\theta) = n\,\lambda\,, \qquad \textbf{(3.3)}$$

is meet [157], where n is an integer. By scanning through different angles (but keeping the Bragg-Brentano geometry), peaks in the reflected signal appear when Equation (3.3) is satisfied, allowing the use of a single x-ray wavelength. The position of a peak indicates a given lattice spacing that can be correlated to a particular crystal orientation, assuming the composition of the sample is known. In this work, the different crystallographic orientations will be referred to by the Miller indices (hkl).

The intensity, position, and width of the XRD θ-2θ peaks can be analyzed to learn about the structure of a sample. From the position and intensity the lattice constant and relative prevalence of the different orientations within the examined plane can be deduced. Shifts in the peak position from reference values to lower or higher angles indicate a larger or smaller lattice constant, respectively [158]. For polycrystalline films this shift can be caused by impurities such as dopants in the thin-films. The width of a peak is characterized using the full width at half the maximum (FWHM). Smaller FWHM values indicate better film quality. The FWHM of peak at a particular angle ($\beta(2\theta)$) can be used to calculate a grain size, as using the Scherrer formula [159,160],

$$L_{vert} = \frac{K\,\lambda}{\beta(2\theta_{Br})\cos(\theta_{Br})}, \tag{3.4}$$

where L_{vert} is the linear vertical dimension of the grains, K is a dimensionless constant which depends on the shape of the crystals, and generally has a value of 0.9 [157]. The subscript Br indicates that the angle θ satisfies the Bragg condition (Equation (3.3)). This grain size estimated corresponds to the thickness of the coherently scattering layers in the vertical direction. Thus, lattice distortions such as defects and strain reduce the estimated grain size.

Another XRD measurement is the so-called rocking curve or ω scan. For this measurement the x-ray source and detector are set to a particular angle for an orientation (hkl) of interest, while the sample is 'rocked' through a range of angles (ω). Since only (hkl) planes parallel to the incident beam give a signal, the signal generally drops of after scanning a few degrees. The ω scan, thus, tests to what degree the crystallites of a given orientation are aligned. It is worth noting that the ω scan can be made over a wider range of angles (ω) when a higher order equivalent peak is examined; as there is a larger 2θ about which the sample can be rocked.

All XDR (X'Pert Pro diffractometer, Philips) scans were made using copper K_α radiation. This radiation has a wavelength of λ=0.154 nm [161]. To create this radiation, high-energy electrons impinge on a copper target, and some of these electrons knock core electrons out of their orbitals. K_α radiation is created when an electron in the second orbital decays to the first orbital by emitting one such x-ray. To shorten measurement times a 128 channel detector was used (X-Celerator, Philips). The 128 channels were spread over 1.56°, so the measurements were not made in perfect Bragg-Brentano geometry. The relative error in the FWHM on such a system has been estimated to be between +20 and -3 % [162]. This asymmetry in error comes from the fact that slight sample misalignments will tend to give too large rather than too small values of FWHM.

Since only crystalline planes parallel to the surface are examined by θ-2θ scans, it is important to note that other crystal orientations may exist, which are not observed. However, sputtered ZnO:Al thin-films are preferentially c-axis oriented [13,163,164]. Thus, it can safely be assumed that the most common orientation is measured in θ-2θ scans.

The grain size estimated by XRD (Equation (3.4)) is sensitive to any crystallographic defects including dopants both intrinsic and extrinsic. Thus, for the polycrystalline ZnO:Al films examined within this work very small vertical grain sizes are estimated. Cross-sectional imaging techniques, such as SEM imaging, yield larger grain size estimates as only larger defects such as grain boundaries are observed. Within this work the grain size from XRD measurements will be treated as an indicator of crystal quality (like FWHM), rather than the actual dimensional size of a grain.

3.4.9. Hall Effect

The fundamentals of the Hall effect are described in Section 2.3.4 (page 16). Within this work Hall effect measurements (920 Hall set-up, Keithley) were made on 8x8 mm^2 ZnO:Al samples. All measurements were made in van der Pauw (coplanar) geometry [83]. Electrical contacts were made to each of the four corners with silver paste. The relative error in measurements for resistivity, carrier concentration, and mobility is estimated to be around one, five, and five percent, respectively [162]. However, the error of a given sample depends on the ratio between the contact and sample sizes. To address this sample-particular error, at least two measure-

ments were made on each sample generally at a current of 1 and 10 mA. When displaying such data, the average value of the measurements was taken, and bars indicated the deviation in values.

When calculating the electrical properties at the surface for a ZnO:Al thickness series using the two layer model (Equations (2.21) and (2.22)), the electrical properties of the thinnest sample were used to represent those of the bulk for the next thickness in the series. Similarly when calculating the surface properties of the third film in the series, the electrical properties of the second film were used to represent those of the bulk. Figure 3.10 gives a schematic diagram for calculating surface properties by representing the bulk by the electrical properties of the previous sample.

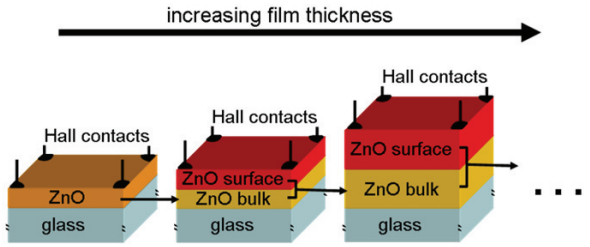

Figure 3.10: Schematic diagram for determining the surface properties of a ZnO:Al sample using the two layer model. The bulk electrical properties of a sample are represented by those of the next thinner sample.

3.4.10. Optical Spectrometer

The optical properties such as total transmission (T_t), diffuse transmission (T_d), and reflection (R) were measured using an optical spectrometer with an integrating sphere (Lambda 950, Perkin Elmer). This spectrometer uses a double monochromator to select a specific wavelength (λ, with resolution of two nanometers) originating from a deuterium and tungsten lamp. The monochromatic light is chopped at a certain frequency to allow lock-in measurement and is then split into two beams (reference and sample) before entering the integrating sphere. For total transmission measurements, the sample was placed in the sample beam in front of the integrating sphere, and a white reflector was placed on the opposite side of the integrating sphere to include the directly transmitted beam. In this way, all light transmitted though the sample was counted. For diffuse transmission measurements, the sample was placed in the sample beam in front of the integrating sphere, and an absorber was placed on the opposite side of the integrating sphere to exclude the directly transmitted beam. In this way, only the light not directly transmitted was counted. For reflection measurements, the sample was placed in the sample beam after passing through the integrating sphere directly. In this orientation, only light reflected back from the sample was counted. For all measurements, samples were oriented such that the light was first incident upon the glass (as it would in a solar cell device).

By comparing the total transmission (T_t) and reflection (R) to the initial beam, the absorption can be calculated using Equation (2.29). The haze (H) is often used to characterize light scattering properties of a sample. It is defined as the ratio between the diffuse (T_d) and total transmission (T_t),

$$H(\lambda) = \frac{T_d(\lambda)}{T_t(\lambda)} \quad \textbf{(3.5)}$$

It should be noted that haze depends on the RMS roughness of the surface [165], and a higher haze does not always indicate higher solar cell current [42].

Within this work, total transmission, diffuse transmission, and reflection measurements were made on etched ZnO:Al surfaces and reflection measurements were made from solar cells. Diiodomethane (CH_2I_2) was used for refractive index matching during total transmission and reflection measurements, to avoid measurement errors due to light scattering and internal light trapping [166].

3.4.11. Solar Cell Characterization

Solar cell characteristics (Section 2.9.2 (page 34)) were determined by measuring the current density as a function of voltage (SMU 238, Keithley) while cells were illuminated. A class A double source (xenon and halogen) solar simulator (WXS-140S-Super, Wacom) was used for illumination. Measurements were performed under standard test conditions, which includes a solar spectrum at an air mass of 1.5 (AM 1.5), radiation of 100 mW/cm^2, and a temperature of 25 °C. The sun simulator was calibrated between 190 and 1100 nm prior to solar cell measurement using a photodiode (S1236-8BQ, Hamamatsu). From the current density-voltage curve the short circuit current density, open circuit voltage, and fill factor were determined (see Section 2.9.2 (page 34)). The efficiency was determined by comparing the maximum power to the incident power (Equation (2.40)). Measurements showed deviations of less than two percent upon repeated measurements of the same solar cell. Within this work, current density-voltage curves were measured not only under AM 1.5 but also with red (OG 590) and blue (BG 7) filters blocking all but particular parts of the spectrum. These filters allow the comparison of the solar cell properties in the long and short wavelength regions, respectively. Thus, changes within a series can be attributed to changes within the long or short wavelength region.

3.4.12. Quantum Efficiency

To measure the quantum efficiency (QE) of the solar cells (Equation (2.41)), the spectral response (SR) of a solar cell was examined as a function of wavelength (λ). The spectral response is defined as the ratio of the generated photo current density (j_γ) to the illuminated power density, where the illuminated power density is given by the product of the photon energy (E_γ) and flux (Φ_γ). Thus, the spectral response as a function of wavelength is given by

$$SR(\lambda) = \frac{j_\gamma(\lambda)}{E_\gamma(\lambda)\,\Phi_\gamma(\lambda)} \quad \textbf{(3.6)}$$

The quantum efficiency (Equation (2.41)) can be expressed in terms of the spectral response. To do so, the number of collected photo-generated electron-hole pairs (N_e) can be expressed as the quotient of the photo current density and the charge of an electron (e), and the number of incident photons (N_γ) is given by the flux (Φ_γ). The spectral response can be substituted in using Equation (3.6), and the photon energy (E_γ) can be expressed in terms of constants

(Planck's (h) and the speed of light in vacuum (c)) and wavelength, using Equation (2.33); leaving the following expression,

$$QE(\lambda) = \frac{N_e(\lambda)}{N_\gamma(\lambda)} = \frac{j_\gamma(\lambda)}{e\Phi_\gamma(\lambda)} = \frac{SR(\lambda)\, E_\gamma(\lambda)}{e} = SR(\lambda)\, \frac{h\, c}{e\, \lambda} \quad \textbf{(3.7)}$$

For quantum efficiency measurements within this work, a cell was illuminated with a chopped beam of monochromatic light from a xenon lamp and the spectral response (SR) at this particular wavelength was measured by lock-in techniques. The spectral range between 300 and 1100 nm was examined in 10 nm increments.

Recall that for tandem solar cells, the current is limited to that of the smaller of the two subcell currents (Section 2.9.1 (page 32)). To address this challenge, the quantum efficiency was measured for the top and bottom subcells separately by saturating the bottom and top cells continuously with light that is only absorbed in these cells, respectively. In this way, the cell being measured always had the limiting current. The short circuit current density was calculated from the quantum efficiency measurements using Equation (2.42). The relative error in quantum efficiency measurements was less than two percent. Additional details on quantum efficiency measurements can be found elsewhere [167,168].

4. Growth of ZnO:Al

The following chapter examines different aspects related to the growth of sputtered polycrystalline ZnO:Al. Understanding the relationships between growth conditions and the resultant film properties is vital for the optimization of ZnO:Al thin-films for use in solar cells. To do so, the electrical and structural properties are examined as a function of deposition conditions. The surface electrical and structural properties are examined to better understand how the ZnO:Al film properties evolve with thickness. Sputtered ZnO:Al has been observed to grow both epitaxially and perpendicularly to a textured substrate surface [20,21]. To check the dominant affinity during growth, the growth of ZnO:Al on a previously texturized ZnO:Al film is examined. Finally, while it is well known that the sputtered ZnO:Al films grow c-axis oriented, it is unclear if this polar crystal orientation grows with Zn- or O-termination. To this end, the growth and etching properties of ZnO:Al sputtered onto the polar surfaces of ZnO single crystals are compared to that of glass substrates.

4.1. Influence of Deposition Conditions

The following sections explore the relationships among deposition conditions, such as temperature and target aluminum concentration; changes in physical properties, such as an air break; and the structural and electrical properties of the as-deposited ZnO:Al films. For each deposition condition, a series of film thicknesses were deposited to determine how the effects of the different deposition conditions evolve with film thickness.

4.1.1. Structure as a Function of Thickness

This section examines the relationship between deposition conditions and the structure of the resultant films: specifically, how the ZnO:Al structure varies with thickness, deposition temperature, target doping concentration, and vacuum breaks.

The following four series of ZnO:Al films were deposited onto CG in a small area (10x10 cm^2) sputtering system using a ZnO target with 0.5 w/w% Al_2O_3 doping: (1) 'heated single deposition,' in which the substrate was heated to approximately 400 °C, and ZnO:Al was deposited in one continuous deposition; (2) 'RT single deposition,' where the substrate was not intentionally heated, and all material was deposited in one continuous deposition; (3) 'RT hourly pulsed' in which the substrate was not intentionally heated, and material was deposited in five minute pulses and the sample was allowed to cool in vacuum for one hour between pulses; and (4) 'RT daily pulsed,' where the substrate was not intentionally heated, material was deposited in five minute pulses, and the sample was removed from vacuum for at least one day between every layer. Thicknesses were varied for deposition series (1) and (2) by sputtering for times between 1.5 and 80 minutes and 1.5 and 100 minutes, respectively. Thicknesses were varied for deposition series (3) and (4) by changing the total number of pulses, with the maxi-

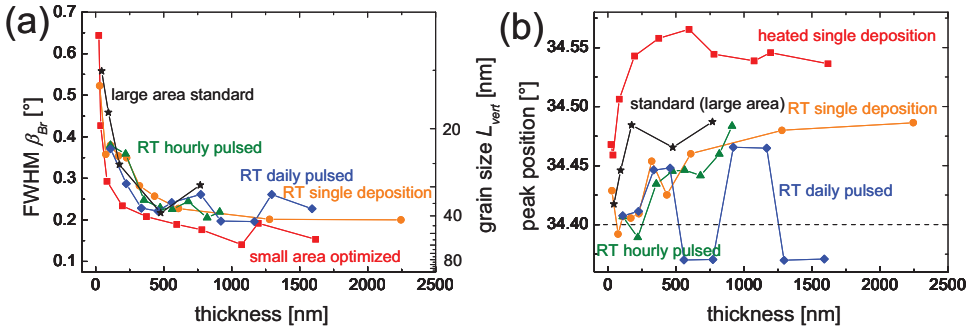

Figure 4.1: Structural properties of the variously deposited ZnO:Al thin-films. (a) FWHM of the (002) peak (left axis) and grain size (right axis), as well as, (b) peak position as a function of film thickness.

mum number of pulses 8 and 15, respectively. More details on these depositions can be found in Section 3.1.1 (page 37).

An additional thickness series of the standard ZnO:Al (Section 3.1.2.1 (page 38)) was prepared in a large area (30x30 cm^2) in-line sputtering system using a ZnO target with 1 w/w% Al_2O_3 doping. For this 'standard (large area)' deposition, the CG substrates were heated to approximately 300 °C, all material was deposited in a single plasma process, and the carrier was moved dynamically past the target, effectively stopping and restarting deposition without cooling or breaking vacuum. Film thicknesses were varied by changing the total number of passes the substrates made in front of the target between 2 and 32. Additional deposition details can be found in Section 3.1.2.1 (page 38). Film thicknesses were determined by surface profiling. The structural properties of the differently deposited ZnO:Al films were determined by θ-2θ XRD scans (Section 3.4.8 (page 55)) and the subsequent analysis of the highly dominant ZnO (002) peak.

Thickness measurements showed almost identical growth rates for the RT daily and hourly pulsed depositions at 22.3 and 22.5 nm/min, while the growth rate of the RT single deposition was slightly reduced at 21.5 nm/min. The heated single deposition samples also showed a fairly constant although further reduced growth rate of 18.6 nm/min. The standard (large area) samples also showed a constant growth rate of 24 nm/pass (6 nm · m/min).

The ZnO (002) orientation was by far the dominant orientation observed, and therefore was the only orientation analyzed. The characterization of the (002) peak, as measured by θ-2θ XRD scans, are given in Figure 4.1. The FWHM of the (002) peak (Figure 4.1 (a, left axis)) decreases with increasing thickness for all deposition conditions. The vertical grain sizes (Figure 4.1 (a, right axis)) increase with increasing thickness for all deposition conditions (see Equation (3.4)). At a thickness of approximately 800 nm, the largest thickness for which films were made for all five deposition techniques, the FWHM exhibits a spread of 0.1° with values between 0.18 and 0.28° (vertical grain size between 30 and 46 nm). Films thicker than 800 nm showed only slightly smaller FWHM values. All RT-deposited ZnO:Al exhibited similar values at similar thicknesses. The heated single deposition series generally exhibited the lowest FWHM values, while the standard (large area) samples had slightly larger values similar to the RT series.

Figure 4.1 (b) gives the (002) peak position as a function of thickness and deposition method; the position of the peak for a single crystal ZnO sample is indicated at 34.40° [169]. For all

deposition methods, the trend is a shift to higher peak positions with increasing thickness. All RT deposited and the standard (large area) series seem to approach a value around 34.50°, although many of the values from the RT daily pulsed series approached a value of 34.37°. The heated single deposition reaches slightly higher values up to 34.56°.

The lower growth rate observed in the heated single deposition and RT single deposition is likely due to the poor sticking coefficient (higher mobility) of the incoming hot atoms. Sublimation from ZnO crystals has been observed at temperatures as low as 380 C [170]. The decrease in the FWHM (increase in vertical grain size) indicates an improvement in the ZnO:Al film quality with increasing thickness. The increase in the peak position with increasing thickness observed in Figure 4.1 (b) indicates a smaller distance between lattice planes, which in turn indicates stronger tensile stress. The larger grain sizes observed with increasing film thickness can be partly attributed to a survival-of-the-fastest growth process [85]. Micro strain, defects, and doping, however, may destroy the wide range order, so the actual grain size is limited far below the film thickness.

For all series, the FWHM and position of the (002) peak converge to a certain value with increased thickness, which may indicate a relaxation in film properties with increased thickness. The FWHM and peak position values approached depend on the different deposition conditions for each series. One major factor is the substrate temperature. Increasing the substrate temperature leads to better adatom mobility and higher quality films: however, stress due to the different coefficients of thermal expansion for ZnO:Al and CG are also introduced. Another major factor is the aluminum concentration of the target, since the aluminum atom is smaller that zinc atom it replaces. Other factors may include the dynamic nature of deposition, which changes the direction of incoming atoms changes over time; vacuum breaks that introduce surface contaminants; and the two different systems used for sputtering and thus have different degrees of ion bombardment (see Section 2.7 (page 25)).

4.1.2. Electrical Properties as a Function of Thickness

This section examines the relationship between deposition conditions and the electrical properties of the resultant films. Specifically, how the ZnO:Al electrical properties vary with thickness, deposition temperature, target doping concentration, and vacuum breaks are examined.

The same five ZnO:Al film thickness series examined in the previous section are also examined in this section. One additional ZnO:Al thickness was added to the standard (large area) series. This film was deposited using 64 passes in front of the ZnO target with 1 w/w% Al_2O_3 doping. All other deposition conditions were the same; see Section 3.1.2.1 (page 38) for more details. Electrical properties were determined by Hall measurements using van der Pauw geometry (Section 3.4.9 (page 56)) [83].

The mobility and carrier concentration of the electrons in the variously deposited ZnO:Al films are given in Figure 4.2 (a) and (b), respectively. For all deposition methods except the heated single deposition, the mobility increased with increasing ZnO:Al film thickness steeply for thin films and saturated after 300 to 1000 nm were deposited. The maximum value approached with long deposition times or a large number of passes did, however, vary depending on deposition technique. The mobility for the heated single deposition increased with thickness until a thickness of 800 nm, after which it dropped sharply. The mobility of the RT-deposited samples was similar up to a thickness of about 400 nm. For thicker films, the RT single deposi-

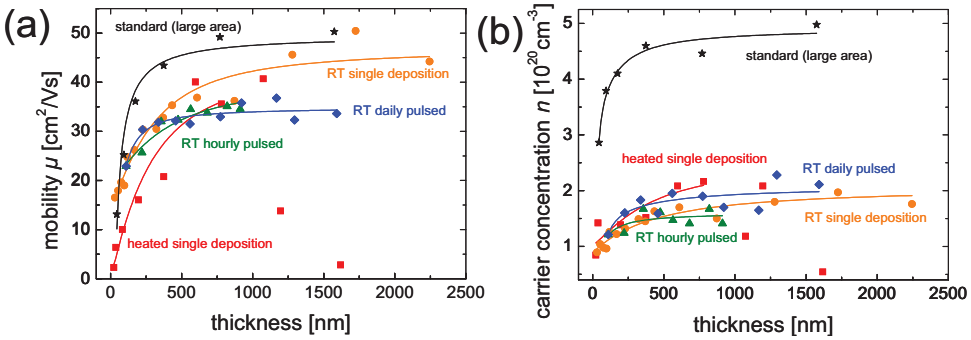

Figure 4.2: Electrical properties of the variously deposited ZnO:Al thin-films. (a) Mobility and (b) carrier concentration as a function of film thickness. Curves are meant to guide the eye.

tion exhibited higher values than either the RT hourly or daily pulsed samples. Generally, the highest mobility values were observed in the standard (large area) series, exhibiting values up to 50 cm^2/Vs.

The carrier concentration is given in Figure 4.2 (b). Like the mobility, it increases with thickness for all films except the heated single deposition. Of the samples prepared in a small area sputtering system, the heated single deposition series showed some of the highest values in carrier concentration up to a thickness around 800 nm, after which it dropped sharply. Of the RT-deposited series, the RT daily pulsed showed the highest carrier concentrations. The standard (large area) films had carrier concentrations at least twice those of the other series prepared due to the higher aluminum concentration in the target.

As discussed in Section 2.3 (page 11), the conductivity in a degenerately doped semiconductor can be simplified to a product of the electron charge, mobility, and carrier concentration (Equation (2.7)). Increasing ZnO:Al film thickness increased both electron mobility and concentration (Figure 4.2); however, the mobility generally increased by a larger factor than the carrier concentration, around 5 and 1.5, respectively. The carrier concentration is thus less dependent on film thickness than the mobility.

The sharp decrease in mobility and carrier concentration observed in heated single deposition series with thicknesses over 800 nm can be attributed to cracks in the ZnO:Al film. These cracks were observed by an optical microscope after short etches in HCl. A possible reason for the formation of these cracks is the different coefficients of thermal expansion for ZnO and CG. The inadvertent heating of the substrate during the RT single depositions may account for the higher mobility observed in this series as compared to the pulsed RT series. The thermocouple at the metal plate of the radiative heating system measured temperatures as high as 122 °C; temperatures at the substrate are likely to be even higher as an insulating vacuum is located between. That heating improves mobility can also be seen in the purposely heated samples (heated single deposition and standard (large area)), as these series exhibit the highest mobility values for thicknesses above 500 nm consistently (Figure 4.2 (a)). However, the heated series exhibited the lowest mobility values for the very thin-films; this may indicate that the nucleation density is lower in the high temperature deposited films. A lower nucleation density would lead to film coalescence only after thicker film depositions.

The doubling in carrier concentration between samples prepared in the small and large area sputtering systems corresponds to the different target doping concentrations, with 0.5 and

1 w/w%, respectively. The increase in carrier concentration observed in the RT daily pulsed films as compared to the RT hourly pulsed films may be due to an increase in defects introduced by breaking the vacuum and exposing the sample to air approximately every 100 nm. Like aluminum doping, native defects in ZnO tend to be n-type [171], thus increasing the carrier concentration.

4.1.3. Discussion

The preceding sections showed that both structural and electrical properties improve with increasing ZnO:Al film thickness regardless of deposition conditions. To clarify this behavior, the mobility of the variously deposited films are plotted as a function of the FWHM of the (002) peak (bottom axis) and the vertical grain size (top axis) in Figure 4.3. Notice that there is in general a linear trend between an improvement in structural (FWMH) and electrical (mobility) properties. Only the heated single deposition series did not follow this trend, although some of these outlying points can be attributed to cracks in the ZnO:Al film.

Since mobility varies with film quality (FWHM and grain size), a barrier model [44,69,73,74,172,173] can be used to explain the trends observed (see Section 2.3.3 (page 14)). The mobility within individual grains is assumed to be high, and depletion regions are believed to form at the boundaries between grains [174]. For an electron to participate in the conduction, it must have high enough energy to overcome the potential barriers or the barrier must be thin enough to tunnel through. Thus, the mobility measured is not the mobility of the electrons within a ZnO:Al grain, but an effective mobility which depends strongly on transport across grain boundaries. As the film quality increases, through an increase in collective grain size or higher quality grain boundaries, less or lower potential grain boundaries must be crossed and the effective mobility increases.

The carrier concentration, on the other hand, does not depend strongly on the density of grain boundaries, but is a bulk effect. Effects in carrier concentration are only observed in the

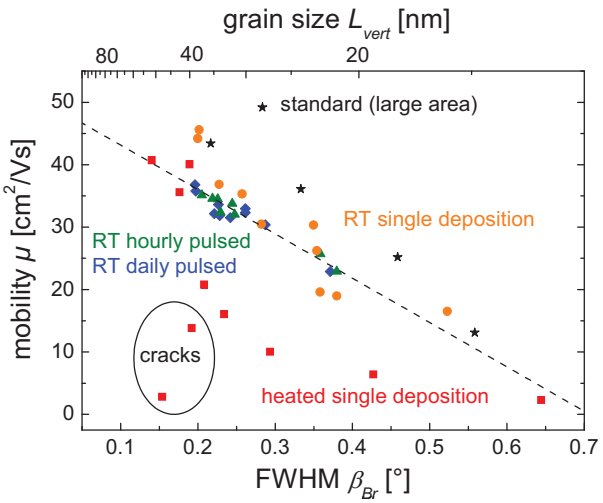

Figure 4.3: Bulk mobility as a function of FWHM (bottom) and grain size (top) for the variously deposited ZnO:Al thin-films.

very thin films where a larger percentage of the total atoms are located at grain boundaries, as seen in the first few hundred nanometers of thickness shown in Figure 4.2 (b). The observation that carrier concentration depends less strongly on thickness than mobility agrees with the results of Agashe *et al.* [22] and Fortunato *et al.* [23].

4.2. Surface Properties

The previous sections focused on how the bulk ZnO:Al electrical and structural properties changed with increasing thickness and deposition conditions. The following sections focus on the surface electrical and structural properties of the standard (large area) ZnO:Al, one of the thickness series examined in the previous sections, and how these properties vary with thickness.

4.2.1. Surface Electrical Properties

The deposition parameters of the standard ZnO:Al films are described in Section 3.1.2.1. Various thicknesses were deposited by changing the total number of passes, between 2 and 64. Using the bulk Hall measurements presented in Section 4.1.2 (page 63), the approximate surface mobility and carrier concentrations were calculated using the two-layer model for the Hall effect, Equations (2.19) and (2.20), as discussed in Section 2.3.4 (page 16). To move from the two-layer model to the more realistic continuous variation model, functions for mobility and carrier concentration variation must be assumed, see Section 2.3.4 (page 16). Both mobility and carrier concentration were assumed to increase asymptotically towards a maximum value with thickness taking the following forms,

$$\mu(z) = \mu_{\infty}(1 - c_{\mu}^{z}) \tag{4.1}$$

and

$$n(z) = n_{\infty}(1 - c_{n}^{z}), \tag{4.2}$$

respectively, where μ_{∞} and n_{∞} represent the mobility and carrier concentration at infinite thickness, and c_{μ} and c_{n} are constants between zero and one that control the rate at which the asymptote is approached. The values of the four constants were optimized by fitting the solutions of continuous variation equations (Equations (2.27) and (2.28)) to the measured mobility and concentration data.

Exponential functions for mobility and carrier concentration were assumed for a few reasons. First, calculated surface properties seemed to indicate this behavior (Equations (2.21) and (2.22)). Second, these equations satisfy the boundary conditions that mobility and carrier concentration are zero with no thickness. A simple constant value that would also fit the calculated surface carrier concentration curve well would, however, not satisfy this boundary condition. Finally, exact solutions to the continuous variation model (Equations (2.27) and (2.28)) were possible using these assumptions (Equations (4.1) and (4.2)).

Figure 4.4 shows the surface and bulk mobility and surface and bulk carrier concentration as a function of ZnO:Al film thickness. The measured mobility and carrier concentration are indicated by blue squares in Figure 4.4 (a) and (b), respectively. As previously described in Section 4.1.2 (page 63), both increase with increasing thickness towards a maximum value, alt-

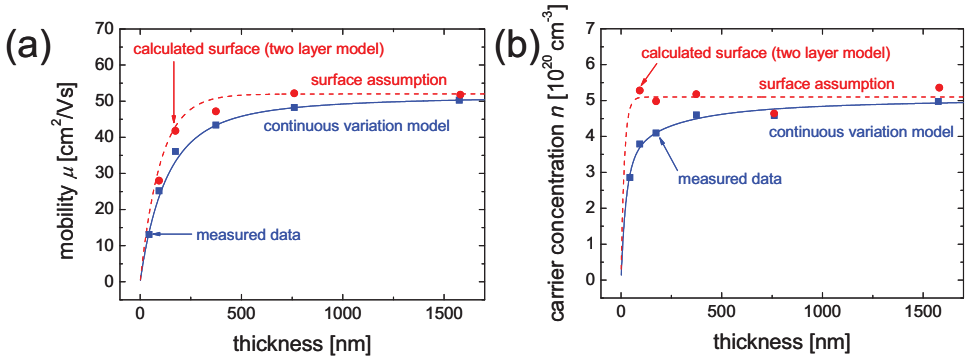

Figure 4.4: ZnO:Al (a) mobility and (b) carrier concentration as a function of film thickness. The measured and calculated surface data are represented by blue squares and red circles, respectively. The continuous variation model and the surface assumptions are represented by the blue solid and red dashed curves, respectively.

hough the carrier concentration approaches this value faster. The surface mobility and carrier concentration as calculated from the measured data using the two-layer model (Equations (2.21) and (2.22)) are indicated by red squares in Figure 4.4 (a) and (b), respectively. Since the electrical difference between two thicknesses is attributed to the surface of the thicker sample, the calculated surface properties tend to exhibit higher mobility and carrier concentration than that of the bulk. The calculated surface mobility increases with increasing thickness, while the calculated surface carrier concentration remains relatively constant at around $5\text{x}10^{20}$ cm^{-3}.

Exact solutions to Equations (2.27) and (2.28) were obtained using Maple 11 (a commercially available computer algebra system) assuming the asymptotic forms for surface mobility and carrier concentration (Equations (4.1) and (4.2)). The solutions, however, are not shown due to their size. The optimum values for μ_∞, n_∞, c_μ, and c_n were determined to be 52 cm^2/Vs, $5.2\text{x}10^{20}$ cm^{-3}, 0.99, and 0.94, respectively. The assumed forms of mobility and carrier concentration as a function of thickness are indicated by a dashed red line in Figure 4.4 (a) and (b), respectively. These asymptotic curves follow the calculated surface mobility and carrier concentration relatively well. The curves for the bulk mobility and carrier concentration, as determined from the continuous variation model with asymptotic variation assumptions, are indicated by a solid blue line in Figure 4.4 (a) and (b), respectively. The optimized values for μ_∞, n_∞, c_μ, and c_n, were determined by fitting these curves simultaneously. These values are relatively well fixed, as the least square error more than doubled when μ_∞ was varied by +6 and -2.5 %, n_∞ was varied by ±2.5 %, c_μ was varied by ±1 %, and c_n was varied by +1 and -1.5 %.

4.2.2. Surface Morphology and Grain Size

This section focuses on the surface morphology of the standard ZnO:Al as a function of thickness. The same samples examined in the previous section are evaluated here. To examine the planar growth of ZnO:Al, a 4x4 µm^2 area of the surface was examined by AFM. Lateral grain sizes were estimated using a watershed algorithm. Like surface mobility and carrier concentration in the previous section, the average lateral grain diameter (square root of average grain

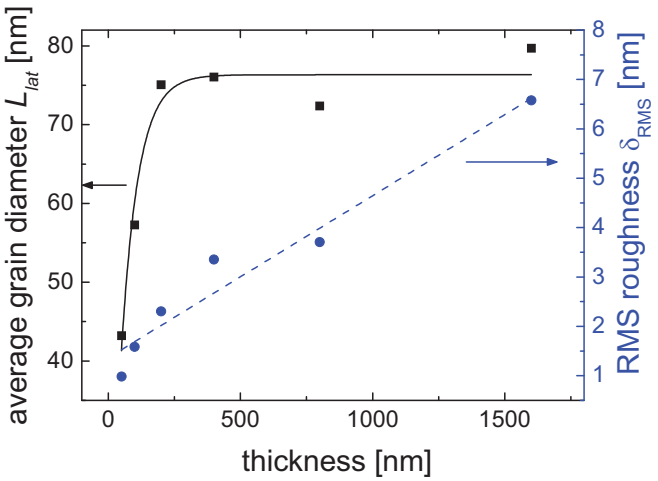

Figure 4.5: Surface properties of as-deposited ZnO:Al films as a function of film thickness. Left-axis, average grain area (black squares). Right-axis, RMS roughness (blue circles).

size) was fit by an asymptotic function with the form assumed previously for the electrical data,

$$L_{lat}(z) = L_{\infty}(1 - c_L^z)\,, \tag{4.3}$$

where L_{∞} is the average lateral grain diameter at infinite thickness, and c_L is a constant between zero and one which governs how quickly this limit is approached.

The AFM images of the standard ZnO:Al films with various thicknesses are presented together with the initial sites of etching on these films in Section 6.1.1.2 (page 92). The average grain diameter is given in Figure 4.5 (black squares). The average grain diameter increases with increasing thickness up to 200 nm, after which it remains relatively constant. The average grain diameter is well fit by Equation (4.3), with values of 76 nm and 0.98 for L_{∞} and c_L, respectively.

The RMS roughness of the as-deposited films is also shown in Figure 4.5 (blue circles). Unlike the grain diameter, the RMS roughness does not level off, but continues to increase with increasing film thickness.

A TEM image was taken of an approximately 800 nm thick standardly deposited ZnO:Al sample to examine the vertical growth. This sample was deposited onto a silicon wafer to avoid the buildup of charge during FIB preparation of the ZnO:Al cross-section. The bright field TEM image of a ZnO:Al cross-section is shown in Figure 4.6. A nucleation and growth region, comprised of many small grains, can be seen in approximately the first 200 nm of growth (directly above the Si substrate), after which the column diameter and boundaries remains fairly constant with increasing thickness with a diameter of around 50 nm.

Both AFM and TEM indicated that the grain sizes remain constant after a thickness of approximately 200 nm. The FWHM of the (002) peak showed a relatively constant grain size after the deposition of ZnO:Al reached a thickness around 500 nm, see Figure 4.1(a). This indicates that the quality (FWHM) of the film continues to improve even after the grain boundaries become relatively fixed. Additionally, an averaging effect may be seen in the FWHM data, as the XRD collects information from more than just the surface, while the AFM is sensitive to only the surface.

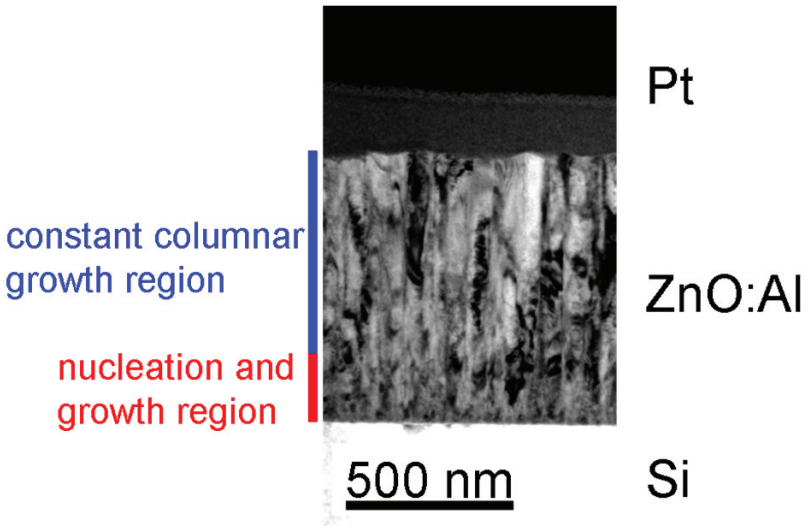

Figure 4.6: Cross-sectional bright field TEM image of ZnO:Al on a Si substrate.

4.2.3. Discussion

Compared to the bulk properties, surface electrical and morphological properties showed a similar dependence on thickness. Specifically, the surface mobility and grain size increased with thickness up to 200 nm, remaining fairly constant with further increases in thickness. Surface carrier concentration, on the other hand, remained fairly constant with increasing thickness, thus a barrier model can be used to explain the relationship between surface electrical and structural properties.

In Section 4.1.3 (page 65), the bulk mobility of variously deposited films was observed to increase with decreasing FWHM (increasing vertical grain size), see Figure 4.3. In a similar man-

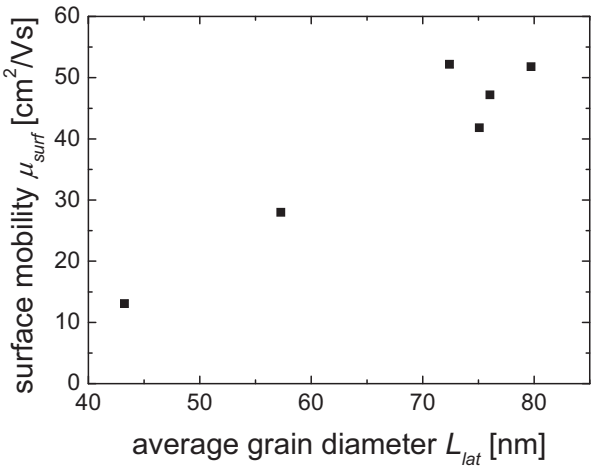

Figure 4.7: Surface mobility as a function of the average grain width.

ner, Figure 4.7 gives the surface mobility as a function of the average grain width at the surface; as the lateral grain diameter increases so does the mobility, so the quality of the ZnO:Al films improves with increasing grain size.

4.3. Growth of ZnO:Al on Etched ZnO:Al

It has been observed that ZnO sputtered onto a texturized silicon substrate orients such that the c-axis is perpendicular to the substrate [20]; however it has also been observed that sputtered ZnO:Al can follow the underlying substrate epitaxially [175]. This section examines the effects of depositing ZnO:Al onto a previously textured ZnO:Al surface with and without a buffer layer between the two ZnO:Al layers to determine the influence the underlying ZnO:Al has on growing ZnO:Al.

To observe the orientation of the columnar growth, a standard, approximately 800 nm thick film was deposited onto a silicon wafer with native oxide. A silicon substrate was used to avoid charging problems when imaging the cross-section with an SEM, see Section 3.4.5 (page 52). The sample was texturized standardly by etching in 0.5 w/w% HCl for 40 seconds, then rinsed with DI water and blown dry with nitrogen (see Section 3.2 (page 39)). An approximately

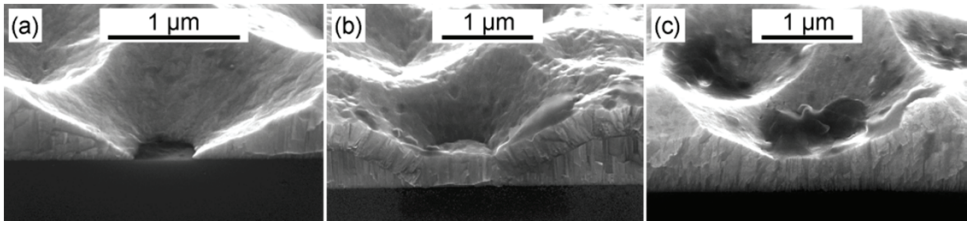

Figure 4.8: SEM images of (a) etched ZnO:Al on a Si wafer, and the after the subsequent deposition of approximately 400 nm ZnO:Al (b) with and (c) without a 10 nm SiO_x buffer.

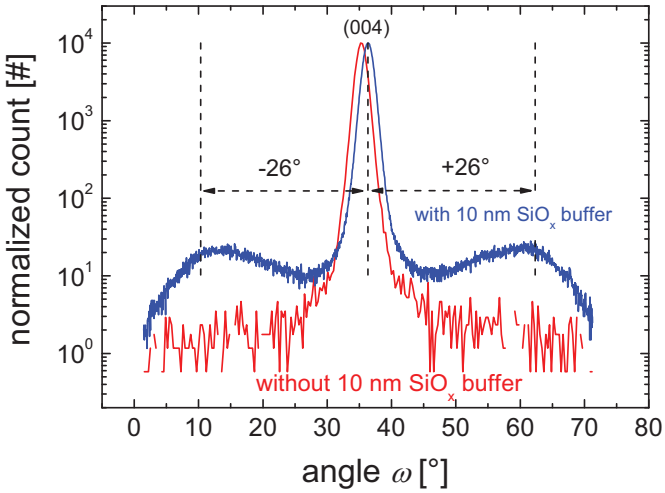

Figure 4.9: XRD ω scans of the ZnO (004) peak from etched ZnO:Al with (blue) and without (red) a 10 nm SiO_x buffer before the deposition of an additional 400 nm of ZnO.

10 nm thick buffer layer of SiO_x was deposited by electron beam evaporation (Leybold AG) onto a portion of the textured ZnO:Al surface. Next, half of a standard ZnO:Al deposition (approximately 400 nm) was deposited onto the samples with and without the SiO_x buffer. The growth on the two types of surfaces was characterized by cross-sectional imaging by SEM and ω XRD scans of the ZnO (004) peak. The equivalent (004) peak was examined rather than the stronger (002) peak because it allowed for a wider range of angles to be scanned, since the scan range is limited to the angle θ of the peak examined (see Section 3.4.8 (page 55)).

Additionally, to examine the effects the growth of new ZnO:Al on a previously textured ZnO:Al surface has on surface roughness and structure, a standardly deposited and textured ZnO:Al sample was imaged at the same location by AFM before and after the deposition of an additional 200 nm of ZnO. In this case no SiO_x buffer was deposited. The method used to reposition the sample before and after ZnO:Al deposition is described in Section 3.4.2.3 (page 47).

Figure 4.8 (a) shows a cross sectional SEM image of the ZnO:Al surface after a standard etch. Although the ZnO:Al was deposited on a silicon wafer, the etching characteristics were not noticeably altered. SEM images of ZnO:Al growth on the textured surface with and without a SiO_x buffer are shown in Figure 4.8 (b) and (c), respectively. In Figure 4.8 (b), the SiO_x buffer breaks the contact between the ZnO:Al layers and the new ZnO:Al deposited on this textured surface orients such that the columnar growth is perpendicular to the substrate. In Figure 4.8 (c), the ZnO:Al deposited onto textured ZnO:Al without a buffer layer follows the columnar growth of the initial deposition.

The XRD ω scans of the ZnO (004) peak for samples with and without the SiO_x buffer are shown in Figure 4.9. To make comparison easier, the maximum counts were normalized to the same value. The ZnO:Al deposited onto the textured ZnO:Al surface with (blue) and without (red) a SiO_x buffer exhibits three and one peaks, respectively. The two additional broad peaks in the buffered samples have a maximum at angles ±26° from the (004) main peak. Also noteworthy is the shift of the (004) peak from 35.2 to 36.3° with the inclusion of a buffer layer.

AFM images of the same location before and after the deposition of 200 nm of ZnO:Al on a textured ZnO:Al surface are shown in Figure 4.10 (a) and (c), respectively. The reconstructed AFM, shown in Figure 4.10 (b), shows not only the topography of a standard etch with gray scale (like Figure 4.10 (a)), but also indicates the areas where the deposition of 200 nm of ZnO:Al will be less than or greater than the mean increase of the entire surface, as marked in

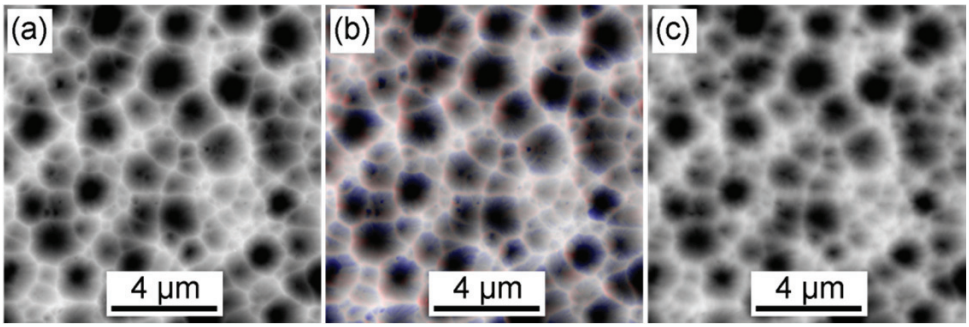

Figure 4.10: AFM images of (a) a standardly etched ZnO:Al surface, and (c) the same location after the deposition of an additional 200 nm of ZnO:Al. (b) Shows a reconstructed standardly etched ZnO:Al surface, where red and blue indicate, respectively, areas that will have the slowest and fastest growth with the deposition of 200 nm ZnO:Al.

red and blue respectively. Details on the construction of images such as these are given in Section 3.4.2.4 (page 49). Even though this description is given for an etching process, it can also be applied to the inverse process, where marked areas represent slowest and fastest growth rather than fastest and slowest etching, respectively. Notice that the crater rims tend to grow slower than the crater walls. The RMS roughness of Figure 4.10 (a) and (c) are 117 and 113 nm, respectively.

As expected, breaking the contact between the textured ZnO:Al and new ZnO:Al with a SiO_x buffer 'resets' the c-axis and epitaxial growth is not observed [20]. The additional broad peaks in the scan with a SiO_x buffer correspond to the surface angles on the originally etched surface. The most common surface angle as measured by this XRD ω, $\pm 26°$, agrees with the most common surface angle as determined by the statistical analysis of an AFM scan (Section 3.4.2.1 (page 44)), see Figure 3.1. This prevalent surface angle would lead to crater opening angle around 128°; this is in agreement with the measurements of Kluth *et al.* [42], albeit a somewhat elaborate method of measuring the opening angle.

The deposition of ZnO:Al onto textured ZnO:Al without a SiO_x buffer appears epitaxial, as the growth direction from the previous layer is kept. Kuppusami *et al.* [175] and Ellmer [176] observed that RF-sputtered doped-ZnO films grow epitaxially on sapphire and Zn-terminated ZnO single crystals, respectively. The smoothing effect observed in Figure 4.10 is relatively small; the RMS roughness decreased by only 4 nm with the deposition of a 200 nm film. This likely arises from the incoming atoms seeking to minimize energy by depositing on the more tightly packed crater walls rather than on the less tightly packed crater rims [177].

4.4. Growth of ZnO:Al on ZnO

As discussed in Section 2.2 (page 10), ZnO is a polar crystal, with the c-axis directions (001) and (00-1) being terminated by zinc and oxygen, respectively. It was observed in Section 4.1.1 (page 61) as well as by others [20] that sputtered ZnO:Al grows c-axis oriented. It is, however, unclear which termination (Zn or O) dominates the surface on foreign substrates. This section endeavors to determine the termination of standardly deposited ZnO:Al films by examining and comparing the growth and etching characteristics of ZnO:Al sputtered onto CG and the polar surfaces of ZnO single crystals.

ZnO single crystals with polished (00±1) planes (Zn- and O-terminated) and a size of 1x1 cm^2 were purchased from CrysTec GmbH. The polarity of the crystal faces was specified, and confirmed by etching a small portion in HCl and examining the etching characteristics (see Section 2.5 (page 21)) [33,34]. ZnO single crystals with both polarities were glued to a CG substrate using silver paste. In this manner, ZnO:Al could be sputtered onto a Zn-terminated single crystal, an O-terminted single crystal, and CG simultaneously.

ZnO:Al was sputtered under standard conditions (Section 3.1.2.1 (page 38)). Two different film thicknesses were deposited by making the standard number of passes (32) and twice the standard number of passes (64) in front of the target. The thicknesses of the ZnO:Al deposited onto the Zn- and O-terminated surfaces were determined by masking off a small portion of the surface with silver paste prior to deposition. After deposition, the silver paste was removed using acetone, and the thickness of the deposited films was determined by surface profiling. Since CG does not etch in HCl, the deposited thickness was determined by surface profiler after

etching around a hydrophobic ink point to the CG substrate; further details are given in Section 3.4.1 (page 42). The morphology on all as-deposited surfaces was determined by AFM.

To determine the polycrystalline films' etching behavior, samples were then etched in HCl 0.5 w/w% solution. ZnO:Al films deposited onto the Zn-terminated single crystals or CG with 32 and 64 passes were etched for 40 seconds. Films deposited onto the O-terminated crystals with 32 and 64 passes were etched for 10 and 20 seconds, respectively. For all samples, hydrophobic ink points were used to prevent an area from being etched. The difference between this unetched area and the newly etched surface was measured by surface profiler. The morphology of all etched surfaces was determined by AFM.

Table 4.1 lists the thickness and growth rate of sputtered ZnO:Al on the various substrates. The growth rate on the Zn-terminated single crystal and CG are almost identical, with an average growth rate of 23 nm/pass (6 nm · m/min). The growth rate on the O-terminated single crystal was only 66 % that of the other two substrates at around 16 nm/pass (4 nm · m/min).

Table 4.1: Growth and etching parameters and characteristics of polycrystalline ZnO:Al deposited onto O-terminated ZnO, Zn-terminated ZnO, and CG.

substrate	O-terminated ZnO		Zn-terminated ZnO		CG	
# of passes	32	64	32	64	32	64
thickness [nm]	555	977	771	1434	731	1451
growth rate [nm/pass]	17	15	24	22	23	23
RMS roughness [nm]	37	98	3.5	4.5	5.2	6.2
grain density [μm^{-2}]	--	--	227	192	158	133
etch time [s]	10	20	40	40	40	40
removed thickness [nm]	159	310	186	227	160	204
etch rate [nm/s]	16	16	4.7	5.7	4.0	5.1

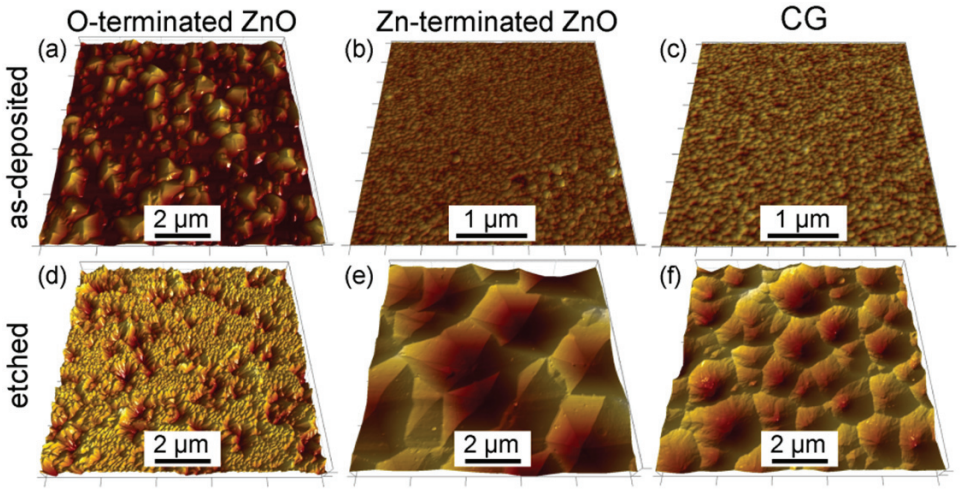

Figure 4.11: AFM images of as-deposited polycrystalline ZnO:Al on (a) O-terminated ZnO, (b) Zn-terminated ZnO, and (c) CG. AFM images of etched polycrystalline ZnO:Al on (d) O-terminated ZnO, (e) Zn-terminated ZnO, and (f) CG.

AFM images of the as-deposited ZnO:Al surfaces with 64 passes on O-terminated ZnO, Zn-terminated ZnO, and CG are shown in Figure 4.11 (a), (b), and (c), respectively. Note that a 10x10 µm^2 area was scanned on O-terminated ZnO substrates while a 4x4 µm^2 area was scanned on Zn-terminated and CG substrates. The ZnO:Al sputtered onto the O-terminated ZnO exhibits relatively large pyramidal features as-deposited. These approximately 500 nm pyramids (for the film with 64 passes) give the substrate a hazy appearance without etching. In contrast, the as-deposited structures on both the Zn-terminated ZnO and CG consist of many small (50-100 nm) grains in a relatively flat plane.

RMS roughness and grain density for the AFM scans shown in Figure 4.11 as well as those from the scans on the thinner films are listed in Table 4.1. The RMS roughness of the ZnO:Al deposited onto the Zn-terminated ZnO and CG are fairly similar, with the roughness on the CG tending to be slightly higher. The RMS roughness of ZnO:Al deposited on the O-terminated ZnO is a factor of 9 and 18 higher for the samples with 32 and 64 passes, respectively. As also observed in Section 4.2.2 (page 67), the RMS roughness increases with thickness; on Zn-terminated ZnO and CG the increase in RMS when doubling the thickness was about 25 %; on O-terminated ZnO the increase was 265 %. The grain density was higher on the Zn-terminated ZnO than on CG. In both cases, thicker films lead to a slight reduction in grain density. The grain densities were not determined for ZnO:Al on the O-terminated side, as two types of grains coexist; the large pyramidal grains and small columnar grains making up the relatively flat areas between the pyramids (similar to those on Zn-terminated ZnO or CG).

Table 4.1 lists the etching times, the removed thicknesses, and the etch rates of the ZnO:Al deposited on the various substrates. Like the growth rate, the etch rates of ZnO:Al on the Zn-terminated ZnO and CG are very similar, around 5 nm/s. The etch rate of ZnO:Al on the O-terminated ZnO side is more than a factor of three faster at 16 nm/s.

AFM images of the etched ZnO:Al surfaces with 64 passes on O-terminated ZnO, Zn-terminated ZnO, and CG are shown in Figure 4.11 (d), (e), and (f), respectively. A 10x10 µm^2 area was scanned for all the etched surfaces. Etched ZnO:Al on a O-terminated ZnO substrate develop a few craters and valleys surrounded by plateaus of small hillocks. Etched ZnO:Al on a Zn-terminated ZnO or CG substrate develop craters covering the entire surface. The craters on the Zn-terminated ZnO tend to be larger, oriented, and possess hexagonal symmetry, while the craters on CG show no preferred orientation or symmetry, having instead a more conical shape.

As mentioned in the previous section, RF-sputtered doped-ZnO films have been shown to grow epitaxially on sapphire and Zn-terminated ZnO single crystals [175,176]. Minegishi *et al.* observed that the growth rate of O-terminated ZnO is slower than Zn-terminated ZnO on a sapphire substrate [109,110]. Similarly, Kato *et al.* observed the growth rate of O-terminated ZnO on a sapphire substrate to be slower than Zn-terminated ZnO on a ZnO single crystal [177]. This difference in growth rates was attributed to the kinetics at the growing Zn- and O-terminated surfaces [177]. Specifically, the sticking coefficient for a zinc atom on an oxygen layer of Zn-terminated ZnO is higher than that of a zinc atom on an oxygen layer of O-terminated ZnO, since there are three and one dangling bonds, respectively.

Possible reasons for the as-deposited textured growth of ZnO:Al on O-terminated ZnO (Figure 4.11 (a)) include the flipping of grain polarity from O- to Zn-terminated during the growth process, the growth of ZnO:Al with another orientation beginning at the underlying substrate, and the formation of a crystal with other orientations during the growth process.

Regarding the flipping of polarity, Jo *et al.* observed the formation of inversion twin boundaries in sintered ZnO [34]. If such boundaries are formed during the sputtering process, the faster progressing Zn-terminated growth would overtake neighboring O-terminated columns leading to textured growth. In this case the different surface feature sizes would be due to the c-axis polarity flipping at different points in time during growth.

With regard to the growth of an orientation other than (00-1) (O-termination) beginning at the underlying substrate, Zhang *et al.* observed the growth rate of ZnO:Al on ion beam treated glass to be slower and textured in comparison to the faster and relatively flat growth on untreated glass [180]. They observed that certain sparsely distributed but faster growing ZnO orientations originated at the glass and overtook neighboring grains, giving texture. The texture on the ZnO:Al grown on the O-terminated ZnO could originate in a similar manner from sparsely distributed orientations other than O-terminated that start at the ZnO substrate and overtake more slowly progressing O-terminated growth with increasing thickness. Defects in the ZnO single crystal or edge dislocations generated during the initial growth may be the nucleation sites for differently oriented grains. In this case the different size surface textures would arise from the different growth rates associated with the particular orientation.

Finally, a combination of the two previous suggestions could also account for the textured as-deposited surface, specifically the formation of a crystal with other orientations during the growth process. Due to its high deposition rate, sputtering is not the ideal method for epitaxial growth. As such, imperfections within growing grains and at grain boundaries may provide sites for another ZnO orientation to nucleate. If these orientations grow more quickly than the O-terminated face texture will form.

The growth rates and surface structures of sputtered ZnO:Al on Zn- and O-terminated ZnO single crystals follow the trends previously observed (see Table 4.1 and Figure 5.1 (a) and (b)) [33,34]. The growth rate and surface structure of sputtered ZnO:Al on CG follow the trends characteristic of Zn-termination very closely (Table 4.1 and Figure 5.1 (c)). From this it is concluded that the ZnO:Al surface on CG is at least primarily Zn-terminated. The etching characteristics support this conclusion (see Section 2.5 (page 21)) [33,34]; slower progressing and crater forming etches are observed for ZnO:Al on CG and Zn-terminated ZnO single crystals, while faster progressing and more general etching is observed for ZnO:Al on O-terminated ZnO single crystals.

The difference in grain size observed between ZnO:Al grown on Zn-terminated ZnO and CG may arise from the non-epitaxial growth on the amorphous CG substrate. As presented in Section 4.2.2 (page 67), during the first 200 nm of ZnO:Al growth, various grain orientations compete for dominance. The average grain size increases as the fastest growing grains dominate neighboring grains. The epitaxially grown grains, on the other hand, already have the same orientation and so grow at the same rate.

The differences in etching behavior between the polycrystalline ZnO:Al grown on Zn-terminated ZnO and CG can be explained in a similar manner. The amorphous CG substrate gives no preferential orientation for growth, and simply, the fastest growing directions dominate. However, these fast growing (001) columns grow at the same rate regardless of their rotational orientation on the CG, and no rotational orientation is favored. Köhl *et al.* observed this type of growth, vertically aligned but rotationally not aligned, on sputtered ZnO by TEM [181]. This lack of orientation between neighboring columns breaks the hexagonal sym-

metry of etched craters resulting in more conical shapes as previously suggested by Hüpkes [162].

4.5. Summary

This chapter has focused on a variety of different aspects concerning the growth of sputtered ZnO:Al. Comparing differently sputtered ZnO:Al thickness series showed that: (1) heating (even inadvertently) tends to increase the vertical grain size (quality) and form more compact films (Section 2.7 (page 25)), leading to higher electrical mobilities; (2) pulsed deposition can be used to prevent inadvertent heating; (3) vacuum breaks increase the carrier concentration, which could be due to an increase in the defect density, as intrinsic defects -like the extrinsic aluminum doping- are generally n-type (Section 2.3.2 (page 12)) [60]; and (4) increasing the doping level in the target leads to decreased vertical grain sizes and increased carrier concentration. The changes in electrical properties generally corresponded to changes in structural properties, and a barrier model (Section 2.3.3 (page 14)) was used to explain this behavior.

The surface electrical and structural properties of the standard ZnO:Al were examined as a function of thickness. The assumption that surface mobility and carrier concentration improve asymptotically with thickness followed the electrical properties observed in the bulk well. It was shown that surface mobility improves with increased film thickness up to a thickness of 800 nm, surface grain size increases with film thickness up to a thickness of 200 nm, and that carrier concentration reaches a maximum value within the first 100 nm (see Figure 4.4 and Figure 4.5). Like the bulk electrical mobility, the change in surface electrical mobility was attributed to improved electrical transport (Section 2.3.3 (page 14)). The increase in grain size was attributed to a survival-of-the-fastest growth mechanism (Section 2.7 (page 25)). The almost thickness-independent nature of carrier concentration was attributed to the high ratio of atoms in a grain to atoms on an internal surface (grain boundary), even for relatively thin films.

The growth of ZnO:Al on a previously textured ZnO:Al surface was examined with and without a SiO_x buffer layer between the ZnO:Al layers. It was shown that the ZnO:Al deposits epitaxially on the textured ZnO:Al surface without a buffer. With a buffer between the ZnO:Al layers, the c-axis was reset, and the new growth was perpendicular to the previous texture. XRD ω scans confirmed the alignment of the ZnO:Al columns with and without the SiO_x buffer, and predicted crater opening angles that match those observed previously. The epitaxial growth of ZnO:Al on textured ZnO:Al follows the previous surface structure so closely that the deposition of an additional 200 nm showed only a slight reduction in RMS roughness.

It was concluded that the typical termination of the standard ZnO:Al deposition process is zinc by comparing the characteristics of ZnO:Al grown on the ZnO polar surfaces to that of CG. Both growth and etching characteristics indicated this termination. The larger grain sizes and conical rather than hexagonal craters observed on ZnO:Al deposited onto CG as compared to Zn-terminated ZnO, were attributed to a survival-of-the-fastest growth mechanism in the nucleation region, and the lack of a preferred rotational orientation for the (001) columns, respectively.

5. Post-Deposition Heat Treatments

This chapter examines the effects heat treatments, such as annealing and damp-heat, have on sputtered ZnO:Al films. Annealing ZnO:Al films with a silicon cap is shown to improve the electrical properties. These improvements are primarily related to an increase in mobility, so do not come at the cost of worse optical properties; in fact optical properties are shown to improve slightly. The stability of the electrical properties for standard and annealed ZnO:Al are investigated by accelerated aging in damp-heat. To better understand the damp-heat degradation process, the experiments are done in a deuterated water (D_2O) atmosphere. The isotopic marker provides a way to differentiate between hydrogen (and small amounts of deuterium) built into the film during growth from deuterium built into the film during damp-heat exposure. Since the physical explanations for these processes are similar, much of the discussion is given together at the end of the chapter.

5.1. Annealing of ZnO:Al for High Mobility

Ruske *et al.* recently introduced a method for improving electron mobility in ZnO:Al thin-films by capping ZnO:Al films with silicon, then annealing the samples at high temperatures [28]. This section examines the effects such annealing processes have on ZnO:Al further by investigating different ZnO:Al films and properties. The electrical effects are first examined as a function of ZnO:Al film thickness, then the effects of annealing on the morphological and optical properties are examined for a standard ZnO:Al film.

5.1.1. Electrical Effects of Annealing

ZnO:Al films with thicknesses between approximately 50 and 1600 nm were deposited under standard conditions (Section 3.1.2.1 (page 38)) by varying the total number of passes in front of the ZnO:Al target between 2 and 64. The as-deposited electrical properties of such films were characterized in Section 4.1.2 (page 63). The same or equivalent ZnO:Al films were capped with 50 nm of n-type silicon by PECVD, annealed at 650 °C for 24 hours, and then dry etched in an NF_3 plasma to remove the silicon cap (for more details, see Section 3.2.2 (page 40)).

The electrical properties of the as-deposited and annealed ZnO:Al films are shown in Figure 5.1. The resistivity as a function of thickness for the as-deposited and annealed ZnO:Al films is given in Figure 5.1 (a). The resistivity of both the as-deposited and annealed samples decreases to an asymptote with increasing ZnO:Al thickness. Annealing the samples decreases the resistivity between 30 and 40 % for all samples.

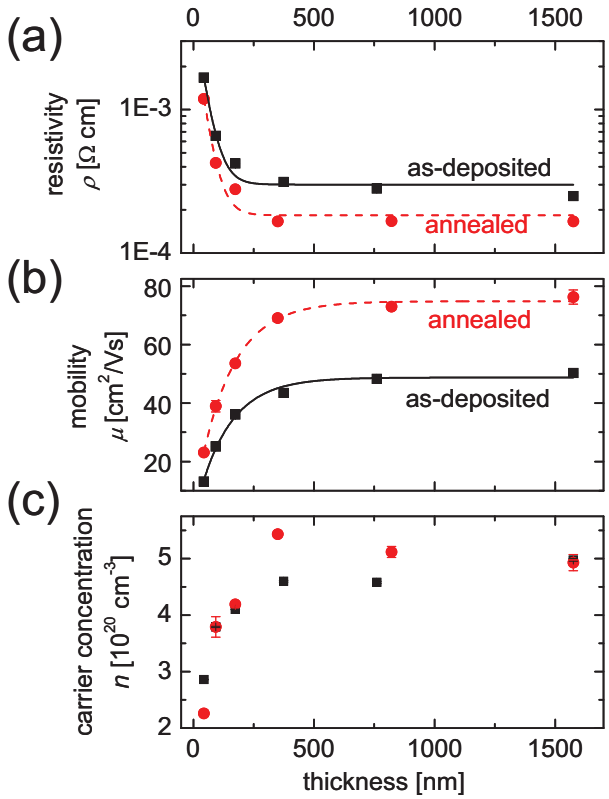

Figure 5.1: Effects of annealing on ZnO:Al electrical properties. (a) resistivity, (b) mobility, and (c) carrier concentration as a function of thickness and annealing.

The electrical properties are broken down into electron mobility and concentration (Equation (2.7)) in Figure 5.1 (b) and (c), respectively. As observed in Section 4.1.2 (page 63), the mobility increases with increasing thickness for the as-deposited ZnO:Al films; the same holds true for the films after annealing. The mobility, however, is increased during the annealing process. The mobility of the thinnest ZnO:Al film increased from 13.1 to 23.1 cm^2/Vs, which corresponds to a relative increase of 76 %. This was the largest relative increase in mobility; the other mobilities were increased between 50 and 60 % by annealing, with no clear trends with thickness. Mobilities as high as 76.2 cm^2/Vs were obtained after annealing. The carrier concentration (Figure 5.1 (c)), on the other hand, appears to be relatively unaffected by the annealing process. The deviations in carrier concentration were less than 20 %, and many points show very little variation. Some of the largest differences in carrier concentration are observed on films where an equivalent film thickness was annealed (the approximately 400 and 800 nm films). In these cases, the different depositions may account for some of the difference in carrier concentration.

5.1.2. Effects on Surface Morphology

In the previous section, it was observed that annealing can improve the electron mobility in a ZnO:Al thin-film. This section examines what effect annealing has on the morphology of a sputtered ZnO:Al film by imaging the same location with AFM before and after annealing.

Standard ZnO:Al films with as-deposited thicknesses around 800 nm were deposited onto CG (Section 3.1.2.1 (page 38)). A ZnO:Al sample was etched in the standard manner, for 40 seconds in 0.5 w/w% HCl (Section 3.2.1.1 (page 40)). The etch was made prior to annealing, as it has been observed that post-deposition annealing of ZnO:Al leads to a reduced etch rate and decrease in crater density [120]. Silver grids were deposited onto the as-deposited and etched samples to aid with repositioning before and after the annealing process (Section 3.4.2.3 (page 47)). AFM scans were made on the as-deposited and etched ZnO:Al surfaces. The ZnO:Al films were then capped with 50 nm of n-type silicon by PECVD, annealed at 650 °C for 24 hours, and then dry etched in an NF_3 plasma to remove the silicon cap (Section 3.2.2 (page 40)). Using the silver grid and the repositioning techniques discussed in Section 3.4.2.3 (page 47), AFM scans were made at the same locations on the as-deposited and etched ZnO:Al films after annealing.

Figure 5.2 contains AFM images of an as-deposited and etched ZnO:Al film before (Figure 5.2 (a) and (d), respectively) and after annealing (Figure 5.2 (b) and (e), respectively). To make comparison easier, the AFM images are presented in top view with a gray scale set to the same range for all as-deposited and for all etched samples; additionally, the difference between the pre- and post-annealing images are indicated in Figure 5.2 (c) and (f) for the as-deposited

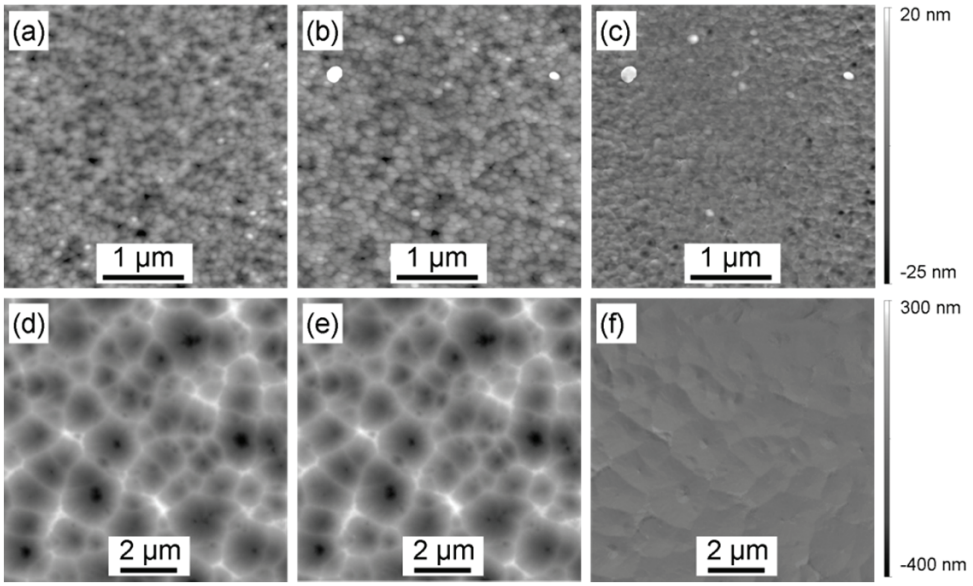

Figure 5.2: AFM images at the same location of as-deposited ZnO:Al (a) before and (b) after annealing and etched ZnO:Al surfaces (d) before and (e) after annealing. The positive (lighter) and negative (darker) differences between the pre- and post-annealing steps are shown in (c) and (f) for as-deposited and etched ZnO:Al, respectively.

and etched ZnO:Al, respectively. In these images lighter and darker gray indicate higher and lower height after annealing, respectively.

Notice that the grain structure before and after annealing (Figure 5.2 (a) and (b)) remain the same and no significant changes outside of a few dust specs are noticeable. The other small changes may be due to AFM measurement artifacts and variations in the shape of the AFM tip (Section 3.4.2 (page 43)) [141-143] leading to variations of less than a few nanometers in well aligned areas. The RMS roughness of the surface was 5.8 nm prior to annealing and 6.5 nm after annealing, but if the few large dust specs are removed by a height threshold, the RMS roughness remains 5.8 nm after annealing. The grain density was 117 and 132 μm^{-2} before and after annealing. No significant difference is observed on the etched ZnO:Al sample and the difference between the scans were generally within 10 nm, the RMS roughness was 117 nm before and 118 nm after annealing, and the crater density was 1.4 μm^{-2} both before and after annealing. In the etched case, the larger features and scan size lead to almost negligible AFM measurement artifacts and tip shape effects.

To check if the presence of the silver grid affected the annealing process, AFM measurements at locations away from the grid were also examined. These locations showed very similar morphology. Additionally, the resistivity of the ZnO:Al film decreased, as expected, with annealing. From these results it is concluded that the annealing process does not affect the morphology of the ZnO:Al surface strongly.

5.1.3. Optical Effects of Annealing

This section examines the effects annealing has on the optical properties of a ZnO:Al thin-film. A standard ZnO:Al film (Section 3.1.2.1 (page 38)) was texture etched in 0.5 w/w% HCl for 40 seconds. The total transmission, diffuse transmission, and reflection were measured by optical spectrometer (Section 3.4.10 (page 57)) before and after the annealing process (capping with silicon, annealing at 650 °C, and dry etching in NF_3). CH_2I_2 was used for index matching during total transmission and reflection measurements.

Figure 5.3 gives the optical properties of the ZnO:Al film pre- and post-annealing as a function of wavelength. The total transmission (T_t), reflection (R), and absorption (A) as calculated

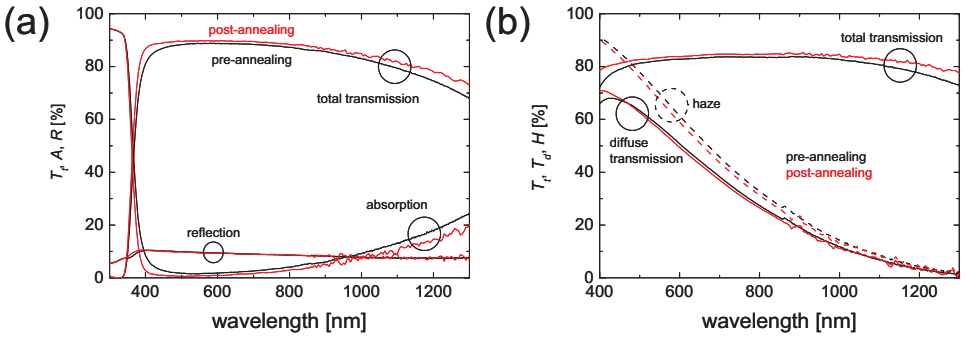

Figure 5.3: Optical properties of texturized ZnO:Al before (black) and after (red) annealing. (a) The total transmission (T_t), reflection (R), and absorption (A) as a function of the wavelength of the incoming light. (b) The total transmission, diffuse transmission (T_d), and haze (H) (dashed) as a function of the wavelength of the incoming light.

using Equation (2.29) (page 19) are shown in Figure 5.3 (a). Notice that the total transmission increases across the whole spectrum after annealing. The increase is especially strong in the short wavelength region between 350 and 450 nm, and in the long wavelength region above 1100 nm, with total increases in transmission as large as six percent. The reflection is practically identical before and after annealing, so the increase in total transmission can be attributed to a decrease in absorption.

The total transmission, diffuse transmission (T_d), and haze (H) as calculated using Equation (3.5) (page 58) are given in Figure 5.3 (b). As presented in Figure 5.3 (a), the total transmission increases across the whole measured spectrum after annealing. The diffuse transmission increases in the short wavelength region between 400 and 475 nm, and decreases slightly across most of measured spectrum between 475 and 1000 nm. The increase in total transmission and slight decrease in diffuse transmission leads to a reduction in the haze of the ZnO:Al film after annealing.

5.2. Damp-Heat Degradation

Damp-heat degradation is a method of accelerating the aging process of a material by exposing it to a harsh environment, and is often applied to a material to check the long-term stability (see Section 2.8.2 (page 31)). This section examines the electrical and compositional changes in ZnO:Al films as a function of damp-heat exposure. To differentiate between hydrogen incorporated into the film during or directly after deposition from hydrogen incorporated into the film during damp-heat exposure, damp-heat experiments were made using deuterated water (D_2O). First, the electrical properties of the standard ZnO:Al is examined, followed by that of a high mobility (annealed) ZnO:Al as presented in the previous section.

5.2.1. Damp-Heat Degradation of Standard ZnO:Al

To check the effects of damp-heat treatment on the electrical properties of ZnO:Al films, as-deposited and texture etched standard ZnO:Al thin-films (Section 3.1.2.1(page 38)) were placed into an exsiccator with either a source of DI (H_2O) or deuterated (D_2O) water. This exsiccator was placed into an oven with an approximate temperature of 88 °C for periods between 24 and 1000 hours (see Section 3.2.3 (page 41)). To explore the nature of the absorbed deuterium and determine the electrical effects of longer exposure times, the sample exposed to the D_2O damp-heat for 304 hours was then exposed to an H_2O treated damp-heat (under the same conditions) for times up to about 700 hours.

The electrical properties of the standard ZnO:Al films (both as-deposited and after etching) are given in Figure 5.4 as a function of the total damp-heat (H_2O, D_2O, or D_2O followed by H_2O) exposure time. The resistivity, Figure 5.4 (a), increases fairly linearly over the 1000 hours measured. The resistivity of the as-deposited and etched samples increased with line slopes of 0.6 and 2.4 μΩ cm/hr, respectively. The total resistivity increased by a factor of two and eight over the 1000 hours for the as-deposited and etched ZnO:Al samples, respectively.

The mobility as a function of total damp-heat exposure time is given in Figure 5.4 (b). Over the 1000 hours of damp-heat exposure, the mobility of the unetched samples degraded from between 48.5 and 50.5 to 18.0 cm^2/Vs. Similarly, the mobility of the etched sampled degraded

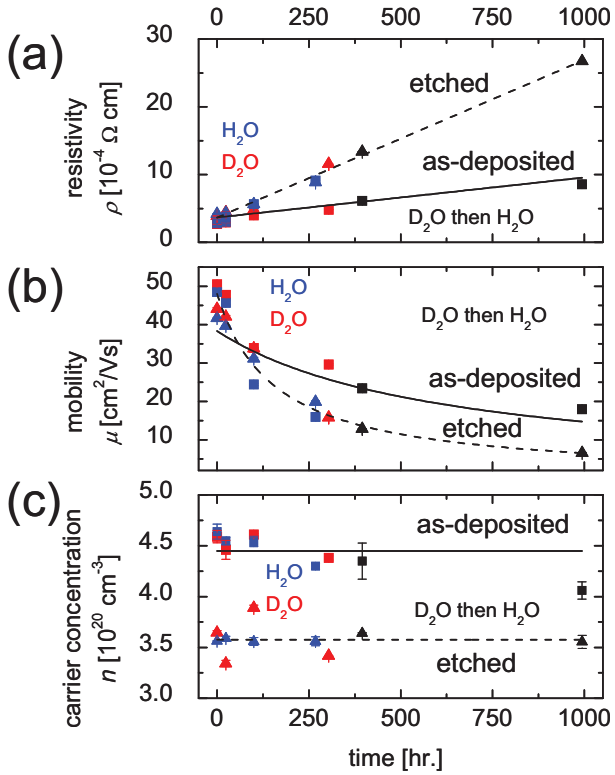

Figure 5.4: Electrical effects of damp-heat exposure in H_2O (blue), D_2O (red), or D_2O then H_2O (black) on etched (▲) and unetched (■) ZnO:Al. (a) Resistivity, (b) mobility, and (c) carrier concentration as a function of damp-heat exposure time.

from between 41.6 and 44.1 to 6.6 cm^2/Vs. The 63 and 85% drops in mobility for the as-deposited and etched ZnO:Al samples, respectively, accounts for the bulk of the increase in resistivity.

The carrier concentration is shown in Figure 5.4 (c) as a function of total damp-heat exposure time. The carrier concentration decreased slightly for the as-deposited ZnO:Al samples. This decrease is about 10 % over the 1000 hours, which is small compared to the relative decrease in mobility observed for the same samples. The carrier concentration in the etched samples is reduced as compared to the as-deposited samples and remained relatively constant throughout the experiment. Constant fits of the carrier concentration were 4.4 and $3.6x10^{20}$ cm^{-3} for as-deposited and etched samples, respectively.

Since the resistivity and carrier concentration exhibit fairly linear and constant behavior, respectively, the mobility is fit as the inverse of the product of electron charge, carrier concentration, and resistivity (see Equation (2.3) and (2.7)). This fit follows the mobility trend for the etched ZnO:Al samples closely. Deviations from the fit, however, are observed in the as-deposited samples. This is due to the slight decrease in carrier concentration over time.

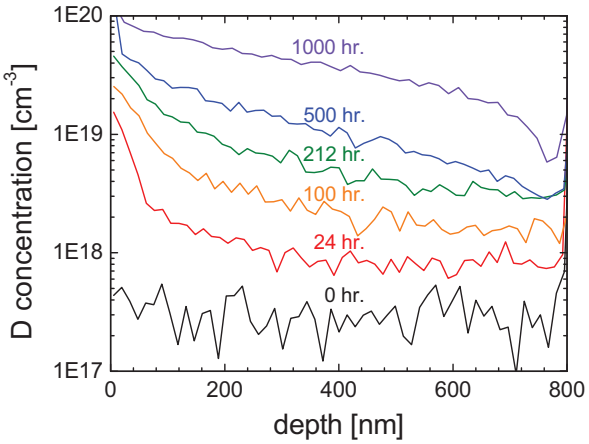

Figure 5.5: Deuterium concentration as a function of depth for ZnO:Al films exposed to a D_2O damp-heat for various lengths of time.

Figure 5.5 gives the deuterium concentration profiles for standard ZnO:Al films treated in a D_2O damp-heat for 0, 24, 100, 212, 500, and 1000 hours. For all SIMS profiles, the sputtering time was correlated to the film thickness as measured by surface profiler. SIMS results are presented as a function of sputtering depth, thus the surface corresponds to a depth of zero. Notice that the deuterium concentration increases with increasing D_2O damp-heat exposure time. Further, over the 1000 hours of exposure, the level does not saturate. For all deuterium concentration profiles, the highest levels are at the ZnO:Al surface and decrease with depth, indicating that the primary source of deuterium was on the ZnO:Al face exposed to air. The ZnO:Al film treated for 24 hours in a D_2O damp-heat (red) shows deuterium concentrations higher than that of the reference untreated film at all depths. Thus, ZnO:Al films were completely penetrated by deuterium within the first 24 hours of exposure.

Figure 5.6 gives the deuterium concentration profiles of the as-deposited ZnO:Al films exposed to a D_2O damp-heat for the first 304 hours, then an H_2O damp-heat for 24, 91, or 689

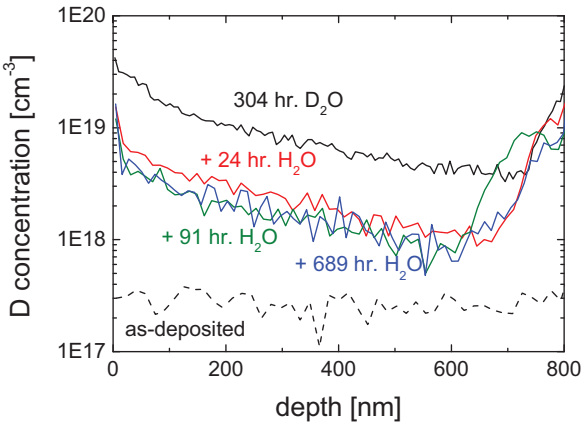

Figure 5.6: Deuterium concentration as a function of depth for ZnO:Al films exposed to a D_2O damp-heat for 304 hours (black solid), followed by exposure to a H_2O damp-heat for 24 (red), 91 (green), and 689 (blue) hours. An as-deposited reference is also indicated (black dashed).

hours. After the 304 hours of D_2O damp-heat exposure, the deuterium concentration is between the values observed in Figure 5.5 for 212 and 500 hours of exposure. The average deuterium concentration between the depths of 100 and 600 nm after 304 hours of exposure to a D_2O damp-heat (black solid line) was 8.6×10^{18} cm^{-3}, which is a factor of 32 larger than that of the reference (no damp-heat, black dashed line) at 1.7×10^{17} cm^{-3}. The deuterium concentration is reduced sharply after 24 hours of exposure to an H_2O damp-heat (red solid line), with an average concentration of 2.3×10^{18} cm^{-3} between 100 and 600 nm. Thus, 74% of the deuterium atoms were replaced within 24 hours of H_2O damp-heat exposure. While longer H_2O damp-heat exposure periods of 91 (green solid line) and 689 (blue solid line) hours do replace a larger percentage of the deuterium atoms, up to 82%, the bulk are changed within the first 24 hours.

5.2.2. Damp-Heat Degradation of Annealed ZnO:Al

This section examines the stability of annealed standard ZnO:Al in a damp-heat environment. As-deposited and texture-etched standard ZnO:Al films were capped with 50 nm of n-type silicon by PECVD, annealed at 650 °C for 24 hours, and then dry etched in an NF_3 plasma to remove the silicon cap (Section 3.2.2 (page 40)). These annealed ZnO:Al samples as well as

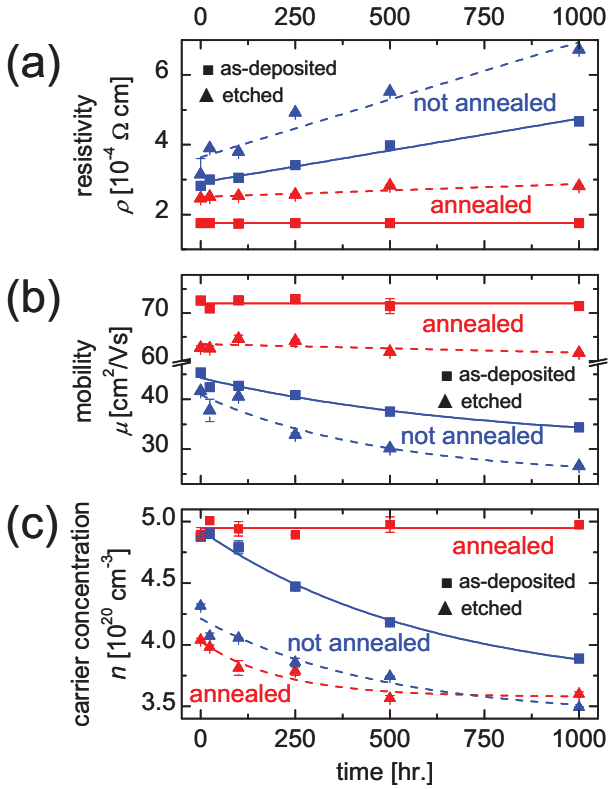

Figure 5.7: Electrical effects of D_2O damp-heat exposure on etched (▲) and unetched (■) ZnO:Al annealed (red) and not annealed (blue). (a) Resistivity, (b) mobility, and (c) carrier concentration as a function of damp-heat exposure time.

reference unannealed etched and unetched ZnO:Al samples were placed into an exsiccator with a source of D_2O.

Electrical properties of the annealed and not annealed ZnO:Al, both as-deposited and texture-etched, as a function of D_2O damp-heat exposure time are given is Figure 5.7. As observed in Section 5.1.1 (page 77), annealing the ZnO:Al yields films with lower resistivity. Additionally, like the results presented in the previous section, the resistivity of the as-deposited and etched ZnO:Al samples which were not annealed (blue) increases linearly with damp-heat exposure, Figure 5.7 (a). Although it is worth noting that the degree of degradation was less in this case than the previous experiment, with the resistivity of the as-deposited and etched ZnO:Al film increasing at a rate of 255 and 330 nΩ cm/hr. The resistivity of the annealed ZnO:Al samples show no degradation in the as-deposited case and only slight degradation at a rate of 37 nΩcm/hr in the etched case over the 1000 hours.

The mobility and carrier concentration are given in Figure 5.7 (b) and (c) as a function of damp-heat exposure, respectively. As expected from the previous experiments in this chapter, the annealed samples showed an increase in mobility and similar carrier concentrations, and the mobility and carrier concentration of the not annealed samples decreased with damp-heat exposure time. The mobility of the annealed ZnO:Al samples, however, remained relatively constant over the 1000 hours of damp-heat exposure for both as-deposited and etched films. The carrier concentration of the annealed, as-deposited (solid red line) ZnO:Al remained constant with damp-heat exposure, while it degraded slightly for the etched annealed (dashed red line) ZnO:Al. The degradation in the carrier concentration of the etched annealed ZnO:Al film amounts to 11 % over the 1000 hours, which is smaller than the 19 % degradation observed in the etched not annealed ZnO:Al film.

Deuterium profiles, as determined by SIMS measurements, are given in Figure 5.8 for the as-deposited ZnO:Al films before and after 1000 hours of damp-heat exposure for both annealed and not annealed samples. The average deuterium concentration prior to damp-heat exposure between a depth of 100 and 700 nm was 2.2 and 2.0×10^{17} cm^{-3} for the not annealed and an-

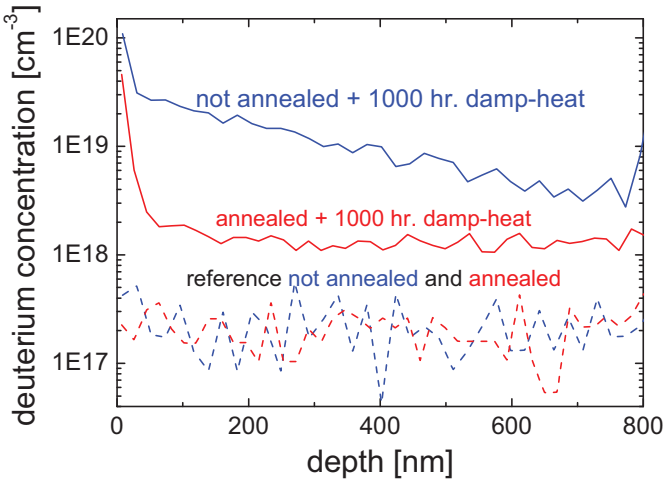

Figure 5.8: Deuterium concentration as a function of depth for annealed (red) and not annealed (blue) ZnO:Al films exposed to 1000 hours of D_2O damp-heat. Reference samples not exposed to the D_2O damp-heat are also indicated (dashed).

nealed samples, respectively. This difference is negligible when dealing with SIMS measurements, where orders of magnitude differences in elemental concentrations are generally examined. Exposing the annealed and not annealed films to a D_2O damp-heat increased the averaged deuterium concentration between a depth of 100 and 700 nm by a factor of 6 and 50 to $1.3x10^{18}$ and $1.0x10^{19}$ cm^{-3}, respectively. Both samples exposed to the deuterated damp-heat showed the highest concentration of deuterium at the surface within the first 50 nm. Like the damp-heat experiment in the previous section (Figure 5.5), the slope of the deuterium profile for the not annealed ZnO:Al indicates that the deuterium source was on the side exposed to atmosphere (with concentration decreasing with depth). Interestingly, the deuterium profile of the annealed ZnO:Al is relatively constant, other than the high concentration at the surface.

5.3. Discussion

This chapter has described the effects of heat treatments and damp-heat exposure on sputtered ZnO:Al films. Since the explanation for the effects of these two post-deposition heat treatments are similar, the discussions of the electrical, optical, and chemical effects are presented together in this section.

Electrical: The reduction in resistivity observed after annealing ZnO:Al films (Figure 5.1 and Figure 5.7) stems primarily from an increase in the electron mobility. Similarly, the increase in resistivity observed after ZnO:Al exposure to damp-heat (Figure 5.4) was attributed primarily to a decrease in the electron mobility. These changes in mobility cannot be attributed to a change in ionized impurity scattering (see Section 2.3.3 (page 14)), since the carrier concentration remains fairly constant. It is concluded that the main reason for these changes in mobility is changes in electrical transport across the grain boundaries.

Regarding annealing, it has been suggested that this improvement in electrical transport is the result of a decrease in trap (defect) density at the grain boundaries (Equation (2.13b)) due to the reconstruction at the grain boundaries during annealing [28]. This grain boundary reconstruction takes place on the atomic scale; little to no effects are observed on the grain and surface structure before and after annealing (Figure 5.2). Some of the improvement in electron transport may also be due to the healing of crystallographic defects within the individual grains, such as dislocations [28]. The exact mechanism, however, is still unknown. It can also be concluded that not all the effects of grain boundary on electron transport are healed, as the annealed films still show a strong thickness dependency up to about 400 nm (see Figure 5.1).

As for damp-heat exposure, the degradation in electrical transport may result from an increase in the trap density at the grain boundaries due to the adsorption of atmospheric gasses. When water or another molecule is adsorbed at this internal surface, a trap can be created and the doping effect of aluminum in ZnO:Al is compensated. The local carrier concentration is reduced; this in turn creates or increases depletion regions and raises the potential barrier (Equation (2.13b)). Since the exsiccator and oven were filled with air, the samples could have been exposed to a large number of chemical contaminations. Many different compounds modify ZnO electrically, as evidenced by its use as a gas sensor [182,183]. Some potential reactions include the adsorption of water to form zinc hydroxide ($ZnO + H_2O \rightarrow Zn(OH)_2$) [184,185] or the adsorption of carbon dioxide to form zinc carbonate ($ZnO + CO_2 \rightarrow ZnCO_3$) [186], alt-

hough more complex reactions from the same gases such as the formation of $Zn(OH)CO_3H$ from ZnO, CO_2, and H_2O are also possible [186]. Samples placed in the oven next to the exsiccator that were exposed to the heat but not the high humidity did not degrade noticeably. From this it can be concluded that H_2O or D_2O is the source or at least a catalyst for degradation.

The relative stability of the carrier concentration (Figure 5.4 (c)) agrees with the results of Klenk [125]. A reduction in carrier concentration with damp-heat exposure was, however, observed in the reference films treated with the annealed (high mobility) ZnO:Al films and by others [124]. A possible explanation for this discrepancy is the isolation of some grains effectively decreasing the carrier concentration; as barriers at some grains become too high the electrons in these grains cannot participate in conduction. The difference in carrier concentration between the as-deposited and texture-etched ZnO:Al films is likely due to the overestimation in film thickness by surface profiler (see Section 3.4.1(page 42)). This may also lead to an underestimation of the resistivity for the etched ZnO:Al films.

In view of Kirchhoff's current law (Equation (2.38)), it can be concluded that the whole film is affected by the damp-heat treatment since the resistivity increases (Figure 5.4 (a)) as the resistance for all current paths is increased. This is confirmed by SIMS, which showed that deuterium penetrated the whole film within the first 24 hours of exposure (Figure 5.5). Electrically, it was observed that the ZnO:Al films degraded in a similar manner, regardless of whether the sample was exposed to an H_2O or a D_2O damp-heat (see Figure 5.4). This is further evidenced as the electrical trends of the samples treated first in D_2O then in H_2O damp-heats continue in the same manner as those treated in D_2O or H_2O alone. From this it is concluded that the degradation in a D_2O-rich atmosphere accurately represents that of an H_2O-rich atmosphere.

A few reasons for the faster degradation of the electrical properties of the etched ZnO:Al films than those of the as-deposited films (Figure 5.4) include: an increase in the surface area through texturization; the preferential etching of grain boundaries in HCl, leading to wider gaps between grains; and the higher density of grain boundaries on the thinned films (see Section 4.2.2 (page 67). A thinner film thickness also allows for faster degradation, as higher deuterium concentrations are observed near the exposed surface (see Figure 5.5).

Optical: The healing of defects by annealing can also explain the increase in transmission in the short wavelength region (Figure 5.3 (a)). It has been suggested that annealing ZnO:Al decreases point or dislocation defect densities [28,69]. Decreasing the number of defects will decrease the number of states within the band gap, in turn decreasing the amount of light absorbed by these types of defects. The increase in transmission in the longer wavelength region is likely due to the higher electron mobility, since the plasma frequency (Equation (2.31)) will sharpen with increased electron mobility [121]. While the absorption of light at the plasma frequency will be stronger, it will be reduced over the visible part of the spectrum.

It is not entirely clear why the diffuse transmission decreases while the total transmission increases (Figure 5.3 (b)). A slight decrease in the refractive index could account for this, although the reflection is constant. Other explanations include a reduction in the amount of scattering that occurs at particularly large grain boundaries as quality of the grain boundary improves, and residual effects of the silicon cap (unobserved by AFM) and its removal.

It has been observed previously that the optical properties of ZnO:Al remain relatively constant upon damp-heat exposure [124].

Chemical: To further analyze the damp-heat treated samples, the equivalent deuterium densities were calculated from all SIMS measurements by integrating the deuterium concentration between the depths of 100 and 700 nm and subtracting the deuterium background of the reference samples (not exposed to damp-heat). Figure 5.9 gives the equivalent deuterium areal densities as a function of total damp-heat exposure time for the ZnO:Al films exposed only to a D_2O damp-heat for times up to 1000 hours (black squares, see also Figure 5.5), ZnO:Al films exposed to a D_2O damp-heat for 304 hours then exposed to a H_2O damp-heat for up to 700 hours (red circles, see also Figure 5.6), and reference and high-mobility (annealed) ZnO:Al films exposed to a D_2O damp-heat for 1000 hours (blue stars, see also Figure 5.8).

The buildup of deuterium in the ZnO:Al is fairly linear with exposure time and the films did not saturate over the 1000 hours examined (Figure 5.9). Similarly, the resistivity of the films increased linearly with damp-heat exposure (Figure 5.4 and Figure 5.7). While this may indicate a relationship between water uptake and electrical degradation, the exact relationship remains unclear, as the degree to which samples degraded electrically and the amount of deuterium incorporated into the film varied from one series to another. This difference may be attributed to slightly varying degradation conditions, or more likely, to the use of different ZnO:Al targets during sputtering. Other than this parameter, the films were deposited identically; it is well documented that the degree to which a ZnO:Al film degrades depends strongly on deposition conditions [20,124,125,187].

The result that the fairly large D_2O molecules apparently penetrate the whole thickness of the samples within the first 24 hours of exposure (Figure 5.5) demonstrates that diffusion is along grain boundaries, since water molecules are too big to penetrate bulk ZnO [43]. High-resolution TEM (HRTEM) imaging of polycrystalline ZnO:Al films has shown that the grain boundaries are a few atomic layers thick [188]. The relatively open structure of the grain boundaries and imperfect bonding between grains allows the grain boundaries to be exposed to

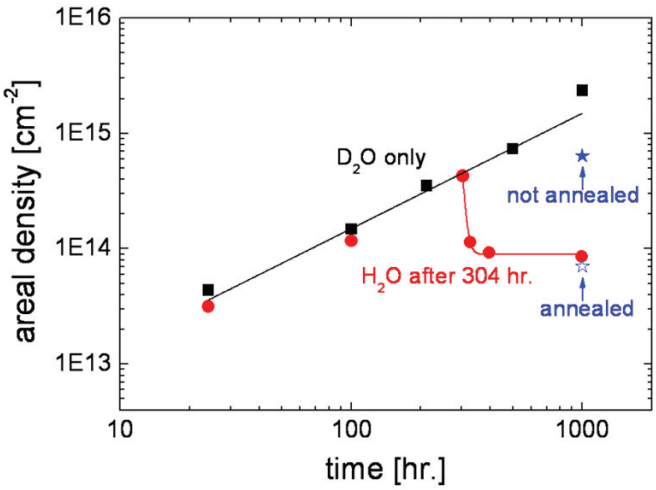

Figure 5.9: Deuterium areal density as a function of damp-heat exposure (H_2O or D_2O) time for all samples within this chapter.

various atmospheric gases and makes them more susceptible to physical adsorption or chemical reactions.

From the fast D-H replacement mechanism at a relatively low temperature (Figure 5.6 and Figure 5.9), it can be concluded that the water incorporated during damp-heat is only weakly bound and can therefore be removed easily. This effect was demonstrated by Tohsophon *et al.*, who showed that vacuum annealing could be used to restore the electrical properties of damp-heat treated ZnO:Al films to near initial states [124]. This hints that the bulk of the degradation stems from processes that can be reversed at fairly low temperatures (around 100 °C), such as the pyrolysis of $Zn(OH)_2$ to ZnO and H_2O [189].

Finally, the simultaneous reduction in electrical degradation (Figure 5.7) and deuterium uptake (Figure 5.8 and Figure 5.9) after annealing further hint that water is the source or at least an accelerant for electrical degradation. Like the improvement in mobility, the reduction in water adsorption for annealed samples can be attributed to the reconstruction at the grain boundaries during the annealing process [28]. Further, the annealing process does not appear to alter the hydrogen content within the ZnO:Al film, as deuterium profiles prior to damp-heat exposure were equivalent (Figure 5.8). The relatively constant deuterium depth profile observed in high-mobility (annealed) ZnO:Al that was exposed to a D_2O damp-heat for 1000 hours may indicate that the film is saturated, and further exposure would not alter deuterium concentration.

6. Etching ZnO

This chapter explores various aspects of the etching of ZnO. To begin, HCl, the standard acid used for texturizing the ZnO:Al surfaces is examined. In particular, the source of crater formation is investigated by examining the relation between as-deposited films and the initial points of etching, as well as observing how the HCl etch evolves on polycrystalline ZnO:Al films. Additionally, various parameters controlling the etching process are explored and modified to control the surface features resulting from the HCl etching process. Next, other acids that behave similarly to the standard HCl etch are examined. A wide range of acids are examined, including both organic and inorganic, and strongly and weakly dissociating. Similarities in etching behavior and ways to control the resultant surface structure are shown. Finally, the HF etch is investigated and is shown to texturize ZnO:Al uniquely as compared to the other acids examined. The etch evolution of this etch and ways to control surface features are presented. This chapter will identify etching behavior and trends; the following chapter uses the results presented here and previous knowledge on etching to form an etch model for polycrystalline ZnO:Al films.

6.1. HCl Etch

While the etch evolution and process of etch progression is well understood for the ZnO single crystals [31,33,190], there are few models for polycrystalline ZnO [31,35]. Despite the lack of models, trends have been observed on variously deposited series. In general, processes which lead to compact films have a lower density of etching sites [1,9,11-14,40,41]. Further, using a series of reactively MF-sputtered ZnO films, Hüpkes *et al.* showed that even though the resultant structure from various chemical (both acidic and basic) and physical etching methods vary, the density of the points of attack decreased for all etch types as the oxygen partial pressure was decreased [31]. This section will focus on confirming, clarifying, and making new observations by examining how the HCl etch evolves and how it can be controlled. Observations such as these are vital to the development of a polycrystalline ZnO:Al etch model.

6.1.1. HCl Etch Evolution

The stepwise etch-imaging process introduced in Section 3.4.2.3 (page 47) was used to observe the initial sites and the long-term etch evolution of the HCl etch. Since the alignment method relies on the photolithographic deposition of a silver grid, it is important to know what effects these processes or the presence of a silver grid have on the etching process. This section will proceed as follows: the integrity of the realignment method will be presented, followed by a few applications for this method, namely the observation of initial etching sites as related to as-deposited samples, the long-term etch evolution of the HCl etch, and the etching of new ZnO:Al deposited on previously texturized ZnO:Al surfaces.

6.1.1.1. Integrity of Realignment Method

Figure 6.1 (a) and (b) show SEM images of standardly deposited ZnO:Al samples etched for 30 seconds in HCl 0.5 w/w% without and with the silver grid, respectively. Despite the additional process steps and the presence of the silver grid, the resultant etch features appear unchanged. Due to the partly isotropic nature of the HCl etch on polycrystalline ZnO:Al, the substrate under the silver grids are also etched causing many of the markers to wash away after long enough etch times, see Figure 6.1 (b) and Figure 3.4. However, as discussed previously in Section 3.4.2.3 (page 47) the grid remains long enough for uniquely identifiable crater patterns to develop, which aid with repositioning after the grid is washed away. While etching effects of the silver grid, such as acting as a catalyst or changing crater formation, cannot be totally excluded, the effects appear to be minimal. Thus, it is assumed that samples with the silver grid generally etch in the same manner as those without, and can be used to study the polycrystalline ZnO:Al system.

While the etch features remained unchanged, it is important to note that the etch rates of the samples etched in this stepwise manner are faster than those observed in the static etching in same HCl solution. This is most likely due to the dynamic nature of these very short etches, which limits the formation of pH gradient close to the etching surface. The effects motion has on the etch rate are further discussed in Section 6.1.2.1 (page 101). In general, the etch rates of the stepwise etching were approximately twice as fast as those of similar static etches. The higher etch rate observed in these samples is also due to the underestimation of actual etching time. As etching continues during the transfer of the sample from the etching bath to DI water rinse; this error in actual etching time is compounded with each additional etching step.

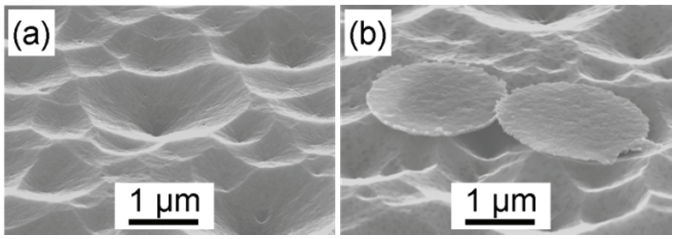

Figure 6.1: SEM images of HCl etched ZnO:Al thin-films (a) without and (b) with the silver grid.

6.1.1.2. Initial Etch Sites as a Function of ZnO:Al Thickness

To observe the initial sites of etching, standardly deposited ZnO:Al with thicknesses between 50 and 1600 nm (by factors of two) were imaged at the same location before and after one second of etching in a very dilute 0.125 w/w% HCl solution. Etching steps were compared by constructing a local etch rate from the two images, details on this process are given in Section 3.4.2.4 (page 49). After only the initial one second of etching, it remains unclear which etching sites will progress the fastest, forming the craters that provide effective light scattering [13]. To see which of the initial etching sites progress the fastest, the process of imaging, etching, and imaging again was repeated three times on an 800 nm thick sample.

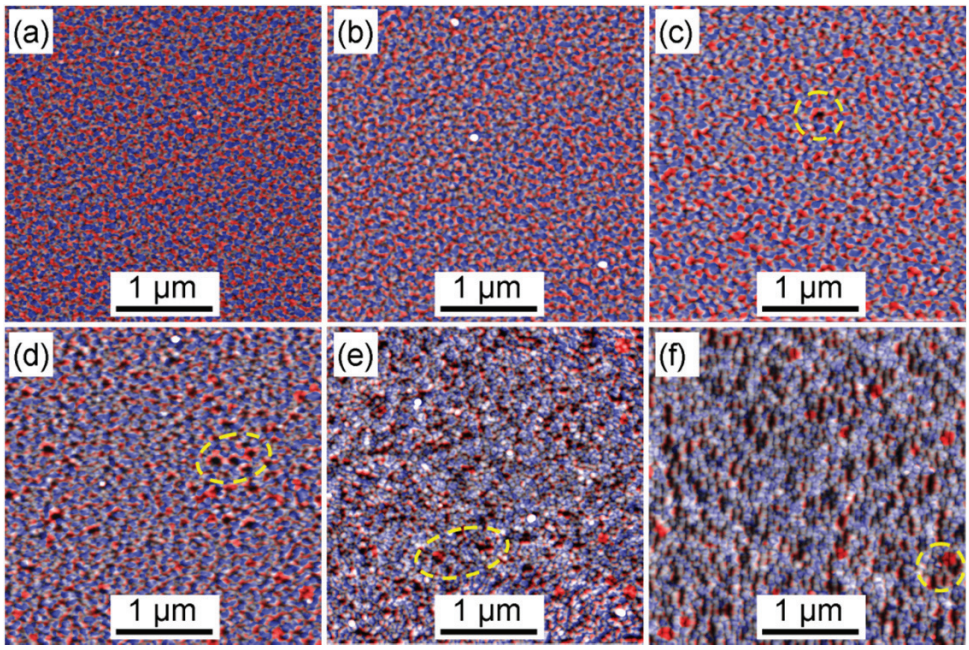

Figure 6.2: AFM images of the as-deposited films with approximately (a) 50, (b) 100, (c) 200, (d) 400, (e) 800, and (d) 1600 nm thickness. Images were reconstructed using the etched image and the differences between etched and unetched (see Section 3.4.2.4 (page 49)). Red indicates areas with an etch rate faster than the median, while blue indicates areas with an etch rate slower than the median. Yellow ovals on the 200 nm and thicker images indicate some etching locations that correspond to crater-like structures in the as-deposited state.

Additionally, to measure the density of etching sites as a function of ZnO:Al thickness, samples were etched in the standard 0.5 w/w% HCl for four seconds. The crater density and size was calculated using a watershed algorithm over an area of 200 µm^2 (two 10x10 µm^2 AFM scans); more details on calculating crater density using a watershed algorithm are found in Section 3.4.2.2 (page 46).

The reconstructed AFM images shown in Figure 6.2 give not only the topology of the as-deposited samples (gray scale), but also a local etch rate of the films with different thicknesses. Areas that etched faster than the median value are highlighted in red, while areas that etched slower than the median value are highlighted in blue. On very thin films, with thicknesses of 50 or 100 nm, about half of the film is etched faster than the median while the other half etched slower than the median (Figure 6.2 (a) and (b)). On the thicker films, the sites of accelerated etching segregate to particular points leaving plateaus where etching occurs more slowly than that of the median (Figure 6.2 (c-f)). This separation becomes more pronounced with increasing film thickness.

Figure 6.3 shows the same location as-deposited and after three one-second etching steps in the dilute (0.125 %) HCl solution. After these etching steps, the largest (fastest progressing) craters have diameters up to 500 nm. Three different etching characteristics are marked in Figure 6.3: as-deposited depressions that exhibit accelerated etching (solid blue ellipse), accelerated etching without the presence of an as-deposited depressions (dotted green ellipse), and as-deposited depressions where accelerated etching does not occur (dashed red ellipse). Three

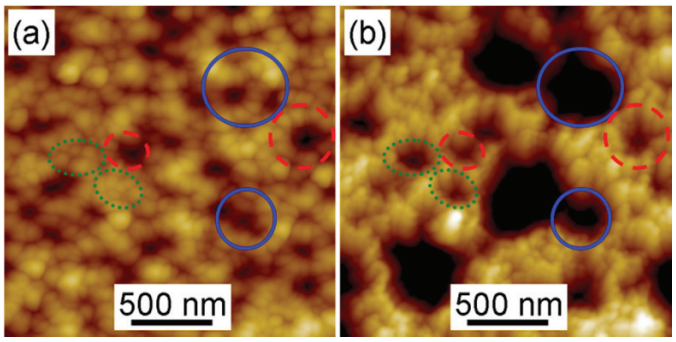

Figure 6.3: Same location on an approximately 800 nm thick ZnO:Al film (a) as-deposited, and (b) after three one-second etching steps in 0.125 % HCl. Blue solid line ovals indicate locations where etching starts close to an as-deposited depression, green dotted line ovals indicate locations where etching starts without depression, and red dashed line ovals indicate depressions where accelerated etching did not occur.

one-second etching steps is still fairly early in the texturizing process; only the locations with the fastest etching will contribute to texture useful for solar cells, see Section 6.1.1.3 (page 96). Notice that most, if not all, of the large craters had an as-deposited depression at the center of the crater.

Figure 6.4 shows AFM images with the craters marked by watershed algorithm to determine the density of etch sites as a function of ZnO:Al thickness. An etching time of four seconds was chosen to try to avoid over- and underestimation of crater density. Too short etching time could lead to overestimation, as the natural as-deposited depressions are on the same scale as the etched features (see Figure 6.3, dashed ellipse). Too long an etching time would lead to an underestimation of etch site density, as faster growing craters overtake more slowly growing craters after prolonged etching, see Section 6.1.1.3 (page 96). The 50 nm film is not included in Figure 6.4 since the film was completely etched away within the four seconds. In general, the etch site density decreases with initial film thickness. The average crater density and area as a function of as-deposited film thickness are shown in Figure 6.5 (a). The crater density decreases with increasing thickness until the initial ZnO:Al film is approximately 400 nm thick; even thicker films have relatively constant crater densities. The average crater area increases accordingly, since all points on the surface are assigned to one crater or another. The RMS roughness of these slightly etched films is shown in Figure 6.5 (b) and increases with increasing thickness until a thickness of 800 nm, after which it remains fairly constant.

The growth and grain size of films with various thicknesses was discussed in Section 4.2.2 (page 67). Recall that the c-axis orientation quickly dominates other orientations as it has a minimum of surface free energy [107,108], and that this survival-of-the-fastest growth period showed an increase in grain size with increasing thickness up to 200 nm, see Figure 4.5. For films with thicknesses greater than 200 nm, the grain size remained relatively constant (see also Figure 4.5). The etching behavior in this nucleation region follows a similar trend. The highest density of etching sites was observed on the thinnest films. As the number of grain boundaries decreased with increasing thickness, the number of etching sites also decreased, see Figure 6.2 and Figure 6.5 (a). While the grain size does not increase with thicknesses over 200 nm, the number of etching sites continued to decrease until a thickness of approximately 400 nm, after which the density of craters remains relatively constant, see Figure 6.4 and Figure 6.5 (a).

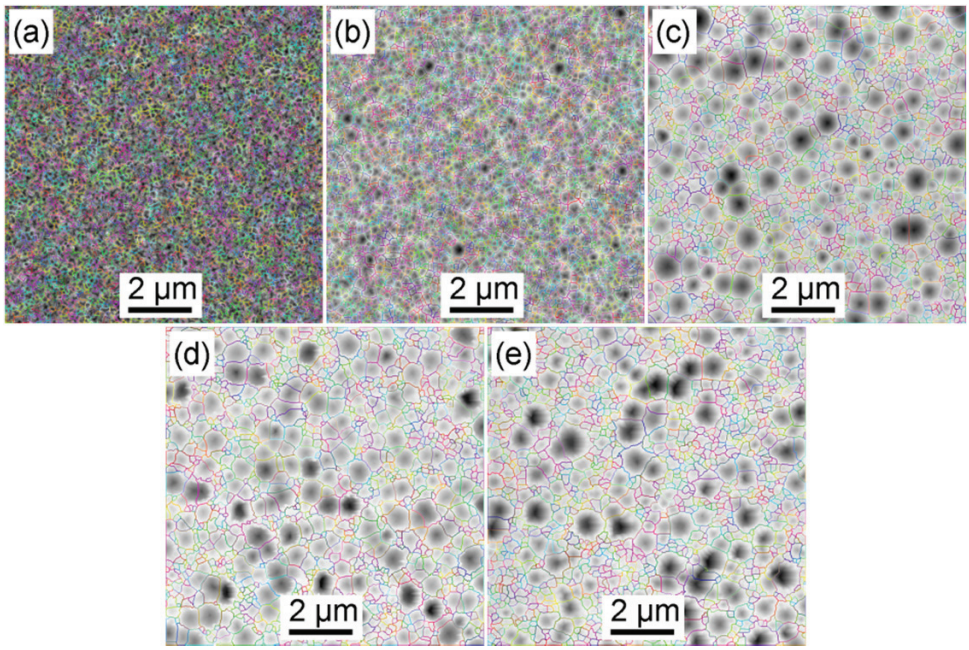

Figure 6.4: AFM images with the craters outlined in randomly assigned colors by a watershed algorithm. The initially (a) 100, (b) 200, (c) 400, (d) 800, and (e) 1600 nm thick films were etched in HCl 0.5 w/w% for four seconds.

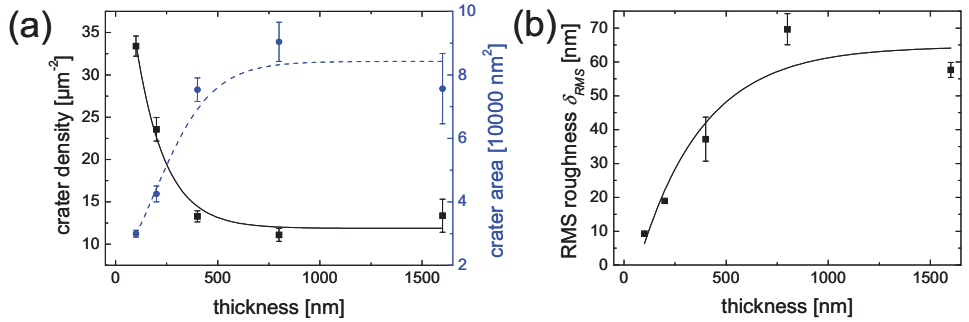

Figure 6.5: (a) Crater density (black, left axis) and average crater area (blue, right axis); (b) RMS roughness as a function of film thickness for films in Figure 6.4.

The transition from many etch sites to fewer etch sites with increasing thickness observed in Figure 6.2 and Figure 6.5 (a) explain why the RMS roughness after etching also increases with increasing thickness. The thin films with a higher density of etch sites (Figure 6.2 (a) and (b)) leads to an almost homogeneous etching of the film, as the boundaries between craters run together quickly. For thicker films (Figure 6.2 (c-f)), the craters can reach much larger sizes before the crater boundaries meet.

It is unclear what exactly causes the formation of the depressions observed in the as-deposited state which often exhibit accelerated etching, as seen in Figure 6.2 (c-f) and Figure 6.3. Some possible explanations include: (1) shadowing effects caused by chance and the

dynamic nature of the deposition process; (2) the O-terminated polarity of a single ZnO column, as O-terminated surface has been observed to grow more slowly than the Zn-terminated surface [177,194,195]; and (3) areas of lower density caused by certain 'peculiar' grain boundaries caused by strong disorder or unfavorable growth such as a triple grain boundary, a strong orientation mismatch between neighboring grains, or both.

Of these explanations the latter is favored, as it could also explain why similar trends were observed for both chemical and physical etching [31]. The term 'peculiar' is used as most of the grain boundaries do not exhibit this behavior, indicating there is something unique about these grain boundaries. Regarding O-terminated growth as the source of the depressed regions, it seems unlikely that an O-terminated column could progress past the nucleation region. This growth is not preferred and may be overtaken quickly by Zn-terminated growth [108,177] (see also Section 4.4 (page 72)), although the overgrowth of an O-terminated grain could also lead to a region of lower density.

To summarize, the number of etching sites decreases with increasing film thickness, as etching sites segregate to particular locations. The sites with the fastest etching are often related to depressed features in the as-deposited state. It was proposed that these peculiar grain boundaries of accelerated etching are related to less dense growth resulting from strong disorder or unfavorable growth conditions.

6.1.1.3. Long-term HCl Etch Evolution

To observe the long-term etch evolution on ZnO:Al surfaces, the stepwise etch-imaging process described in Section 3.4.2.3 (page 47) was applied to a standardly prepared polycrystalline ZnO:Al film. An incremental etching time of two seconds was used for cumulative etch times between zero and 18 seconds, and four seconds between cumulative etch times of 18 and 30 seconds. All etches were performed at RT (about 25 °C) in a HCl 0.5 w/w% solution. Following all etching steps, the process was stopped by rinsing the sample with DI water and drying it with nitrogen. To compare line scans and estimate the fraction of the ZnO:Al remaining, the AFM data was shifted by setting the glass level to zero in the sample when the etch had progressed far enough to expose the substrate. For the line scans where glass level was not observed, the maximum AFM value was assumed to correspond to the maximum thickness measured by surface profiler, see Section 3.4.1 (page 42). This approach fits relatively well, as the AFM and surface profiler thickness measurements showed a deviation of less than 30 nm on samples where the glass substrate was observed and both thickness measurements were measured.

Figure 6.6 and Animation 6.1 (located in Appendix (page 157)) show AFM images taken at the same location on a ZnO surface at steps in the etching process. The craters are created within the first few seconds then expand with further etching. To illustrate this further the evolution of single line scans at the same location is shown in Figure 6.7. The location of the lines relative to the total scanned area is indicated in Figure 6.6 (e, gray line). Even though the etching process was stopped and restarted many times, the same points were etched in subsequent etching steps, see Figure 6.6, Figure 6.7, and Animation 6.1. While some etching sites are present during the first etching steps and then disappear (positions 3 and 6.5 µm in Figure 6.7), and others appear only later (positions 2 and 8 µm in Figure 6.7), most are present throughout the entire etching process. After 18 seconds of etching, the glass was reached at

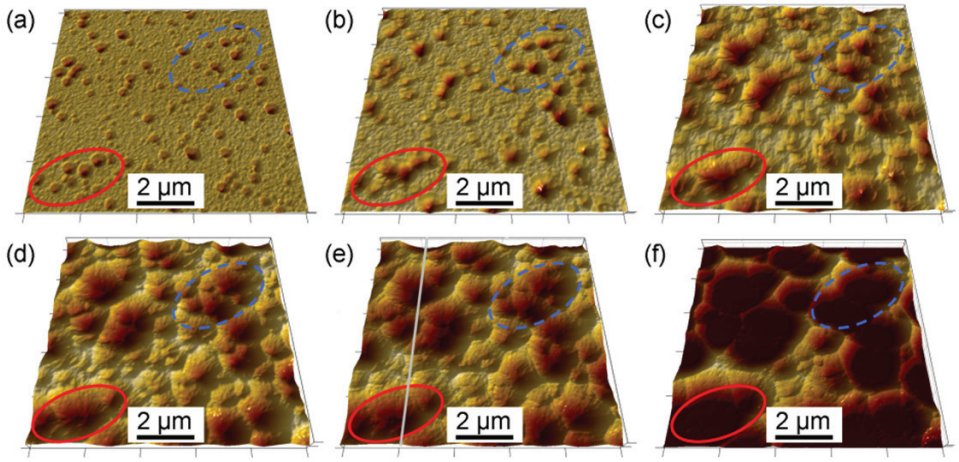

Figure 6.6: AFM images taken at cumulative etch times of 2, 4, 8, 12, 16, and 30 seconds shown in (a), (b), (c), (d), (e), and (f), respectively. The line in (e) indicates the area of the line scan analysis. Additional images are shown in Animation 6.1.

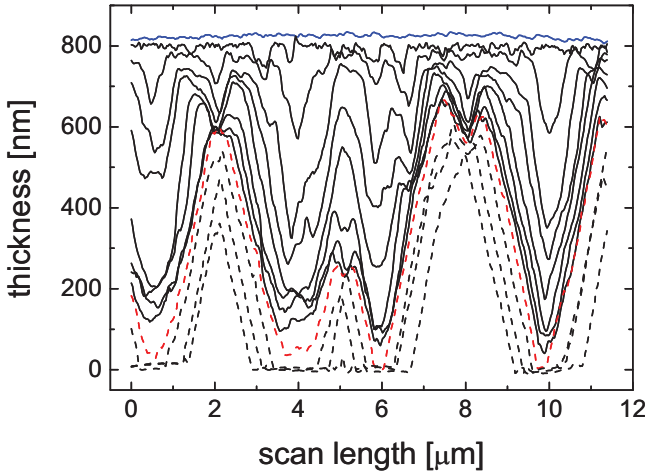

Figure 6.7: Line scans at approximately the same location throughout the etching process. The original thickness is marked in blue, and the thickness when the glass was first observed is marked in red; thereafter the lines are dashed rather than solid.

some points (see Figure 6.7 (red dashed line)), while other points still had thicknesses over 660 nm, showing that the etching rate varies by at least a factor of 4.5 between etch sites and other locations on the film surface.

The fraction of the original ZnO:Al material remaining, peak in surface angular distribution, RMS roughness, and crater density and area as calculated from the AFM data (Animation 6.1) are presented as a function of cumulative etch time in Figure 6.8. The percentage of the ZnO:Al film remaining, as estimated by the combination of surface profiler and AFM measurements (Section 3.4.1 (page 42)), decreases linearly with an etch rate of 3.9 %/s up to a cumulative etch time of 18 seconds, see Figure 6.8 (a, red). The deviation to a different etch rate

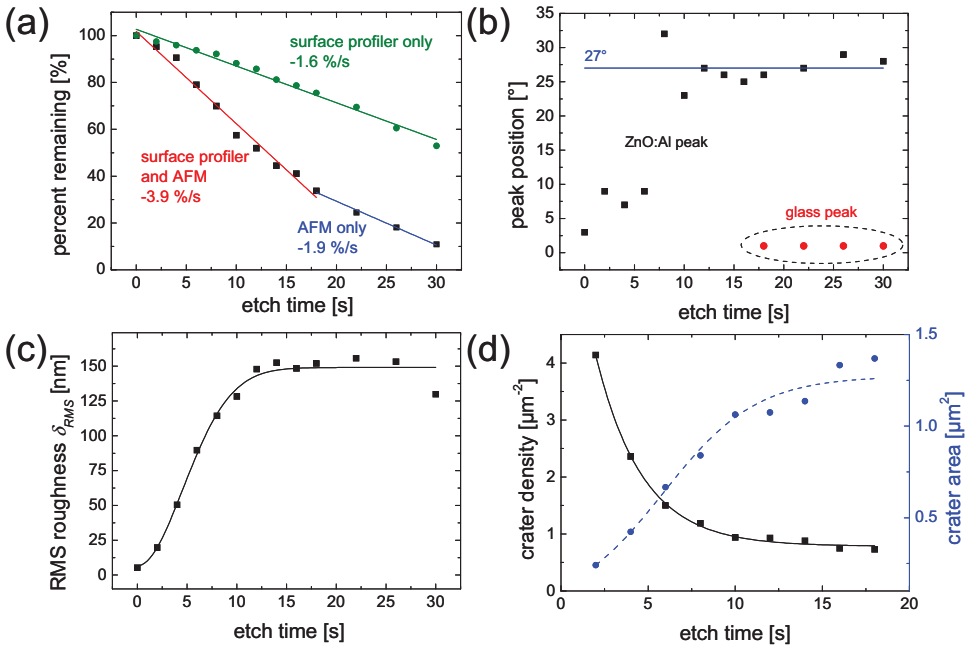

Figure 6.8: The evolution of various attributes of the ZnO:Al surface as function of cumulative etch time, as calculated from the AFM data sown in Animation 6.1. (a) Percentage of the remaining ZnO:Al, (b) peak position of the surface angular distribution, (c) The RMS roughness, (d) crater density (left axis, black solid line) and average crater area (right axis, dashed blue line).

of 1.9 %/s (Figure 6.8 (a, blue)) with etch times longer than 18 seconds can be attributed to two main factors. First, 18 seconds is the point at which the glass first appeared, exposing less ZnO to the HCl solution than during earlier etching steps. Second, after the glass appeared, longer etching steps were taken (four rather than two seconds). This longer etching time may allow thicker regions of depleted acid to form as the acid is not refreshed as often. The percentage remaining as estimated by only surface profiler measurements is also shown in Figure 6.8 (a, green). The percentage remaining also decreases linearly, although the rate of 1.6 %/s is less than half the rate measured when the AFM correction is included.

Two distinct areas in the peak angular distribution can be observed in Figure 6.8 (b). First, the initial etching steps between zero and six seconds yield peak positions around 10°, except for the as-deposited case which had an even lower value of 2.5°. A peak position of 10° is typical for as-deposited films, as shown in Figure 3.1 (b). The bulk of the surface is thus covered with relatively flat plateaus after up to six seconds of HCl etching (see Animation 6.1 frame 4). The lower peak position observed in the as-deposited case may be due to the lower lateral resolution used when imaging this series. This resolution was used because the formation and growth of relatively large features was of primary interest in this experiment, rather than the relatively small initial site of etching (Section 6.1.1.2(page 92)) or grain growth (Section 4.1.1(page 61)). In the second region, between eight and 30 seconds, a peak in angular distribution corresponding to a typical crater wall is observed. A second peak at approximately 0° appears on samples etched between 18 and 30 seconds; this peak corresponds to the glass,

see Section 3.4.2.1 (page 44)and Figure 3.1 (b). The peaks related to the glass are marked in red, see Figure 6.8 (b). The average angle of the crater wall inclination over the second was 27°, as indicated in Figure 6.8 (b, blue line). This corresponds to a typical crater opening angle of 126°, which is in agreement with the results of Kluth *et al.* [42].

The RMS roughness as a function of cumulative etch time is given in Figure 6.8 (c). It increases approximately linearly between zero and 12 seconds. It then remains more or less constant until the final etch time measured, where it once again begins to decrease. As previously mentioned and evidenced in Figure 6.7, some craters grow faster than others; with longer etching times, the most quickly growing craters will overtake plateaus and more slowly growing craters. Figure 6.8 (d) gives the density and average area of the craters as a function of cumulative etch time as estimated by a watershed algorithm. The data is well fit by an asymptotic function, which is expected for survival-of-the-fastest growth [196], or the survival-of-the-fastest etching sites, in this case.

From the evolution of the HCl etch it appears that the points of attack are built into the film during growth, since if the points of attack were due to the state of the sample in the HCl solution or particular adsorbates on the ZnO surface, subsequent etching steps would affect different points; thus confirming the observation of Hüpkes *et al.* [31]. Crater formation in HCl can be likened to the growth of polycrystalline ZnO:Al, see Section 4.1.1 (page 61). First, there is a nucleation region as many craters begin at peculiar grain boundaries (Section 6.1.1.2 (page 92)). Next, in a manner similar to survival of survival-of-the-fastest growth the craters expand around the peculiar grain boundary. These craters exhibit a preferential angle on the crater wall (Figure 6.8 (b)). While expanding plateaus and more slowly progressing craters are overtaken (Figure 6.7 and Figure 6.8 (d)) and the RMS roughness increases (Figure 6.8 (c)). After the survival-of-the-fastest growth period, an almost steady state surface is reached, as angles, RMS roughness, and crater density change only slightly with increased etch times (Figure 6.8 (b-d)). Finally, with no analogy to polycrystalline ZnO:Al growth, the glass is reach and all features are lost.

6.1.1.4. Reset Etch Sites on Texture-etched ZnO:Al

This section will examine the effects depositing a new layer of ZnO:Al has on etching. In Section 4.3 (page 70) the growth of ZnO:Al on a textured ZnO:Al substrate was examined. It was shown that the columnar structure of 'new' ZnO:Al follows that of the 'old' ZnO:Al. Here the etching properties of such a ZnO:Al double layer are examined. As described in more detail in Section 4.3 (page 70), a standardly deposited and etched ZnO:Al film received an additional

Table 6.1: ZnO:Al film thickness, change in thickness from a given step, and total change in thickness were the standardly etched substrate is the reference thickness.

step	thickness d [nm]	Δd_{step} [nm]	Δd_{total} [nm]
standardly etched substrate	653	--	--
approx. 200 nm deposition	828	175	175
10 seconds etching	794	-34	141
20 seconds etching	746	-48	93
30 seconds etching	706	-40	53
40 seconds etching	661	-45	8

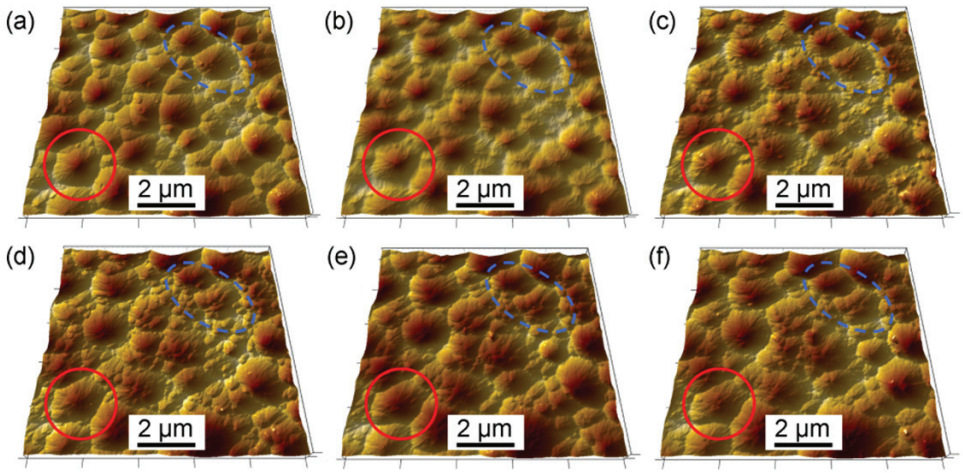

Figure 6.9: AFM images at the same location on a ZnO:Al film after (a) a standardly etched, (b) the deposition of an additional 200 nm of ZnO:Al, and after a subsequent etch in 0.125 % HCl for (c) 10, (d) 20, (e) 30, and (f) 40 seconds. Red and blue ellipses indicate the same locations.

deposition of approximately 200 nm of ZnO:Al. The sample was then stepwise etched in a dilute HCl 0.125 w/w% solution in 10 second increments. Between each deposition and etching step the thickness of the film was measured by surface profiler, and the surface topography at the same location was imaged by AFM, using the method described in Section 3.4.2.3 (page 47).

The film thicknesses, change in thickness from the previous step, and total change in thickness with respect to the etched standard are listed in Table 6.1. The standardly etched substrate is used as the reference thickness to which other substrate thicknesses are compared. Figure 6.9 and Animation 6.2 (located in Appendix (page 157)) show AFM images at the same location after each deposition and etching step. Figure 6.10 shows the reconstructed standardly etched samples: the construction of figures such as these is described in Section 3.4.2.4 (page 49). The surface of the standardly etched substrate (Figure 6.9 (a)) is compared to the surface after the deposition of 200 nm (Figure 6.9 (b) and Figure 4.10 (b)) and cumulative etch times of ten and 30 seconds in Figure 6.10 (a) and (b), respectively. The red and blue shading represent areas which were etched faster and slower than the mean value, respectively.

The new ZnO:Al has different etching sites, as seen in Figure 6.9 (c) and (d), many small craters appear within the newly deposited ZnO:Al. The comparison between the original etch and ten seconds into the etching of the new growth shows that new etch sites (marked in red) are located on both craters and plateaus of the original etch and are not related to the initial surface, see Figure 6.10 (a). However, with longer etching times (30 to 40 seconds), most of the new craters vanish and the surface appears similar to that of the original etch, see Figure 6.9 (e) and (f). The comparison between the original etch and 30 seconds into the etching the new growth show that craters tend to be etched more quickly than plateaus, see Figure 6.10 (b). This behavior would be expected when the same point is etched, see Section 6.1.1.3 (page 96).

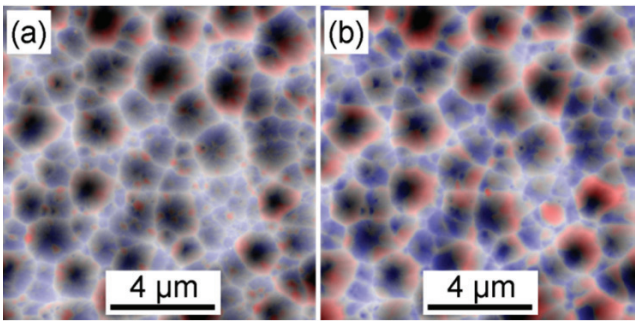

Figure 6.10: Reconstructed AFM images of the standard etch after etching freshly deposited ZnO:Al for (a) 10 and (b) 30 seconds, where red and blue shading represent areas of strongest and weakest etching, respectively.

In Section 4.3 (page 70) the ZnO:Al columns were shown to follow those of the underlying ZnO:Al layer on textured ZnO:Al. In this section it has been observed that the etching sites are not the same for the new and old ZnO:Al, thus the growth is not perfectly epitaxial. However, after the new ZnO:Al top layer is etched away the etching sites seem to return to those of the underlying ZnO:Al

6.1.2. Controlling the Etch Process

In the last section, etch crater evolution was investigated for standard etch processes, specifically in a static 0.5 w/w% HCl solution at RT. Many parameters, such as the solution dynamics, temperature, and concentration can change how quickly the HCl is etched. The following sections will examine how each of these parameters affects the etch rate and the resultant surface features.

6.1.2.1. Affects of Sample or Etchant Dynamics

In Section 6.1.1.1 (page 92), it was noted that the dynamic nature of the stepwise etch process leads to etch rates higher than those of a statically etched sample. To further explore the rela-

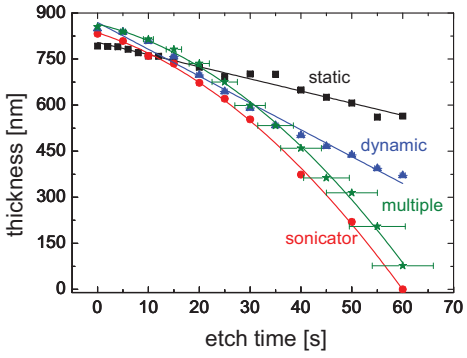

Figure 6.11: Sample thickness as a function of etch time and type of movement. Movement types examined include static (black), dynamic (blue), multiple (green), and sonicator (red). Lines were added to guide the eye.

Table 6.2: Etch rate and statistics of the resultant surface textures for ZnO:Al substrates etched with various states of motion.

etch method	static	dynamic	multiple	sonicator
etch rate [nm/s]	2.9	7.3	8.3	9.1
RMS roughness [nm]	137	133	143	126
crater density [μm^{-2}]	1.16	0.92	1.33	1.14
peak angular distr. [°]	23	24	22	22
FWHM angular distr. [°]	19	18	17	16

tionship between the motion of the sample or solution and the etch rate and resultant surface structures, standard ZnO:Al samples were etched in HCl 0.5 w/w% solutions with different states of motion. The examined states of motion included: static, where the samples were still except upon entrance and exit from the solution; dynamic, where the samples were kept in lateral motion during the whole etch time by hand; multiple, where the sample was etched in five second intervals and then stopped and restarted; and sonicator, where the samples and solution were kept in constant motion. AFM measurements were made on samples with a removed thickness of 150-200 nm. All thickness measurements were made by surface profiler.

The various film thicknesses as a function of etch time and method are shown in Figure 6.11. Not surprisingly, the statically etched samples (black squares) had the slowest average etch rate of 2.9 nm/s, while the samples kept in motion had average etch rates of 7.3, 8.3, and 9.1 nm/s for the dynamic, multiple, and sonicator etches, respectively. The increase in etching rate with motion is likely due to the faster convection, and thus a faster refreshing of the acid solution. Accordingly, etches performed in the sonicator, where the sample and solution were kept moving at the fastest rates examined, showed the highest etch rates. Notice that while multiple etching steps lead to high etch rates, the error in actual etching time becomes larger with increasing etch steps as it compounds.

Table 6.2 gives the RMS roughness, crater density, as well as the peak and FWHM of the angular distribution as calculated from the AFM measurements of the substrates etched with different states of motion. No clear effects to the surface structure are observed by increasing the motion of the sample during the etching process.

6.1.2.2. Temperature and Concentration

To examine the effect of HCl concentration and temperature, standard ZnO:Al samples were etched at various temperatures between RT (approximately 25 °C) and 90 °C and concentrations between 0.03125 (=1/32) and 4 w/w% (by factors of two). Etch times were adjusted such that 150-200 nm of ZnO:Al was removed, as determined by surface profiler measurements. After etching, all samples were characterized by optical microscope; additionally select samples were characterized by AFM.

Figure 6.12 (a) and (b) give the etch rate of the ZnO:Al thin-film as a function of HCl solution temperature for different concentrations, and as a function of HCl solution concentration for different temperatures, respectively. Temperature error bars were determined by measuring the temperature of the solution before and after etching, and range between 0 and 2 °C. Positive and negative etch rate error bars were estimated assuming one second error in etch time leading to shorter or longer etching, respectively. This error becomes significant for samples with large etch rates (above 40 nm/s) as an error of one second is up to 25% of the total etch-

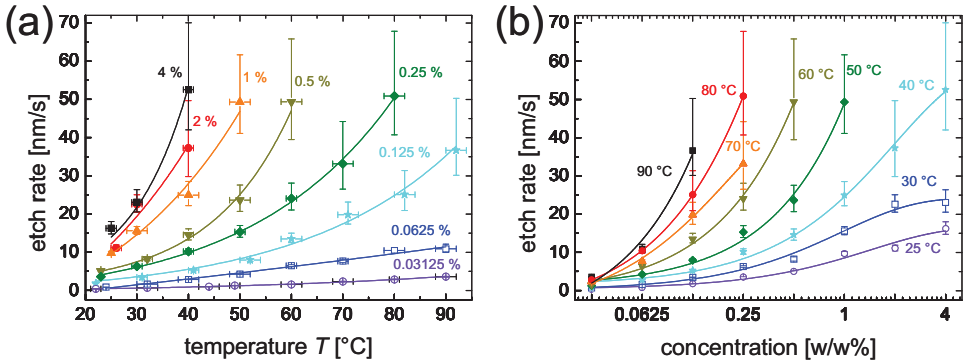

Figure 6.12: ZnO:Al etch rate as a function of (a) HCl temperature with different concentrations indicated by different colors, and (b) HCl concentration with different temperatures indicated by different colors.

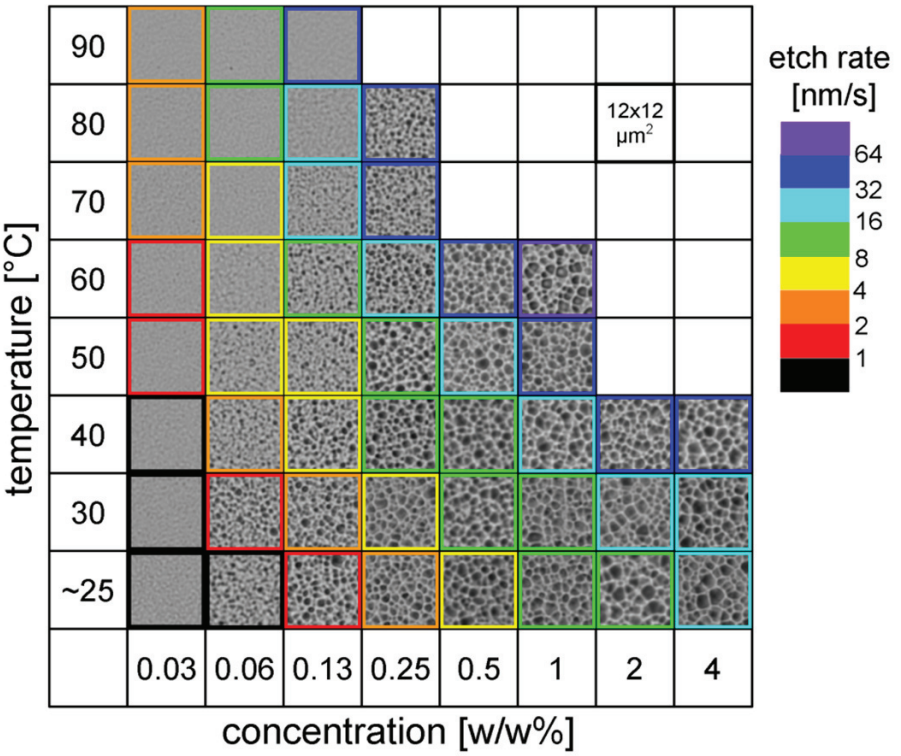

Figure 6.13: Approximately 12x12 µm² optical images of etched ZnO:Al thin-films as a function of HCl concentration and temperature. Color boxes encasing the optical images indicate a range for the etch rate.

ing time. The etch rates increase with temperature and concentration. The temperature dependence is relatively linear for low concentrations and more than linear for high concentrations.

Figure 6.13 shows a matrix of optical microscope images organized by the temperature and concentration of the HCl solution. Note that the color code of the image frames provides the

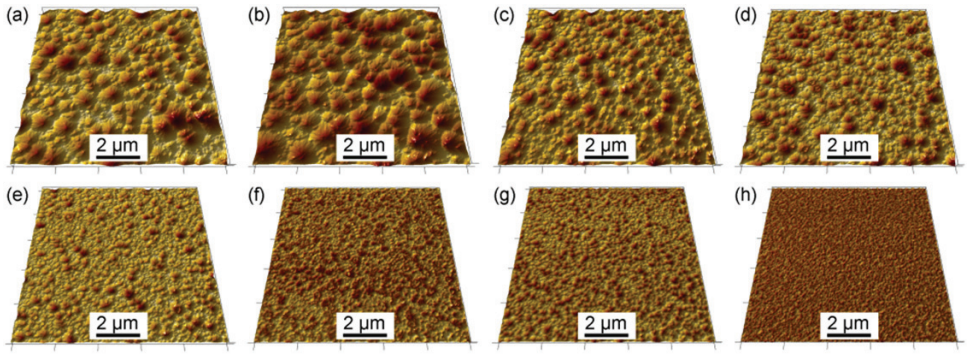

Figure 6.14: AFM images of ZnO:Al surfaces etched in 0.125 w/w% HCl at various temperatures, (a) 25 (RT), (b) 30, (c) 40, (d) 50, (e) 60, (f) 70, (g) 80, and (h) 90 °.

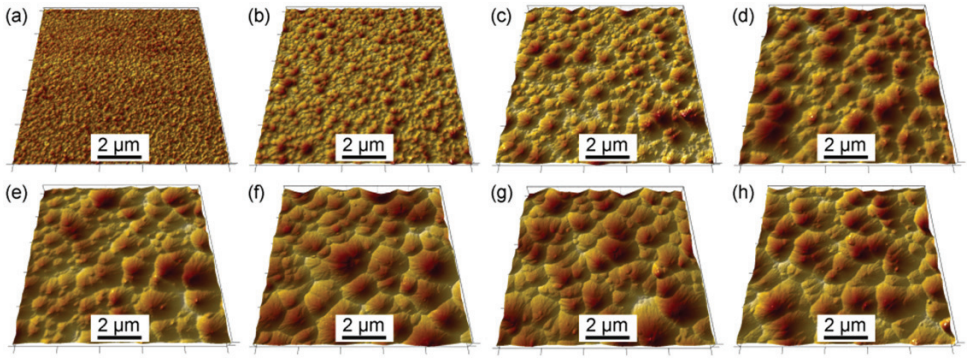

Figure 6.15: AFM images of ZnO:Al surfaces etched at RT in various concentrations of HCl, (a) 0.03125, (b) 0.0625, (c) 0.125, (d) 0.25, (e) 0.5, (f) 1, (g) 2, and (h) 4 w/w%.

etch rate range as given by the scale on the right side. The optical images do not show the exact surface since the resolution is not high enough to observe small features and the optical contrast does not necessarily reveal the shape of the feature. However, the density and size distribution of craters even below the micrometer range is identifiable. The density of the resultant craters increases both by increasing HCl temperature and lowering the HCl concentration. To more precisely observe the differences in surface structure with different temperatures and concentrations, three series of AFM measurements were taken. First, the HCl concentration was held constant at 0.125 w/w% while the temperature was varied, see Figure 6.14. Second, the temperature was held constant at RT while the HCl concentration was varied, see Figure 6.15. Third, the etch rate was held fairly constant at around 25 nm/s (as seen in Figure 6.12) while temperature and concentration were varied, see Figure 6.16. Here the optically observed trends are confirmed. Additionally, one can see that the constant etch rate series also covers a wide range of crater densities.

Figure 6.17 gives the matrix of crater densities as calculated by watershed algorithm from the optical images (see Figure 6.13, although only 12x12 µm^2 sections are shown). Calculations were made on the full optical images of approximately 80x105 µm^2). The range of crater densities were 0.55-2.2 µm^{-2}. Figure 6.18 gives the statistical evaluations of the AFM images shown in Figure 6.14, Figure 6.15, and Figure 6.16. Figure 6.18 shows the crater density and average

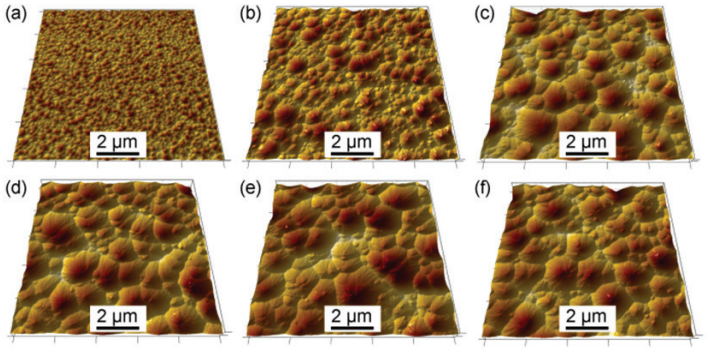

Figure 6.16: AFM images of ZnO:Al surfaces etched with approximately the same etch rate resulting from various combinations of HCl concentration and temperature, (a) 0.125 w/w% at 80 °C, (b) 0.25 w/w% at 60 °C, (c) 0.5 w/w% at 50 °C, (d) 1 w/w% at 40 °C, (e) 2 w/w% at 30 °C, and (f) 4 w/w% at 30 °C.

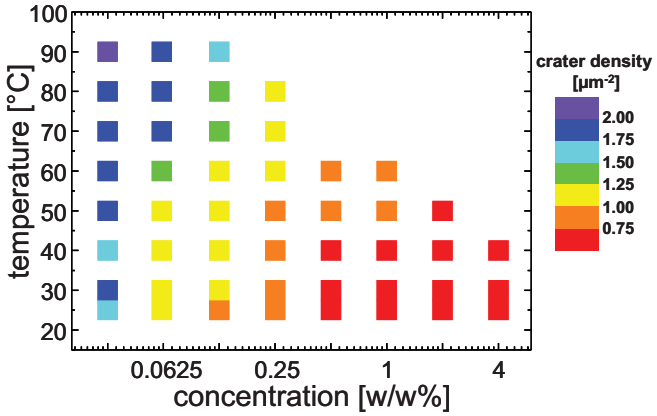

Figure 6.17: Crater density as a function of HCl concentration and temperature, as estimated by watershed algorithm of optical images.

crater area (a and b) as well as RMS roughness (c and d) as function of the acid temperature (a and c) and HCl concentration (b and d). The graphs exhibit data for the series with varying and constant etch rates. Figure 6.18 (e) gives the peak in angular distribution for a constant temperature as a function of HCl concentration. No clear trend was observed in the constant concentration series. Instead, the range of values observed are indicated at 0.125 w/w%.

It is important to note the difference in crater densities calculated from optical (Figure 6.17) and AFM (Figure 6.18 (a) and (b)) images; densities calculated from the AFM data are a minimum of three times larger than those calculated from optical images. As the temperature is increased or the concentration decreased, causing the crater density to increase, the discrepancy between AFM and optical analysis also increases up to a factor of 16. This difference arises from the fact that many of the craters have sizes below the limit of what an optical microscope can resolve, meaning that as the average crater size is reduced, a larger percentage of the craters cannot be optically resolved. The crater densities presented in Figure 6.17 therefore only show the general tendencies.

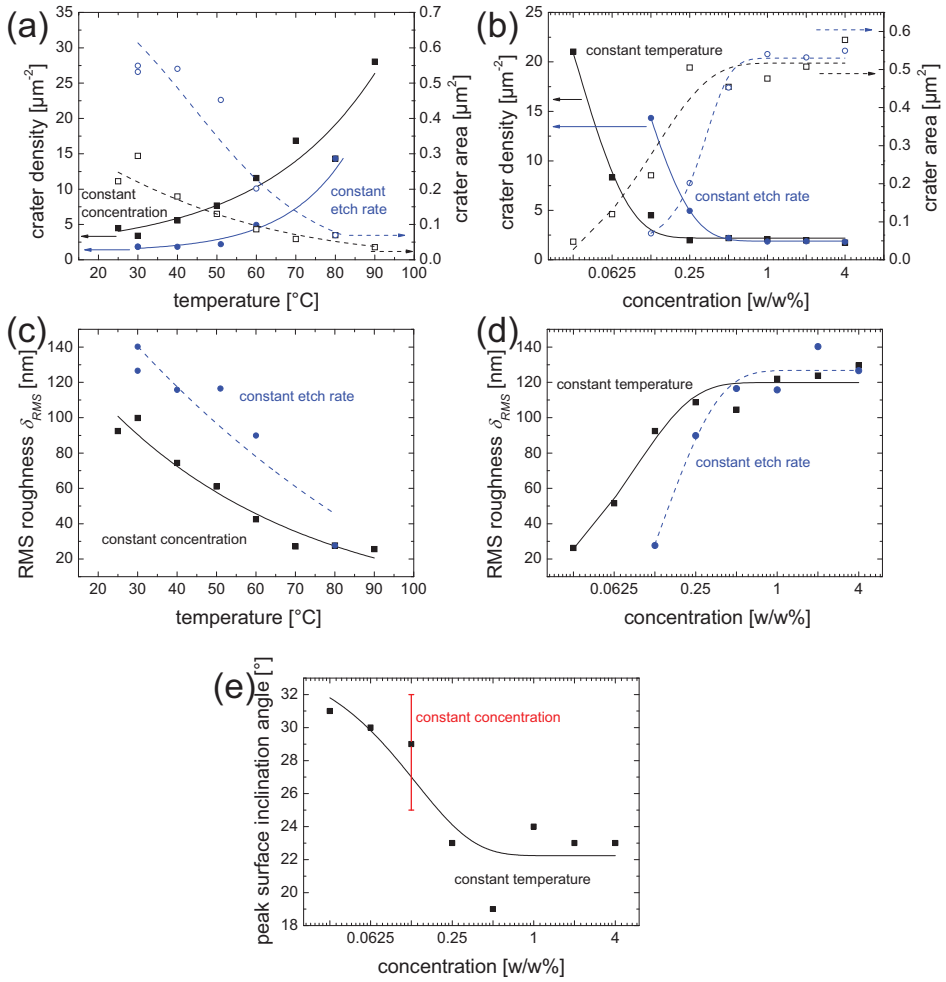

Figure 6.18: Analysis of AFM data. Crater density (solid lines and symbols) and area (dashed lines and open symbols) are given as a function of temperature and concentration (both black squares) are give in (a) and (b), respectively. RMS roughness as a function of temperature and concentration are given in (c) and (d), respectively. The crater density, area, and RMS roughness for the samples with a constant etch rate are also indicated in (a-d, blue circles). (e) The peak surface inclination angle as a function of concentration, the bars at 0.125 w/w% (red) indicate the range of values observed when etching at different temperatures.

From the Arrhenius equation (Section 2.5 (page 21)) it is not surprising that the etch rate increases with increasing temperature (see Figure 6.12). Likewise, from collision theory [95] it not surprising that etch rate increases with increasing concentration (see Figure 6.12), within these relatively low concentrations, as the collision rate between the hydronium ions and the etching sites will also be higher. The modification of resulting surface structures (see Figure 6.13) by HCl temperature and concentration, however, cannot be explained by these theories

alone and reveals some information on the etching mechanism as discussed later (see Chapter 7 (page 119)).

Analysis of optical images shows that increasing temperature yields surfaces with a much higher density of craters, while increasing concentration yields surfaces with lower density of craters (see Figure 6.13 and Figure 6.17). Like the optical images, AFM images show an increase in crater density from 3.4 to 28 μm^{-2}, decrease in crater size from 0.3 to 0.04 μm^2, and decrease in RMS roughness from 100 to 26 nm with increasing HCl temperature (Figure 6.14 and Figure 6.18 (a) and (c)). A decrease in crater density from 21 to 1.9 μm^{-2}, increase in crater size from 0.05 to 0.6 μm^2, and increase in RMS roughness from 26 to 130 nm with increasing HCl concentration is observed (Figure 6.15 and Figure 6.18 (b) and (d)). Additionally, the samples etched at a constant rate show similar trends, however the effect of temperature and concentration are compounded by the adjustment of the respective other parameter. Specifically, samples etched in HCl with high temperatures and low concentrations have a higher density of small craters than those etched in HCl with low temperatures and high concentrations (Figure 6.16 and Figure 6.18 (a-d)).

Decreasing HCl concentration additionally yields surfaces with smaller opening angles, as the peak in surface inclination angle distribution shifts to larger values, see Figure 6.18 (e). The same trend, however, was not observed in the temperatures series; instead the spread in measured values, also indicated in Figure 6.18 (e), may indicate the range of scattering error which arises from measuring at various sites.

To help explain the different densities of craters, a pseudo activation energy was calculated; 'pseudo' in that this activation energy is related to the etching of defects in ZnO:Al thin-film rather than etching ZnO itself. Zn-terminated ZnO does not generally etch in HCl, as craters only form at defects [33,34,197]. A pseudo activation energy was calculated for each of the concentration series by linearizing the etch rate data on an Arrhenius plot,

$$\ln k = \ln A_{col} - \frac{E_a}{R_{gas}}\left(\frac{1}{T}\right). \qquad \textbf{(6.1)}$$

The frequency factor (A_{col}) can be calculated from the y-intercept, and the activation energy (E_a) can be deduced from the slope. In general, the activation energy is the amount of energy that must be absorbed by a system to cause it to react. In this case, the pseudo activation energy is related to the amount of energy required for an etch to proceed vertically along a peculiar grain boundary. Thus, a decrease in the pseudo activation energy indicates an increase in the probability of etch progression and the subsequent crater formation.

The activation energies calculated are plotted as a function of concentration in Figure 6.19 (a). As HCl concentration is decreased, the pseudo activation energy is also decreased. The positive and negative error bars were calculated by examining the range of slopes (related to E_a) possible due to a one second error in etch time. Thus, the maximum pseudo activation energies were calculated from linearized (Arrhenius plot) data sets where the lower half of the temperature series were assumed to be underestimated and the higher half of the temperatures were assumed to be overestimated. By contrast, the minimum pseudo activation energies were calculated from linearized data sets where the lower half of the temperature series were assumed to be overestimated and the higher half of the temperatures were assumed to be underestimated. The error in etching times is very small for low concentrations as etch rates were quite slow, and increases with concentration as etching times were shortened. Additional uncer-

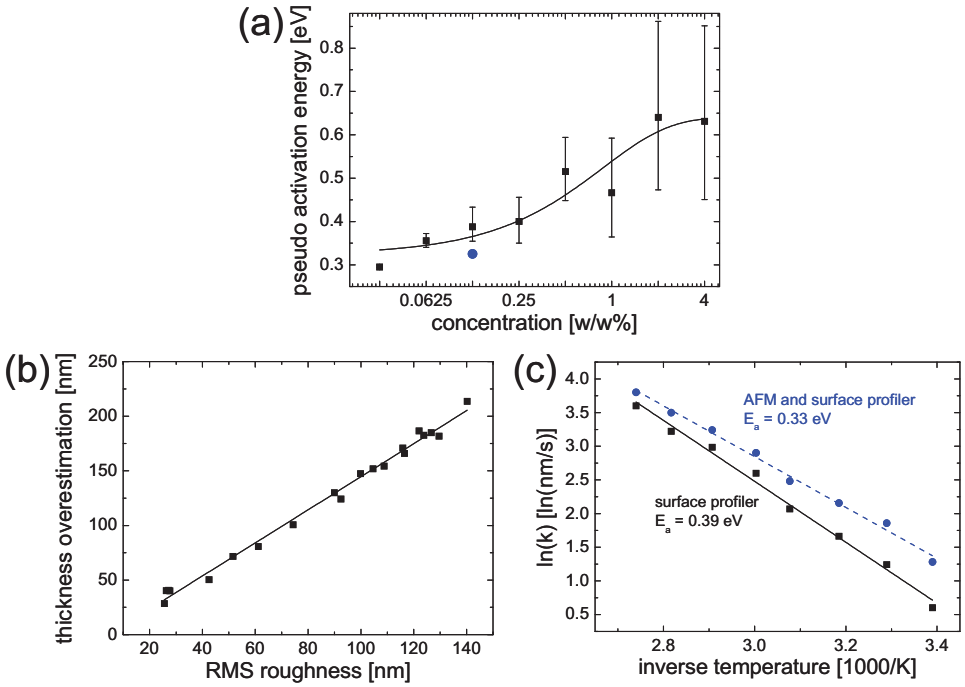

Figure 6.19: (a) Pseudo activation energy as calculated for each concentration from the individual temperature series. The blue circle indicates a corrected value for HCl 0.125 w/w% as determined by AFM data. (b) Thickness overestimation as determined from AFM images as a function of the RMS roughness. (c) Arrhenius plots to determine the activation energy of HCl 0.125 w/w% using the etch rates determined by surface profiler (black) and AFM and surface profiler (blue).

tainties come from the relatively small data set (three points) from which the activation energy is extrapolated at the highest concentrations (2 and 4 w/w%).

Another type of error in etch rate measurement is introduced by the different underestimations in removed thicknesses calculated by surface profiler (Section 3.4.1 (page 42)) for surface structures with various kurtoses. When the surface structures are small, the craters do not go very deeply into the film and the underestimation in etch rate by surface profiling is small. On the other hand, when the surface structures are large, the craters go hundreds of nanometers (see Section 6.1.1.3 (page 96)) into the film and the underestimation is larger. The thickness overestimation ($AFM_{95\%}$-AFM_{mean}, see Section 3.4.1 (page 42)) for all AFM measurements presented in this section is plotted as a function of RMS roughness in Figure 6.19 (b). Notice that despite the slight changes in peak angular distribution observed with different concentrations (Figure 6.18 (e)) the overestimation depends linearly on RMS roughness.

Using the corrected etched thickness values (Equation (3.1)), a new pseudo activation energy was calculated for the HCl 0.125 w/w% temperature series, see Figure 6.19 (a, blue circle) and (c, blue line). Since lower etching temperatures have larger etching error (Figure 6.19 (b)), etch rates increase in the low temperature (larger inverse temperature) region more than in the high temperature (smaller inverse temperature) region, see Figure 6.19 (c). This decrease in slope on the Arrhenius plot shows that activation energy shifts to lower values when more ac-

curate etch rates are used. It should be noted, however, that the example HCl concentration used (0.125 w/w%) is likely to have exhibited the largest shift in pseudo activation energy due to underestimations in etch rates. Since this concentration series showed the widest range of surface features (see Figure 6.13), it will exhibit the largest changes in slope on the Arrhenius plot.

6.2. Other Acids

Many different acids were used to texturize ZnO:Al substrates and, most of the acids examined behaved in a manner similar to that of HCl. This section will explore the surface features resulting from etching in various acids and mixtures of acids, as well as show that a weak organic acid (very different from HCl) can be used like HCl to control the density of etching sites by altering both the temperature and concentration.

6.2.1. Resultant Surface Morphologies

The morphology of polycrystalline ZnO:Al etched in acids and mixtures other than HCl are explored in this section. Standard ZnO:Al films were etched in the following acids, listed in order of strongest to weakest dissociation constants: sulfuric acid (H_2SO_4), nitric acid (HNO_3), phosphoric acid (H_3PO_4), and acetic acid (CH_3CO_2H). ZnO:Al substrates were also etched in *aqua regia*, one part HNO_3 and three parts HCl, which exhibits unique etching properties such as etching gold and other royal metals, from which the name is derived; and piranha, a mixture of H_2SO_4 and hydrogen peroxide (H_2O_2), which is often used for removing organic substances from surfaces.

SEM images of standard ZnO:Al etched in H_2SO_4, HNO_3, H_3PO_4, CH_3CO_2H, *aqua regia*, and piranha are shown in Figure 6.20 (a), (b), (c), (d), (e), and (f), respectively. Note that the removed thicknesses were not the same for all samples. The glass is visible in half of the figures, which leads to observation of larger craters, as higher densities of craters are seen earlier in the

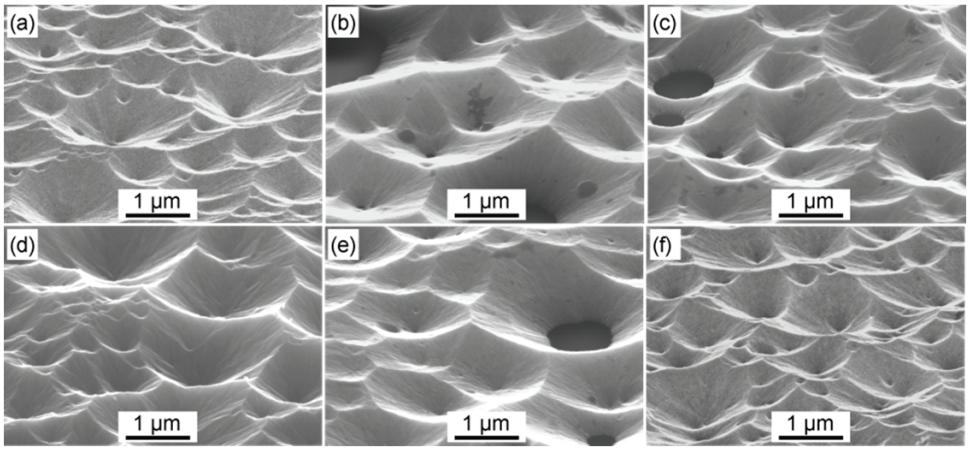

Figure 6.20: SEM images of standardly deposited ZnO:Al etched in (a) H_2SO_4, (b) HNO_3, (c) H_3PO_4, (d) CH_3CO_2H, (e) *aqua regia*, and (f) piranha.

etch process, see Section 6.1.1.3 (page 96). Additionally, in Section 6.1.2.2 (page 102) it was shown that different concentrations of HCl influence the number of etching sites, and so the crater density may also depend on the concentration of the acid used. Despite differences in acid strength (dissociation), concentration, and etch rates the surface features for all the etches appear similar, with relatively large (> 1 µm) features covering the surface. Further these craters appear to exhibit opening angles typical to that of HCl (between 120 and 135°, although they were not directly measured from these SEM images) [25].

6.2.2. Controlling the Etch Process

In Section 6.1.2.2 (page 102) it was shown that the density of etching points can be controlled by changing the HCl temperature and concentration. This section will show that the same holds true for CH_3CO_2H, which was shown to exhibit similar etching characteristics in the previous section. CH_3CO_2H was chosen because it is a very different acid than HCl, a weak organic acid with a huge anion, as opposed to a strong halogenide acid.

Standard ZnO:Al samples were etched in 0.25 w/w% CH_3CO_2H at various temperatures between RT (approximately 25 °C) and 90 °C. Etch times were adjusted such that approximately 150 nm of ZnO:Al was removed, as determined by surface profiler. Additionally, ZnO:Al sam-

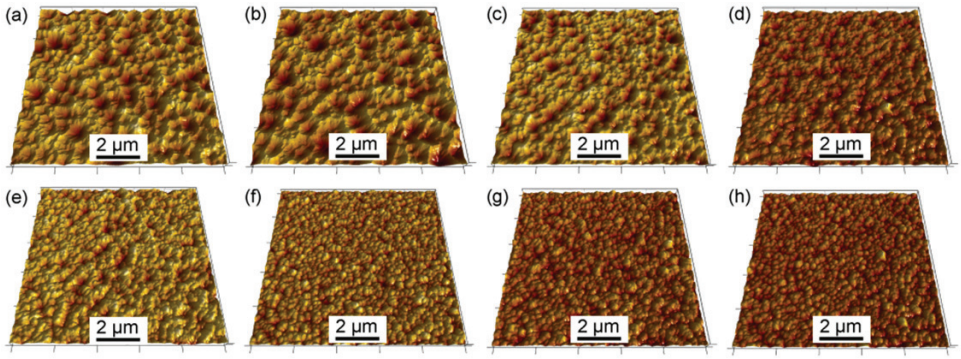

Figure 6.21: AFM images of standard ZnO:Al etch in 0.25 w/w% CH_3CO_2H at (a) 25, (b) 30, (c) 40, (d) 50, (e) 60, (f) 70, (g) 80, and (h) 90 °C.

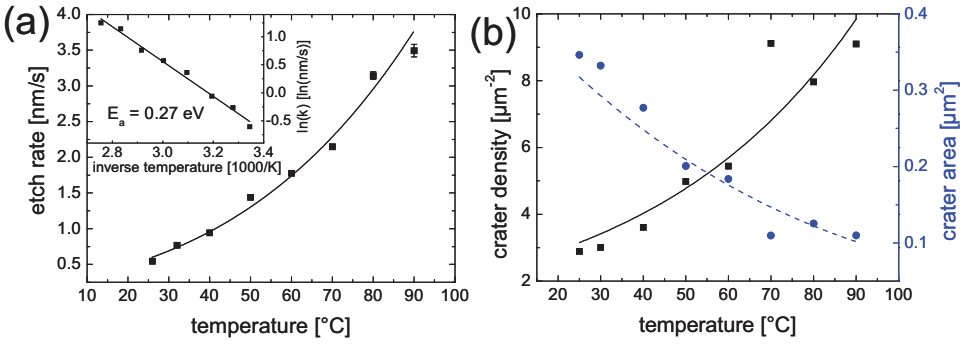

Figure 6.22: (a) Etch rate and (b) crater density and area as a function of etching temperature in 0.25 w/w% CH_3CO_2H. A pseudo activation energy is calculated in the inset to (a) by linearizing on an Arrhenius plot.

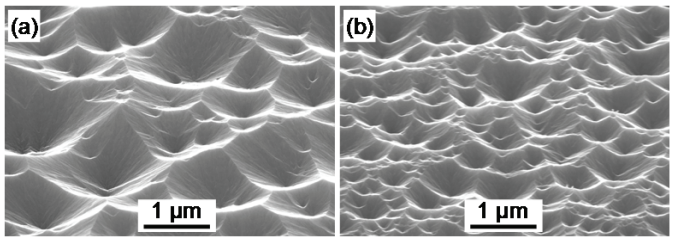

Figure 6.23: Standard ZnO:Al etched in (a) 25 and (b) 0.25 w/w% CH_3CO_2H.

ples were etched at RT in CH_3CO_2H with concentrations of 25 and 0.25 w/w%. Approximately 80 nm of ZnO:Al were removed from the samples, as determined by surface profiler.

AFM images of the ZnO:Al surfaces etched at various temperatures in 0.25 w/w% CH_3CO_2H are shown in Figure 6.21. The etch rate as determined by surface profiler and the crater density and size as determined by watershed analysis of the AFM images (Figure 6.21) are shown in Figure 6.22 (a) and (b), respectively. Figure 6.23 (a) and (b) show SEM images of the ZnO:Al after etching in 25 and 0.25 w/w% CH_3CO_2H, respectively.

As predicted by the Arrhenius equation (Equation (2.37)) and previously observed for etching in HCl solutions, increasing the temperature of the CH_3CO_2H solution increases the etch rate, compare Figure 6.12 to Figure 6.22 (a). A pseudo activation energy of 0.27 eV was calculated by linearizing on an Arrhenius plot (Equation (6.1)), see inset in Figure 6.22 (a). This activation energy is close to those observed for etching in HCl at low concentrations (Figure 6.19 (a)). Like HCl, the density of etching sites increases in CH_3CO_2H with increasing temperature, compare Figure 6.14 to Figure 6.21, and Figure 6.18 (a) to Figure 6.22 (b).

Additionally, the trend in concentration observed in HCl, larger features resulting from higher concentrations (see Figure 6.15 and Figure 6.18 (b)), also holds true for CH_3CO_2H, as the features resulting from an etch in 25 w/w% are at least twice the size of those etched in 0.25 w/w%, see Figure 6.23. Since the very different acids HCl and CH_3CO_2H show similar trends for controlling surfaces features, specifically higher temperatures and lower concentrations yielding higher crater densities, it seems likely that most acids, regardless of whether strong or weak, inorganic or organic, behave like HCl.

6.3. HF Etch

All acids examined in this work until now exhibited similar surfaces after etching, as well as similar trends in crater density dependence on temperature and concentration. This section examines the properties of hydrofluoric acid (HF), which exhibits unique etching behavior and concentration dependence as compared to the other acids. First the evolution of the HF etch on a standard ZnO:Al surface is explored, then ways to control the resultant surface features are presented.

6.3.1. HF Etch Evolution

Before examining the evolution of the HF etch, the etch rate of the standard HF concentration used throughout this work (1 w/w%) was measured and compared to that of 0.5 w/w% HCl.

The HF etch rate for standard ZnO:Al was calculated by etching a series of ZnO:Al films with approximately the same as-deposited thicknesses in 1 w/w% HF for times up to 150 seconds. Apart from the motion introduced during sample submersion and removal, the samples were statically etched. Thicknesses were measured using a surface profiler. Results showed a fairly linear decrease in thickness with increasing etch time for HF. At 1.3 nm/s, this etch rate is about one third that of 0.5 w/w% HCl, which has an etch rate of 4.0 nm/s (Figure 6.11).

Like the observation of the HCl etch evolution (Section 6.1.1 (page 91)), the repositioning of the sample between etching steps was enabled by a series of markers, see Section 3.4.2.3 (page 47). Due to the slower etch rate of 1 w/w% HF compared to 0.5 w/w% HCl, larger etching steps of ten rather than two seconds were taken up to a cumulative etch time of 40 seconds. Unlike the HCl evolution, this etch was not followed until the glass was reached. Instead, the longer-term general (rather than specific to one site) HF etch evolution on standard ZnO:Al samples etched in 1 w/w% HF for 70, 90, and 150 seconds were imaged by AFM.

Figure 6.24 and Animation 6.3 (located in Appendix (page 157)) show the HF etch evolution at the same location from the as-deposited state to 40 seconds of etching. Like the HCl etch (Section 6.1.1.3 (page 96)) stopping and restarting the HF etch does not change the etching sites and the fastest progressing craters dominate the surface. It seems likely that the catalyst for HF etching is also built into the film during growth and related to the gain boundaries.

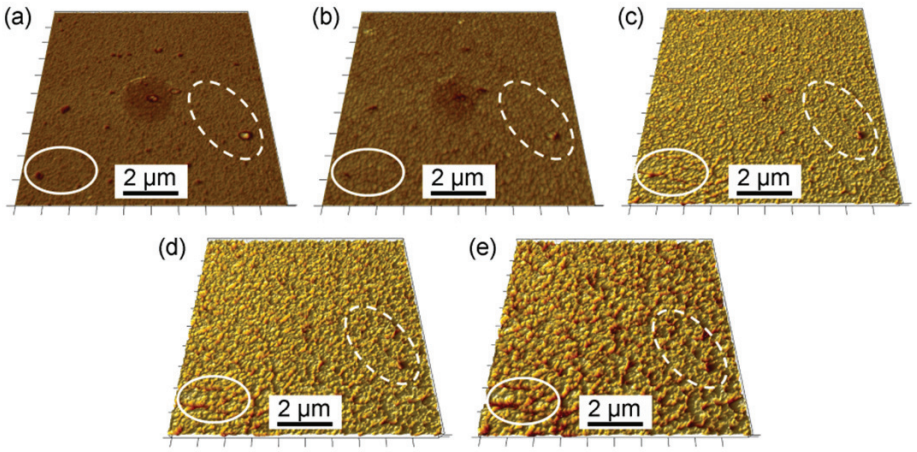

Figure 6.24: Same location on a standardly deposited ZnO:Al substrate (a) as-deposited, and after (b) 10, (c) 20, (d) 30, and (e) 40 seconds of cumulative etching in 1% w/w% HF. Ellipses indicate the same locations on all AFM scans.

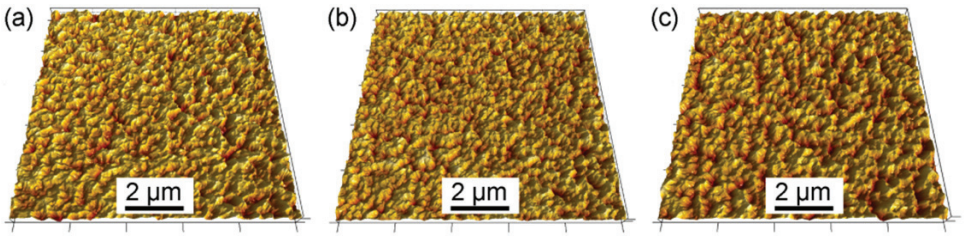

Figure 6.25: AFM images of ZnO:Al etched in HF for (a) 70, (b) 90, and (c) 150 seconds.

Interestingly, in the as-deposited state and after ten seconds of etching the remnants of the photolithographically deposited grid are visible in the center of the AFM scans, see Figure 6.24 (a) and (b). As discussed in Section 3.4.2.3 (page 47), AFM scans were generally made at the site of defects in the grid, as they were easily identifiable and provided larger possible scan areas. It is unclear why a remnant of the grid was visible on this sample but not on the other samples where the same realignment process was used; one possible reason is that this defect was created by sonication during acetone lift-off rather than during exposure or development. Defects created during exposure or development come from a thin layer of photoresist between the ZnO:Al and the evaporated silver, thus buffering the substrate during silver deposition. In Section 6.1.1.1 (page 92), it was stated that the deposition processes and presence of the silver grid did not alter the etching process. This can also be seen here, as after 20 seconds of HF etching (Figure 6.24 (c)) no affects of the silver grid deposition remain. Further, the etch progresses is the same in the center of the AFM images (at the site of grid silver deposition) as elsewhere.

AFM images of HF-etched surfaces after longer etch times are shown in Figure 6.25. With longer etching times, the surface features do not change much; only the general film thickness is reduced. Statistics from the AFM images of the short-term (Figure 6.24) and long-term

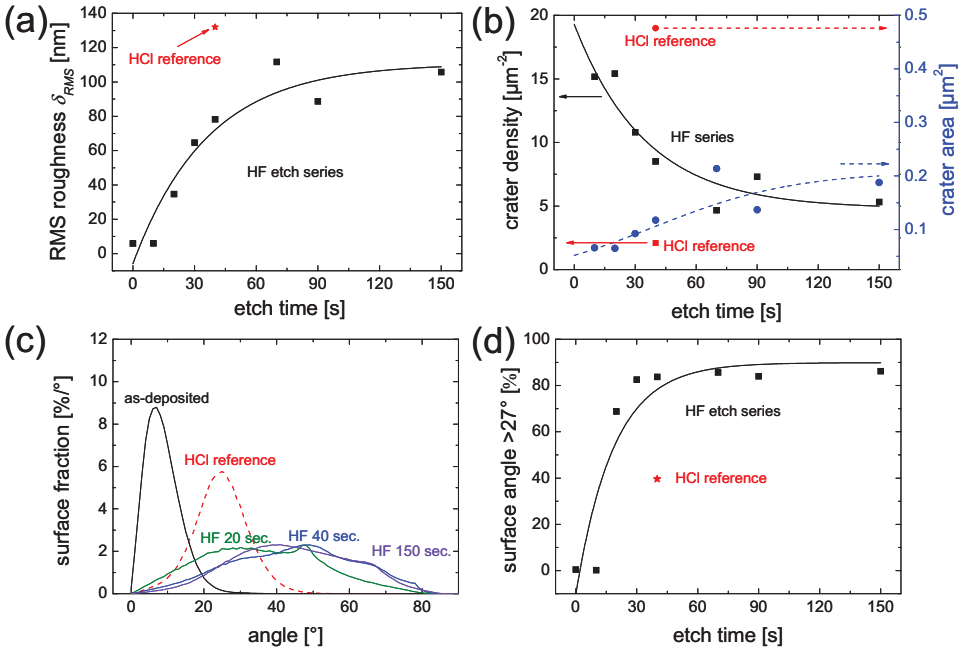

Figure 6.26: Statistics derived from the AFM images of ZnO:Al etched in HF for different lengths of time. (a) RMS roughness as a function of etch time, a standard HCl reference is indicated by the red star. (b) Crater density (black squares left axis) and area (blue circles right axis) as a function of etch time, standard HCl reference is indicated by the same symbols in red. (c) Histogram of the surface angular distribution in 1° increments for ZnO:Al as-deposited (black), etched for 20 (green), 40 (blue), and 150 (violet) seconds in HF, as well as an HCl reference etch (red dashed). (d) Percentage of surface exhibiting angles larger than 27° after HF etching as a function of etching time, HCl reference is indicated by a red star.

(Figure 6.25) etch evolutions are given in Figure 6.26. A red star or curve represents the corresponding data of an HCl-etched standard ZnO for reference (40 seconds of etching in 0.5 w/w% HCl).

The RMS roughness is shown in Figure 6.26 (a) to increase with increasing HF etch time. The RMS roughness is fit by an asymptotic function approaching a value around 100 nm. Despite the smaller crater size, the RMS roughness is 75% that of a reference HCl etched substrate (at 130 nm).

Figure 6.26 (b) shows the crater density and average crater area as a function of HF etch time. The average crater area increases asymptotically to a saturation value around 0.2 µm², while crater density decreases. The final density of craters is more than a factor of two higher than that of a reference HCl standard etch. Like the HCl etch, a survival-of-the-fastest mechanism takes place during crater growth, though the crater density stabilizes at higher values. Thus, the fully evolved surface structure is seen with a smaller removed thickness than that of HCl. This is seen by comparing the AFM image after 40 seconds of etching (Figure 6.24 (e)) to those of 70, 90, and 150 seconds of etching (Figure 6.25), recalling that the etch rate in 1 w/w% HF is only one third that of 0.5 w/w% HCl.

Figure 6.26 (c) shows the angular distribution of surface angles in the as-deposited state and after 20, 40, and 150 seconds of HF etching. The angular distribution after 40 second of HCl etching is also included for reference. The as-deposited and HCl reference etch exhibit relatively Gaussian distributions in angles centered about 7° and 26°, respectively. HF etching, on the other hand, yields angular distributions with poorly defined peaks and very broad FWHM values of about 40°. The peak position shifts slightly during the etch evolution up to about 40 seconds of etching.

That the general features are sharper after HF etching than HCl etching is clearly seen by comparing the percentage of the surface features possessing angles larger than 27° (the peak angle from the standard HCl etch [25]), see Figure 6.26 (d). On fully evolved HCl and HF surfaces, 40% and 85% of the angles were steeper than 27°, respectively. This shift in the angular distribution to higher values is what allows high RMS values in combination with higher crater density. This was not the case when crater density was increased by increasing HCl temperature or decreasing HCl concentration, compare Figure 6.26 (a) to Figure 6.18 (c) and (d).

To summarize, etching in HF gives unique surface features as compared to all other acids examined. These unique features seem to arise for two reasons: first, the HF etch has a higher density of etching sites than the HCl etch (see Figure 6.26 (b)); second, the HF etch yields much sharper features (see Figure 6.26 (c) and (d)).

6.3.2. Controlling the Etch Process

It was observed in Section 6.1.2 (page 101) that there are many ways to control the HCl etch process, including sample or solution dynamics, and changing the solution concentration and temperature. This section explores ways to control the etch features by the unique properties of the HF process. Due to the inherent dangers of working with HF [198], only concentrations will be varied as a way to control the etch process. Additionally, due to the different etching characteristics of HF and HCl, several mixtures of the two acids are examined as possible way to control the etching process. The results in this section are focused on the principle variation of features observed by microscopy.

6.3.2.1. HF Concentration

Etching characteristics of HF at various concentrations was tested by etching standardly deposited ZnO:Al substrates in HF solutions with concentrations of 1, 0.5, 0.25, and 0.125 w/w%. All substrates were etched for 120 seconds, rinsed with DI water, and blown dry with nitrogen. The etch rates were determined by surface profiler, and surface morphology was imaged by SEM.

Etch rates of 1.4, 1.2, 1.1, and 1.1 nm/s were calculated for the 1, 0.5, 0.25, and 0.125 w/w% HF solutions, respectively. Notice that a reduction in HF concentration by a factor of eight leads to only a 25 % decrease in etch rate, thus a new series with a constant removed thickness was not necessary. This small effect on etch rate is likely due to the self-buffering nature of weak acids, due to the concentration dependent clustering of HF molecules [199]. As the HF concentration is decreased a higher percentage of the HF molecules dissociate, yielding an only slightly decreased etch rate.

Figure 6.27 (a), (b), (c), and (d) give SEM images of the ZnO:Al substrates etched in HF with concentrations of 1, 0.5, 0.25, and 0.125 w/w%, respectively. With decreasing HF concentration, the crater density and mean surface angle appear to decrease and become more HCl-like, although crater diameters are about half that of the standard HCl etch. The relationship between concentration and crater density for HF etching is the opposite of that observed in HCl (Figure 6.15) and CH_3CO_2H (Figure 6.23), where decreasing concentrations yielded surfaces with higher densities of craters.

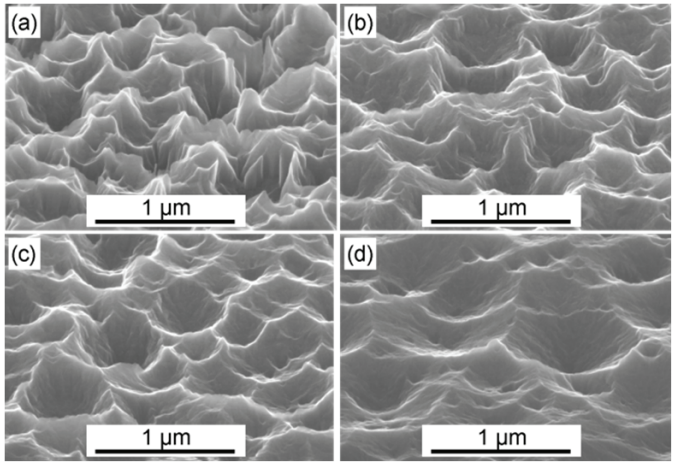

Figure 6.27: SEM images of standard ZnO:Al etched in (a) 1, (b) 0.5, (c) 0.25, and (d) 0.125 w/w% HF.

6.3.2.2. HF:HCl Mixtures

Since HF and HCl etch the surface in different ways (small-sharp and large-gentle craters, respectively) surfaces with feature size between these may be obtained by etching in various combinations of HF and HCl. To examine this possibility, standard ZnO:Al films were etched in mixtures of HF and HCl, where the HF concentration was held constant at 1 w/w%, while

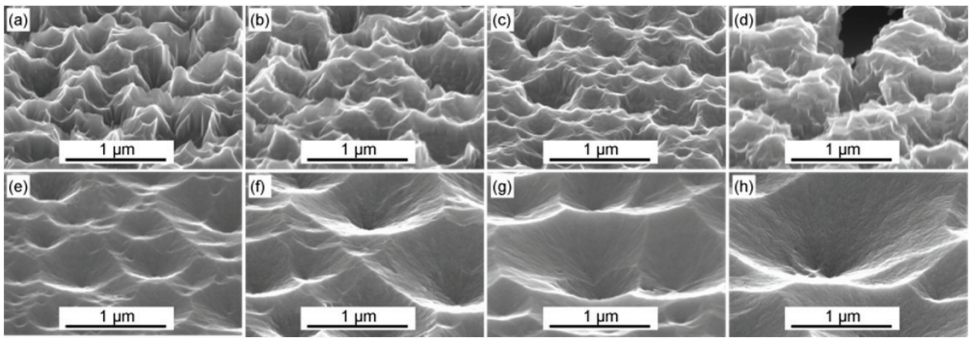

Figure 6.28: Standard ZnO:Al films etched in various mixtures of HF w/w%:HCl w/w%; (a) 1:0, (b) 1:0.25, (c) 1:0.375, (d) 1:0.5, (e) 1:0.625, (f) 1:0.75, (g) 1:1, and (h) 0:0.5.

the HCl concentration was varied from 0 to 1 w/w% in 0.125 w/w% steps. Etching times were adjusted such that approximately 150 nm of the originally 800 nm thick film was removed, as determined by a surface profiler. Surfaces were subsequently characterized by SEM.

Figure 6.28 shows SEM images of the standard ZnO:Al etched in various mixtures of HF and HCl. Notice that the surface features can be varied from small to large with crater sizes ranging from 300 nm (no HCl) to 2 µm (only HCl), see Figure 6.28 (a) and (h). By increasing the HCl concentration the size of the crater is gradually increased.

The transition of crater opening angles and size, however, is not smooth and it appears that one etching process (HF or HCl) dominates the other. Specifically, Figure 6.28 (b), (c), and (d) with HCl concentrations equal to or below 0.5 w/w% have steep features more similar to that of the HF etch alone (Figure 6.28 (a)), while Figure 6.28 (e), (f), and (g) with HCl concentrations equal to or above 0.625 w/w% have smoother features more similar to that of the HCl etch alone (Figure 6.28 (h)).

6.4. Summary

In this chapter the evolution of the HCl etch was examined both in the short- and long-term by examining the initial points of etching and the etch progression through the whole sample. From these experiments, it was concluded that certain peculiar defects are the catalyst for crater formation, and that these defects are built into the film during the deposition process. These defects seem to be related to grain boundaries, since the grain boundaries and points of crater formation decrease the thicker the film is grown. Additionally, the initial sites of etching seem to be related to depressed regions in the as-deposited film, which may form at areas with the most disorder. Etching ZnO:Al newly deposited onto previously etched films showed new crater formation in the new ZnO:Al; however, as the newly deposited ZnO:Al was etched away, etching sites return to the previous points. This confirms that the sites of accelerated etching are built into the film. HCl solution and sample dynamics, concentration, and temperature were shown to change the ZnO:Al etch rate. The temperature and concentration were also shown to change the density of craters by up to a surprisingly high factor of ten.

All other acids examined, except HF, showed etching behavior similar to HCl, including similar densities of craters and preferential crater opening angles. CH_3CO_2H, a weak organic acid,

exhibited the same trends as HCl, a strong inorganic acid, with regard to the increase in crater density with increasing temperature or decreasing concentration.

HF etching was shown to exhibit unique etching characteristics, specifically higher crater densities and sharper features. Like HCl (and the other acids examined), changing the concentration changed the density of craters. In HF, though, the relationship was the inverse: decreasing HF concentration leads to a decrease in the density of craters, as well as smoother features. Using the different etching behaviors of HF and HCl, it was shown that the density of craters could be controlled by using various mixtures of HF and HCl to etch craters with sizes between 300 nm and 2 µm.

7. Etching Model

Chapter 6 presented the results of etching in various acids. This chapter uses the etching trends observed to come up with a model for the etching process in ZnO:Al. First, the etching behaviors observed by others and in the previous chapter are summarized and a few experiments are suggested to clarify etching behavior. Next, the results of the additional etching experiments are reported. Finally, a model for the etching process is presented.

7.1. Etching Trends so Far

The following list summarizes the polycrystalline ZnO etching trends observed so far in the literature and in the previous chapters of this work.

- Increasing ZnO thin-film compactness by sputtering with low deposition pressures, high deposition rates, high substrate temperatures, or high dopant concentrations decreases the density of craters formed by HCl etching [13,24-26,29,191-193].
- The density of etching sites from various chemical (both acidic and basic) and physical (ion beam) increase or decrease together, depending on the sputtering conditions [31].
- Initial density of etching sites decreases with increasing film thickness (Section 6.1.1.2 (page 92)).
- The density of etching sites decreases with post-deposition annealing [120].
- Fastest progressing etch sites occur at depressed regions on as-deposited surface (Section 6.1.1.2 (page 92)).
- Stopping and restarting etch process does not alter etching sites (Section 6.1.1.3 (page 96)).
- Etch sites often run through whole film. (Section 6.1.1.3 (page 96)).
- While new ZnO:Al deposited on previously etched ZnO:Al has new etching sites, original points return when new ZnO:Al is etched away (Section 6.1.1.4 (page 99)).
- Increasing HCl temperature or decreasing concentration increases the density of etching sites (Section 6.1.2.2 (page 102)).
- Most acids, both strong and weak as well as organic and organic, exhibit HCl-like etching behavior (Section 6.2.1 (page 109)).
- CH_3CO_2H showed similar temperature and concentration dependence as HCl, with an increase in crater density with increasing temperature or decreasing concentration (Section 6.2.2 (page 110)).
- Etching in HF yields a higher density of etch sites than HCl (Section 6.3.1 (page 111)).

- Crater walls resulting from HF etching are generally steeper than those resulting from HCl etching and do not exhibit a strongly preferred angle of inclination (Section 6.3.1 (page 111)).
- The relationship between crater density and HF concentration is opposite that of HCl, as crater density decreases with decreasing concentration (Section 6.3.2.1 (page 115)).
- Crater density can be controlled by etching in various mixtures of HF:HCl (Section 6.3.2.2 (page 115)).
- Crater wall tends to be either HCl- or HF-like (Section 6.3.2.2 (page 115)).

From these observations a few physical reason for the observed etching behavior were proposed. First, from the observation the initial etching points (Section 6.1.1.2 (page 92)) and the long-term etch evolution (Section 6.1.1.3 (page 96)) it was proposed that peculiar grain boundaries are the catalyst for accelerated etching. They are peculiar in that the bulk of the grain boundaries are not etched so rapidly. Second, from the observations that the etching sites tend to correspond to the depressed regions in the film (Section 6.1.1.2 (page 92)), that both chemical and physical etching densities vary together [31], and that the density of craters depend on the compactness of the film [13,24-26,29,191-193], it was proposed that the peculiar grain boundaries correspond to sites of strong disorder. Third, from the observation that the number of etching sites can be increasing or decreasing by changing etchant temperature or concentration (Section 6.1.2.2 (page 102) and Section 6.2.2 (page 110)), as well as etching solution (Section 6.3.1 (page 111)), it was proposed that grain boundaries can have different potentials for etching.

To test these proposed parts of an etching model, a few additional experiments are made to contradict or confirm the assumptions and give validity. To check if the density of etching sites corresponds to sites of strong disorder, samples are imaged at the same location following etching in KOH then HCl. To see if defects can have different potentials for etching, single crystal ZnO samples are etched in different acids, at different temperatures, and at different concentrations. Finally, to check if grain boundaries could be the source of accelerated etching, TEM images of slightly etched films are taken.

7.2. Etching in KOH then HCl

It has been observed that the density of craters resulting from HCl, KOH, and ion beam etches increase or decrease together on a given ZnO:Al surface [31]. To better understand the relationship between craters that form in basic and acidic solutions, the HCl etch evolution is examined on a previously KOH etched surface.

The stepwise etch-imaging process described in Section 3.4.2.3 (page 47) was used to examine how the HCl etch evolves on a KOH etched substrate. First, a standardly deposited ZnO:Al film was etched in 30 w/w% KOH for 400 seconds. Subsequent etching steps were performed in an HCl 0.5 w/w% solution for cumulative etching times of 5, 10, and 20 seconds; all etching steps were performed at RT. The etching process was stopped by rinsing the sample with DI water and drying with nitrogen. Film thicknesses were determined by surface profiler, and surface topography was measured at the same location after each etching step by AFM. To com-

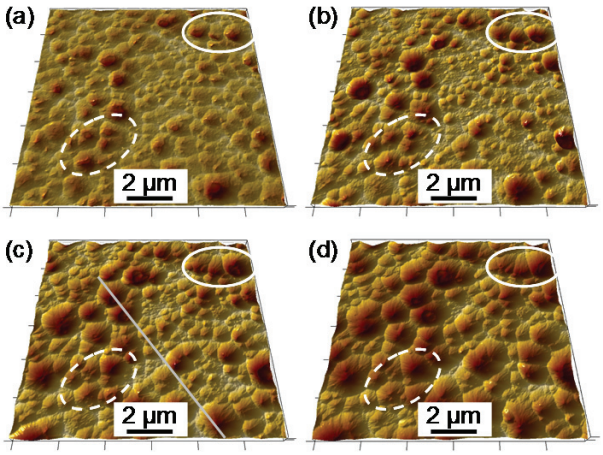

Figure 7.1: AFM images at the same location on a standardly deposited ZnO:Al surface after 400 seconds of etching in 30 w/w% KOH, and an additional 5, 10, and 20 cumulative seconds of etching in 0.5 w/w% HCl are shown in (a), (b), (c), and (d), respectively. Gray line in (c) indicates the approximate location of the line scans shown in Figure 7.2. Also see Animation 7.1.

Table 7.1: Statistical evaluations of the AFM data presented in Figure 7.1.

etching step	RMS roughness δ_{RMS} [nm]	crater density [µm^{-2}]	average crater size [µm^2]	peak in angular dist.[°]
KOH 400 seconds	49	2.7	0.37	10
HCl 5 seconds	84	3.4	0.29	15
HCl 10 seconds	102	2.5	0.39	26
HCl 20 seconds	116	1.6	0.62	24

pare line scans from the different etching steps, the maximum AFM value was assumed to correspond to the maximum thickness measured by surface profiler. In Section 6.1.1.3 (page 96) it was noted that the deviation between surface profiler and AFM was less than 30 nm.

AFM images taken at the same location on a standardly deposited ZnO:Al surface after 400 seconds of KOH etching, and after an additional 5, 10, and 20 cumulative seconds of HCl etching are shown in Figure 7.1 (a-d), respectively, as well as Animation 7.1 (located in Appendix (page 157)). Notice that the craters formed by KOH etching continue when subsequently etched in HCl. The RMS roughness, crater density, average crater area, and most prevalent surface angle as calculated from the AFM images in Figure 7.1 are listed in Table 7.1. For the shorter HCl etching times (five and ten cumulative seconds) the crater density and average crater size is very close to that of the KOH etched surface, as the same locations are etched. For the longest HCl etching time, the crater density decreased, thus increasing the average crater area. This, however, is not due to different etching sites between HCl and KOH, but rather the merging of craters as some craters progress faster than others (see Section 6.1.1.3 (page 96)). The RMS roughness of a KOH etched surface is relatively small at 49 nm but increases with increasing HCl etch time up to 116 nm, it follows that an increase in roughness without changing the number of craters can only occur if the craters exhibit generally steeper angles, as seen in Table 7.1.

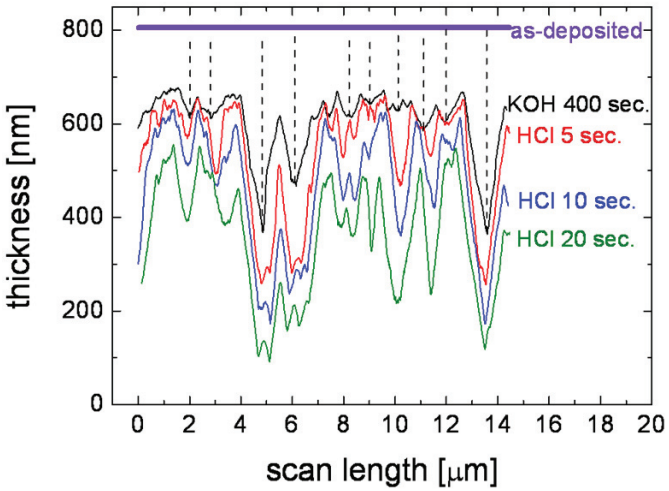

Figure 7.2: As-deposited film thickness and AFM line scans at approximately the same location at each etching step. The as-deposited thickness is marked in violet. AFM line scans after 400 seconds of etching in 30 w/w% KOH, and an additional 5, 10, and 20 cumulative seconds of etching in 0.5 w/w% HCl are indicated by black, red, blue, and green lines, respectively.

Line scans at approximately the same location after each etching step are given in Figure 7.2. The location of the line scan with respect to the AFM images is indicated by the gray line in Figure 7.1 (c); the approximate as-deposited thickness is also indicated. The dashed markers in Figure 7.2 indicate dips in KOH etched surface. Notice that these dips evolve into higher height contrast craters with increasing HCl etching.

Since ZnO is an amphoteric oxide, it is not surprising that it etches in both basic and acidic solutions [31,33]. It is interesting, however, that these solutions attack the same points (see Figure 7.1 and Figure 7.2). Since in single crystals, the etching of O- and Zn-terminated surfaces are prohibited in bases and acids, respectively, and is only possible at defects [33]. The fact the same locations are etched in basic and acidic solutions gives validity to the hypothesis that craters form at sites with larger disorder, as these low density regions may be more easily penetrated by both hydronium and hydroxide ions.

7.3. Etching Single Crystal ZnO

In Chapter 6 it was shown that the density of craters on a polycrystalline ZnO:Al surface could be controlled by etching in different acids, at different temperatures, and at different concentrations. This section examines if the same holds true for single crystal ZnO samples. The etching process for single crystal ZnO is well understood, with craters forming on the Zn-terminated side only at defects in the crystal [33,34,197]. This more simple system is first used to compare the effects of etching in HCl to those of HF. Then the effects of etching in HCl with extremely different temperatures and concentrations are examined.

7.3.1. HF and HCl

Single crystal ZnO with polished (001) planes were purchased from CrysTec GmbH. To check if 0.5 w/w% HCl and 1 w/w% HF etch the same locations, confocal microscope images of the Zn-terminated side were taken after etching in one of the acids for 120 seconds, and again (at the same location) after etching in the other acid for an additional 120 seconds. Further, the general evolution of craters on single crystal ZnO was observed by etching samples in either the HCl or HF solutions for 60, 120, 240, and 480 seconds. Five confocal microscope images with an area of 158x158 μm^2 were taken of each etch time and acid. The number of craters and width of each crater was measured on each of these images.

As expected, no general etch rate was detected by surface profiler on the Zn-terminated side of the single crystals for acid etching, indicating etching only occurred at defects [33,34,197]. Figure 7.3 (a) and (c) are confocal microscope images of the ZnO single crystals etched for 120 seconds in HCl and HF, respectively. The craters on the crystal etched in HCl have widths ranging from less than 1 µm to about 7 µm in width, while the craters on the sample etched in HF exhibit a significantly more narrow width distribution between 2.5 and 6 µm. The same locations after a second etching step in HF and HCl, respectively, are shown in Figure 7.3 (b) and (d). Notice that the acids do attack the same defects, albeit at different rates.

Figure 7.4 presents a statistical evaluation of the craters on ZnO single crystals etched for 60, 120, 240, or 480 seconds in HCl or HF. Figure 7.4 (a), (b), and (c) give, respectively, the crater density, average width, and relative standard deviation in width (standard deviation divided by average crater width). The densities of craters given in Figure 7.4 (a) seem to asymptotically increase over time for HCl and remain constant for HF. This, however, is somewhat misleading, since in Figure 7.3 it was observed that the acids etch the same points, indi-

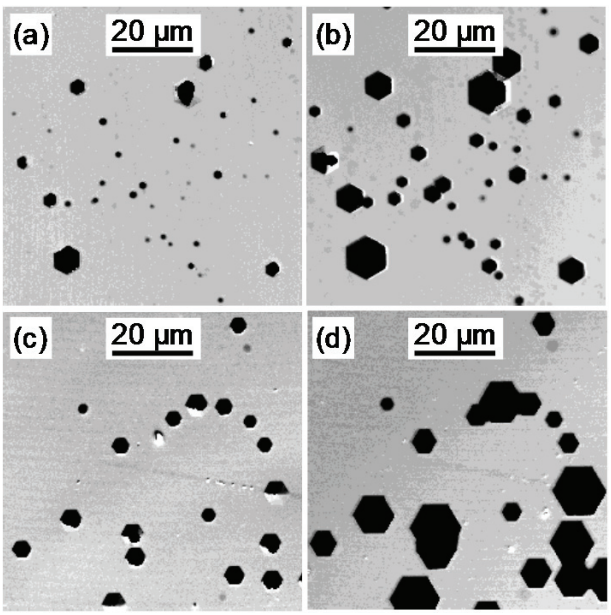

Figure 7.3: Confocal microscope images of Zn-terminated ZnO etched in (a) HCl, (b) HCl followed by HF, (c) HF, and (d) HF followed by HCl.

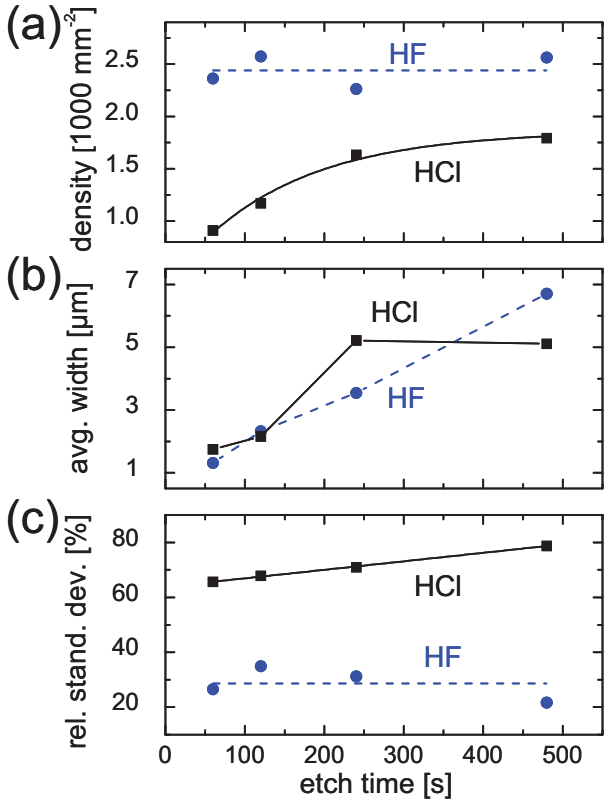

Figure 7.4: Crater (a) density, (b) average width, and (c) relative standard deviation of ZnO single crystals etched in HCl (■, solid) and HF (●, dashed) as a function of etch time.

cating the density of craters should in fact be the same. This underestimation in HCl etch density is likely caused by the wide spread in crater sizes, as many craters were too small (less than one micrometer) to be clearly resolved by confocal microscopy while other large craters overtake and hide more slowly progressing craters, see Figure 7.3 (a). More craters growing to sizes large enough to be resolved by confocal microscope could explain why the average crater size decreased between 240 and 480 seconds of etching, while it increased fairly linearly for the HF etch, see Figure 7.4 (b). The relative standard deviation plots, Figure 7.4 (c), clearly illustrate that the widths of the HF etched craters are more uniform than those of an HCl etch, as the ratio of standard deviation to average crater width remains close to 30 % for HF, while it increased linearly in time from 60 to 80 % for HCl.

The more homogeneous etching of ZnO single crystals in HF than HCl (Figure 7.4 (c)) can be used to explain the higher densities of craters observed in the HF etching of polycrystalline ZnO:Al, see Section 6.3.1 (page 111). To do so, it is assumed that the peculiar defects on a given polycrystalline ZnO:Al surface etch at a wide variety of rates in an HCl solution. This appears to be the case for single crystal ZnO, see Figure 7.4. As survival-of-the-fastest crater growth progresses, many craters are overtaken, effectively merging into one, thus reducing crater density. On the other hand, it is assumed that the peculiar defects on a given polycrystalline ZnO:Al surface etch at more homogeneous rates in an HF solution. This appears to be

the case for single crystal ZnO, see Figure 7.3 and Figure 7.4. Therefore, as survival-of-the-fastest crater growth progresses, a smaller number of craters are overtaken, leading to an apparently higher density of craters.

7.3.2. HCl Temperature and Concentration

To test if the density of craters on single crystal ZnO samples exhibit the same temperature and concentration dependencies as those observed on polycrystalline materials (section 6.1.2.2 (page 102)), ZnO single crystals were etched under some of the extreme conditions seen in Figure 6.13. Specifically, to test the effects of temperature single crystals were etched in 0.125 w/w% HCl at RT (~25 °C) and 90 °C. To test the effects of concentration single crystals were etched at RT in 0.03125 and 4 w/w% HCl solutions. Since no general etching occurs on the Zn-terminated side, etching times were adjusted such that an equivalent of 600 nm would have been removed from a polycrystalline ZnO:Al substrate, as calculated from the etch rates seen in Figure 6.12. The etching parameters of temperature, concentration, and time are given in Table 7.2. After etching the O-terminated side of the single crystals was covered with an absorbent dye and five optical microscope images with an approximate area of 80x105 μm^2 were taken of each of the four samples. The number of craters and width of each crater was measured on each of these images. To give a better overview, a single image, with an approximate area of 390x520 μm^2, was taken of each of the four samples.

The larger scale optical images, 390x520 μm^2, of the ZnO single crystals etched in solutions with extremely different temperatures and concentrations are shown in Figure 7.5. The crater

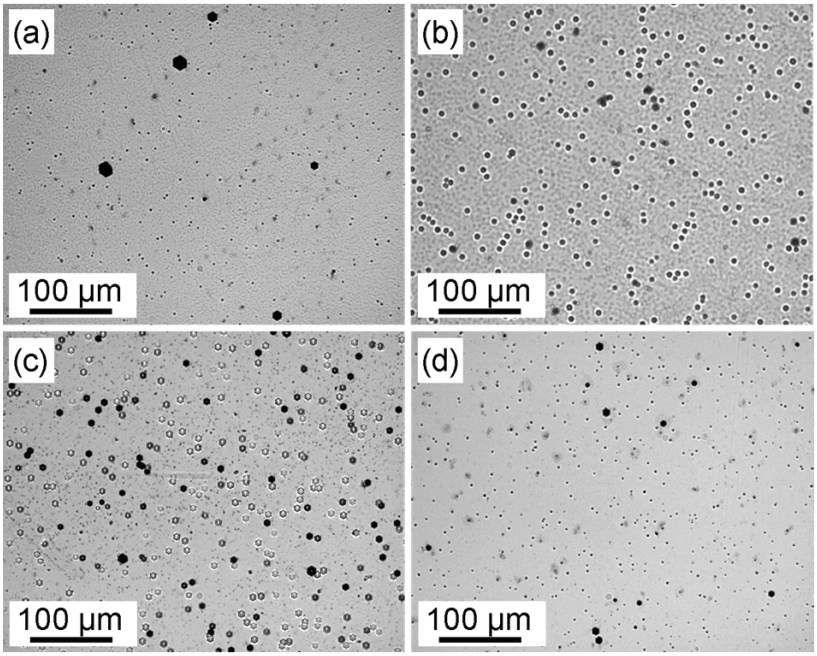

Figure 7.5: Optical microscope images of Zn-terminated ZnO single crystals etched at (a) 25 °C in 0.125 w/w% HCl, (b) 90 °C in 0.125 w/w% HCl, (c) 25 °C in 0.03125 w/w% HCl, and (d) 25 °C in 4 w/w% HCl.

Table 7.2: HCl etching solution parameters and resultant crater statistics for single crystal ZnO etched at various temperatures and concentrations. As calculated from optical images, like those seen in Figure 7.5.

etch parameters	Figure 7.5 (a)	Figure 7.5 (b)	Figure 7.5 (c)	Figure 7.5 (d)
temperature [°C]	25	90	25	25
concentration [w/w%]	0.125	0.125	0.03125	4
etch time [s]	330	16	1560	35
crater statistics				
crater density [1000 mm^{-2}]	6.1±2.9	8.6±0.8	8.4±0.5	6.9±0.6
average crater width [µm]	2.0±0.6	4.5±0.2	5.8±1.1	1.5±0.1
relative standard deviation [%]	71±27	19±10	33±18	98±13

density, average crater width, and relative standard deviation in width (standard deviation divided by average crater width) calculated from five 80x105 µm^2 areas are given in Table 7.2. The standard deviation in values between the five individual areas was used to estimate the range of accuracy in the measurements; it is given as a plus or minus following each statistic.

Despite having the O-terminated side coated with an absorbent dye, slightly different marbling effects are seen in the background of the optical images (Figure 7.5). Increasing the etching temperature from RT to 90 °C increases the homogeneity of the craters. This is seen by comparing the range of crater sizes in Figure 7.5 (a) to (b), or by comparing the relative standard deviation (ratio between standard deviation and average crater width) which decreases from 71 to 19 % with the increase in temperature (Table 7.2). Similarly decreasing the concentration from 4 via 0.125 to 0.03125 w/w% increases the homogeneity of the crater sizes. This is seen by comparing the range of crater sizes in Figure 7.5 (d) to (a) to (c) or by comparing the relative standard deviation which decreases from 98 via 71 to 33 % with decreasing concentration (Table 7.2).

A lower crater density was calculated on the less homogeneously etched ZnO crystals in Figure 7.5 (a) and (d) than the more homogeneously etched ZnO crystals in Figure 7.5 (b) and (c), see Table 7.2. As discussed in the previous section, this probably arises from some small craters not being counted because the craters were too small to resolve with an optical microscope. Notice also that the crater density calculated for the relatively homogeneous HF etches were around 2500 mm^{-2} (Figure 7.4), while the crater density calculated for the relatively homogeneous high temperature or low concentration were around 8500 mm^{-2} (Table 7.2). This factor of more than three in crater density is possibly due to the different ZnO crystal batches from which the samples originated.

In this section it has been shown that increasing the temperature or decreasing the concentration of HCl leads to more homogeneous etching of defects on the Zn-terminated side of ZnO single crystal. In the previous section it was proposed that the more homogeneous etching of defects in HF than HCl is what gave a perceived higher density of craters, as fewer craters are over taken in the survival-of-the-fastest method of crater growth. Similarly, the perceived higher density of craters observed when etching polycrystalline ZnO:Al samples in HCl at high temperatures or low concentrations (Section 6.1.2.2 (page 102)) may arise from the more homogeneous etching of the peculiar defects.

7.4. TEM of Initial Etching Sites

To further examine the relationship between grain boundaries and the initial site of crater formation, planar ZnO:Al samples and cross-sectional ZnO:Al lamella were examined by TEM. ZnO:Al was standardly deposited onto CG and a silicon wafer. Both samples were etched in a 0.125 w/w% HCl solution for two seconds, to distinguish initial crater formation from as-deposited structures (see Section 6.1.1.2 (page 92)). Planar TEM samples (Figure 3.8 (a)) were made from the ZnO:Al deposited on CG by grinding, dimple grinding, and argon ion milling the glass side of a substrate. Cross-sectional TEM samples (Figure 3.8 (b)) were prepared from the ZnO:Al sample deposited onto silicon using the AFM assisted lamella preparation technique presented in Section 3.4.6 (page 53). The silicon substrate was used to avoid charge buildup when imaging with the SEM or thinning with the FIB. In Section 4.3 (page 70) it was observed that similar craters form on ZnO:Al deposited onto Si as CG; it is assumed that these craters form by the same mechanism. TEM images were taken in the bright and various dark fields using an electron accelerating voltage of 200 kV.

Figure 7.6 (a) and (b) contains bright field images at two locations on a planar TEM sample. Recall from Section 3.4.6 (page 53) that the contrast in this type of image corresponds to a mass-thickness contrast [151]. Thus, the brightest areas correspond to thin or amorphous regions, while dark areas correspond to thick or strongly scattering crystalline regions. The shallow craters etched into the ZnO:Al surface will appear as bright regions, such craters are indicated in Figure 7.6 (a) and (b). Additionally, Figure 7.6 (c) displays a bright field image of a single crater in higher resolution. Notice that the center of the crater (the brightest region) is in all cases close to or on a triple grain boundary. It is important to note, however, that the grain boundaries also appear brighter since they are less organized regions and therefore diffract less of the incoming electrons [151].

Figure 7.7 (a-c) give three different dark field images of a planar sample at the same location. Recall from Section 3.4.6 (page 53) that in a dark field image, only grains that scatter electrons to a particular solid angle are observed. A composite image of the three different dark fields and the bright field at the same location are shown in Figure 7.7 (d) and (e), respectively. The locations of two craters are indicated in each of the five images. The dark field images confirm that the crater centers are made of at least three differently oriented regions, and thus at least three different grains. Some regions remain dark in the composite image (Fig-

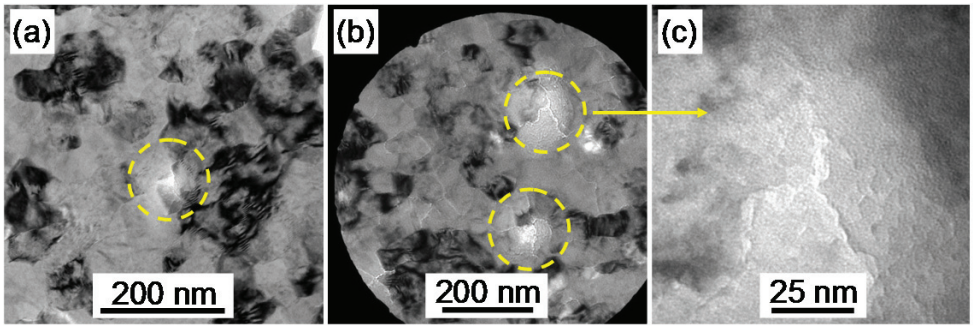

Figure 7.6: Bright field TEM images of slightly etched planar ZnO:Al samples. Images (a) and (b) were taken at different locations, while (c) is a higher magnification of a single crater in (b).

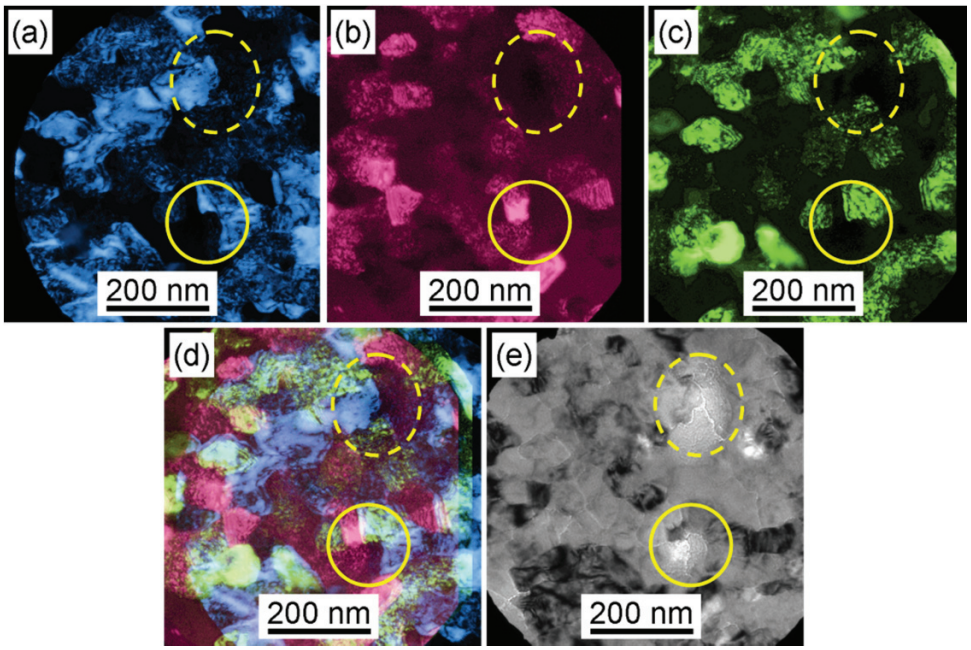

Figure 7.7: Dark field TEM images of three different reflections on a planar view prepared ZnO:Al sample colored blue, red, and green in (a), (b), and (c), respectively. (d) A composite image of the three different reflections in (a), (b), and (c). (e) Bright field image of the same location. Ellipses mark approximately the same location in each image.

ure 7.7 (d)). These remaining dark regions only indicate electrons were not scattered to these three particular solid angles, thus the regions could be amorphous or disorganized regions such as grain boundaries or even voids, areas cropped off by the aperture, or grains with a different orientation.

Three different dark field images of the cross-sectional lamella prepared through the center of a crater are shown in Figure 7.8 (a-c). A composite of the three dark field images and a bright field image at the same location are shown in Figure 7.8 (d) and (e), respectively. The center of the crater is made of at least three differently oriented regions, and thus at least three different grains. Notice that one of the grains ends exactly at the center of the crater, see Figure 7.8 (b). This is expected if a triple grain boundary was at the center of the crater, since geometrically no matter how the sample is rotated one grain will always end at the center when viewed from the side.

Planar TEM measurements indicated triple grain boundaries were at least close to or even incident with the center of crater formation, and a cross-sectional TEM measurement confirmed that such a grain boundary was in fact exactly at the center of a crater. However, due to the small number of samples measured (about ten planar and only one cross-sectional), the results do not provide conclusive proof that certain triple grain boundaries are the source of accelerated etching. That said, none of the TEM measurements made contradicted the idea that regions of high disorder, such as triple grain boundaries, are the catalyst of accelerated etching and it is assumed to be generally valid.

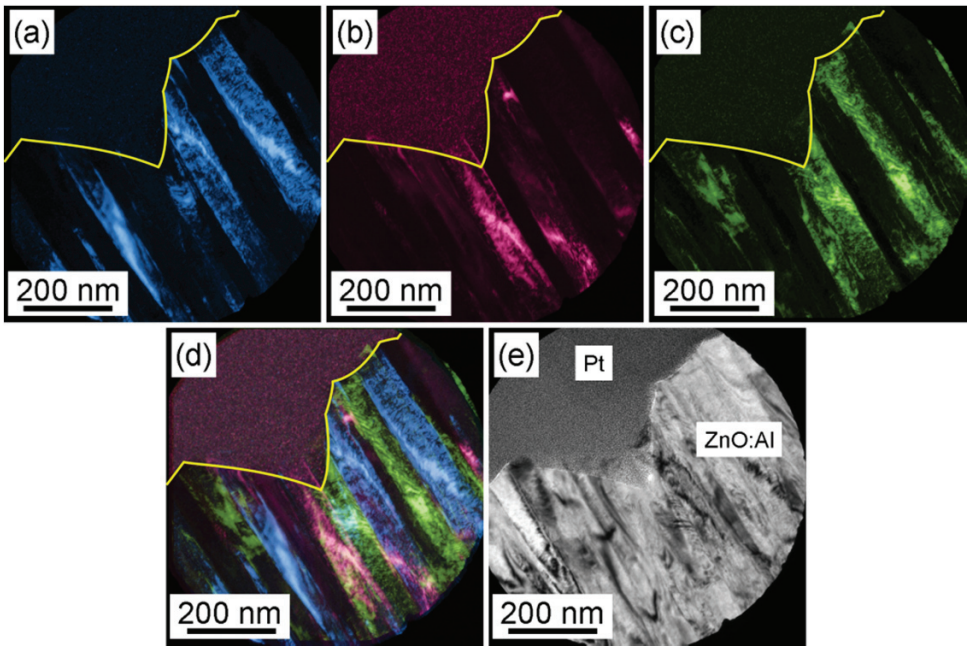

Figure 7.8: Dark field TEM images of three different reflections on a ZnO:Al lamella sample colored blue, red, and green in (a), (b), and (c), respectively. (d) A composite image of the three different reflections in (a), (b), and (c). (e) Bright field image of the same location. The crater is outlined in yellow in (a-d).

7.5. Polycrystalline ZnO:Al Etching Model

In Chapter 6 new results on etching of ZnO were reported, and in the previous sections additional etching trends were described to have a closer look on the details of the etching process. Specifically, it was shown that both basic and acidic solutions etch the same location. Defects on ZnO single crystals have different potentials for etching, and this potential for etching can be changed by altering the temperature or concentration of the etch solution and by using different acids. Characterization of both planar and cross-sectional TEM images showed triple grain boundaries to be a likely crater center. These observations as well as those listed in Section 7.1 (page 119) were used to formulate three postulates for a polycrystalline ZnO:Al etching model. This section will proceed as follows: a postulate will be stated, the etching trends which lead to the postulate will be outlined, then possible physical explanations for these etching behaviors will be given.

(1) Sputtered ZnO:Al is grown Zn-terminated. This (001) plane, like Zn-terminated single crystals, does not etch, however, every grain boundary has potential to etch as other planes are accessible to the etchant. This etching potential depends on the compactness of the grain boundary, less compact (more porous) regions having a higher potential for etching. The potential varies not only across the surface, but also perpetuates vertically

through the film, although the potential may vary vertically. Figure 7.9 (a) gives a schematic representation of this postulate.

Thornton *et al.* developed a model for sputtered metals that relates the substrate temperature and sputtering pressure to film density [32]. For sputtered ZnO:Al films the density is similar for different deposition conditions, so Kluth *et al.* extended the model to ZnO:Al films and attributed a specific compactness to each film without any specific information on what this means [25]. It has often been reported that increasing this "compactness" decreases the density of craters formed on an ZnO thin-film by HCl etching [13,24-26,29,191-193]. Similarly, in Section 6.1.1.2 (page 92) it was observed that the density of initial etching sites decreases with increasing ZnO:Al film thickness. Etching behaviors such as these can be explained by grain boundaries with less order having higher potential for etching than those with more order. A physical explanation for this behavior is that less-ordered grain boundaries can be more easily

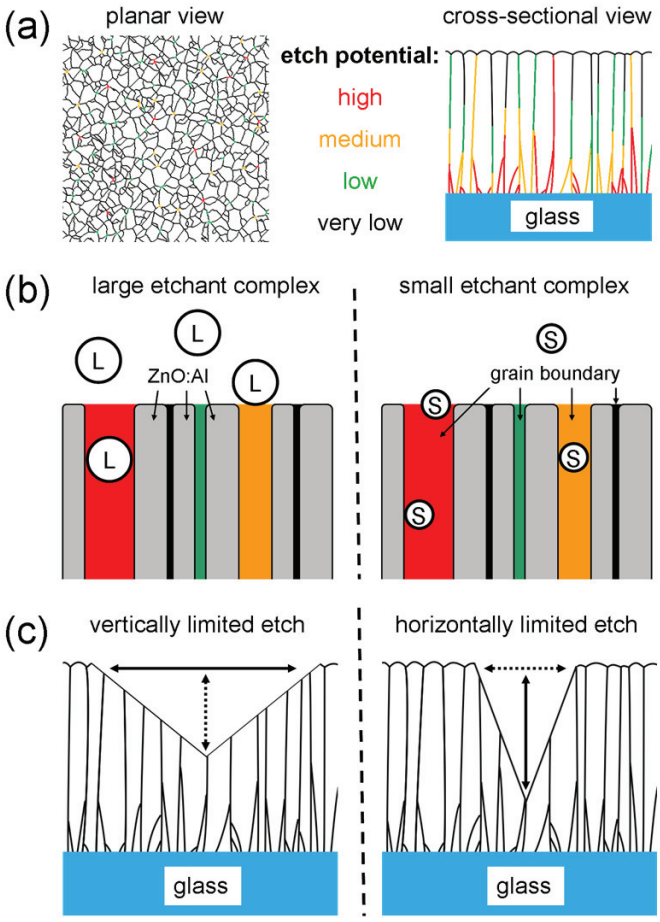

Figure 7.9: Schematic diagrams of the three etching model postulates. (a) Every grain boundary has potential for etching. (b) The etchant solution defines a threshold for etching. (c) Vertical and horizontal etch rates are defined by the solution.

penetrated by the etching agent allowing etching on a generally Zn-terminated polycrystalline ZnO surface (see Section 4.4 (page 72)).

In Section 6.1.1.3 (page 96), Section 6.1.1.4 (page 99), and Section 7.2 (page 120), it was observed that stopping and restarting the etching process does not affect the etching sites, etching returns to the same points after etching even after a new ZnO:Al deposition, and that basic and acidic solutions etch the same locations. From these observations it can be concluded that the sites of accelerated etching are built into the films during deposition rather than catalysis by surface adsorbates. A physical reason for this etching behavior is related to the columnar growth of sputtered ZnO:Al. After the nucleation and survival-of-the-fastest growth periods, the column size remains fairly constant (Section 4.2.2 (page 67)), and peculiar grain boundaries, such as some triple grain boundaries (Section 7.4 (page 127)), are simply perpetuated with increased thickness as further growth does not create more nuclei, but thickens the previously grown crystals in an epitaxial-like manner (Section 4.3 (page 70)).

In Section 6.1.1.2 (page 92) it was seen that the sites of the fastest etching were often related to depressed regions in the as-deposited films. Physically, sites with the highest disorder are energetically unfavorable for the incoming atoms. Thus, disordered regions will not grow as quickly leaving depressed regions.

(2) The etchant solution and conditions define an etching threshold. Grain boundaries with etching potentials above the threshold are more actively etched. This threshold depends on the size and the concentration of the etchant complex involved. Figure 7.9 (b) gives a schematic representation of this postulate.

In Section 6.1.2.2 (page 102) and Section 6.2.2 (page 110) it was observed that the density of craters increased with increasing HCl and CH_3CO_2H temperature, respectively. Thus, increasing temperature lowers the threshold, allowing more grain boundaries with lower etch potentials to be etched, as confirmed by single crystal ZnO etching (Section 7.3.2 (page 125)). A possible physical explanation relates to the size of the ionic clusters formed by the hydronium ion together with neutral water molecules [200]. At lower temperatures large clusters are formed with the surrounding polar water molecules to delocalize the positive charge [201,202]. As the solution temperature is increased the weak hydrogen bonds are broken, effectively making a smaller ion. The smaller water-hydronium clusters are then able to penetrate smaller and thus more grain boundaries than the larger water-hydronium clusters, leading to a higher density of craters, see Figure 7.9 (b).

Similarly, in Section 6.1.2.2 (page 102) and Section 6.2.2 (page 110) it was observed that the density of craters increased with decreasing HCl and CH_3CO_2H concentration, respectively. Thus, decreasing the concentration lowers the threshold, allowing more grain boundaries with lower etch potentials to be etched, as confirmed by single crystal ZnO etching (Section 7.3.2 (page 125)). A possible physical explanation relates to the self-limiting nature of what would be the most actively etched regions in a higher concentration solution. Due to the extremely low hydronium concentration, when an ion is used up only a very small pH gradient is formed. Thus the ion is not readily replenished by another which would continue the accelerated etching. Instead, the ions find more localized sites where slightly accelerated etching occurs, creating a higher density of craters.

In Section 6.3.1 (page 111), etching in HF was shown to create a higher density of craters than HCl or other acids. Like the temperature and concentration dependence in HCl, single crystal ZnO etching showed that the higher density of craters arises from the more homogeneous etching of defects (Section 7.3.1 (page 123)). Since dissociated HCl and HF molecules will both form large water-hydronium clusters, the physical explanation does not solely depend on the size of the etching agent, but also the tendency of these molecules to dissociate. HCl and HF have acidic dissociation constants of $<< 0$ (total dissociation) and 3.2, respectively [203]; thus, in an HCl solution practically all of the solved HCl molecules form the large water-hydronium clusters. On the other hand, in an HF solution, at a given time many of the molecules are not dissociated and remain relatively small as compared to the water-hydronium clusters. These small molecules can penetrate more defects. If the HF molecule then dissociates, it can form a crater at a grain boundary where the penetration of water-hydronium clusters is sterically prohibited.

That the unique etching characteristics come from both the small and weak nature of the HF molecule is also seen in the etching characteristics of CH_3CO_2H (Section 6.2 (page 109)). Like HF, this weak acid does not fully dissociate, but due to the large size of the molecule smaller grain boundaries cannot be penetrated before dissociation. Like HCl, etching is limited to the largest peculiar defects and the surface. This could explain why all acids or mixtures of acids observed in Section 6.2.1 (page 109) showed HCl-like etching behavior, as the acids or mixtures were either strongly dissociating or too large to give etching densities as high as HF when not dissociated.

It should be mentioned that this is a very simplified view of the chemical interactions taking place, and the true nature of HF in a solution remains a strongly debated topic [204]. The dissociation constant of HF is anomalously small, Giguere and Turrell suggested that HF may actually dissociate strongly, however, the interaction with water is so strong that the hydronium and fluoride ion are bound as a pair, effectively leading to HF being a weak acid [205]. If this is the case, the hydronium-fluoride ion complex formed may be effectively smaller that the water-hydronium clusters formed when the ions are separated.

(3) The vertical and horizontal etch rates are also defined by the solution. The vertical etch rate progresses along peculiar grain boundaries and is limited by the nature of the grain boundary, as well as, the mobility and size of the etching agents. The horizontal etch rate is limited by the concentration of etchants and the crystal structure. If the vertical etch rate is the limiting etch rate, the characteristic crater opening angles are formed as defined by the (101) plane. On the other hand, if the horizontal etch rate is the limiting factor, steeper opening angles are exposed. Figure 7.9 (c) gives a schematic representation of this postulate.

In Section 6.1.1.3 (page 96) it was shown that as a crater evolves, a dominant angle of inclination appears. This characteristic opening angle is assumed to be related to preferential etching to the (101) plane [25,31,33,34]. For surfaces such as this, the etching process is limited vertically, see Figure 7.9 (c). A physical reason for this etching behavior is similar to those discussed in Postulate (2) and relate to the size of the etching agent. In the vertically limited case, large etchants cannot penetrate deeply into the ZnO:Al film and reactions are generally limited to the surface. Thus, when etching occurs at the peculiarly large grain boundaries, the etch will

expand horizontally very quickly until the (101) planes are reached.

Etching in HF (Section 6.3.1 (page (111)), on the other hand, does not exhibit a characteristic opening angle, and sharper features are observed. For surfaces such as these, the etching process is limited horizontally, see Figure 7.9 (c). In this case, reactions are not limited to the surface as the small and less likely to dissociate HF molecules can penetrate the ZnO:Al film before dissociating. Since many of HF molecules in the etchant solution are not dissociated, the horizontal etch rate along the (101) plane is limited.

In Section 6.3.2.1 (page 115), it was observed that reducing HF concentration leads to more HCl-like features with larger craters and characteristic opening angles. This effect can be attributed to the presence of a larger number of single HF molecules in the case of low concentrations. As the concentration is reduced, the probability of the formation of large, hydrogen bonded HF clusters decreases due to the presence of less HF. Therefore, a relatively higher percentage of the HF molecules dissociate. As the ratio of dissociated molecules to non-dissociated molecules increases, the probability for the presence of protonated water clusters is higher, and a more HCl-like etching behavior can be expected: the comparably large water-hydronium clusters are more limited to reactions at the surface and the larger peculiar grain boundaries.

8. Solar Cell Applications

While chapters 4-7 focused mainly on the physical properties of ZnO:Al, this chapter introduces engineering applications, utilizing the knowledge obtained in the other chapters to improve silicon thin-film solar cell performance. Improvements include optimizing the crater size for amorphous silicon solar cells, creating modulated surfaces for high-efficiency tandem cells, and texturizing compact ZnO:Al films for microcrystalline silicon cells effectively.

8.1. Optimizing the Crater Size for Amorphous Silicon Thin-Film Solar Cells

Many different ways to control the density of craters on a texturized ZnO:Al surface were presented in Chapter 6, including etching in HCl at various temperatures and concentrations (Section 6.1.2.2 (page 102)), in various mixtures of HF:HCl (Section 6.3.2.2 (page 115)), and in various concentrations of HF (Section 6.3.2.1 (page 115)). The following two sections use the ability to control the crater size with various HF:HCl mixtures and HF concentrations to optimize the surface structure for amorphous silicon thin-film solar cells.

8.1.1. HF:HCl Mixtures

It was shown in Section 6.3.2.2 (page 115) that etching in mixtures of HF:HCl yielded craters with shapes between those of the large relatively smooth craters resulting from etching in HCl (0.5 w/w%) only, and those of the small jagged craters resulting from etching in HF (1 w/w%) only. In this section the optimum mixture of HF:HCl for amorphous silicon solar cells on a standardly deposited ZnO:Al substrate is investigated.

Standard ZnO:Al films (Section 3.1.2.1 (page 38)) were etched in mixtures of HF:HCl, where the HF concentration was held constant at 1 w/w%, and the HCl concentration was varied between 0.25 and 1 w/w% by a steps of 0.25 w/w%. Etches were also performed in solutions of only HCl (0.5 w/w%) and HF (1 w/w%). Etching times were adjusted so that approximately 150 nm of the originally 800 nm thick film was removed, as measured by surface profiler. Reflection, total transmission, and diffuse transition measurements on the variously etched films were performed using an optical spectrometer with an integrating sphere. Diiodomethane was used for refractive index matching during absorption determination. Additionally, to determine the effect the HF etch has on the CG substrate, a substrate was imaged by AFM after 180 seconds of etching.

The active amorphous silicon layers were deposited using PECVD (Section 3.3 (page 41)). Back contacts consisting of approximately 80 nm of ZnO and 700 nm of silver were deposited by RF-sputtering and thermal evaporation, respectively. Test cells had an area of 1 cm^2. The current density-voltage characteristics of the solar cells were measured at 25 °C under white (AM 1.5) illumination and under filtered red (OG 590), and blue (BG 7) illumination.

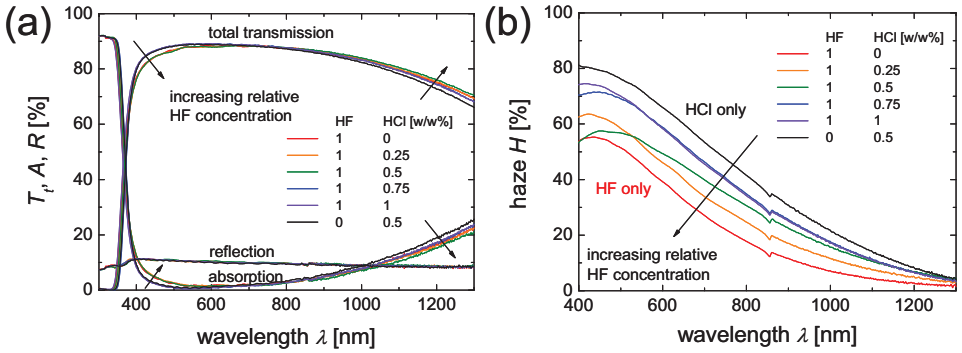

Figure 8.1: (a) Total transmission (T_t), absorption (A), reflection (R), and (b) haze (H) as a function of wavelength (λ) for the various HF:HCl mixtures.

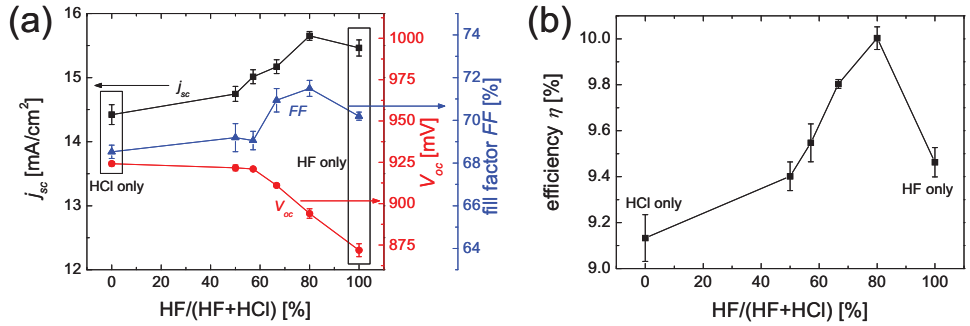

Figure 8.2: (a) The short circuit current density (j_{sc}, black), open circuit voltage (V_{oc}, red), and fill factor (FF, blue) of amorphous silicon thin-film solar cells as a function of the relative concentration of HF in the etching solution. (b) Efficiency (η) as a function of the relative concentration of HF in the etching solution.

Figure 8.1 shows optical results for the ZnO:Al films etched in various mixtures of HF:HCl. The total transmission, absorption, and reflection are shown as a function of wavelength and etching solution in Figure 8.1 (a). As the relative concentration of HF (HF/(HCl+HF)) is increased, the total transmission decreases in the shorter wavelength region (400-600 nm) and increases in the longer wavelength region (700-1300 nm). Since the reflection remains the same for all samples, the absorption showed the opposite trends as total transmission. The haze (diffuse transmission/total transmission) as a function of wavelength and etching solution is shown in Figure 8.1 (b). The haze decreases across the entire measured spectrum with increasing relative HF concentration.

Surface profiler measurements showed that the CG was etched at a rate of about 1 nm/s in the 1 w/w% HF solution. AFM analysis of a CG surface after etching in HF for 180 seconds exhibited a root mean square (RMS) roughness of 0.9 nm.

The amorphous silicon cell had a total thickness of 375 nm. The results of the amorphous solar cells on ZnO:Al surfaces etched in various mixtures of HF:HCl are shown in Figure 8.2. The average characteristics (short circuit current density, open circuit voltage, and fill factor) of the five best current density-voltage curves for each HF:HCl mixture are given in Figure 8.2 (a) as a function of the relative HF concentration. A standard deviation of the five cells

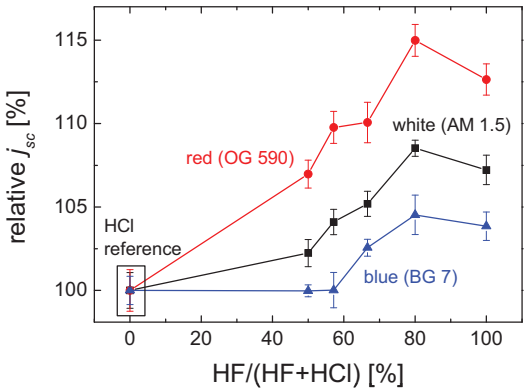

Figure 8.3: Short circuit current density (j_{sc}) of amorphous silicon thin-film solar cells as a function of the relative concentration of HF in the etching solution as compared to the HCl reference under white (AM 1.5), red (OG 590), and blue (BG 7) filtered illumination.

is indicated in the positive and negative direction. The short circuit current density and fill factor show similar trends, increasing from 14.4 mA/cm^2 and 68.5 % to 15.7 mA/cm^2 and 71.5 %, a respective increase of eight and five percent. Increasing the relative HF concentration further to 100 % (only HF) decreased the short circuit current density and fill factor to 15.5 mA/cm^2 and 70.2 %, respectively. The open circuit voltage, on the other hand, shows almost the exactly opposite effect, decreasing five percent from 924 to 872 mV with increasing relative HF concentration. The average efficiency of the five best cells on the substrates etched in various mixtures of HF:HCl are given as a function of the relative HF concentration in Figure 8.2 (b). Increasing the relative HF concentration from zero (HCl only) to 80 % increased the solar cell efficiency from 9.1 to 10.0 %, a relative increase in efficiency of ten percent. Increasing the HF concentration further to 100 % decreased the solar cell efficiency to 9.5 %.

To explore the origins of the increase in short circuit current density further, the solar cells on ZnO:Al etched in various HF:HCl mixtures were also characterized under red and blue illumination. Figure 8.3 gives the short circuit current density relative to the HCl only substrate as a function of relative HF concentration and illumination. The current increased under both red and blue illumination, with a maximum increase of 15 and 5 %, respectively. The maximum for both coincide with the overall maximum short circuit current density at a relative HF concentration of 80 %.

The RMS roughness (less than one nanometer) introduced to the CG by HF etching is negligible and assumed to decrease further with decreasing relative HF concentration [206]. The changes in transmission, absorption, and haze (Figure 8.1) are attributed to the change in feature sizes of the etched ZnO:Al surfaces. The small jagged features from HF rich etches cause a higher degree of internal reflection, increasing the absorption in the small wavelength region. The differences observed in the long wavelength region may be attributable to different effective ZnO:Al thicknesses, as the crater shape depends on the acid mixture. As predicted from scalar scattering theory, the haze (Figure 8.1 (b)) increases with increasing roughness [165,207].

The higher degree of internal reflection in the small wavelength region may cause a slight increase in the blue short circuit current density, as the scattered light is generally absorbed in the higher refractive index material (silicon) [208]. Additionally, the slightly higher transparen-

cy in the long wavelength region may account for a slight increase in the red short circuit current density. However, the optical effects on the film are too small to account for the changes observed in the solar cells (see Figure 8.2). The trend in haze is opposite that of the trend in short circuit current density, thus it can be concluded, as others have previously [42], that a low haze substrate does not necessarily mean a low short circuit current density. Since the optical properties can account for only slight changes in solar cell performance, they will be ignored in the next section.

Since red light is not readily absorbed in these 375 nm solar cells, the improvement in short circuit current density under red illumination (Figure 8.3) can be attributed to better light trapping. The blue light, on the other hand, is readily absorbed in solar cells of this thickness. The increase in short circuit current density under blue illumination cannot be attributed to better light trapping (Figure 8.3), but instead indicates better electrical performance between the ZnO:Al and the p-type silicon layer (Figure 8.3). This is also seen in the improved fill factor (Figure 8.2 (a)). Two possible reasons for the improved electrical characteristics are: first, improved growth and thus contact between the amorphous silicon on the HF textured surfaces; and second, an effective thinning of the silicon p-layer due to an increase in the surface area from the sharper structures present on ZnO:Al etched in an HF-rich solution (see Section 6.3.2.2 (page 115)). The increase in surface area may also account for some of the decreases in open circuit voltage with increasing the relative HF concentration (Figure 8.2 (a)), as the increase in contact area will raise the electron-hole recombination [129].

To conclude, crater surface structures were varied by etching ZnO:Al in various mixtures of HF:HCl. Amorphous silicon solar cells were deposited on the different substrates and characterized. The optimum solution tested consisted of a mixture of HF and HCl with concentrations 1 and 0.25 w/w%, respectively. The solar cell improvement was attributed to both better light trapping and contact between the ZnO:Al and p-type silicon layers.

8.1.2. HF Concentration

In Section 6.3.2.1 (page 115) it was shown that the ZnO:Al crater size and shape could be controlled by etching in different concentrations of HF. Specifically, a high HF concentration (1 w/w%) solution yielded small jagged craters, while a low HF concentration (0.125 w/w%) solution yielded larger, smoother craters. Although the shape of these craters is more HCl-like, the crater size is around half that of the standard HCl etch. The optimum HF concentration for amorphous silicon solar cells on a standardly deposited ZnO:Al substrate is investigated in this section.

Standard ZnO:Al films (Section 3.1.2.1 (page 38)) were etched in HF with concentrations between 0.0625 (1/16) and 1 w/w%, by factors of two. A reference HCl (0.5 w/w%) etch was also performed. Etching times were adjusted so that approximately 150 nm of the originally 800 nm thick film was removed, as measured by surface profiler. The active amorphous silicon layers were deposited using PECVD (Section 3.3 (page 41)). Back contacts consisting of approximately 80 nm of ZnO and 700 nm of silver were deposited by RF-sputtering and thermal evaporation, respectively. Test cells had an area of 1 cm^2. The current density-voltage characteristics of the solar cells were measured at 25 °C under white (AM 1.5) illumination and under filtered red (OG 590), and blue (BG 7) illumination.

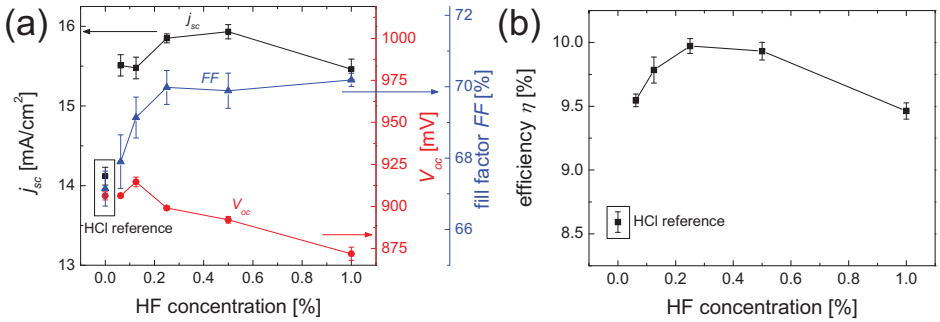

Figure 8.4: (a) The short circuit current density (j_{sc}, black), open circuit voltage (V_{oc}, red), and fill factor (FF, blue) of amorphous silicon thin-film solar cells as a function of the concentration of the HF etching solution. (b) Efficiency (η) as a function of the HF etching solution concentration.

The amorphous silicon cell had a total thickness of 375 nm. The results of the solar cells on ZnO:Al surfaces etched in various HF concentrations are shown in Figure 8.4. The average characteristics (short circuit current density, open circuit voltage, and fill factor) of the five best current density-voltage curves for each HF concentration are given in Figure 8.4 (a) as a function of HF concentration: the reference HCl (0.5 w/w%) etch is indicated at zero HF concentration. A standard deviation of the five cells is indicated in the positive and negative direction. The short circuit current density increased from 15.5 to 15.9 mA/cm^2 as the HF concentration was increased from 0.0625 to 0.5 w/w%. The short circuit current density decreased to 15.5 mA/cm^2 as the HF concentration was further increased to 1 w/w%. The maximum short circuit current density showed a 13 % relative improvement compared to the reference HCl etch at 14.1 mA/cm^2. The fill factor increased from 67.9 to 70.0 % as the HF concentration was increased from 0.0625 to 0.25 w/w%. The fill factor remained relatively constant as the HF concentration was further increased to 1 w/w%. The maximum fill factor (1 w/w% HF) showed a five percent increase over the reference HCl etch at 67.1 %. The open circuit voltage decreased from 906 to 872 mV as the HF concentration was increased from 0.0625 to 1 w/w%. The lowest HF series value corresponds to a four percent decrease in open circuit voltage, as compared to the HCl reference at 906 mV.

The average efficiency of the five best cells is given as a function of HF concentration in Figure 8.4 (b). The efficiency increased from 9.5 at an HF concentration of 0.0625 w/w% to maximum values of 10.0 and 9.9 % at HF concentrations of 0.25 and 0.5 w/w%, respectively. The efficiency decreased back to 9.5 % as the HF concentration was further increased to 1 w/w%. The maximum efficiency showed a 15 % improvement over that of the reference HCl etch at 8.6 %.

To explore the origins of the increase in short circuit current density further, the solar cells on ZnO:Al etched at various HF concentrations were also characterized under red and blue illumination. Figure 8.5 gives the short circuit current density relative to the HCl etched substrate as a function of HF concentration and illumination. The current increased under both red and blue illumination, with a maximum increase of 22 and 7 %, respectively. The maximum improvement in short circuit current density coincides under white and red illumination at an HF concentration of 0.5 w/w%, which is also close to the maximum improvement under blue illumination.

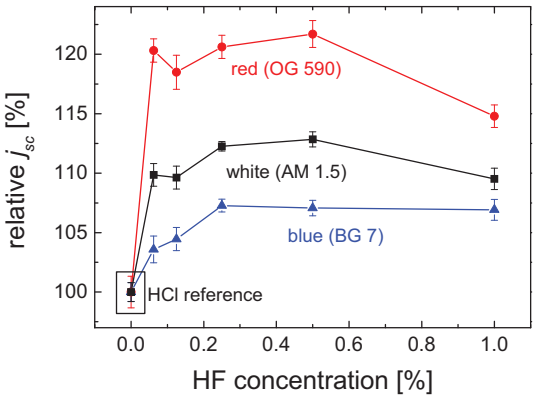

Figure 8.5: Short circuit current density (j_{sc}) of amorphous silicon thin-film solar cells as a function of the concentration of HF compared to the HCl reference under white (AM 1.5), red (OG 590), and blue (BG 7) filtered illumination.

In the previous section it was observed that the differences in the optical properties (total transmission, absorption, and reflections) were not large enough to explain the differences in solar cell properties, and the same is assumed to be the case here. Like the previous section, the improvements in short circuit current density under red illumination (Figure 8.5) can be attributed to better light trapping, as the red light is not readily absorbed, while the improvement in the blue light (Figure 8.5) is attributed to a better electrical contact between the ZnO:Al and p-type silicon layers. This improvement in electrical contact is also observed as a higher fill factor (Figure 8.4 (a)). The reasons for the improved electrical characteristics are the same as those given in the previous section; specifically, improved silicon growth on the optimized structures and an effective thinning of the p-layer due to the sharper HF-induced features (see Section 6.3.2.1 (page 115)). The increase in surface area may also partly explain the decreases in open circuit voltage observed with increasing the HF concentration (Figure 8.4 (a)), as electron-hole recombination will also increase [129].

To conclude, crater surface structures were varied by etching ZnO:Al in various concentrations of HF. Amorphous silicon solar cells were deposited on the different substrates and characterized. The optimum HF concentration is between 0.25 and 0.5 w/w%. The solar cell improvement was attributed to both better light trapping and contact between the ZnO:Al and p-type silicon layers.

8.2. Modulated Surfaces

Modulated surface textures are of particular interest in improving light trapping because different feature sizes scatter light differently. Kambe *et al.* [209] fabricated modulated features on SnO_2:F using a CVD process. Isabella *et al.* [210] introduced modulated features to a ZnO:Al surface using a combination of etched glass or a one dimensional periodic array and standard ZnO:Al etching techniques (HCl). Additionally, Sönderström *et al.* [211] tailored the ZnO:B of the front and intermediate contact to the specific subcells in a tandem solar cell.

In this section, a method to fabricate and control modulated surface features is presented first, and the surfaces are morphologically and optically characterized. Then, tandem solar cell are deposited onto differently prepared modulated surfaces and characterized.

8.2.1. Etching Modulated Surfaces

In Section 6.3.1 (page 111), it was observed that the crater density resulting from etching in HF was higher than that of HCl. The higher density of craters was attributed to the more homogeneous etching of defects in the HF solution (see Section 7.3.1 (page 123)). The different etching behaviors of the two acids are used in this section to fabricate modulated surfaces on a ZnO:Al thin-film.

To make modulated surfaces, standard ZnO:Al thin-films were first etched for 50 seconds in a 0.5 w/w% HCl solution. Samples were then etched for 5, 10, 20, or 40 seconds in a 1 w/w% HF solution. Reference HCl- and HF-only surfaces were also made by etching in the respective solutions for 50 and 40 seconds. The approximately 50 nm variation in as-deposited thickness (see Section 3.1.2.1 (page 38)) within a standard deposition, were used to reduce the thickness variation after etching; by etching the thinnest and thickest films for the shortest and longest times respectively. Thickness, sheet resistance (R_{sh}), and morphology were determined by surface profiler, four point probe, and SEM, respectively. Reflection, total transmission, and diffuse transmission measurements on the variously etched films were performed using an optical spectrometer with an integrating sphere. Diiodomethane was used for refractive index matching during total transmission and reflection measurements.

SEM images of sputtered ZnO:Al textured with a single etching step in 0.5 w/w% HCl or 1 w/w% HF are shown in Figure 8.6 (a) and (f), respectively. Etching in HCl yields state-of-the-art craters with diameters between one and two micrometers (see Section 6.1.1.3 (page 96)). Etching in HF, on the other hand, yields craters with diameters between 300 and 500 nm (see Section 6.3.1 (page 111)).

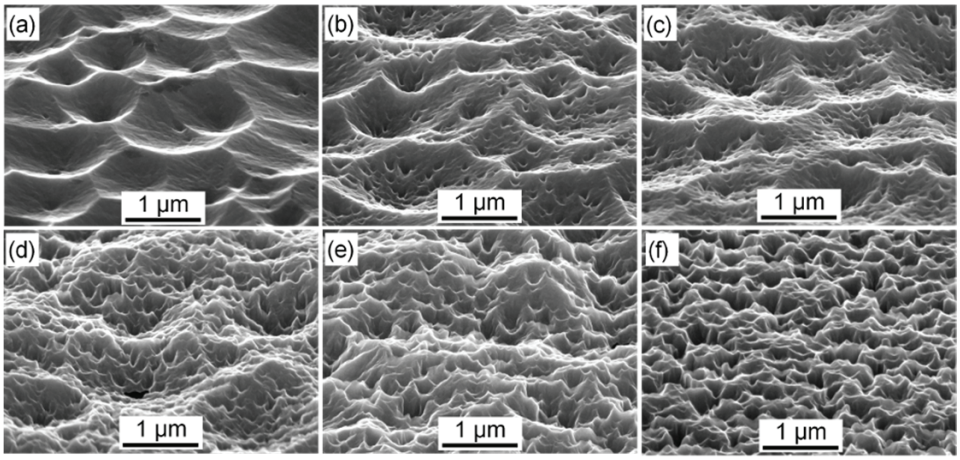

Figure 8.6: ZnO:Al substrates etched in (a) HCl 0.5 w/w% for 50 seconds, HCl 0.5 w/w% for 50 seconds followed by HF 1 w/w% for (b) 5, (c) 10, (d) 20, and (e) 40 seconds, and (f) HF 1 w/w% for 40 seconds.

Table 8.1: HCl and HF etch times, and resultant changes in sheet resistance (R_{sh}) and thickness (d) for the surfaces in Figure 8.6.

surface	etch time [s]		R_{sh} [Ω/sq.]		thickness d [nm]	
Figure 8.6	HCl	HF	before	after	before	after
(a)	50	0	3.2	5.7	788	661
(b)	50	5	2.9	5.5	821	670
(c)	50	10	3.1	6.4	882	696
(d)	50	20	3.0	7.4	831	626
(e)	50	40	2.9	8.3	859	670
(f)	0	40	3.1	4.2	794	746

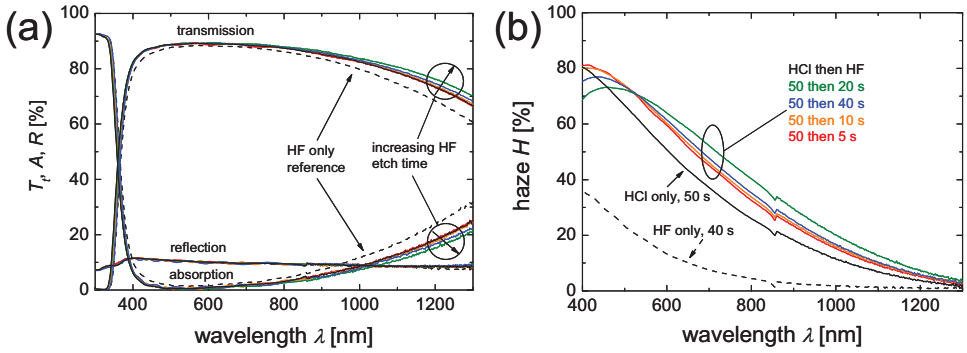

Figure 8.7: (a) Total transmission (T_t), absorption (A), reflection (R), and (b) haze (H) as a function of wavelength (λ) for the various single and modulated etched surfaces.

Figure 8.6 (b-e) contains SEM images of ZnO:Al surfaces texturized by the two-step etching process. The etching time for the first HCl-based etch was held constant at 50 seconds, while the second HF-based etch was varied; the 5, 10, 20, and 40 second increments are shown in Figure 8.6 (b), (c), (d), and (e), respectively. The first HCl-based etch yields large smooth craters, while the second HF-based etch introduces smaller jagged craters superimposed on the larger craters. As the duration of the second HF-based etch is increased, the small features deepen and the overall surface becomes more jagged.

Table 8.1 lists the sheet resistance and thickness of the ZnO:Al films before and after etching. As expected, the sheet resistance generally increases and the thickness generally decreases with increasing etch times. Due to the large difference in etching times, the removed thickness varied over a wide range; 127 and 48 nm were removed for the HCl- and HF-only etches, respectively. While a maximum of 205 nm was removed in the two-step etching process on the modulated ZnO:Al samples.

The optical properties of the modulated and reference ZnO:Al samples are shown in Figure 8.7. The total transmission, absorption, and reflection as a function of wavelength are shown in Figure 8.7 (a). Transmission in the shorter wavelength region (400-600 nm) is almost identical for the HCl only and the modulated surfaces, while it is slightly reduced for the HF only surface. In the longer wavelength region (700-1300 nm), transmission generally increases with an increase in the duration of the second HF etching step. The only exception to this trend is the sample with a second HF etching time of 20 seconds, which exhibited higher total transmission than the sample with a second HF etching step of 40 seconds. The HF-only etched surface also

showed the lowest transmission values over this longer wavelength region. Since the reflection remained relatively constant, the absorption trends appeared inverse to those in total transmission.

The haze measurements as a function of wavelength and etching method are shown in Figure 8.7 (b). Like the total transmission, the haze generally increases with an increasing duration of the second HF-based etching step. Once again, the only exception was a second etching step of 20 seconds in HF, which had higher haze than that of 40 seconds. Like total transmission, the HF-only etch also showed the lowest haze values, across the whole measured spectrum (400-1300 nm), exhibiting an average value of 8 %. The average haze value over the same range was 29 and 37 % for the HCl-only and maximum modulated surface structure, respectively.

The increased absorption in the long and short wavelength regions on the ZnO:Al sample etched only in HF is due likely to the largest film thickness (Table 8.1) -and thus the largest free carrier absorption- and steep angles causing strong internal light trapping, respectively. The decrease in absorption in the longer wavelength region with an increasing duration of the second HF-based etching step can be attributed to a decrease in free carrier absorption. This is directly related to the film thickness. Notice that the modulated surface with the lowest absorption (Figure 8.7 (a), HCl 50 seconds then HF 20 seconds) has the thinnest thickness (Table 8.1).

The increase in haze observed from HF-only to HCl-only, and further to two-step etching is likely related to an increase in the ZnO:Al surface roughness, as predicted by scalar scattering theory [165,207]. The reduction in haze observed between the second HF-based etching step of 20 and 40 seconds is likely related to the loss of some of the underlying HCl-induced features. If allowed to progress too long (more than 20 seconds) the HF-induced features dominate and erase the HCl-induced features (see Figure 8.6 (e)).

Despite the differences in ZnO:Al sheet resistance after etching (Table 8.1), the sheet resistance of all samples remained relatively low (less than 9 Ω/sq.). The differences in the sheet resistance of the ZnO:Al should not alter the performance of the solar cells deposited on top noticeably, since the electrical transport will still be predominantly limited by the active silicon layer.

8.2.2. Solar Cell on Modulated Surfaces

In this section, tandem (amorphous/microcrystalline) silicon solar cells are deposited onto the modulated and reference ZnO:Al surfaces prepared in the previous section and characterized.

The active amorphous and microcrystalline silicon layers were deposited using PECVD (see Section 3.3 (page 41)). Back contacts consisting of approximately 80 nm of ZnO and 700 nm of silver were deposited by RF-sputtering and thermal evaporation, respectively. Test cells had an area of 1 cm^2. The current density-voltage characteristics of the solar cells were measured at 25 °C under white (AM 1.5) illumination. Quantum efficiency measurements were made on the most efficient cells at 25 °C without a bias current. Cell reflection measurements were made on the same cells.

The top (amorphous) and bottom (microcrystalline) solar cells had a thickness of 560 nm and 1.2 µm, respectively. The resulting solar cell parameters of the cells prepared on ZnO:Al surfaces etched in HCl for 50 seconds then HF for different durations, as well as a reference

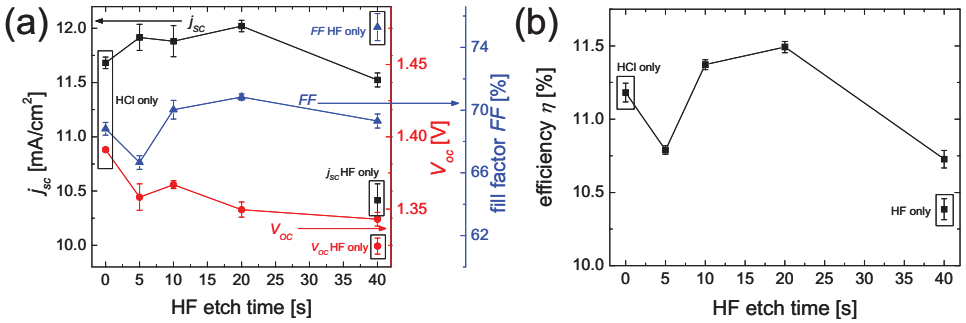

Figure 8.8: (a) The short circuit current density (j_{sc}, black), open circuit voltage (V_{oc}, red), and fill factor (FF, blue) of tandem silicon thin-film solar cells as a function of the duration of the second etching step in HF. (b) Efficiency (η) as a function of the duration of the second etching step in HF. Values for a reference substrate etched only in HF are also indicated.

only HF etched sample are, shown in Figure 8.8. The average characteristics (short circuit current density, open circuit voltage, and fill factor) of the five best current density-voltage curves for each ZnO:Al surface are given in Figure 8.8 (a) as a function of the duration of the second HF-based etching step: the reference HF-only sample is indicated at 40 seconds. A standard deviation of the five cells is indicated in the positive and negative direction. The short circuit current density increased from 11.7 to 12.0 mA/cm^2 as the length of the HF etching step was increased from 0 to 20 seconds. The short circuit current density decreased to 11.5 mA/cm^2 as the HF etching step was further increased to 40 seconds. The short circuit current density of the HF-only etched substrate exhibited the lowest value at 10.4 mA/cm^2. The fill factor showed the same trends as the short circuit current density for the samples etched in HCl then HF, increasing from 68.8 to 70.8 % as the HF etching step was increased from 0 to 20 seconds, then decreasing to 69.3 % as the HF etching step was further increased to 40 seconds. The reference HF-only etched sample exhibited the highest fill factor value at 75.3 %. The open circuit voltage decreased from 1.39 to 1.34 V as the HF etching step was increased from 0 to 40 seconds. The HF-only reference exhibited an even lower open circuit voltage value of 1.32 V.

The average efficiency of the five best cells is given as a function of the length of the second HF-based etching step in Figure 8.8 (b). The efficiency increased from 11.2 to 11.5 % as the HF etching step was increased from 0 to 20 seconds. The efficiency decreased to 10.7 % as the HF etching step was further increased to 40 seconds. The reference HF-only etch showed the lowest efficiency at 10.4 %.

The short circuit current density and fill factor values presented in Figure 8.8 can be somewhat misleading, since both of these characteristics depend strongly on how well the current is matched between the two subcells [212]. To get insight into how well the subcells are matched and observe the effects of modulated surfaces on which subcells absorb light, quantum efficiency measurements were made and analyzed, see Figure 8.9. The quantum efficiency for the top and bottom solar cells as well as the total (top+bottom) quantum efficiency are shown in Figure 8.9 (a) as a function of wavelength and etch. Figure 8.9 (a) also contains the reflection (100-R) of the solar cells. To prevent this figure from becoming too crowded, only the results for the HCl reference (solid black line), the HF reference (dashed black line), and the best modulated surface (HCl 50 second then HF 20 seconds, solid green line) are shown. The HF etched top subcell shows the highest quantum efficiency, while the bottom cell shows the low-

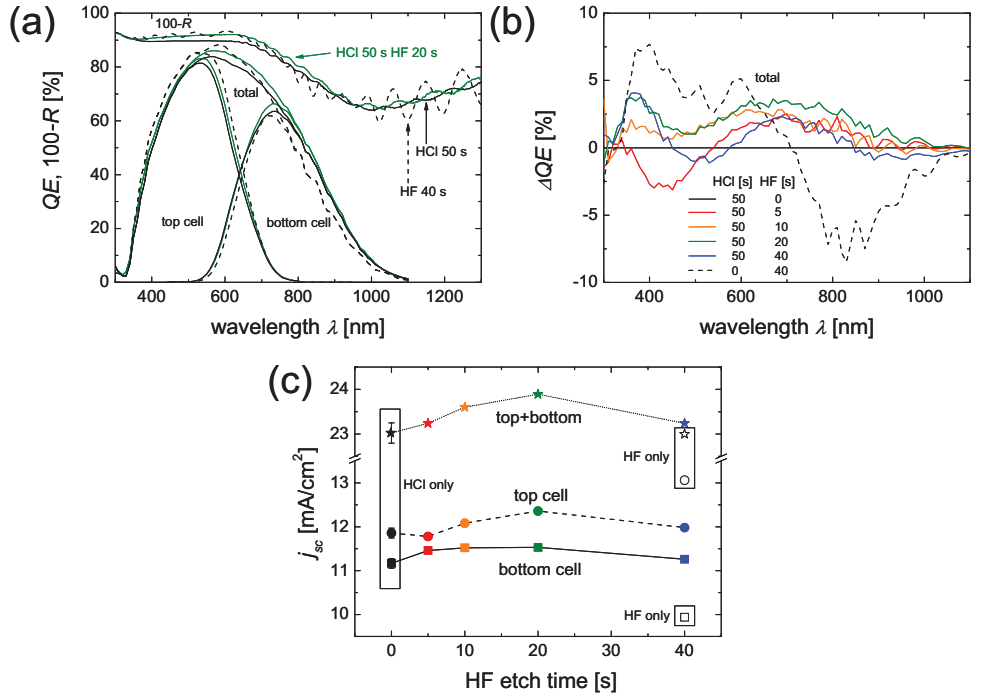

Figure 8.9: (a) Quantum efficiency (QE) for the top and bottom subcells, the total quantum efficiency, and the cell reflection (R) as a function of wavelength and etch. (b) Difference in quantum efficiency (ΔQE) with respect to the HCl-only etch as a function of wavelength and etch. (c) Short circuit current density (j_{sc}) as determined from the quantum efficiency for the top (•) and bottom (■) subcells, as well as the total (★) as a function of the duration of the second etching step in HF. A HF-only reference is also indicated.

est quantum efficiency levels. The quantum efficiency of the HCl reference and the best modulated surface show fairly similar trends, however the modulated surface exhibits higher values over the 350-900 nm wavelength region. Cell reflection measurements show a reduction for the HF etched reference over the 350-800 nm wavelength region. Similarly, the best modulated surface showed a reduction in reflection over the 350-900 nm wavelength region.

The change in the total quantum efficiency relative to the HCl-only etch ($\Delta QE = QE_{HCl_{x},HF_{y}} - QE_{HCl50}$) is presented for all surfaces as a function of wavelength in Figure 8.9 (b). For the modulated surfaces, three wavelength regions will be addressed: the short wavelength region (300-500 nm), which depends solely on the top subcell; the middle wavelength region (500-900 nm), which depends on both the top and bottom subcells from 500 to 750 nm, and solely on the bottom subcell for longer wavelengths; and the long wavelength region (900-1100 nm), which depends solely on the bottom cell. In the short wavelength region, the quantum efficiency decreases up to 3.1 % after a short HF etch time of five seconds. However, the quantum efficiency in the short wavelength region increases with longer HF etching times, exhibiting a maximum of 4 % absolute improvement over the HCl-only reference after 40 seconds. In the middle wavelength region, the quantum efficiency increases with increasing HF etch times up to 20 seconds, where an increase with a maximum of 3.6 % (absolute) over the HCl-only reference is observed. Increasing the HF etch time further to 40 seconds reduces the

quantum efficiency with respect to the 20 second etch, although the quantum efficiency remains generally higher than that of the HCl-only reference. In the long wavelength region, only slight changes with respect to the HCl-only reference are observed, with 20 seconds of HF etching showing slight improvement and 40 seconds showing slight degradation.

The HF-only reference exhibits a distinctly different behavior with respect to the HCl-only reference. Rather than showing distinctions in a short, medium, and long wavelength regions of the spectrum, distinctions are seen solely in the top (300-700 nm) and bottom (700-1100 nm) subcells. The quantum efficiency in the top subcell increased as much as 7.7 % (absolute), while the quantum efficiency in the bottom subcell decreased as much as 8.5% (absolute).

Figure 8.9 (c) gives the short circuit current density as a function of the HF etch time for the top and bottom subcells, as calculated from the quantum efficiency (Figure 8.9 (a)) normalized to the AM 1.5 spectrum (see Section 3.4.12 (page 58)), see Equation (2.42). The sum of the two currents and the HF-only reference are also shown. The top and bottom subcells (and consequently the sum of the two) show similar trends, increasing, respectively, from 11.9 and 11.2 mA/cm^2 to 12.4 and 11.5 mA/cm^2 as the HF etch time was increased from 0 to 20 seconds. The current in the top and bottom subcells decreased to 12.0 and 11.2 mA/cm^2, respectively, after a longer HF etching time of 40 seconds. The HF-only reference exhibited the highest and lowest short circuit current densities in the top and bottom subcells, at 13.1 and 9.9 mA/cm^2, respectively.

The electrically measured short circuit current densities in the solar cells (Figure 8.8 (a)) were always limited to the lowest short circuit current densities calculated by quantum efficiency measurements (Figure 8.9 (c)). The solar cells were bottom limited in all cases; a slight mismatch is advantageous as the top (amorphous) subcell will suffer from light induced degradation [128]. The large short circuit current density mismatch (3.2 mA/cm^2) seen in the HF-only etched cell likely accounts for the high fill factor.

Compared to HCl alone, etching in only HF moves current from the bottom to the top cell. The sum of the current from the top and bottom subcells is 23 mA/cm^2 (Figure 8.9 (b)) for both the HCl- and HF-only etches. The HF-etched structures may prove economically beneficial, because a thinner amorphous cell can be used, additionally this would reduce the amount of light induced degradation [213]. Modulated surfaces, on the other hand, increase the current in both the top and bottom subcells. This may prove beneficial for increasing the overall efficiency of tandem solar cells. The increase in the quantum efficiency for the modulated surfaces (especially the sample etched in HCl then HF for 50 and 20 seconds, respectively) is primarily due to better light in-coupling, as observed in the lower cell reflection (Figure 8.9 (a)).

8.3. Texturizing Compact ZnO:Al Films

As discussed in Chapter 7 and observed by many others, the surface morphology after etching depends strongly on the ZnO:Al deposition conditions [13,24-26,29,191-193]. The current state-of-the-art is to tailor the deposition conditions of ZnO:Al to optimize electrical, optical, and the resultant etch features simultaneously. Balancing these different properties is not easy - changes to the deposition conditions that improve one property can degrade another. For example, increasing the substrate temperature of the standard ZnO:Al deposition (above 300 °C) improves the electro-optical properties of the resultant ZnO:Al film, but the surface structure

becomes type III (relatively flat with a few large craters, see Section 2.7 (page 25)) [24]. The challenge is even greater for industry, where the ZnO:Al throughput also becomes an issue.

In this section, a method for separating the optimization of electro-optical from texturization properties is presented first, and to understand how this etching process progresses, the evolution of the surface is examined. Then, using the new etching techniques, industrially relevant ZnO:Al substrates are texturized for microcrystalline solar cell application.

8.3.1. HCl Etch Evolution on HF Etched Compact ZnO:Al

This section presents a new etching technique to give good light trapping texture to a compact ZnO:Al surface which texturizes poorly under the current state-of-the-art etching conditions.

High-rate ZnO:Al samples were deposited at a higher temperature and pressure than standard ZnO:Al samples (see Section 3.1.2.2 (page 39)). The deposition rate of the high-rate and standard (low-rate) ZnO:Al samples were 6 and 100 nm · m/min, respectively [24,132]. Additionally, high-rate depositions were performed using rotatable targets. This is also of interest to industry, since the costs can be further reduced by using the ZnO:Al target more efficiently [26,106].

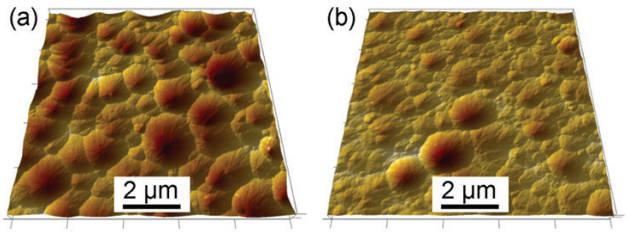

Figure 8.10: AFM images of (a) standard (low-rate) ZnO:Al etched in HCl for 40 seconds, and (b) high-rate ZnO:Al etched in HCl for 50 seconds.

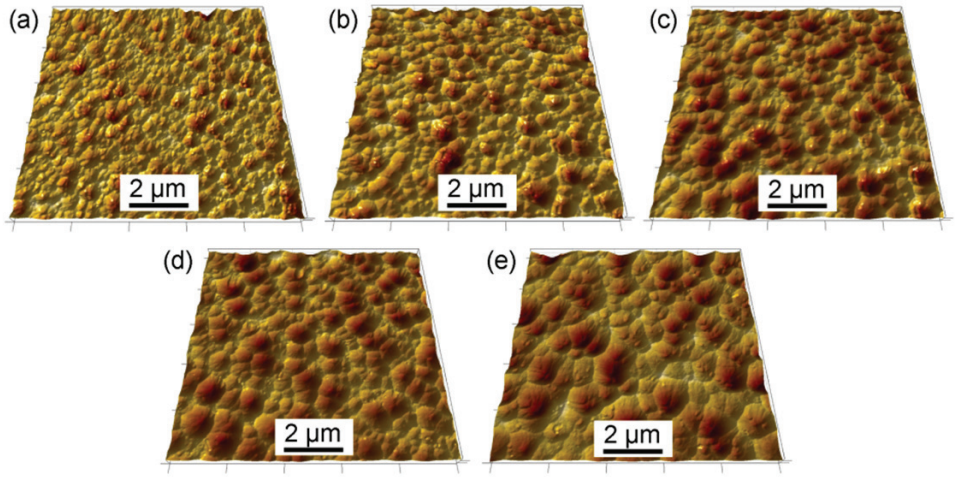

Figure 8.11: AFM images of high-rate ZnO:Al etched in HF for 120 seconds then HCl for (a) 0, (b) 2, (c) 4, (d) 8, and (e) 16 seconds.

The high-rate samples were etched in 1 w/w% HF for 120 seconds. Following the HF etch, samples were etched in 0.5 w/w% HCl for 2, 4, 8, and 16 seconds. For reference, standard (low-rate) and high-rate ZnO:Al samples were etched in 0.5 w/w% HCl for 40 and 50 seconds, respectively. The surface morphologies were measured by AFM, and the height and angular distributions were characterized using the techniques outlined in Section 3.4.2.1 (page 44).

To observe the evolution of this two-step etching process, a high-rate deposited ZnO:Al sample was imaged at the same location by AFM between subsequent etching steps (see Section 3.4.2.3 (page 47)). AFM images were taken after etching for 100 seconds in 1 w/w% HF, and after an additional 5, 10, and 15 cumulative seconds of etching in 0.125 w/w% in HCl.

AFM images for the standard (low-rate) and high-rate reference etches (HCl) are shown in Figure 8.10 (a) and (b), respectively. The standard ZnO:Al exhibits type II texture (see Section 2.7(page 25)), which has been shown to exhibit good light trapping capabilities for microcrystalline solar cells [24]. The high-rate ZnO:Al exhibits type III texture, inhomogeneous texture with a few large craters but mostly flat or shallow craters and low roughness [26,132].

AFM images of the high-rate ZnO:Al etched first in HF for 120 seconds then HCl for times between 0 and 16 seconds are shown in Figure 8.11. The high-rate substrate etched only in HF is shown in Figure 8.11 (a). Like the standardly deposited ZnO:Al, etching high-rate ZnO:Al in HF leads to a higher density of craters (see Section 6.3.1 (page 111)). These craters have generally smaller diameters (around 300 nm) and more jagged surface features. AFM images of high-rate ZnO:Al etched in HF for 120 seconds followed by HCl for 2, 4, 8, and 16 seconds are shown in Figure 8.11 (b), (c), (d), and (e), respectively. As the HCl etching time is increased, the diameter of the craters increases and the crater density decreases. After the longest HCl etching step (16 seconds, Figure 8.11 (e)), relatively flat plateaus, like those observed on the high rate deposited sample etched in only HCl (Figure 8.10 (b)), begin to appear.

Height and angle distributions as calculated from the AFM images presented in Figure 8.10 and Figure 8.11 are given in Figure 8.12. Median centered height histograms, quantized into 10 nm increments, are shown in Figure 8.12 (a). Etching in only HCl yields a broad and narrow distributions of feature heights for the standard (low-rate, dashed black line) and high-rate (solid black line) ZnO:Al substrates, respectively. Etching the high-rate ZnO:Al in only HF

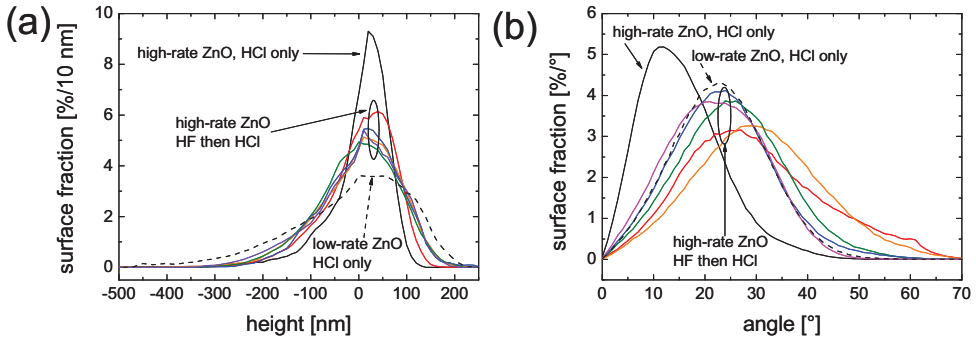

Figure 8.12: (a) Histograms of feature height in 10 nm increments, and (b) Surface angular distribution in one degree increments. The low-rate and high-rate reference surfaces are indicated by dashed and solid black lines, respectively. The 120 second HF etch followed by 0, 2, 4, 8, and 16 seconds of HCl etching are solid red, orange, green, blue, and violet lines, respectively.

(red line) gives a larger distribution of height values. The height distribution is increased further with the application of a second HCl-based etching step (orange, green, blue, and violet lines). Note, however, that the widest height distributions resulting from two-step etching are not as wide as the standard ZnO:Al reference. Thus, the RMS roughness and optical properties such as haze remain smaller on these two-step textured surfaces than the standard HCl etch.

Angular distributions of the surfaces quantized into one degree increments are shown in Figure 8.12 (b). Etching in only HCl yields a broad distribution with a peak at 23° and a narrow distribution with a peak at 12° for the low- and high-rate ZnO:Al substrates, respectively. Etching in HF alone or the shortest additional HCl etching time (two seconds) yields sharp surface features as seen by the higher peak in angular distribution at 27° and 29°, respectively. Notice also that for these etches, a significant fraction of the surfaces is covered with very step angles (above 50°). For samples with a second etching step in HCl between 4 and 16 seconds, the angular distributions shift to a spectrum very similar to that of the standard ZnO:Al, with peak angular distributions between 20° and 24°. Like the standard ZnO:Al surface, there are almost no very steep angles. The sample etched for eight seconds in HCl as a second etching step has an angular distribution that most closely matches that of the standard ZnO:Al.

The HCl etch evolution on an HF-etched high-rate ZnO:Al surface is shown in Figure 8.13 and Animation 8.1 (located in Appendix (page 157)). The same location was imaged after etching for 100 seconds in HF (Figure 8.13 (a)), and three additional five second etches in a very dilute HCl (0.125 %) solution (Figure 8.13 (c)). Figure 8.13 (b) shows an unetched surface reconstructed from the longest etched surface and the differences between each etching step. The construction of an image such as this is discussed in Section 3.4.2.4 (page 49). The red, orange, and yellow colors represent the high-rate ZnO:Al areas that were etched during the 0-5, 6-10, and 11-15 seconds etching steps, respectively. The areas marked by ellipses are meant to guide the eyes and indicate the same physical area in all three images. The HCl etch evolves on the HF etched high rate ZnO:Al by first etching the middle of the craters then expanding outward radially with each etching step, smoothing the sharp features and reducing the number of craters in the process.

To explain how this two-step etching process functions, recall from the polycrystalline ZnO:Al etch model (Section 7.5 (page 129)) that (1) all grain boundaries have potential to be

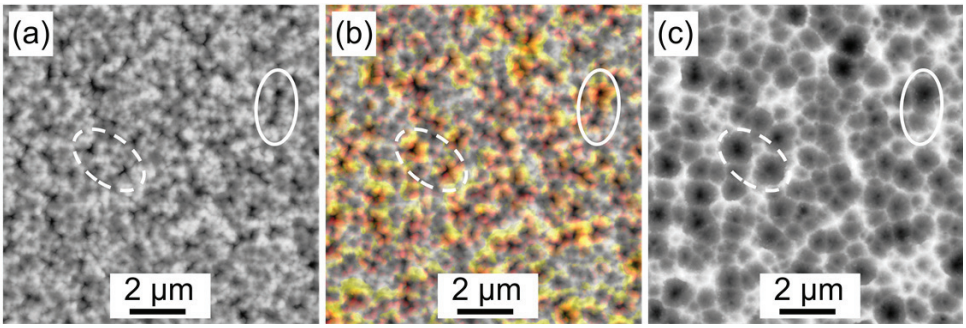

Figure 8.13: AFM images of the HCl etch evolution on an HF etched high-rate ZnO:Al substrate. Substrates after (a) etching in HF for 100 seconds and (c) after three additional five-second etching steps in HCl. (b) Contrast gives the HF etched surface as in (a), while colors indicate the areas etched in the incremental etching steps, 0-5 seconds red, 6-10 seconds orange, and 11-15 seconds yellow. Ellipses indicate the same location in the three images.

etched, which depends on deposition conditions; and (2) the etching solution defines the threshold above which grain boundaries with given potentials will be etched. The high-rate ZnO:Al was deposited at a high temperature and pressure, both of which lead to compact film growth, or in terms of the model, films where the grain boundaries generally have a lower potential to be etched. Highly concentrated HF solutions (1 w/w% or higher) have a low threshold due to the smalls size of the molecule and weak dissociation constant (Section 7.5 (page 129)). Thus, etching in such solutions leads to a higher crater density and the more homogeneous etching of defects (Section 7.3.1 (page 123)), as seen in Figure 8.11 (a).

With regard to postulate (3) of the polycrystalline ZnO:Al etch model, the HF etch is vertically limited, as characterized by the sharp surface features, see Figure 8.12 (b, red). Features such as these lead to poor electrical performance in microcrystalline solar cells [214,215]. By switching to a horizontally limited solution (HCl) for the second etching step, the sharp HF-induced features are eroded radially from the crater centers (see Figure 8.13) until the characteristic (101) plane is exposed, giving the distinctive crater wall angle of inclination (see Figure 8.12 (b, blue)) [25,33,34]. If the second etching step is too long, the effects of the HF etch are lost and the surface begins to return to the poor HCl-only texture, see Figure 8.11 (e) and Figure 8.12 (b, violet)

Using a two-step etch process in HF then HCl, high-rate ZnO:Al, which previously exhibited inhomogeneous surfaces texture, can be homogeneously textured with craters of smaller size but similar shape to those of the standard HCl etched surface.

8.3.2. Cell Results

In this section, the texturization process presented in the previous section is used to texturize industrially relevant ZnO:Al for use in microcrystalline solar cells. Three types of industrially relevant ZnO:Al thin-films will be examined; (1) high-rate deposition from a ceramic target onto a CG substrate (Section 3.1.2.2 (page 39)), (2) reactive high-rate deposition from a metallic target onto a CG substrate (Section 3.1.2.3 (page 39)), and (3) unknown deposition conditions onto a float glass substrate. The final example was supplied by a project partner in industry. Throughout this section, the three substrates will be referred to as high-rate ceramic ZnO:Al, high-rate reactive ZnO:Al, and ZnO:Al on float glass, respectively. Using only standard HCl-only texturization, each of these films exhibited type III (Section 2.7 (page 25)) texture.

High-rate ceramic ZnO:Al samples were etched in 1 w/w% HF for 80 seconds, then 0.5 w/w% HCl for 0, 2, 4, 8, 16, and 32 seconds. High-rate reactive ZnO:Al samples were etched in 1 w/w% HF for 60 seconds, then 0.5 w/w% HCl for 0, 12, and 16 seconds. Samples with ZnO:Al on float glass were etched in 1 w/w% HF for 120 seconds, then 0.5 w/w% HCl for 0, 12, 16, and 30 seconds. For reference, a sample of each of the industrially relevant ZnO:Al types was etched in 0.5 w/w% HCl for 60 seconds.

The active microcrystalline silicon layers were deposited using PECVD (Section 3.3 (page 41)). For comparison, low-rate (standard) ZnO:Al and substrates etched in 0.5 w/w% HCl for 50 seconds were included during each deposition. Back contacts consisting of approximately 80 nm of ZnO and 700 nm of silver were deposited by RF-sputtering and thermal evaporation, respectively. Test cells had an area of 1 cm^2. The current density-voltage characteristics of the solar cells were measured at 25 °C under white (AM 1.5) illumination.

All microcrystalline silicon cells had a total thickness of 1.2 µm. The average characteristics of the five best solar cells on the various industrially relevant ZnO:Al films are shown in Figure 8.14. A standard deviation of the five cells is indicated in the positive and negative direction. The short circuit current density as a function of sample type and HCl etch duration is given in Figure 8.14 (a). The ZnO:Al from high-rate ceramic, high-rate reactive, and on float glass exhibit low short circuit current densities after a standard HCl etch at 20.9, 19.1, and 18.0 mAcm^2, respectively. HF etching alone increases the current to 22.0, 20.7, and 20.5 mA/cm^2, which corresponds to a 5, 8, and 14 % increase in short circuit current density, respectively. The short circuit current density increased further to a maximum of 23.4, 21.9, and 21.0 mA/cm^2, after a second etching step in HCl for 16, 12, and 12 seconds, on the ZnO:Al from high-rate ceramic, high-rate reactive, and on float glass, respectively. This corresponds to respective 12, 15, and 17 % improvements in short circuit current densities as compared to the HCl-only etch. With longer HCl etching times, the short circuit current density decreases. The

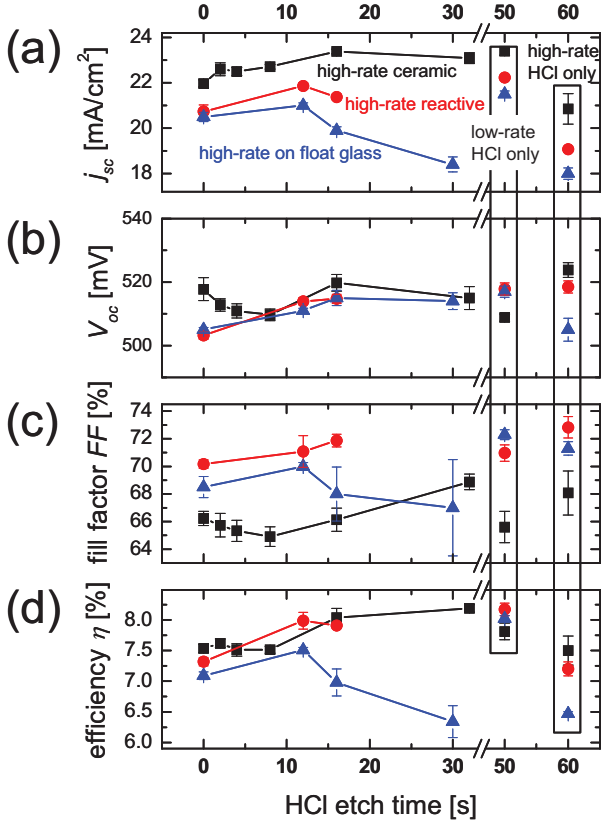

Figure 8.14: (a) The short circuit current density (j_{sc}), (b) open circuit voltage (V_{oc}), (c) fill factor (FF), and (d) efficiency (η) of a microcrystalline silicon thin-film solar cells on industrially relevant ZnO:Al. Specifically, ZnO:Al deposited at a high-rate from a ceramic target (black), under reactive conditions (red), and onto float glass (blue). Reference low-rate (standard) and high-rate HCl-only etches are indicated at 50 and 60 seconds, respectively.

reference HCl-etched low-rate ZnO:Al substrates exhibited short circuit current densities between 21.5 and 23.4 mA/cm^2.

The open circuit voltage, Figure 8.14 (b), shows only slight variations on the ZnO:Al from high-rate ceramic, high-rate reactive, and on float glass, varying between 510 and 523 mV, 503 and 518 mV, and 505 and 518 mV, respectively. This corresponds to variations of less than three percent within a given series. In general, the open circuit voltage increases with increasing HCl etching time. The reference HCl-etched low-rate ZnO:Al substrates had open circuit voltage values similar to those of the industrially relevant substrates between 509 and 517 mV.

The fill factor, Figure 8.14 (c), shows relative changes larger than those observed in the open circuit voltage, but smaller than those observed in the short circuit current density. The fill factor on the ZnO:Al from high-rate ceramic, high-rate reactive, and on float glass vary between 65.0 and 68.9 %, 70.2 and 72.8 %, and 67.0 and 71.3 %, respectively. This corresponds to fill factor variations of six, four, and six percent, respectively. The fill factor generally increased with longer HCl etch times, and values were often observed on the HCl-only etches. The reference HCl-etched low-rate ZnO:Al substrates had fill factors in range similar to those of the industrially relevant substrates between 72.3 and 65.6 %.

Figure 8.14 (d) brings the three previous characteristics together by giving the efficiency as a function of the ZnO:Al deposition method and HCl etch time. The ZnO:Al from high-rate ceramic, high-rate reactive, and on float glass exhibit low efficiencies after a standard HCl etch at 7.5, 7.2, and 6.5 %, respectively. HF etching alone generally increases the efficiency to 7.5, 7.3, and 7.1 %, which corresponds to a zero, one, and nine percent increase in efficiency, respectively. The efficiency is increased further to a maximum of 8.2, 8.0, and 7.5 %, after a second etching step in HCl for 32, 12, and 12 seconds, on the ZnO:Al from high-rate ceramic, high-rate reactive, and on float glass, respectively. This corresponds to a 9, 11, and 15 % improvement in efficiency as compared to the HCl-only etch. The reference HCl-etched low-rate ZnO:Al substrates exhibited efficiencies between 7.8 and 8.2 %.

Industrially relevant ZnO:Al sputtering techniques such as high-rate deposition from a ceramic target, under reactive sputtering conditions, or onto float glass can be more effectively texturized using this two-step etching process. Efficiencies on these industrially relevant ZnO:Al surfaces rivaled those of the relatively expensive low-rate ZnO:Al (see Figure 8.14 (d)). The increase in efficiency for all ZnO:Al deposition types was primarily due to an increase in the short circuit current density (see Figure 8.14 (a)). From this it is concluded that the light trapping on compact ZnO:Al films can be improved using a two-step etch process.

8.4. Summary

This chapter has given three applications for the deeper understanding of the etch process presented in chapters 6 and 7. First, it was shown in Section 8.1 (page 135) that the crater size can be controlled by etching in various mixtures of HF:HCl or in various concentrations of HF. For both series, higher amorphous silicon solar cell efficiencies were obtained on the relatively small features than the relatively large HCl-textured reference (see Figure 8.2 and Figure 8.4). Much of this improved efficiency was due to a higher short circuit current density and thus better light trapping.

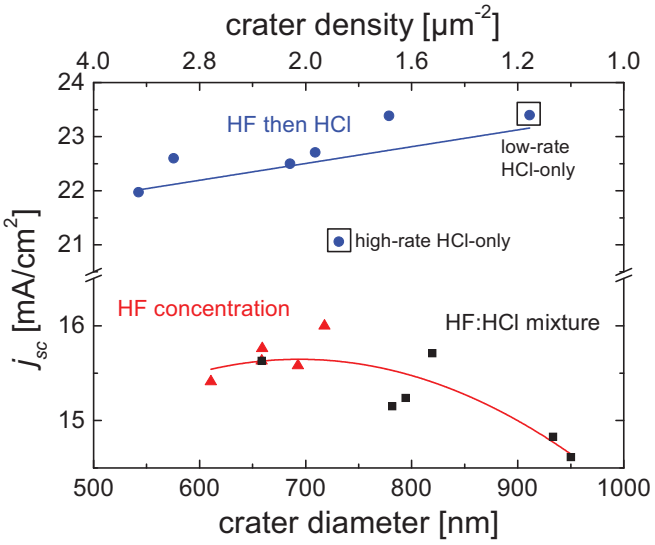

Figure 8.15: Short circuit current density (j_{sc}) as a function of the crater diameter (and density) for amorphous silicon solar cells deposited on ZnO:Al etched in various HF:HCl mixtures (black ■)and HF concentration (red ▲), and microcrystalline silicon solar cells deposited on high-rate ZnO:Al etched in HF then HCl (blue •).

To further explore the relationship between crater size and short circuit current density, AFM measurement were made of the ZnO:Al substrates presented in Section 8.1 (page 135). The crater density and diameter of these measurements were determined by watershed algorithm (Section 3.4.2.2 (page 46)). Figure 8.15 gives the short circuit current density as a function of crater diameter and density for the amorphous silicon solar cells on ZnO:Al etched in HF:HCl mixtures (black) and in various HF concentrations (red). The optimum crater diameter for amorphous solar cells appears to be in the range of 650 to 750 nm. With smaller or larger craters showing a reduction in current. Craters with this diameter were fabricated using HF concentrations between 0.25 and 0.5 w/w%, although it may be possible to find an HF:HCl mixture that would give the same results.

Next, it was shown in Section 8.2 (page 140) that modulated ZnO:Al surfaces can be made using a two-step etching process first in HCl then in HF (Figure 8.6). These surfaces were shown to increase haze (Figure 8.7) and tandem solar cell efficiency (Figure 8.8). Once again, a large part of the improved efficiency was due to a higher short circuit current density. Quantum efficiency measurements of the subcells showed that the current is improved in both top and bottom subcells (Figure 8.9). This improvement was attributed to better light in-coupling. Since the modulated and HF etched surfaces increase current in the top (amorphous) cell, etches such as these may allow for the use of thinner amorphous cells, which in turn would reduce fabrication costs and limit the effects of light induced degradation [213].

Finally, in Section 8.3 (page 146) another two-step etching method (using first HF then HCl) was introduced to texturize compact ZnO:Al films. Compact ZnO:Al films, which texturize inhomogeneously with a standard HCl etch, were homogeneously texturized with an HF etch (Figure 8.11). The craters angles soften and expand radially with a second short etching step in HCl (Figure 8.11 and Figure 8.13), yielding surfaces that mimic the reference low-rate

(standard) well (Figure 8.12). This texturization process was applied to industrially relevant ZnO:Al films including samples sputtered at a high-rate from a ceramic target, under reactive conditions, and onto float glass. In all cases large improvements in microcrystalline solar cell efficiency over HCl-only etching were seen, and solar cell results rivaled those of the low-rate references (Figure 8.14 (d)). The bulk of the improvement in efficiency came from better light trapping as seen in the improved short circuit current density (see Figure 8.14 (a)).

To explore the relationship between crater size and short circuit current density further, AFM measurement were made of the ZnO:Al sputtered at a high-rate from a ceramic target, presented in Section 8.3 (page 146). The average crater diameter and density of these AFM measurements were determined by watershed algorithm (Section 3.4.2.2 (page 46)). Figure 8.15 gives the short circuit current density as a function of crater diameter and density for the microcrystalline silicon solar cells on the high-rate ZnO:Al etched in HF then HCl (blue). The reference HCl-only low- and high-rate films are also indicated. The short circuit current density increases with crater diameter over the range of crater sizes obtained. From this it is concluded that the second HCl-based etch should be performed for as long as possible to give craters maximum size, but not so long as to erase all HF-induced features reverting to a relatively flat surface.

The ability to texturize compact ZnO:Al films effectively may lead to higher solar cell efficiencies as the electro-optical properties and surface texture can be optimized separately. Additionally, this process may lead to a reduction in solar cell cost as the higher throughput ZnO:Al films can be easily and effectively texturized.

9. Summary and Outlook

The aim of this work has been to further the understanding of ZnO:Al for the purpose of improving silicon thin-film solar cell efficiency and reducing ZnO:Al production costs. The understanding of ZnO:Al was expanded in three major areas: growth, heat treatments, and etching. With regard to ZnO:Al growth, it was shown that the growth of ZnO:Al under different conditions and with different processes affects the resultant electrical and structural properties. The surface electrical properties (mobility and carrier concentration) were examined, and showed that while carrier concentration is fairly independent of film thickness the mobility is not, and electronic transport across grain boundaries limits mobility in ZnO:Al thin films. ZnO:Al deposited onto a previously etched ZnO:Al surface grows epitaxially, preserving both the original orientation and grain structure. Finally, it was concluded that the standard ZnO:Al grows Zn-terminated by comparing ZnO:Al growth on CG to that of Zn- and O-terminated ZnO single crystals. It was proposed additionally that by comparing the etching behaviors, the conical shape of the etched craters arise from the rotational freedom of the ZnO:Al columns grown on CG.

Concerning heat treatments, it was shown that a layer of amorphous silicon can protect ZnO:Al from degradation during annealing, and ZnO:Al films with various thicknesses were annealed at high temperatures to decrease their resistivity. This decrease in resistivity was primarily due to an increase in mobility, as the carrier concentration was largely unaffected. For thin-films with an as-deposited thickness of about 800 nm, it was shown that this capping and annealing process does not affect the morphology of the film and increases the total transmission across the visible spectrum. Standard ZnO:Al films were shown to electrically degrade upon damp-heat exposure. The degradation was shown to affect the mobility primarily, and is thus likely related to poor transport across grain boundaries. Using deuterium as an isotopic marker, it was shown that the deuterium uptake was fairly linear with time, that the deuterium penetrated the whole film within 24 hours, and that it is replaced quickly by hydrogen upon damp-heat treatment in DI water. From these observations it was concluded that the electrical degradation is related to the absorption of water at the grain boundaries, and that the majority of the reactions causing degradation are fairly weak, such as the formation of zinc hydroxide. Additionally, it was shown that annealed ZnO:Al samples, both as-deposited and etched, were very stable in the harsh damp-heat environment, exhibiting little to no electrical degradation, and very little deuterium uptake.

With regard to etching, it was shown that the initial points of HCl attack on ZnO:Al films of various thicknesses and the long-term HCl etch evolution that indicated etching is related to certain peculiar grain boundaries built into the film during growth. It was shown that ZnO:Al sputtered onto etched ZnO:Al had new sites of crater formation, but as the new ZnO:Al was etched away, the craters returned to the previous locations. The density of craters from an HCl etch was shown to be controllable by altering the temperature and concentration of the etching solution, with higher temperatures and lower concentrations increasing the density of craters. Most acids showed similar etching behavior to that of HCl. CH_3CO_2H, a weak organic acid,

exhibited the same trends as HCl, a strong inorganic acid, with regard to the increase in crater density with increasing temperature or decreasing concentration. HF etching was shown to exhibit unique etching characteristics, specifically, higher crater densities and sharper features. Changing the concentration of HF changed the density of craters, however the trend is opposite that observed in HCl and CH_3CO_2H, as decreasing HF concentration leads to a decrease in the density of craters. Finally, it was shown that the density of craters on a given ZnO:Al surface can be controlled by etching in various mixtures of HF and HCl.

After summarizing the etching trends observed by others and within this work, a few postulates were made and subsequently tested. It was shown that basic and acidic solutions attack the same points on a polycrystalline ZnO:Al sample. The dependence of crater density on the acid concentration, temperature, and type was confirmed on single crystal ZnO samples. Planar and cross-sectional TEM measurements confirmed grain boundaries as the most prevalent catalysts for etching. With the results of these additional experiments, a three-postulate etching model was proposed, the basics of which are: (1) every grain boundary has certain potential to etch, and this potential depends on the compactness of the grain boundary; (2) the etchant solution and conditions define an etching threshold, and grain boundaries with etching potentials above the threshold are more actively etched; (3) the vertical and horizontal etch rates are defined by the solution, and vertically limited etching leads to the characteristic crater opening angles while a horizontal limited etch yields sharper structures.

While the majority of this work focused on furthering the understanding of ZnO:Al, the final results chapter focused on showing that this better understanding ZnO:Al could be used to improve silicon thin-film solar cell efficiency and reduce production costs. Applications included: increasing the efficiency of amorphous silicon solar cells by optimizing the ZnO:Al crater size; improving light trapping and efficiency in tandem silicon solar cells by fabricating modulated ZnO:Al surfaces; and reducing ZnO:Al costs by texturizing industrially relevant films such that the microcrystalline solar cell efficiencies on these inexpensive films rival those of the relatively expensive laboratory ZnO:Al by developing a better method for separating electro-optical optimization from texturization.

The applications for and solar cell improvements from the knowledge gained within this work are far from exhausted. For example, the size of the two features on modulated surfaces could be optimized using mixtures of HF:HCl or various etchant concentrations and temperatures. Modulated features could be fabricated on industrially relevant ZnO:Al thin-films using a triple etch process in HF then HCl and then HF. There are also many aspects of ZnO:Al that are not understood and warrant further research, including the texturization of sputtered ZnO:Al in an in-line process such as dry etching, further control of etching using electrochemical techniques, and an effective way to texturize loose ZnO:Al films, such as those deposited at RT.

Appendix

The animations come from the various etch evolutions observed throughout this work, experimental details are found within the specific chapters. To view the animations first turn to the start page, then for animations starting on an odd page, lay the book on its back cover and flip pages towards the front cover. For animations starting on an even, lay the book on its front cover and flip pages towards the back cover.

Animation 6.1: 13 of 13, HCl 30 sec.

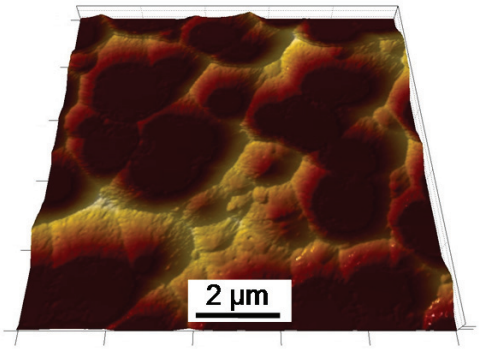

List of Animations

Animation 7.1: 1 of 4, KOH 300 s, then HCl 0 s.

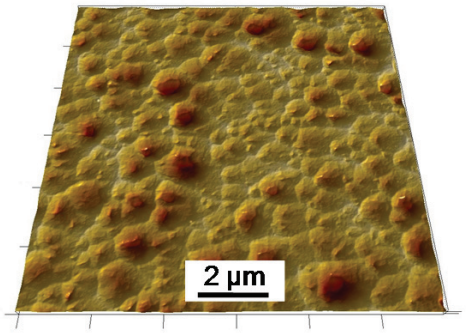

Animation 8.1: 1 of 4, high-rate ZnO:Al HF 100 s, then HCl 0 s.

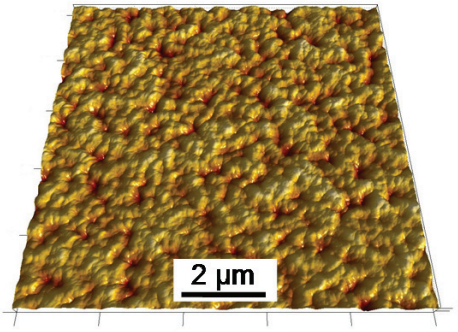

Animation 6.1: 12 of 13, HCl 26 s.

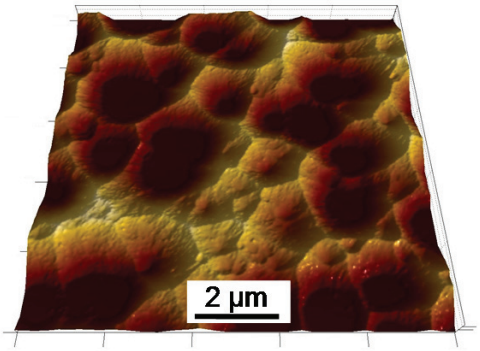

Animation 6.2: 6 of 6, new ZnO:Al on etched ZnO:Al, +200 nm ZnO:Al, HCl 40 s.

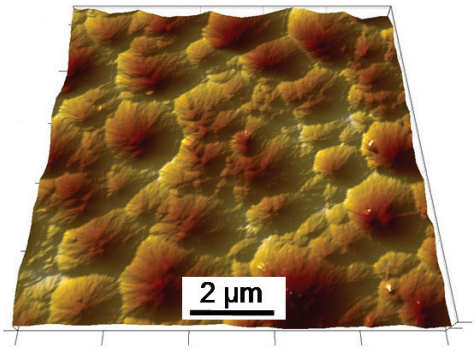

Animation 7.1: 1 of 4, KOH 300 s, then HCl 0 s.

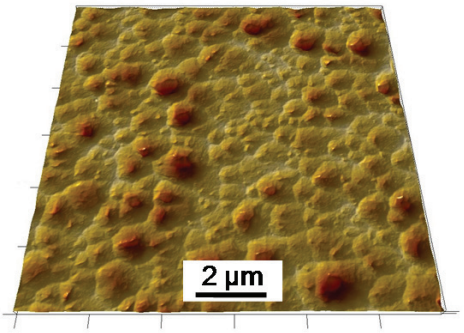

Animation 8.1: 1 of 4, high-rate ZnO:Al HF 100 s, then HCl 0 s.

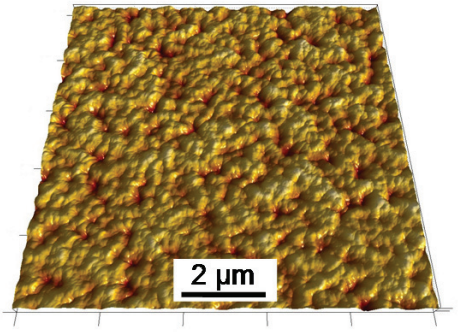

Animation 6.1: 11 of 13, HCl 22 s.

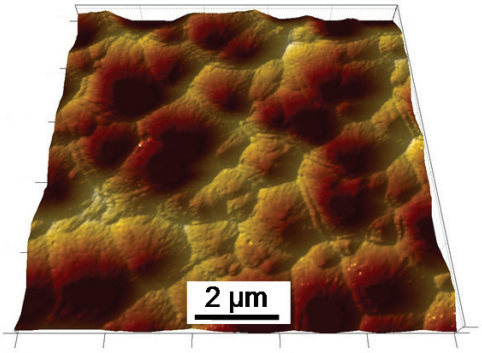

Animation 6.2: 6 of 6, new ZnO:Al on etched ZnO:Al, +200 nm ZnO:Al, HCl 40 s.

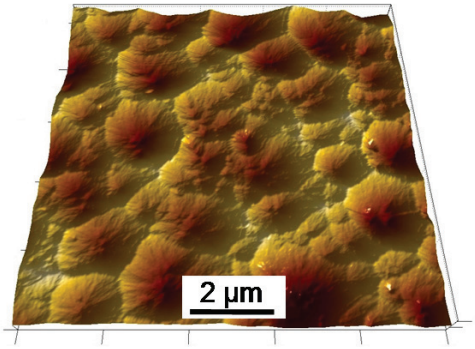

Animation 7.1: 2 of 4, KOH 300 s, then HCl 5 s.

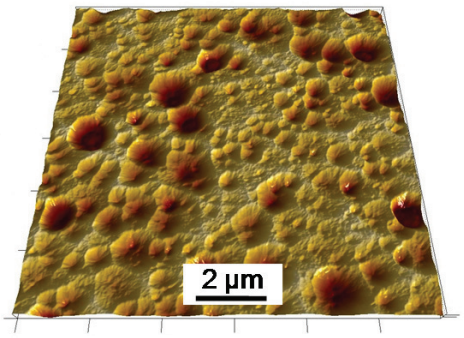

Animation 8.1: 2 of 4, high-rate ZnO:Al HF 100 s, then HCl 5 s.

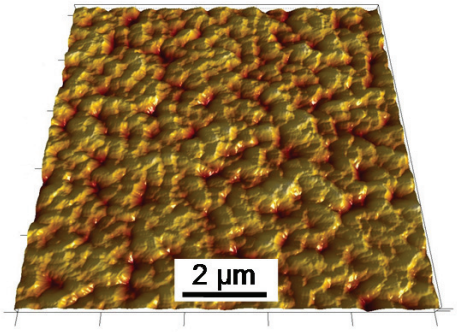

Animation 6.1: 10 of 13, HCl 18 s.

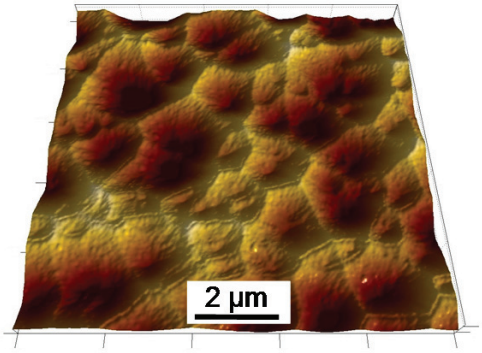

Animation 6.2: 5 of 6, new ZnO:Al on etched ZnO:Al, +200 nm ZnO:Al, HCl 30 s.

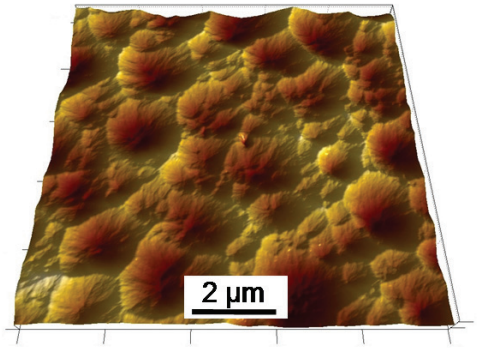

Animation 6.3: 5 of 5, HF 40 s.

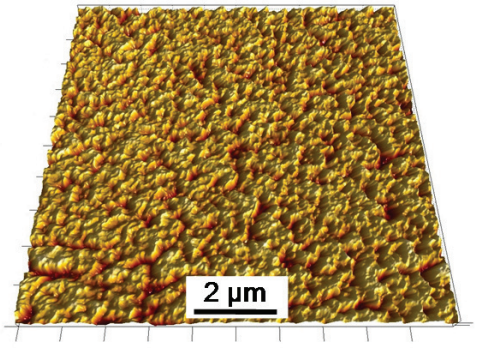

Animation 7.1: 2 of 4, KOH 300 s, then HCl 5 s.

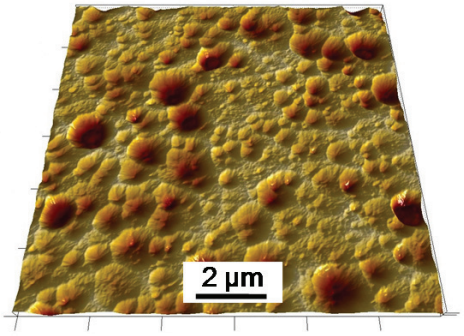

Animation 8.1: 2 of 4, high-rate ZnO:Al HF 100 s, then HCl 5 s.

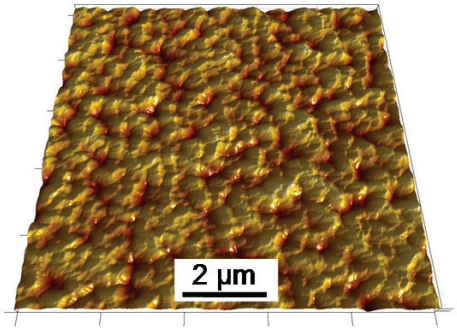

Animation 6.1: 9 of 13, HCl 16 s.

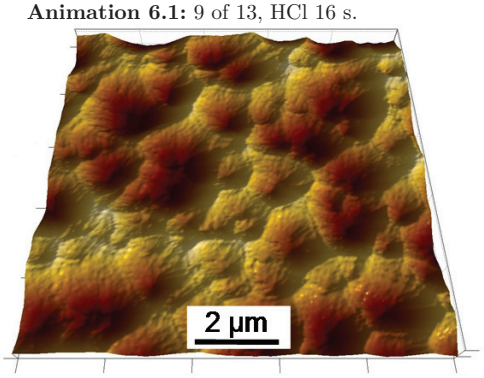

Animation 6.2: 5 of 6, new ZnO:Al on etched ZnO:Al, +200 nm ZnO:Al, HCl 30 s.

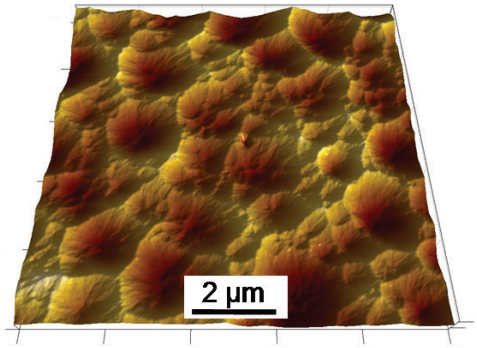

Animation 6.3: 5 of 5, HF 40 s.

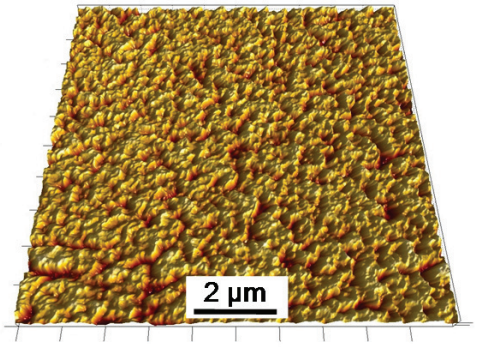

Animation 7.1: 3 of 4, KOH 300 s, then HCl 10 s.

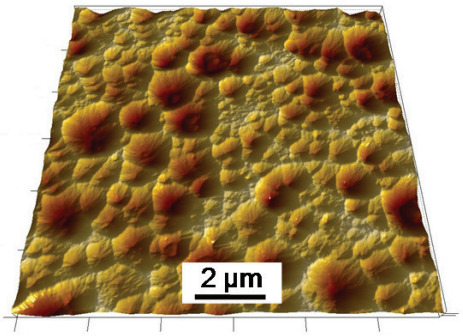

Animation 8.1: 3 of 4, high-rate ZnO:Al HF 100 s, then HCl 10 s.

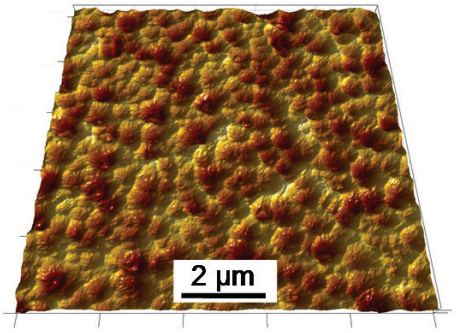

Animation 6.1: 8 of 13, HCl 14 s.

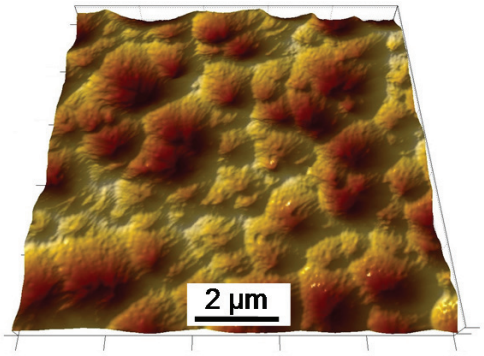

Animation 6.2: 4 of 6, new ZnO:Al on etched ZnO:Al, +200 nm ZnO:Al, HCl 20 s.

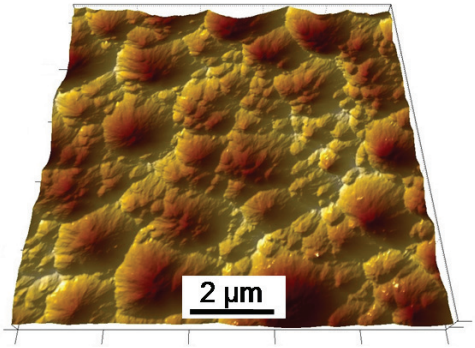

Animation 6.3: 4 of 5, HF 30 s.

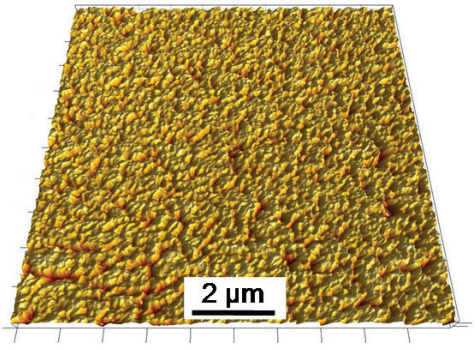

Animation 7.1: 3 of 4, KOH 300 s, then HCl 10 s.

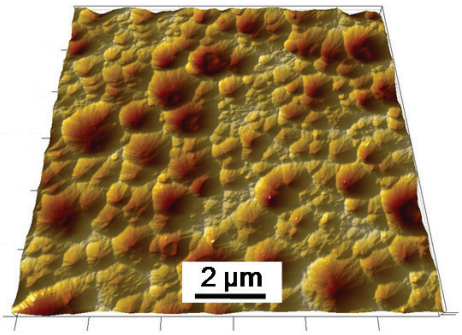

Animation 8.1: 3 of 4, high-rate ZnO:Al HF 100 s, then HCl 10 s.

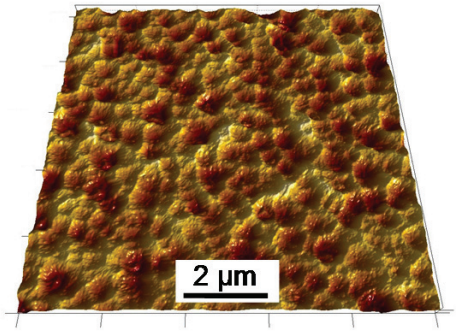

Animation 6.1: 7 of 13, HCl 12 s.

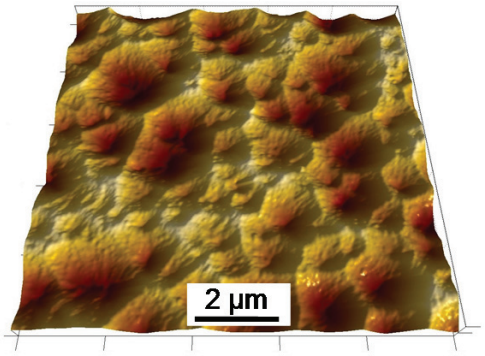

Animation 6.2: 4 of 6, new ZnO:Al on etched ZnO:Al, +200 nm ZnO:Al, HCl 20 s.

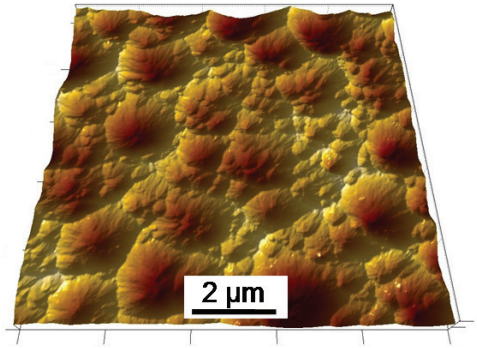

Animation 6.3: 4 of 5, HF 30 s.

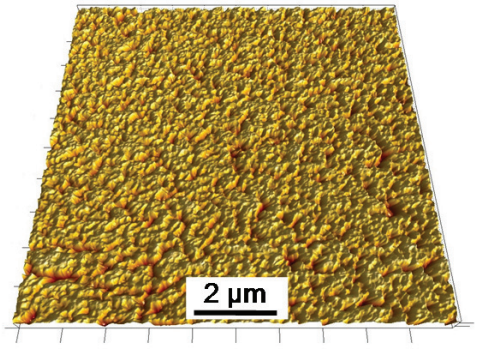

Animation 7.1: 4 of 4, KOH 300 s, then HCl 20 s.

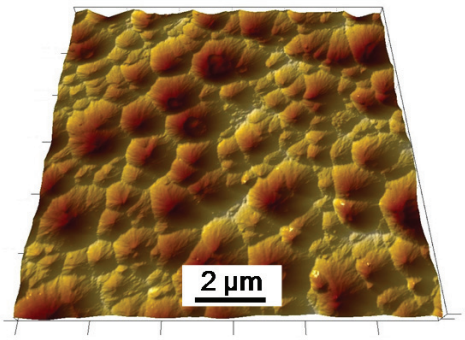

Animation 8.1: 4 of 4, high-rate ZnO:Al HF 100 s, then HCl 15 s.

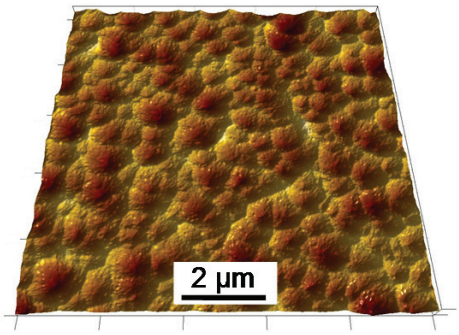

Animation 6.1: 6 of 13, HCl 10 s.

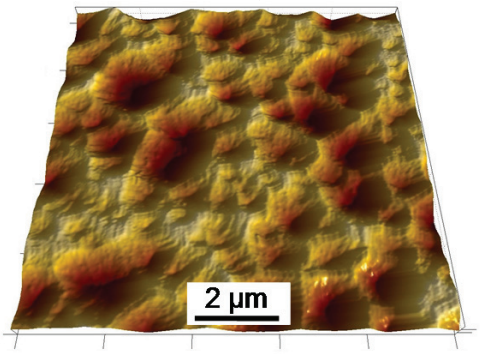

Animation 6.2: 3 of 6, new ZnO:Al on etched ZnO:Al, +200 nm ZnO:Al, HCl 10 s.

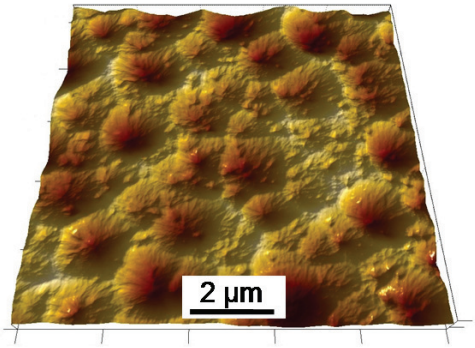

Animation 6.3: 3 of 5, HF 20 s.

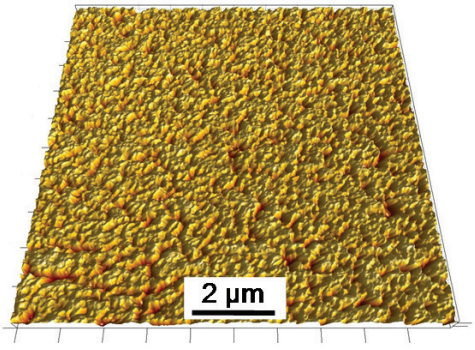

Animation 7.1: 4 of 4, KOH 300 s, then HCl 20 s.

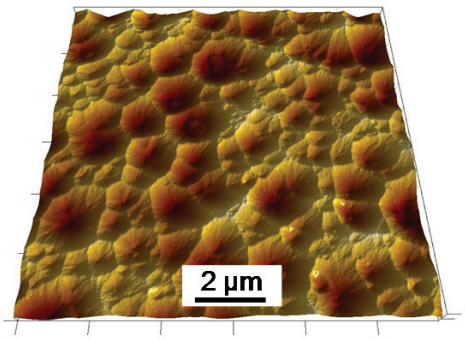

Animation 8.1: 4 of 4, high-rate ZnO:Al HF 100 s, then HCl 15 s.

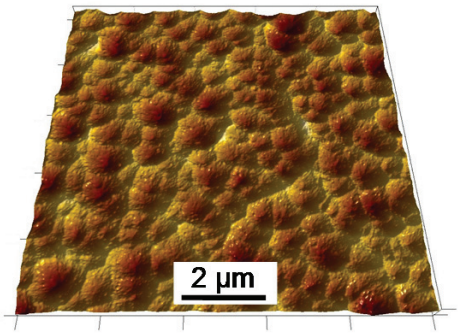

Animation 6.1: 5 of 13, HCl 8 s.

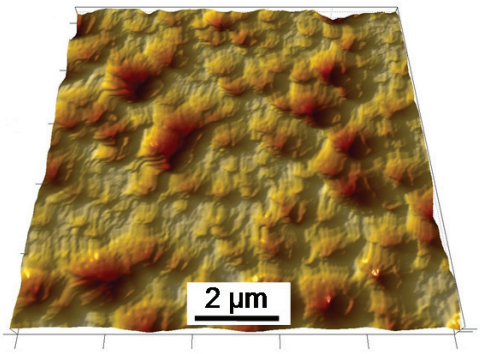

Animation 6.2: 3 of 6, new ZnO:Al on etched ZnO:Al, +200 nm ZnO:Al, HCl 10 s.

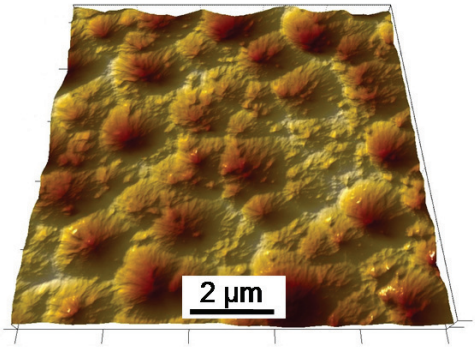

Animation 6.3: 3 of 5, HF 20 s.

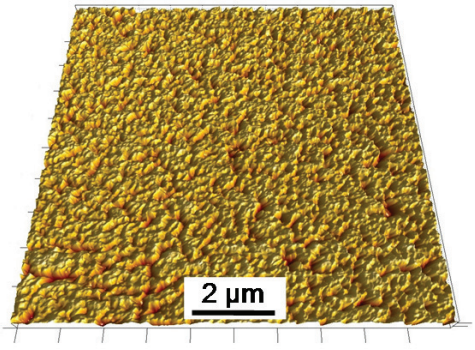

Appendix

Animation 6.1: 4 of 13, HCl 6 s.

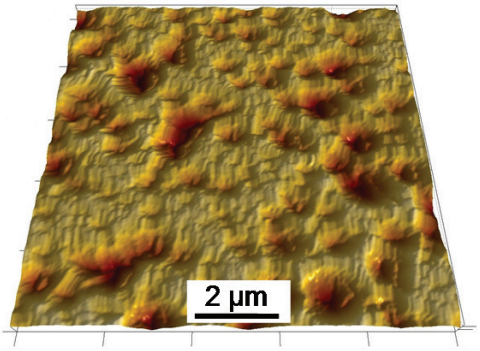

Animation 6.2: 2 of 6, new ZnO:Al on etched ZnO:Al, +200 nm ZnO:Al

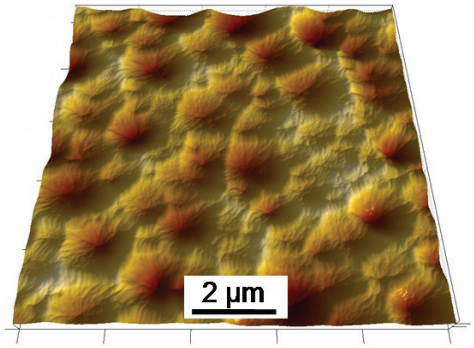

Animation 6.3: 2 of 5, HF 10 s.

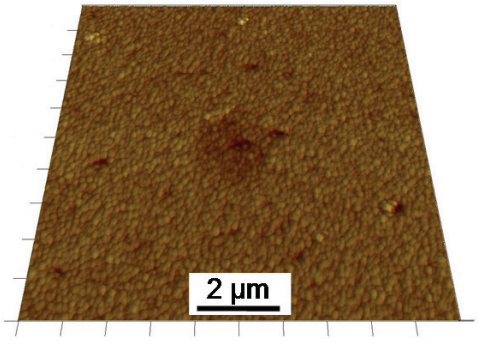

Appendix

Animation 6.1: 3 of 13, HCl 4 s.

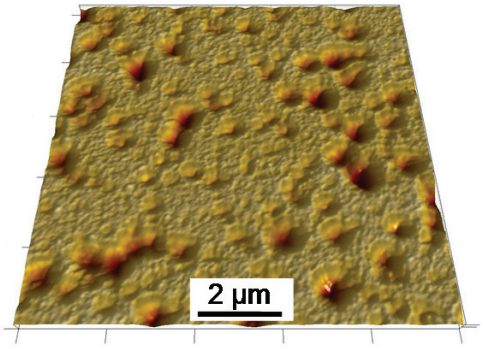

Animation 6.2: 2 of 6, new ZnO:Al on etched ZnO:Al, +200 nm ZnO:Al

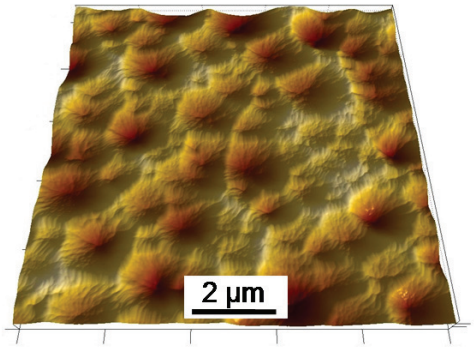

Animation 6.3: 2 of 5, HF 10 s.

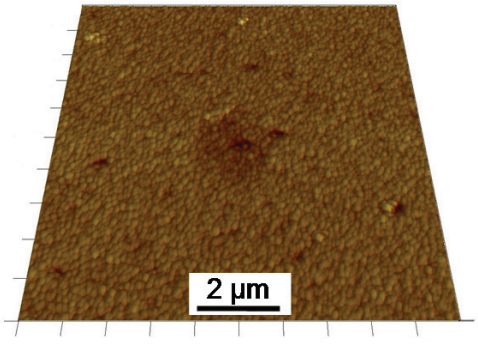

Appendix

Animation 6.1: 2 of 13, HCl 2 s.

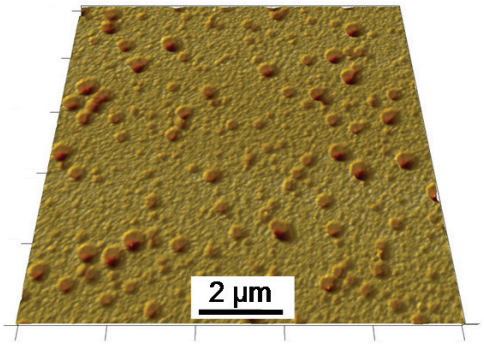

Animation 6.2: 1 of 6, new ZnO:Al on etched ZnO:Al

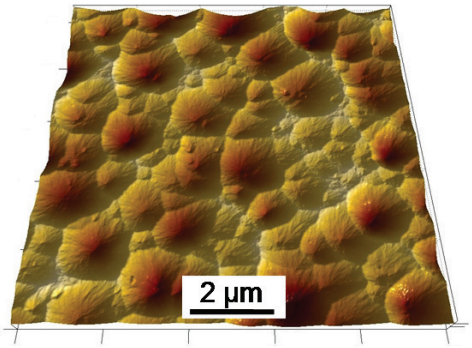

Animation 6.3: 1 of 5, HF 0 s.

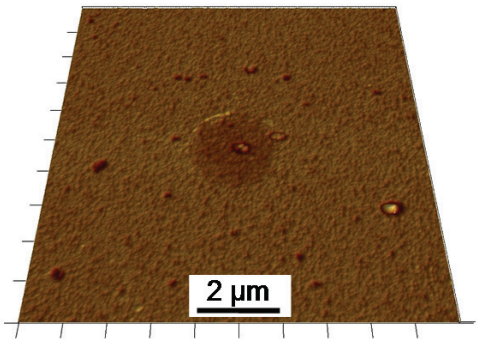

Appendix

Animation 6.1: 1 of 13, HCl 0 s.

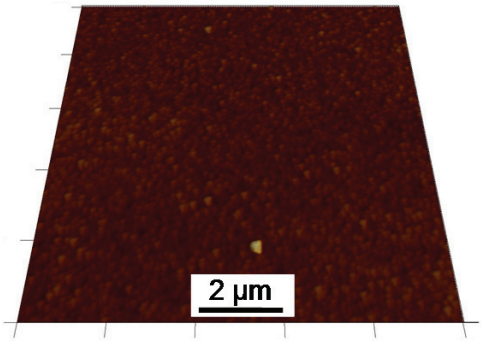

Animation 6.2: 1 of 6, new ZnO:Al on etched ZnO:Al

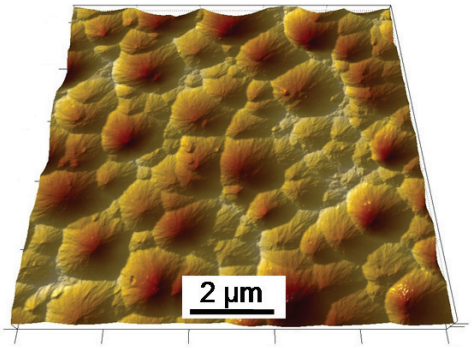

Animation 6.3: 1 of 5, HF 0 s.

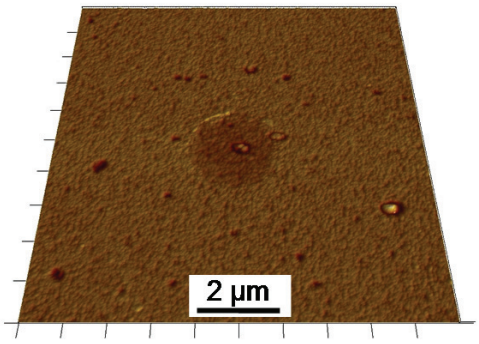

References

[1] S. Shafiee and E. Topal, Energy Policy **37**, 181 (2009).

[2] C. Tamm and E. Cowling, Water Air Soil Pollut. **7**, 503 (1977).

[3] P. M. Cox, R. A. Betts, C. D. Jones, S. A. Spall, and I. J. Totterdell, Nature **408**, 184 (2000).

[4] D. L. Greene, *Costs of Oil Dependence: A 2000 Update* (U.S. Department of Energy, 2000).

[5] O. Morton, Nature **443**, 19 (2006).

[6] N. S. Lewis, Science **315**, 798 (2007).

[7] D. M. Chapin, C. S. Fuller, and G. L. Pearson, J. Appl. Phys. **25**, 676 (1954).

[8] J. Zhao, A. Wang, M. A. Green, and F. Ferrazza, Appl. Phys. Lett. **73**, 1991 (1998).

[9] R. R. King, D. C. Law, K. M. Edmondson, C. M. Fetzer, G. S. Kinsey, H. Yoon, R. A. Sherif, and N. H. Karam, Appl. Phys. Lett. **90**, 183516 (2007).

[10] M. A. Green, Sol. Energy **76**, 3 (2004).

[11] H. Gleskova, I. Cheng, S. Wagner, J. C. Sturm, and Z. Suo, Sol. Energy **80**, 687 (2006).

[12] D. Redfield, Appl. Phys. Lett. **25**, 647 (1974).

[13] O. Kluth, B. Rech, L. Houben, S. Wieder, G. Schöpe, C. Beneking, H. Wagner, A. Löffl, and H. W. Schock, Thin Solid Films **351**, 247 (1999).

[14] K. Sato, Y. Gotoh, Y. Wakayama, Y. Hayashi, K. Adachi, and H. Nishimura, Rep. Res. Lab. Asahi Glass Co. Ltd. **42**, 129 (1992).

[15] S. Faÿ, U. Kroll, C. Bucher, E. Vallat-Sauvain, and A. Shah, Sol. Energy Mater. Sol. Cells **86**, 385 (2005).

[16] K. Krunks, O. Bijakina, V. Mikli, T. Varema, and E. Mellikov, Phys. Scr. **T79**, 209 (1999).

[17] S. Yamabi and H. Imai, J. Mater. Chem. **12**, 3773 (2002).

[18] T. Nakada, Y. Ohkubo, and A. Kunioka, Jpn. J. Appl. Phys. **30**, 3344 (1991).

[19] A. Löffl, S. Wieder, B. Rech, O. Kluth, C. Beneking, and H. Wagner, in *Proceedings of the 14th European Photovoltaic Solar Energy Conference* (Barcelona, Spain, 1996), p. 2089.

[20] R. Klenk, M. Linke, H. Angermann, C. Kelch, M. Kirsch, J. Klaer, and C. Köble, in *Proceedings of the Workshop TCO Für Dünnschichtsolarzellen Und Andere Anwendungen III* (Freyburg, Germany, 2005), p. 79.

[21] N. F. Foster, J. Vac. Sci. Technol. **6**, 111 (1969).

[22] C. Agashe, O. Kluth, J. Hüpkes, U. Zastrow, B. Rech, and M. Wuttig, J. Appl. Phys. **95**, 1911 (2004).

[23] E. Fortunato, A. Gonçalves, V. Assunção, A. Marques, H. Águas, L. Pereira, I. Ferreira, and R. Martins, Thin Solid Films **442**, 121 (2003).

[24] M. Berginski, J. Hüpkes, M. Schulte, G. Schöpe, H. Stiebig, B. Rech, and M. Wuttig, J. Appl. Phys. **101**, 074903 (2007).

[25] O. Kluth, G. Schöpe, J. Hüpkes, C. Agashe, J. Müller, and B. Rech, Thin Solid Films **442**, 80 (2003).

[26] H. Zhu, E. Bunte, J. Hüpkes, H. Siekmann, and S. Huang, Thin Solid Films **517**, 3161 (2009).

[27] N. W. Ashcroft and N. D. Mermin, *Solid State Physics* (Brooks Cole, 1976).

[28] F. Ruske, M. Roczen, K. Lee, M. Wimmer, S. Gall, J. Hüpkes, D. Hrunski, and B. Rech, J. Appl. Phys. **107**, 013708 (2010).

[29] T. Tohsophon, J. Hüpkes, H. Siekmann, B. Rech, M. Schultheis, and N. Sirikulrat, Thin Solid Films **516**, 4628 (2008).

[30] D. Greiner, N. Papathanasiou, A. Pflug, F. Ruske, and R. Klenk, Thin Solid Films **517**, 2291 (2009).

[31] J. Hüpkes, J. Müller, and B. Rech, in *Transparent Conductive Zinc Oxide: Basics and Applications in Thin Film Solar Cells*, edited by K. Ellmer, A. Klein, and B. Rech (Springer, Berlin Heidelberg, 2008), p. 359.

[32] J. A. Thornton, J. Vac. Sci. Technol. **11**, 666 (1974).

[33] A. N. Mariano and R. E. Hanneman, J. Appl. Phys. **34**, 384 (1963).

[34] W. Jo, S. Kim, and D. Kim, Acta Mater. **53**, 4185 (2005).

[35] B. Szyszka, V. Sittinger, W. Dewald, A. Pflug, S. Ulrich, A. Kaiser, and W. Werner, in *52nd Annual Technical Conference Proceedings* (Santa Clara, CA, 2009), p. 42.

[36] L. Groenendaal, F. Jonas, D. Freitag, H. Pielartzik, and J. R. Reynolds, Adv. Mater. **12**, 481 (2000).

[37] Z. Wu, Z. Chen, X. Du, J. M. Logan, J. Sippel, M. Nikolou, K. Kamaras, J. R. Reynolds, D. B. Tanner, A. F. Hebard, and A. G. Rinzler, Science **305**, 1273 (2004).

[38] J. K. Wassei and R. B. Kaner, Mater. Today **13**, 52 (2010).

[39] A. J. Freeman, K. R. Poeppelmeier, T. O. Mason, R. P. H. Chang, and T. J. Marks, MRS Bull. **25**, 45 (2000).

[40] T. Minami, Semicond. Sci. Technol. **20**, S35 (2005).

[41] O. Madelung, *Semiconductors - Basic Data*, 2nd ed. (Springer, 1996).

[42] O. Kluth, C. Zahren, H. Stiebig, B. Rech, and H. Schade, in *Proceedings of the 19th European Photovoltaic Solar Energy Conference* (Paris, France, 2004), p. 1587.

[43] W. Beyer, J. Hüpkes, and H. Stiebig, Thin Solid Films **516**, 147 (2007).

[44] K. Ellmer and A. Klein, in *Transparent Conductive Zinc Oxide: Basics and Applications in Thin Film Solar Cells*, edited by K. Ellmer, A. Klein, and B. Rech (Springer, Berlin Heidelberg, 2008), p. 1.

[45] S. Major, S. Kumar, M. Bhatnagar, and K. L. Chopra, Appl. Phys. Lett. **49**, 394 (1986).

[46] T. Minami, H. Sato, H. Nanto, and S. Takata, Thin Solid Films **176**, 277 (1989).

[47] H. Ko, Y. Chen, S. Hong, H. Wenisch, T. Yao, and D. Look, Appl. Phys. Lett. **77**, 3761 (2000).

[48] S. Major, A. Banerjee, and K. Chopra, Thin Solid Films **108**, 333 (1983).

[49] T. Minami, H. Sato, H. Nanto, and S. Takata, Jpn. J. Appl. Phys. **24**, L781 (1985).

[50] A. B. M. A. Ashrafi, A. Ueta, A. Avramescu, H. Kumano, I. Suemune, Y. Ok, and T. Seong, Appl. Phys. Lett. **76**, 550 (2000).

[51] C. Bundesmann, R. Schmidt-Grund, and M. Schubert, in *Transparent Conductive Zinc Oxide: Basics and Applications in Thin Film Solar Cells*, edited by K. Ellmer, A. Klein, and B. Rech (Springer, Berlin Heidelberg, 2008), p. 79.

[52] H. Morkoç and Ü. Özgür, *Zinc Oxide: Fundamentals, Materials and Device Technology* (Wiley-VCH, 2009).

[53] E. H. Kisi and M. M. Elcombe, Acta Crystallogr., Sect. C: Cryst. Struct. Commun. **45**, 1867 (1989).

[54] M. Han and J. Jou, Thin Solid Films **260**, 58 (1995).

[55] H. Ibach, Phys. Status Solidi B **33**, 257 (1969).

[56] P. Drude, Ann. Phys. **306**, 566 (1900).

[57] S. J. Pearton, D. P. Norton, K. Ip, Y. W. Heo, and T. Steiner, Prog. Mater. Sci. **50**, 293 (2005).

[58] B. Utsch and A. Hausmann, Z. Phys. B: Condens. Matter. **21**, 27 (1975).

[59] K. Maeda, M. Sato, I. Niikura, and T. Fukuda, Semicond. Sci. Technol. **20**, S49 (2005).

[60] T. Minami, H. Nanto, and S. Takata, Jpn. J. Appl. Phys. **23**, L280 (1984).

[61] S. B. Zhang, S. Wei, and A. Zunger, J. Appl. Phys. **83**, 3192 (1998).

[62] B. K. Meyer, J. Sann, D. M. Hofmann, C. Neumann, and A. Zeuner, Semicond. Sci. Technol. **20**, S62 (2005).

[63] C. G. Van de Walle, Phys. Rev. Lett. **85**, 1012 (2000).

[64] D. M. Hofmann, A. Hofstaetter, F. Leiter, H. Zhou, F. Henecker, B. K. Meyer, S. B. Orlinskii, J. Schmidt, and P. G. Baranov, Phys. Rev. Lett. **88**, 045504 (2002).

[65] S. H. Lee, T. S. Lee, K. S. Lee, B. Cheong, Y. D. Kim, and W. M. Kim, J. Phys. D: Appl. Phys. **41**, 095303 (2008).

[66] D. C. Look, D. C. Reynolds, J. R. Sizelove, R. L. Jones, C. W. Litton, G. Cantwell, and W. C. Harsch, Solid State Commun. **105**, 399 (1998).

[67] N. F. Mott, Contemp. Phys. **14**, 401 (1973).

[68] G. Masetti, M. Severi, and S. Solmi, IEEE Trans. on Electron Devices **30**, 764 (1983).

[69] K. Ellmer and R. Mientus, Thin Solid Films **516**, 4620 (2008).

[70] D. Chattopadhyay and H. J. Queisser, Rev. Mod. Phys. **53**, 745 (1981).

[71] E. Conwell and V. F. Weisskopf, Phys. Rev. **77**, 388 (1950).

[72] T. Pisarkiewicz, K. Zakrzewska, and E. Leja, Thin Solid Films **174**, 217 (1989).

[73] J. Y. W. Seto, J. Appl. Phys. **46**, 5247 (1975).

[74] G. Baccarani, B. Riccò, and G. Spadini, J. Appl. Phys. **49**, 5565 (1978).

[75] K. Ellmer and R. Mientus, Thin Solid Films **516**, 5829 (2008).

[76] S. S. Devlin, in *Physics and Chemistry of II-VI Compounds*, edited by M. Aven and J. S. Prener (North-Holland, Amsterdam, 1967), p. 549.

[77] J. Bardeen and W. Shockley, Phys. Rev. **80**, 72 (1950).

[78] D. L. Rode, in *Semiconductors and Semimetals*, edited by R. K. Willardson and A. Beer (Academic, New York, 1975), p. 1.

[79] J. D. Zook, Phys. Rev. **136**, A869 (1964).

[80] P. Wagner and R. Helbig, J. Phys. Chem. Solids **35**, 327 (1974).

[81] C. Erginsoy, Phys. Rev. **79**, 1013 (1950).

[82] A. L. Dawar, A. K. Jain, and C. Jagadish, *Semiconducting Transparent Thin Films* (Taylor & Francis, 1995).

[83] L. J. van der Pauw, Philips Res. Repts. **13**, 1 (1958).

[84] J. F. Chang, H. H. Kuo, I. C. Leu, and M. H. Hon, Sens. Actuators, B **84**, 258 (2002).

[85] A. van der Drift, Philips Res. Repts. **22**, 267 (1967).

[86] R. L. Petritz, Phys. Rev. **110**, 1254 (1958).

[87] N. Ashkenov, B. N. Mbenkum, C. Bundesmann, V. Riede, M. Lorenz, D. Spemann, E. M. Kaidashev, A. Kasic, M. Schubert, M. Grundmann, G. Wagner, H. Neumann, V. Darakchieva, H. Arwin, and B. Monemar, J. Appl. Phys. **93**, 126 (2003).

[88] C. Kittel, *Introduction to Solid State Physics*, 8th ed. (Wiley, 2004).

[89] B. E. Sernelius, K. Berggren, Z. Jin, I. Hamberg, and C. G. Granqvist, Phys. Rev. B **37**, 10244 (1988).

[90] E. Burstein, Phys. Rev. **93**, 632 (1954).

[91] T. S. Moss, Proc. Phys. Soc. B **67**, 775 (1954).

[92] M. Tanenbaum and H. B. Briggs, Phys. Rev. **91**, 1561 (1953).

[93] H. C. Gatos and M. C. Lavine, J. Electrochem. Soc. **107**, 427 (1960).

[94] M. Pourbaix, *Atlas of Electrochemical Equilibria in Aqueous Solutions* (National Association of Corrosion Engineers, Houston, 1974).

[95] M. Trautz, Z. Anorg. Allg. Chem. **96**, 1 (1916).

[96] J. Hu and R. G. Gordon, Solar Cells **30**, 437 (1991).

[97] E. M. Kaidashev, M. Lorenz, H. von Wenckstern, A. Rahm, H. Semmelhack, K. Han, G. Benndorf, C. Bundesmann, H. Hochmuth, and M. Grundmann, Appl. Phys. Lett. **82**, 3901 (2003).

[98] A. Suzuki, T. Matsushita, N. Wada, Y. Sakamoto, and M. Okuda, Jpn. J. Appl. Phys. **35**, L56 (1996).

[99] J. H. Morgan and D. E. Brodie, Can. J. Phys. **60**, 1387 (1982).

[100] M. Jin, J. Feng, Z. De-heng, M. Hong-lei, and L. Shu-ying, Thin Solid Films **357**, 98 (1999).

[101] T. Okamura, Y. Seki, S. Nagakari, and H. Okushi, Jpn. J. Appl. Phys. **31**, 3218 (1992).

[102] T. Yoshida, M. Iwaya, H. Ando, T. Oekermann, K. Nonomura, D. Schlettwein, D. Wöhrle, and H. Minoura, Chem. Commun. 400 (2004).

[103] J. S. Chapin, Res. Dev. **25**, 37 (1974).

[104] W. De Bosscher and H. Lievens, Thin Solid Films **351**, 15 (1999).

[105] U. Heister, J. Krempel-Hesse, J. Szczyrbowski, G. Teschner, J. Bruch, and G. Bräuer, Thin Solid Films **351**, 27 (1999).

[106] J. Müller, J. Liu, J. Schroeder, D. Marquardt, and R. Trassl, in *Proceedings of the 22nd European Photovoltaic Solar Energy Conference* (Milan, Italy, 2007), p. 2229.

[107] S. Pung, K. Choy, X. Hou, and C. Shan, Nanotechnol. **19**, 435609 (2008).

[108] N. Fujimura, T. Nishihara, S. Goto, J. Xu, and T. Ito, J. Cryst. Growth **130**, 269 (1993).

[109] T. Minegishi, J. Yoo, H. Suzuki, Z. Vashaei, K. Inaba, K. Shim, and T. Yao, J. Vac. Sci. Technol. B **23**, 1286 (2005).

[110] T. Minegishi, A. Ishizawa, J. Kim, D. Kim, S. Ahn, S. Park, J. Park, I. Im, D. C. Oh, H. Nakano, K. Fujii, H. Jeon, and T. Yao, J. Vac. Sci. Technol. B **26**, 1120 (2008).

[111] B. A. Movchan and A. V. Demchishin, Phys. Met. Metallogr. **28**, 83 (1969).

[112] J. Hüpkes, B. Rech, O. Kluth, T. Repmann, B. Zwaygardt, J. Müller, R. Drese, and M. Wuttig, Sol. Energy Mater. Sol. Cells **90**, 3054 (2006).

[113] O. Kluth, G. Schöpe, B. Rech, R. Menner, M. Oertel, K. Orgassa, and H. Werner Schock, Thin Solid Films **502**, 311 (2006).

[114] G. Jost, E. Bunte, J. Worbs, H. Siekmann, and J. Hüpkes, in *Proceedings of the 25th European Photovoltaic Solar Energy Conference* (Valencia, Spain, 2010), p. 3078.

[115] H. Zhu, J. Hüpkes, E. Bunte, and S. Huang, Surf. Coat. Technol. **205**, 773 (2010).

[116] T. Minami, H. Nanto, S. Shooji, and S. Takata, Thin Solid Films **111**, 167 (1984).

[117] S. Takata, T. Minami, and H. Nanto, Thin Solid Films **135**, 183 (1986).

[118] T. Minami, T. Miyata, and T. Yamamoto, J. Vac. Sci. Technol. A **17**, 1822 (1999).

[119] M. Berginski, J. Hüpkes, W. Reetz, B. Rech, and M. Wuttig, Thin Solid Films **516**, 5836 (2008).

[120] M. Berginski, Lichtstreuende Oberflächen, Schichten Und Schichtsysteme Zur Verbesserung Der Lichteinkopplung in Silizium-Dünnschichtsolarzellen, Dissertation, Rheinisch-Westfählische Technische Hochschule, 2007.

[121] T. J. Coutts, D. L. Young, and X. Li, MRS Bull. **25**, 58 (2000).

[122] International Electrotechnical Committee 61646 Ed. 2.0, (2008).

[123] H. Stiebig, S. Haas, W. Reetz, A. Gordijn, J. Hüpkes, and W. Beyer, in *Proceedings of the 22nd European Photovoltaic Solar Energy Conference* (Milan, Italy, 2007), p. 1827.

[124] T. Tohsophon, J. Hüpkes, S. Calnan, W. Reetz, B. Rech, W. Beyer, and N. Sirikulrat, Thin Solid Films **511-512**, 673 (2006).

[125] R. Klenk, in *Transparent Conductive Zinc Oxide: Basics and Applications in Thin Film Solar Cells*, edited by K. Ellmer, A. Klein, and B. Rech (Springer, Berlin Heidelberg, 2008), p. 415.

[126] W. Lin, R. Ma, J. Xue, and B. Kang, Sol. Energy Mater. Sol. Cells **91**, 1902 (2007).

[127] T. Minami, T. Miyata, Y. Ohtani, and T. Kuboi, Phys. Status Solidi RRL **1**, R31 (2007).

[128] D. L. Staebler and C. R. Wronski, Appl. Phys. Lett. **31**, 292 (1977).

[129] P. Würfel, *Physics of Solar Cells: From Principles to New Concepts* (Wiley-VCH, 2005).

[130] G. Schöpe, DC-Sputtern Transparenter, Leitfähiger Zinkoxidschichten Für Dünnschichtsolarzellen Von Metallischen Zn:Al-Targets, Diplomarbeit, Fachhochschule Aachen, 1998.

[131] O. Kluth, Texturierte Zinkoxidschichten Für Silizium-Dünnschichtsolarzellen, Dissertation, Rheinisch-Westfählische Technische Hochschule, 2001.

[132] E. Bunte, H. B. Zhu, and J. Hüpkes, in *Proceedings of the 23rd European Photovoltaic Solar Energy Conference* (Valencia, Spain, 2008), p. 2105.

[133] J. Hüpkes, B. Rech, S. Calnan, O. Kluth, U. Zastrow, H. Siekmann, and M. Wuttig, Thin Solid Films **502**, 286 (2006).

[134] C. R. Osterwald, *Terrestrial Photovoltaic Module Accelerated Test-to-Failure Protocol* (National Renewable Energy Laboratory, Golden, Colorado, 2008).

[135] T. Repmann, Stapelsolarzellen Aus Amorphem Und Mikrokristallinem Silizium, Dissertation, Rheinisch-Westfählische Technische Hochschule, 2003.

[136] S. Haas, Untersuchung Und Optimierung Der Serienverschaltung Von Silizium-Dünnschicht-Solarmodulen, Dissertation, Rheinisch-Westfählische Technische Hochschule, 2010.

[137] F. J. Giessibl, Mater. Today **8**, 32 (2005).

[138] G. Binnig, C. F. Quate, and C. Gerber, Phys. Rev. Lett. **56**, 930 (1986).

[139] G. Binnig and H. Rohrer, Rev. Mod. Phys. **71**, S324 (1999).

[140] H. Yamada, in *Roadmap of Scanning Probe Microscopy*, edited by S. Morita (Springer, 2007), p. 101.

[141] S. J. Fang, W. Chen, T. Yamanaka, and C. R. Helms, Appl. Phys. Lett. **68**, 2837 (1996).

[142] R. V. Lapshin, Nanotechnol. **15**, 1135 (2004).

[143] R. H. Bridgham and S. Baumann, Symp. Proc. Electrochem. Soc. **PV 94-9**, 277 (1994).

[144] J. Cao, Charakterisierung Von Gesputterten Und Geätzten ZnO-Schichten Für Silizium-Dünnschichtsolarzellen, Bachelorarbeit, Rheinisch-Westfählische Technische Hochschule, 2010.

[145] M. Schulte, C. Zahren, and H. Stiebig, in *Proceedings of the 21st European Photovoltaic Solar Energy Conference* (Dresden, 2006), p. 1703.

[146] H. Stiebig, M. Schulte, C. Zahren, C. Haase, B. Rech, and P. Lechner, in *Photonics for Solar Energy Systems*, edited by A. Gombert (SPIE, Strasbourg, France, 2006), p. 619701.

[147] S. Beucher and C. Lantuéjoul, in *Proc. Int. Workshop on Image Processing* (Rennes, France, 1979), p. 17.

[148] A. D. Garetto, D. D. Griffis, P. E. Russell, P. D. Rack, and J. Fowlkes, Microsc. Microanal. **11**, 850 (2005).

[149] H. Lüth, *Surfaces and Interfaces of Solid Materials*, 3rd ed. (Springer, 1995).

[150] M. Su, Z. Pan, and V. P. Dravid, J. Microsc. **216**, 194 (2004).

[151] R. Egerton, *Physical Principles of Electron Microscopy* (Springer, 2005).

[152] M. Minsky, Scanning **10**, 138, 128 (1988).

[153] H. Seiler, J. Appl. Phys. **54**, R1 (1983).

[154] E. Schreiber and H. Fitting, J. Electron. Spectrosc. Relat. Phenom. **124**, 25 (2002).

[155] W. Kwong and W. Zhang, in *Semiconductor Manufacturing, 2005. ISSM 2005, IEEE International Symposium On* (2005), p. 469.

[156] L. A. Giannuzzi and F. A. Stevie, Micron **30**, 197 (1999).

[157] H. P. Klug and L. E. Alexander, *X-Ray Diffraction Procedures: For Polycrystalline and Amorphous Materials*, 2nd ed. (Wiley-Interscience, 1974).

[158] H. T. Stokes, *Solid State Physics* (Prentice Hall, 1987).

[159] A. L. Patterson, Phys. Rev. **56**, 978 (1939).

[160] P. Scherrer, Nachr. Ges. Wiss. Götingen Math.-Phys. Kl. **2**, 98 (1918).

[161] M. Deutsch and M. Hart, Phys. Rev. B **26**, 5558 (1982).

[162] J. Hüpkes, Untersuchung Des Reactiven Sputterprozesses Zur Herstellung Von Aluminiumdotierten Zinkoxid-Schichten Für Silizium-Dünnschichtsolarzellen, Dissertation, Rheinisch-Westfählische Technische Hochschule, 2004.

[163] J. G. E. Gardeniers, Z. M. Rittersma, and G. J. Burger, J. Appl. Phys. **83**, 7844(1998).

[164] W. Water and S. Chu, Mater. Lett. **55**, 67 (2002).

[165] H. E. Bennett and J. O. Porteus, J. Opt. Soc. Am. **51**, 123 (1961).

[166] Y. Gotoh, A. Adachi, and M. Mizuhashi, Rep. Res. Lab. Asahi Glass Co. Ltd. **37**, 13 (1987).

[167] J. Metzdorf, Appl. Opt. **26**, 1701 (1987).

[168] F. Ruske, A. Pflug, V. Sittinger, W. Werner, B. Szyszka, and D. Christie, Thin Solid Films **516**, 4472 (2008).

[169] Joint Commitee on Powder Diffraction Standards, Powder Diffraction File 80-0075, (1997).

[170] D. Kohl, M. Henzler, and G. Heiland, Surf. Sci. **41**, 403 (1974).

[171] S. B. Zhang, S. Wei, and A. Zunger, Phys. Rev. B **63**, 075205 (2001).

[172] W. Beyer, H. Mell, and W. D. Gill, Solid State Commun. **27**, 185 (1978).

[173] T. I. Kamins, J. Appl. Phys. **42**, 4357 (1971).

[174] G. D. Mahan, L. M. Levinson, and H. R. Philipp, J. Appl. Phys. **50**, 2799 (1979).

[175] P. Kuppusami, G. Vollweiler, D. Rafaja, and K. Ellmer, Appl. Phys. A **80**, 183 (2004).

[176] K. Ellmer, in *Materials Research Society Symposium Proceedings* (Boston, Massachusetts, 2008), p. 1109-B07-05.

[177] H. Kato, M. Sano, K. Miyamoto, and T. Yao, J. Cryst. Growth **265**, 375 (2004).

[178] H. Kato, M. Sano, K. Miyamoto, and T. Yao, Jpn. J. Appl. Phys. **42**, 2241 (2003).

[179] H. Kato, M. Sano, K. Miyamoto, and T. Yao, Jpn. J. Appl. Phys. **42**, L1002 (2003).

[180] W. Zhang, E. Bunte, M. Luysberg, P. Spiekermann, F. Ruske, and J. Hüpkes, Surf. Coat. Technol. **205**, S223 (2011).

[181] D. Köhl, M. Luysberg, and M. Wuttig, Phys. Status Solidi RRL **3**, 236 (2009).

[182] S. Roy and S. Basu, Bull. Mater. Sci. **25**, 513 (2002).

[183] H. Lim, D. Y. Lee, and Y. Oh, Sens. Actuators, A **125**, 405 (2006).

[184] J. B. L. Martins, E. Longo, J. G. R. Tostes, C. Taft, and J. Andres, J. Mol. Struct. THEOCHEM **303**, 19 (1994).

[185] O. Dulub, B. Meyer, and U. Diebold, Phys. Rev. Lett. **95**, 136101 (2005).

[186] F. Vila, O. N. Ventura, J. Varela, and E. Longo, J. Mol. Struct. THEOCHEM **305**, 175 (1994).

[187] T. Minami, T. Kuboi, T. Miyata, and Y. Ohtani, Phys. Status Solidi A **205**, 255 (2008).

[188] X. Jiang, C. Jia, and R. Hong, J. Cryst. Growth **289**, 464 (2006).

[189] A. S. Shaporev, V. K. Ivanov, A. E. Baranchikov, O. S. Polezhaeva, and Y. D. Tret'yakov, Russ. J. Inorg. Chem. **52**, 1811 (2007).

[190] G. Heiland and P. Kunstmann, Surf. Sci. **13**, 72 (1969).

[191] Y. H. Kim, K. S. Lee, T. S. Lee, B. Cheong, T. Seong, and W. M. Kim, Curr. Appl. Phys. **10**, S278 (2010).

[192] D. Kang, S. Kuk, K. Ji, S. Ahn, and M. Han, Phys. Status Solidi C **7**, 925 (2010).

[193] J. Müller, G. Schöpe, O. Kluth, B. Rech, V. Sittinger, B. Szyszka, R. Geyer, P. Lechner, H. Schade, M. Ruske, G. Dittmar, and H. Bochem, Thin Solid Films **442**, 158 (2003).

[194] J. Chen, S. Jang, F. Ren, Y. Li, H. Kim, D. P. Norton, S. J. Pearton, A. Osinsky, S. N. G. Chu, and J. F. Weaver, J. Elec. Mater. **35**, 516 (2006).

[195] S. H. Lee, T. Minegishi, J. S. Park, S. H. Park, J. Ha, H. Lee, H. Lee, S. Ahn, J. Kim, H. Jeon, and T. Yao, Nano Lett. **8**, 2419 (2008).

[196] C. Ophus, E. Luber, and D. Mitlin, Acta Mater. **57**, 1327 (2009).

[197] M. Valtiner, S. Borodin, and G. Grundmeier, Langmuir **24**, 5350 (2008).

[198] Hydroflouric Acid; MSDS No. 6373CR, http://Msds.dupont.com/Msds/Pdfs/EN/PEN_09004a2f801b4efc.pdf (2005).

[199] G. A. Jeffrey, *An Introduction to Hydrogen Bonding* (Oxford University Press, 1997).

[200] C. J. T. de Grotthuss, Ann. Chim. (Paris) **58**, 54 (1806).

[201] S. S. Iyengar, M. K. Petersen, T. J. F. Day, C. J. Burnham, V. E. Teige, and G. A. Voth, J. Chem. Phys. **123**, 084309 (2005).

[202] E. S. Stoyanov, I. V. Stoyanova, and C. A. Reed, J. Am. Chem. Soc. **132**, 1484 (2010).

[203] D. D. Perrin, *Ionization Constants of Inorganic Acids and Bases in Aqueous Solution*, 2nd ed. (Pergamon, Oxford, United Kingdom, 1982).

[204] K. W. Kolasinski, J. Electrochem. Soc. **152**, J99 (2005).

[205] P. A. Giguere and S. Turrell, J. Am. Chem. Soc. **102**, 5473 (1980).

[206] C. Iliescu, J. Jing, F. E. Tay, J. Miao, and T. Sun, Surf. Coat. Technol. **198**, 314 (2005).

[207] C. K. Carniglia, Opt. Eng. **18**, 104 (1979).

[208] M. Schulte, S. Jorke, C. Zahren, J. Hüpkes, and H. Stiebig, in *Proceedings of the 22nd European Photovoltaic Solar Energy Conference* (Milan, Italy, 2007), p. 2190.

[209] M. Kambe, N. Taneda, K. Masumo, S. Higashi, A. Takahashi, W. Nishida, T. Ikeda, T. Oyama, K. Sato, T. Matsui, H. Sai, and M. Kondo, in *Proceedings of the 24th European Photovoltaic Solar Energy Conference* (Hamburg, Germany, 2009), p. 2290.

[210] O. Isabella, F. Moll, J. Krc, and M. Zeman, Phys. Status Solidi A **207**, 642 (2010).

[211] T. Söderström, F. Haug, V. Terrazzoni-Daudrix, M. Python, and C. Ballif, in *Proceedings of the 24th European Photovoltaic Solar Energy Conference* (Hamburg, Germany, 2009), p. 2412.

[212] M. Zeman, J. A. Willemen, L. L. A. Vosteen, G. Tao, and J. W. Metselaar, Sol. Energy Mater. Sol. Cells **46**, 81 (1997).

[213] A. Gordijn, S. Schicho, S. Muthmann, T. Kilper, H. Zhu, E. Bunte, and J. Hüpkes, Phys. Status Solidi A **207**, 678 (2010).

[214] J. Hüpkes, B. Rech, B. Sehrbrock, O. Kluth, J. Müller, H. P. Bochem, and M. Wuttig, in *Proceedings of the 19th European Photovoltaic Solar Energy Conference* (Paris, France, 2004), p. 1415.

[215] M. Python, E. Vallat-Sauvain, J. Bailat, D. Dominé, L. Fesquet, A. Shah, and C. Ballif, J. Non-Cryst. Solids **354**, 2258 (2008).

Acknowledgments

I would like to thank all those who helped make this work possible. Specific thanks are due to the following people for their contribution:

- Dr. Jürgen Hüpkes, for being an excellent supervisor who struck the perfect balance between directed projects and encouraging self-directed projects, yielding an environment where results were plentiful;

- Prof. Dr. Uwe Rau, for providing this opportunity to work at such a world-renowned institution, and providing feedback on my various projects;

- Prof. Dr. Bernd Rech, for taking the time to read and evaluate this work;

- Dr. Eerke Bunte, for insightful discussion, especially regarding the applications for new etch processes;

- Dr. Sascha E. Pust, for sharing his chemical expertise and his strong contribution to the polycrystalline ZnO:Al etch model;

- Prof. Dr. Reinhard Carius, Dr. Martina Luysberg, Dr. Wolfhard Beyer, Dr. Melanie Schulte, and Dr. Aad Gordijn for availing their knowledge on TEM, AFM, electrical transport, optics, and solar cells, to name a few;

- All those who helped with sample deposition: Janine Worbs and Hilde Siekmann for standard front and back ZnO:Al deposition; Joachim Kirchhoff for silicon deposition; Dr. Matthias Meier, Andreas Mück, and Dr. Dzmitry Hrunski for the NF_3 etching of silicon;

- The many who assisted with sample characterization: Alain Doumit, Ting Guo, and Brigitte Zwaygardt for optical measurements; Silvia Jorke for the post-measurement analysis of AFM images; Wilfried Reetz, Dr. Etienne Moulin, Carsten Grates, and Janis Kroll for solar cell characterization and quantum efficiency measurements; Uwe Zastrow and Lars Nießen for SIMS analysis; Hans Peter Bochem and Elke Brauweiler-Reuters for SEM imaging; Philipp Spiekermann for TEM sample preparation and measurement; Doris Meertens for FIB preparation; Dominik Köhl for XRD analysis; Gunnar Schöpe for laser ablation; and Dr. Torsten Bronger for clean room training;

- Carolin Ulbrich, David Wippler, Katharina Baumgartner, Dr. Bart Pieters, Max Siegloch, Jonas Noll, Sandra Schicho, Marek Warzecha, Wanjiao Böttler, and Maurice Nuys for assistance in manuscript preparation, proofreading, and the German language;

Acknowledgments

- Hongbing Zhu and Wendi Zhang, for the many beneficial collaborations regarding the texturization of ZnO:Al;

- Dr. Florian Ruske and Mark Wimmer at Helmholtz-Zentrum Berlin for many profitable collaborations on the annealing and damp-heat degradation of ZnO:Al;

- Sven Ring and Dr. Frank Säuberlich at Sontor for providing industrially relevant ZnO:Al;

- Andrea Mülheims, Roswitha Bley, and Dirk Schramm for all the behind the scenes work to keep me employed here with contracts, taxes, visas, etc.;

- Dr. Bernhard Mogge for work in securing the rights to the etch processes within the patent office;

- Finally, special thanks are in order for my wife Rebecca Owen, who not only provided emotional support and encouragement, but also acted as editor for my often bad English.

1. **Einsatz von multispektralen Satellitenbilddaten in der Wasserhaushalts- und Stoffstrommodellierung – dargestellt am Beispiel des Rureinzugsgebietes**
   von C. Montzka (2008), XX, 238 Seiten
   ISBN: 978-3-89336-508-1

2. **Ozone Production in the Atmosphere Simulation Chamber SAPHIR**
   by C. A. Richter (2008), XIV, 147 pages
   ISBN: 978-3-89336-513-5

3. **Entwicklung neuer Schutz- und Kontaktierungsschichten für Hochtemperatur-Brennstoffzellen**
   von T. Kiefer (2008), 138 Seiten
   ISBN: 978-3-89336-514-2

4. **Optimierung der Reflektivität keramischer Wärmedämmschichten aus Yttrium-teilstabilisiertem Zirkoniumdioxid für den Einsatz auf metallischen Komponenten in Gasturbinen**
   von A. Stuke (2008), X, 201 Seiten
   ISBN: 978-3-89336-515-9

5. **Lichtstreuende Oberflächen, Schichten und Schichtsysteme zur Verbesserung der Lichteinkopplung in Silizium-Dünnschichtsolarzellen**
   von M. Berginski (2008), XV, 171 Seiten
   ISBN: 978-3-89336-516-6

6. **Politikszenarien für den Klimaschutz IV – Szenarien bis 2030**
   hrsg.von P. Markewitz, F. Chr. Matthes (2008), 376 Seiten
   ISBN 978-3-89336-518-0

7. **Untersuchungen zum Verschmutzungsverhalten rheinischer Braunkohlen in Kohledampferzeugern**
   von A. Schlüter (2008), 164 Seiten
   ISBN 978-3-89336-524-1

8. **Inorganic Microporous Membranes for Gas Separation in Fossil Fuel Power Plants**
   by G. van der Donk (2008), VI, 120 pages
   ISBN: 978-3-89336-525-8

9. **Sinterung von Zirkoniumdioxid-Elektrolyten im Mehrlagenverbund der oxidkeramischen Brennstoffzelle (SOFC)**
   von R. Mücke (2008), VI, 165 Seiten
   ISBN: 978-3-89336-529-6

10. **Safety Considerations on Liquid Hydrogen**
    by K. Verfondern (2008), VIII, 167 pages
    ISBN: 978-3-89336-530-2

11. **Kerosinreformierung für Luftfahrtanwendungen**
von R. C. Samsun (2008), VII, 218 Seiten
ISBN: 978-3-89336-531-9

12. **Der 4. Deutsche Wasserstoff Congress 2008 – Tagungsband**
hrsg. von D. Stolten, B. Emonts, Th. Grube (2008), 269 Seiten
ISBN: 978-3-89336-533-3

13. **Organic matter in Late Devonian sediments as an indicator for environmental changes**
by M. Kloppisch (2008), XII, 188 pages
ISBN: 978-3-89336-534-0

14. **Entschwefelung von Mitteldestillaten für die Anwendung in mobilen Brennstoffzellen-Systemen**
von J. Latz (2008), XII, 215 Seiten
ISBN: 978-3-89336-535-7

15. **RED-IMPACT**
Impact of Partitioning, Transmutation and Waste Reduction Technologies on the Final Nuclear Waste Disposal
SYNTHESIS REPORT
ed. by W. von Lensa, R. Nabbi, M. Rossbach (2008), 178 pages
ISBN 978-3-89336-538-8

16. **Ferritic Steel Interconnectors and their Interactions with Ni Base Anodes in Solid Oxide Fuel Cells (SOFC)**
by J. H. Froitzheim (2008), 169 pages
ISBN: 978-3-89336-540-1

17. **Integrated Modelling of Nutrients in Selected River Basins of Turkey**
Results of a bilateral German-Turkish Research Project
project coord. M. Karpuzcu, F. Wendland (2008), XVI, 183 pages
ISBN: 978-3-89336-541-8

18. **Isotopengeochemische Studien zur klimatischen Ausprägung der Jüngeren Dryas in terrestrischen Archiven Eurasiens**
von J. Parplies (2008), XI, 155 Seiten, Anh.
ISBN: 978-3-89336-542-5

19. **Untersuchungen zur Klimavariabilität auf dem Tibetischen Plateau - Ein Beitrag auf der Basis stabiler Kohlenstoff- und Sauerstoffisotope in Jahrringen von Bäumen waldgrenznaher Standorte**
von J. Griessinger (2008), XIII, 172 Seiten
ISBN: 978-3-89336-544-9

20. **Neutron-Irradiation + Helium Hardening & Embrittlement Modeling of 9%Cr-Steels in an Engineering Perspective (HELENA)**
by R. Chaouadi (2008), VIII, 139 pages
ISBN: 978-3-89336-545-6

21. **in Bearbeitung**

22. **Verbundvorhaben APAWAGS (AOEV und Wassergenerierung) – Teilprojekt: Brennstoffreformierung – Schlussbericht**
von R. Peters, R. C. Samsun, J. Pasel, Z. Porš, D. Stolten (2008), VI, 106 Seiten
ISBN: 978-3-89336-547-0

23. **FREEVAL**
Evaluation of a Fire Radiative Power Product derived from Meteosat 8/9 and Identification of Operational User Needs
Final Report
project coord. M. Schultz, M. Wooster (2008), 139 pages
ISBN: 978-3-89336-549-4

24. **Untersuchungen zum Alkaliverhalten unter Oxycoal-Bedingungen**
von C. Weber (2008), VII, 143, XII Seiten
ISBN: 978-3-89336-551-7

25. **Grundlegende Untersuchungen zur Freisetzung von Spurstoffen, Heißgaschemie, Korrosionsbeständigkeit keramischer Werkstoffe und Alkalirückhaltung in der Druckkohlenstaubfeuerung**
von M. Müller (2008), 207 Seiten
ISBN: 978-3-89336-552-4

26. **Analytik von ozoninduzierten phenolischen Sekundärmetaboliten in *Nicotiana tabacum* L. cv Bel W3 mittels LC-MS**
von I. Koch (2008), III, V, 153 Seiten
ISBN 978-3-89336-553-1

27. **IEF-3 Report 2009. Grundlagenforschung für die Anwendung**
(2009), ca. 230 Seiten
ISBN: 978-3-89336-554-8

28. **Influence of Composition and Processing in the Oxidation Behavior of MCrAlY-Coatings for TBC Applications**
by J. Toscano (2009), 168 pages
ISBN: 978-3-89336-556-2

29. **Modellgestützte Analyse signifikanter Phosphorbelastungen in hessischen Oberflächengewässern aus diffusen und punktuellen Quellen**
von B. Tetzlaff (2009), 149 Seiten
ISBN: 978-3-89336-557-9

30. **Nickelreaktivlot / Oxidkeramik – Fügungen als elektrisch isolierende Dichtungskonzepte für Hochtemperatur-Brennstoffzellen-Stacks**
von S. Zügner (2009), 136 Seiten
ISBN: 978-3-89336-558-6

31. **Langzeitbeobachtung der Dosisbelastung der Bevölkerung in radioaktiv kontaminierten Gebieten Weißrusslands – Korma-Studie**
von H. Dederichs, J. Pillath, B. Heuel-Fabianek, P. Hill, R. Lennartz (2009), Getr. Pag.
ISBN: 978-3-89336-532-3

32. **Herstellung von Hochtemperatur-Brennstoffzellen über physikalische Gasphasenabscheidung**
von N. Jordán Escalona (2009), 148 Seiten
ISBN: 978-3-89336-532-3

33. **Real-time Digital Control of Plasma Position and Shape on the TEXTOR Tokamak**
by M. Mitri (2009), IV, 128 pages
ISBN: 978-3-89336-567-8

34. **Freisetzung und Einbindung von Alkalimetallverbindungen in kohlebefeuerten Kombikraftwerken**
von M. Müller (2009), 155 Seiten
ISBN: 978-3-89336-568-5

35. **Kosten von Brennstoffzellensystemen auf Massenbasis in Abhängigkeit von der Absatzmenge**
von J. Werhahn (2009), 242 Seiten
ISBN: 978-3-89336-569-2

36. **Einfluss von Reoxidationszyklen auf die Betriebsfestigkeit von anodengestützten Festoxid-Brennstoffzellen**
von M. Ettler (2009), 138 Seiten
ISBN: 978-3-89336-570-8

37. **Großflächige Plasmaabscheidung von mikrokristallinem Silizium für mikromorphe Dünnschichtsolarmodule**
von T. Kilper (2009), XVII, 154 Seiten
ISBN: 978-3-89336-572-2

38. **Generalized detailed balance theory of solar cells**
by T. Kirchartz (2009), IV, 198 pages
ISBN: 978-3-89336-573-9

39. **The Influence of the Dynamic Ergodic Divertor on the Radial Electric Field at the Tokamak TEXTOR**
von J. W. Coenen (2009), xii, 122, XXVI pages
ISBN: 978-3-89336-574-6

40. **Sicherheitstechnik im Wandel Nuklearer Systeme**
von K. Nünighoff (2009), viii, 215 Seiten
ISBN: 978-3-89336-578-4

41. **Pulvermetallurgie hochporöser NiTi-Legierungen für Implanat- und Dämpfungsanwendungen**
von M. Köhl (2009), XVII, 199 Seiten
ISBN: 978-3-89336-580-7

42. **Einfluss der Bondcoatzusammensetzung und Herstellungsparameter auf die Lebensdauer von Wärmedämmschichten bei zyklischer Temperaturbelastung**
von M. Subanovic (2009), 188, VI Seiten
ISBN: 978-3-89336-582-1

43. **Oxygen Permeation and Thermo-Chemical Stability of Oxygen Permeation Membrane Materials for the Oxyfuel Process**
by A. J. Ellett (2009), 176 pages
ISBN: 978-3-89336-581-4

44. **Korrosion von polykristallinem Aluminiumoxid (PCA) durch Metalljodidschmelzen sowie deren Benetzungseigenschaften**
von S. C. Fischer (2009), 148 Seiten
ISBN: 978-3-89336-584-5

45. **IEF-3 Report 2009. Basic Research for Applications**
(2009), 217 Seiten
ISBN: 978-3-89336-585-2

46. **Verbundvorhaben ELBASYS (Elektrische Basissysteme in einem CFK-Rumpf) - Teilprojekt: Brennstoffzellenabgase zur Tankinertisierung - Schlussbericht**
von R. Peters, J. Latz, J. Pasel, R. C. Samsun, D. Stolten
(2009), xi, 202 Seiten
ISBN: 978-3-89336-587-6

47. **Aging of ^{14}C-labeled Atrazine Residues in Soil: Location, Characterization and Biological Accessibility**
by N. D. Jablonowski (2009), IX, 104 pages
ISBN: 978-3-89336-588-3

48. **Entwicklung eines energetischen Sanierungsmodells für den europäischen Wohngebäudesektor unter dem Aspekt der Erstellung von Szenarien für Energie- und CO_2 - Einsparpotenziale bis 2030**
von P. Hansen (2009), XXII, 281 Seiten
ISBN: 978-3-89336-590-6

49. **Reduktion der Chromfreisetzung aus metallischen Interkonnektoren für Hochtemperaturbrennstofzellen durch Schutzschichtsysteme**
von R. Trebbels (2009), iii, 135 Seiten
ISBN: 978-3-89336-591-3

50. **Bruchmechanische Untersuchung von Metall / Keramik-Verbundsystemen für die Anwendung in der Hochtemperaturbrennstoffzelle**
von B. Kuhn (2009), 118 Seiten
ISBN: 978-3-89336-592-0

51. **Wasserstoff-Emissionen und ihre Auswirkungen auf den arktischen Ozonverlust**
Risikoanalyse einer globalen Wasserstoffwirtschaft
von T. Feck (2009), 180 Seiten
ISBN: 978-3-89336-593-7

52. **Development of a new Online Method for Compound Specific Measurements of Organic Aerosols**
by T. Hohaus (2009), 156 pages
ISBN: 978-3-89336-596-8

53. **Entwicklung einer FPGA basierten Ansteuerungselektronik für Justageeinheiten im Michelson Interferometer**
von H. Nöldgen (2009), 121 Seiten
ISBN: 978-3-89336-599-9

54. **Observation – and model – based study of the extratropical UT/LS**
by A. Kunz (2010), xii, 120, xii pages
ISBN: 978-3-89336-603-3

55. **Herstellung polykristalliner Szintillatoren für die Positronen-Emissions-Tomographie (PET)**
von S. K. Karim (2010), VIII, 154 Seiten
ISBN: 978-3-89336-610-1

56. **Kombination eines Gebäudekondensators mit H2-Rekombinatorelementen in Leichwasserreaktoren**
von S. Kelm (2010), vii, 119 Seiten
ISBN: 978-3-89336-611-8

57. **Plant Leaf Motion Estimation Using A 5D Affine Optical Flow Model**
by T. Schuchert (2010), X, 143 pages
ISBN: 978-3-89336-613-2

58. **Tracer-tracer relations as a tool for research on polar ozone loss**
by R. Müller (2010), 116 pages
ISBN: 978-3-89336-614-9

59. **Sorption of polycyclic aromatic hydrocarbon (PAH) to Yangtze River sediments and their components**
by J. Zhang (2010), X, 109 pages
ISBN: 978-3-89336-616-3

60. **Weltweite Innovationen bei der Entwicklung von CCS-Technologien und Möglichkeiten der Nutzung und des Recyclings von CO_2**
Studie im Auftrag des BMWi
von W. Kuckshinrichs et al. (2010), X, 139 Seiten
ISBN: 978-3-89336-617-0

61. **Herstellung und Charakterisierung von sauerstoffionenleitenden Dünnschichtmembranstrukturen**
von M. Betz (2010), XII, 112 Seiten
ISBN: 978-3-89336-618-7

62. **Politikszenarien für den Klimaschutz V – auf dem Weg zum Strukturwandel, Treibhausgas-Emissionsszenarien bis zum Jahr 2030**
hrsg. von P. Hansen, F. Chr. Matthes (2010), 276 Seiten
ISBN: 978-3-89336-619-4

63. **Charakterisierung Biogener Sekundärer Organischer Aerosole mit Statistischen Methoden**
von C. Spindler (2010), iv, 163 Seiten
ISBN: 978-3-89336-622-4

64. **Stabile Algorithmen für die Magnetotomographie an Brennstoffzellen**
von M. Wannert (2010), ix, 119 Seiten
ISBN: 978-3-89336-623-1

65. **Sauerstofftransport und Degradationsverhalten von Hochtemperaturmembranen für CO2-freie Kraftwerke**
von D. Schlehuber (2010), VII, 139 Seiten
ISBN: 978-3-89336-630-9

66. **Entwicklung und Herstellung von foliengegossenen, anodengestützten Festoxidbrennstoffzellen**
von W. Schafbauer (2010), VI, 164 Seiten
ISBN: 978-3-89336-631-6

67. **Disposal strategy of proton irradiated mercury from high power spallation sources**
by S. Chiriki (2010), xiv, 124 pages
ISBN: 978-3-89336-632-3

68. **Oxides with polyatomic anions considered as new electrolyte materials for solid oxide fuel cells (SOFCs)**
by O. H. Bin Hassan (2010), vii, 121 pages
ISBN: 978-3-89336-633-0

69. **Von der Komponente zum Stack: Entwicklung und Auslegung von HT-PEFC-Stacks der 5 kW-Klasse**
von A. Bendzulla (2010), IX, 203 Seiten
ISBN: 978-3-89336-634-7

70. **Satellitengestützte Schwerewellenmessungen in der Atmosphäre und Perspektiven einer zukünftigen ESA Mission (PREMIER)**
von S. Höfer (2010), 81 Seiten
ISBN: 978-3-89336-637-8

71. **Untersuchungen der Verhältnisse stabiler Kohlenstoffisotope in atmosphärisch relevanten VOC in Simulations- und Feldexperimenten**
von H. Spahn (2010), IV, 210 Seiten
ISBN: 978-3-89336-638-5

72. **Entwicklung und Charakterisierung eines metallischen Substrats für nanostrukturierte keramische Gastrennmembranen**
von K. Brands (2010), vii, 137 Seiten
ISBN: 978-3-89336-640-8

73. **Hybridisierung und Regelung eines mobilen Direktmethanol-Brennstoffzellen-Systems**
von J. Chr. Wilhelm (2010), 220 Seiten
ISBN: 978-3-89336-642-2

74. **Charakterisierung perowskitischer Hochtemperaturmembranen zur Sauerstoffbereitstellung für fossil gefeuerte Kraftwerksprozesse**
von S.A. Möbius (2010) III, 208 Seiten
ISBN: 978-3-89336-643-9

75. **Characterization of natural porous media by NMR and MRI techniques: High and low magnetic field studies for estimation of hydraulic properties**
by L.-R. Stingaciu (2010), 96 pages
ISBN: 978-3-89336-645-3

76. **Hydrological Characterization of a Forest Soil Using Electrical Resistivity Tomography**
by Chr. Oberdörster (2010), XXI, 151 pages
ISBN: 978-3-89336-647-7

77. **Ableitung von atomarem Sauerstoff und Wasserstoff aus Satellitendaten und deren Abhängigkeit vom solaren Zyklus**
von C. Lehmann (2010), 127 Seiten
ISBN: 978-3-89336-649-1

78. **18th World Hydrogen Energy Conference 2010 – WHEC2010 Proceedings**
Speeches and Plenary Talks
ed. by D. Stolten, B. Emonts (2010)
ISBN: 978-3-89336-658-3

78-1. **18th World Hydrogen Energy Conference 2010 – WHEC2010 Proceedings**
Parallel Sessions Book 1:
Fuel Cell Basics / Fuel Infrastructures
ed. by D. Stolten, T. Grube (2010), ca. 460 pages
ISBN: 978-3-89336-651-4

78-2. **18th World Hydrogen Energy Conference 2010 – WHEC2010 Proceedings**
Parallel Sessions Book 2:
Hydrogen Production Technologies – Part 1
ed. by D. Stolten, T. Grube (2010), ca. 400 pages
ISBN: 978-3-89336-652-1

78-3. **18th World Hydrogen Energy Conference 2010 – WHEC2010 Proceedings**
Parallel Sessions Book 3:
Hydrogen Production Technologies – Part 2
ed. by D. Stolten, T. Grube (2010), ca. 640 pages
ISBN: 978-3-89336-653-8

78-4. **18th World Hydrogen Energy Conference 2010 – WHEC2010 Proceedings**
Parallel Sessions Book 4:
Storage Systems / Policy Perspectives, Initiatives and Cooperations
ed. by D. Stolten, T. Grube (2010), ca. 500 pages
ISBN: 978-3-89336-654-5

78-5. **18th World Hydrogen Energy Conference 2010 – WHEC2010 Proceedings**
Parallel Sessions Book 5:
Stategic Analysis / Safety Issues / Existing and Emerging Markets
ed. by D. Stolten, T. Grube (2010), ca. 530 pages
ISBN: 978-3-89336-655-2

78-6. **18th World Hydrogen Energy Conference 2010 – WHEC2010 Proceedings**
Parallel Sessions Book 6:
Stationary Applications / Transportation Applications
ed. by D. Stolten, T. Grube (2010), ca. 330 pages
ISBN: 978-3-89336-656-9

78 Set (complete book series)

18th World Hydrogen Energy Conference 2010 – WHEC2010 Proceedings
ed. by D. Stolten, T. Grube, B. Emonts (2010)
ISBN: 978-3-89336-657-6

79. **Ultrafast voltex core dynamics investigated by finite-element micromagnetic simulations**
by S. Gliga (2010), vi, 144 pages
ISBN: 978-3-89336-660-6

80. **Herstellung und Charakterisierung von keramik- und metallgestützten Membranschichten für die CO_2-Abtrennung in fossilen Kraftwerken**
von F. Hauler (2010), XVIII, 178 Seiten
ISBN: 978-3-89336-662-0

81. **Experiments and numerical studies on transport of sulfadiazine in soil columns**
by M. Unold (2010), xvi, 115 pages
ISBN: 978-3-89336-663-7

82. **Prompt-Gamma-Neutronen-Aktivierungs-Analyse zur zerstörungsfreien Charakterisierung radioaktiver Abfälle**
von J.P.H. Kettler (2010), iv, 205 Seiten
ISBN: 978-3-89336-665-1

83. **Transportparameter dünner geträgerter Kathodenschichten der oxidkeramischen Brennstoffzelle**
von C. Wedershoven (2010), vi, 137 Seiten
ISBN: 978-3-89336-666-8

84. **Charakterisierung der Quellverteilung von Feinstaub und Stickoxiden in ländlichem und städtischem Gebiet**
von S. Urban (2010), vi, 211 Seiten
ISBN: 978-3-89336-669-9

85. **Optics of Nanostructured Thin-Film Silicon Solar Cells**
by C. Haase (2010), 150 pages
ISBN: 978-3-89336-671-2

86. **Entwicklung einer Isolationsschicht für einen Leichtbau-SOFC-Stack**
von R. Berhane (2010), X, 162 Seiten
ISBN: 978-3-89336-672-9

87. **Hydrogen recycling and transport in the helical divertor of TEXTOR**
by M. Clever (2010), x, 172 pages
ISBN: 978-3-89336-673-6

88. **Räumlich differenzierte Quantifizierung der N- und P-Einträge in Grundwasser und Oberflächengewässer in Nordrhein-Westfalen unter besonderer Berücksichtigung diffuser landwirtschaftlicher Quellen**
von F. Wendland et. al. (2010), xii, 216 Seiten
ISBN: 978-3-89336-674-3

89. **Oxidationskinetik innovativer Kohlenstoffmaterialien hinsichtlich schwerer Lufteinbruchstörfälle in HTR´s und Graphitentsorgung oder Aufarbeitung**
von B. Schlögl (2010), ix, 117 Seiten
ISBN: 978-3-89336-676-7

90. **Chemische Heißgasreinigung bei Biomassenvergasungsprozessen**
von M. Stemmler (2010), xv, 196 Seiten
ISBN: 978-3-89336-678-1

91. **Untersuchung und Optimierung der Serienverschaltung von Silizium-Dünnschicht-Solarmodulen**
von S. Haas (2010), ii, 202 Seiten
ISBN: 978-3-89336-680-4

92. **Non-invasive monitoring of water and solute fluxes in a cropped soil**
by S. Garré (2010), xxiv, 133 pages
ISBN: 978-3-89336-681-1

93. **Improved hydrogen sorption kinetics in wet ball milled Mg hydrides**
by L. Meng (2011), II, 119 pages
ISBN: 978-3-89336-687-3

94. **Materials for Advanced Power Engineering 2010**
ed. by J. Lecomte-Beckers, Q. Contrepois, T. Beck and B. Kuhn (2010), 1327 pages
ISBN: 978-3-89336-685-9

95. **2D cross-hole MMR – Survey design and sensitivity analysis for cross-hole applications of the magnetometric resistivity**
by D. Fielitz (2011), xvi, 123 pages
ISBN: 978-3-89336-689-7

96. **Untersuchungen zur Oberflächenspannung von Kohleschlacken unter Vergasungsbedingungen**
von T. Melchior (2011), xvii, 270 Seiten
ISBN: 978-3-89336-690-3

97. **Secondary Organic Aerosols: Chemical Aging, Hygroscopicity, and Cloud Droplet Activation**
by A. Buchholz (2011), xiv, 134 pages
ISBN: 978-3-89336-691-0

98. **Chrom-bezogene Degradation von Festoxid-Brennstoffzellen**
von A. Neumann (2011), xvi, 218 Seiten
ISBN: 978-3-89336-692-7

99. **Amorphous and microcrystalline silicon applied in very thin tandem solar cells**
by S. Schicho (2011), XII, 190 pages
ISBN: 978-3-89336-693-4

100. **Sol-gel and nano-suspension electrolyte layers for high performance solid oxide fuel cells**
by F. Han (2011), iv, 131 pages
ISBN: 978-3-89336-694-1

101. **Impact of different vertical transport representations on simulating processes in the tropical tropopause layer (TTL)**
by F. Plöger (2011), vi, 104 pages
ISBN: 978-3-89336-695-8

102. **Untersuchung optischer Nanostrukturen für die Photovoltaik mit Nahfeldmikroskopie**
von T. Beckers (2011), xiii, 128 Seiten
ISBN: 978-3-89336-696-5

103. **Impact of contamination on hydrogenated amorphous silicon thin films & solar cells**
by J. Wördenweber (2011), XIV, 138 pages
ISBN: 978-3-89336-697-2

104. **Water and Organic Nitrate Detection in an AMS: Laboratory Characterization and Application to Ambient Measurements**
by A. Mensah (2011), XI, 111 pages
ISBN: 978-3-89336-698-9

105. **Entwicklung eines neuen Konzepts zur Steuerung der thermischen Ausdehnung von glaskeramischen Verbundwerkstoffen mit angepasster Fließfähigkeit am Beispiel der Hochtemperatur-Brennstoffzelle**
von E. Wanko (2011), xi, 134 Seiten
ISBN: 978-3-89336-705-4

106. **Tomographic reconstruction of atmospheric volumes from infrared limb-imager measurements**
by J. Ungermann (2011), xiv, 153 pages
ISBN: 978-3-89336-708-5

107. **Synthese und Identifizierung von substituierten Mg-Al-Cl Doppelhydroxidverbindungen mit Schwerpunkt IR-Spektroskopie**
von B. Hansen (2011), XII, 121 Seiten
ISBN: 978-3-89336-709-2

108. **Analysis of spatial soil moisture dynamics using wireless sensor networks**
by U. Rosenbaum (2011), xxii, 120 pages
ISBN: 978-3-89336-710-8

109. **Optimierung von APS-ZrO2-Wärmedämmschichten durch Variation der Kriechfestigkeit und der Grenzflächenrauhigkeit**
von M. E. Schweda (2011), 168 Seiten
ISBN: 978-3-89336-711-5

110. **Sorption of a branched nonylphenol isomer and perfluorooctanoic acid on geosorbents and carbon nanotubes**
by C. Li (2011), X, 102 pages
ISBN: 978-3-89336-716-0

111. **Electron Transport in the Plasma Edge with Rotating Resonant Magnetic Perturbations at the TEXTOR Tokamak**
by H. Stoschus (2011), iv, 113 pages
ISBN: 978-3-89336-718-4

112. **Diffusion and Flow Investigations in Natural Porous Media by Nuclear Magnetic Resonance**
by N. Spindler (2011), viii, 144 pages
ISBN: 978-3-89336-719-1

113. **Entwicklung und Erprobung des Hygrometer for Atmospheric Investigations**
von T. Klostermann (2011), IV, 118 Seiten
ISBN: 978-3-89336-723-8

114. **Application of functional gene arrays for monitoring influences of plant/seasons on bacterial functions and community structures in constructed wetlands (Bitterfeld, Germany)**
by J. Ning (2011), xiv, 157 pages
ISBN: 978-3-89336-724-5

115. **Wasseraustrag aus den Kathodenkanälen von Direkt-Methanol-Brennstoffzellen**
von A. Schröder (2011), VII, 228 Seiten
ISBN: 978-3-89336-727-6

116. **CITYZEN Climate Impact Studies**
ed. by M. Schultz (2011), 45 pages
ISBN: 978-3-89336-729-0

117. **Software Tools zum interoperablen Austausch und zur Visualisierung von Geodatensätzen über das Internet**
von M. Schultz, M. Decker, S. Lührs (2011), iv, 156 Seiten
ISBN: 978-3-89336-730-6

118. **Optimierung eines Leichtbaudesigns für ein SOFC-Brennstoffzellenstack**
von T. Nguyen-Xuan (2011), III, 154 Seiten
ISBN: 978-3-89336-732-0

119. **Institute of Energy and Climate Research IEK-6:**
Nuclear Waste Management & Reactor Safety Report 2009/2010
Material Science for Nuclear Waste Management
ed. by M. Klinkenberg, S. Neumeier, D. Bosbach (2011), 242 pages
ISBN: 978-3-89336-735-1

120. **Fate of the Antibiotic Sulfadiazine in Yangtze River Sediments: Transformation, Sorption and Transport**
by N. Meng (2011), XII, 111 pages
ISBN: 978-3-89336-736-8

121. **Thermodynamische Eigenschaften gasförmiger und kondensierter Verbindungen für Hochtemperaturanwendungen**
von T. Markus (2011), II, 131 Seiten
ISBN: 978-3-89336-728-3

122. **Ein neues LIF-Instrument für flugzeug- und bodengebundene Messungen von OH- und HO_2-Radikalen in der Troposphäre**
von S. Broch (2011), IV, 160 Seiten
ISBN: 978-3-89336-742-9

123. **Processes in the Yangtze River System - Experiences and Perspectives**
Workshop-Proceedings
ed. by S. Küpper, G. Subklew, R.-D. Wilken (2011), 83 pages
ISBN: 978-3-89336-744-3

124. **Thermo-Mechanical Properties of Mixed Ion-Electron Conducting Membrane Materials**
by B. Huang (2011), 130 pages
ISBN: 978-3-89336-746-7

125. **Growth, Etching, and Stability of Sputtered ZnO:Al for Thin-Film Silicon Solar Cells**
by J. I. Owen (2011), xv, 192 pages
ISBN: 978-3-89336-749-8

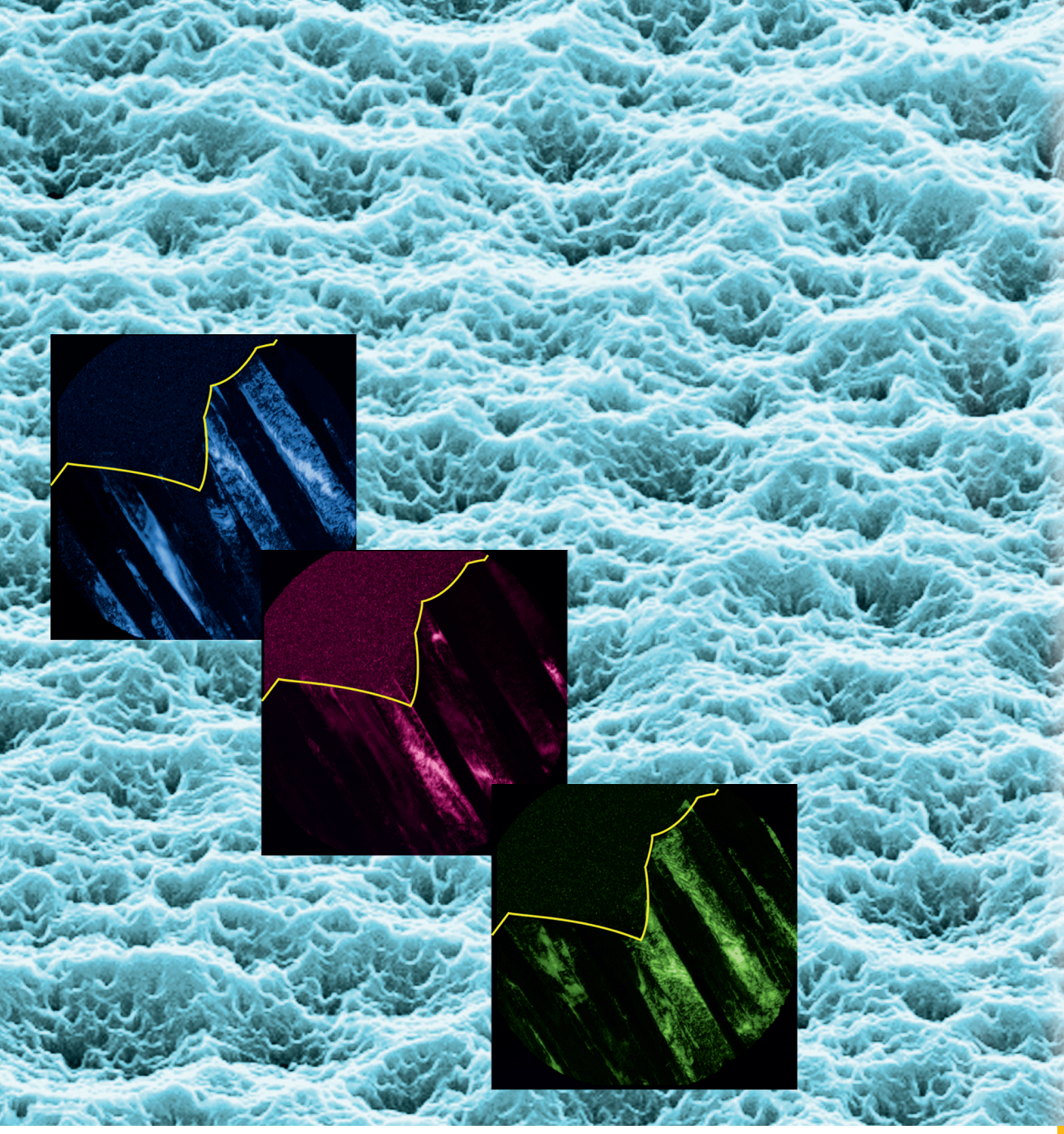

Energie & Umwelt / Energy & Environment
Band / Volume 125
ISBN 978-3-89336-749-8

JÜLICH
FORSCHUNGSZENTRUM